



ScuDo

Scuola di Dottorato ~ Doctoral School

WHAT YOU ARE, TAKES YOU FAR



Doctoral Dissertation
Doctoral Program in Chemical Engineering (32th Cycle)

Supramolecular functionalization of graphene related materials for heat transfer applications and devices

Giuseppe Ferraro

* * * * *

Supervisors

Prof. A. Fina, Supervisor

Doctoral Examination Committee:

Prof. Orietta Monticelli, Università di Genova

PhD. Manuela Melucci, ISOF-Consiglio nazionale delle ricerche

PhD. Simelys Pris Hernandez Ribullen, Politecnico di Torino

Prof. Nunzio Russo, Politecnico di Torino

Prof. Pasquale Longo, Università degli studi di Salerno

Politecnico di Torino

July 21, 2020

This thesis is licensed under a Creative Commons License, Attribution - Non-commercial - No Derivative Works 4.0 International: see www.creativecommons.org. The text may be reproduced for non-commercial purposes, if credit is given to the original author.

I hereby declare that, the contents and organization of this dissertation constitute my own original work and does not compromise in any way the rights of third parties, including those relating to the security of personal data.

.....
Giuseppe Ferraro
Turin, July 21, 2020

Summary

The thermal management in flexible electronic devices requires new materials able to dissipate heat to guarantee for the required lifetime and continuously increasing performance of modern electronic devices.

In recent years, Graphene, which is an allotrope of carbon in form of two- hexagonal lattice in which one atom forms each vertex, has generated a great interest for its unique mechanical, electrical and thermal proprieties. Despite this material is mainly used for electronic and optoelectronic applications, because the production cost is still relatively too high, graphene related materials (GRM) have being exploited are being increasingly exploited.

In fact, graphene research projects around the world are still growing due to the great impact of graphene results and applications. In Europe it has reached its peak in research funding since the European Commission decided to support the Graphene flagship which is the European largest research initiative, tasked with taking graphene from laboratories into the market with 1 billion budget over ten years. The Graphene flagship project includes more than 150 European industrials and academic partners and it involve 16 Work Packages covering almost all areas of graphene from fundamental science to scientific research for industrial applications from health to environment and electronics.

A strong interest in the use of these materials is found in heat management application where both increasingly efficient materials and mechanical characteristics such as flexibility are required. For some years now, in fact, heat spreader GRM based have been developing with thermal conductivity characteristics superior to the most commercially used metals (copper and aluminum) and, at the same time, they have lower density with a consequent greater lightness considering an equal geometry.

Although at microscopic level, the single graphene surface shows thermal conductivity values in the order of miles $\text{Wm}^{-1}\text{K}^{-1}$, the relative macroscopic

artefacts (such as foils or self-supporting membranes) show values much lower than the ideal case caused by defects that may be chemical or physical. The first ones are given by the presence of functional groups or atomic species that interacting with covalent bonds change the hybridization of carbon and therefore interrupt the aromaticity of the material that is the most responsible for the heat transfer. Physical defects, instead, are related to the quality of the material, so not only to the presence of vacancies but also to the surface area, surface/volume ratio, edges, number of layers. Moreover, the quality of the thermal contact between structures and the porosity of the material must also be considered in the manufacture of macrostructures.

Post-treatments are widely used such as thermal annealing, to regenerate sp^2 -hybridization of the graphene plane but, on the other hand, they take place at very high temperatures, increasing the production considerably. Therefore new methods of synthesis are being explored.

Although studies of molecular dynamics and the functional theory of density have theoretically demonstrated the efficacy of molecular junctions, only in recent times, these researches have been developing on graphene materials where the functionalization at the edges, which covalently links several structures, improves heat transfer. An alternative method for the GRM functionalization, that does not introduce chemical defects and preserves the aromatic network, exploits π - π stacking between the surface and the polycyclic aromatic compounds.

In this thesis, both approaches have been used to connect GRM structures aiming at decreasing the thermal resistance at the interface and extending the surface through which heat can be transmitted. The first method exploits the functionalization of graphene-related materials at the edges with bi-functional molecules of different lengths derived from maleic anhydride, in order to investigate the thermal conductivity of these structures connected to themselves with molecular bridges. The Diels Alder reaction has been exploited and Raman spectroscopy characterizations and thermo gravimetric analysis confirmed the functionalization of GnP that was used as raw material for the production of films. The second approach, instead, exploits the supramolecular interactions between graphene related materials and bispyrene-based compounds spaced by aliphatic chains with different lengths. The specifically synthesized bispyrene molecules have the terminal pyrene groups that act as an anchor group to link different GnP during the fabrication process, which has been studied by spectroscopic characterizations (UV-Vis and photoluminescence on dispersion).

Using these functionalized GRMs, the nanopapers have been manufactured using a gravimetric filtration process and tested as heat spreaders. Through light

flash analysis, the thermal diffusivity (that expresses the rate of heat spread) has been studied and considering the nanopapers as porous materials, different models were applied to investigate the relationship between porosity and thermal conductivity of the materials that has been experimentally demonstrated.

By simulating the heating of an electronic component into a device and how it should be cooled, the behaviour of nanopapers for cooling a hot spot was compared with both copper and aluminium heat spreaders. Moreover, from the analysis of thermal gradients and the application of classical mathematical models of finned surfaces it has been possible to understand how the rough surface of nanopapers may affect the heat exchange coefficient with the surround obtaining more performing heat spreader than metallic ones.

Acknowledgment

First, I would like to thank my supervisor Prof. Alberto Fina and PhD Maria del Mar Bernal for their help and support to develop new research skills.

This work has received funding from the European Research Council (ERC) under the European Union's Horizon 2020 research and innovation programme grant agreement 639495 — INTHERM — ERC-2014-STG.

Un riconoscimento particolare va ai miei genitori (la Giaquinta, e Amberogeo) e al mio fratello Luchino, che mi hanno sempre sostenuto soprattutto nei momenti più difficili e senza i quali non sarei mai arrivato a simile risultato. Ringrazio anche il resto della famiglia come nonne, zii e cugini ed in particolare ad Enrico per avermi sempre consigliato come un fratello.

Ringrazio i miei amici di una vita che mi hanno sostenuto e mi accompagnano in questa crescita, in particolare Franca e Marco, il piccolo Megna (il compare) e Nicolette (la commare con la mia nipotina bedda Elenuccia), Giorgio (JJ. Megna) e Ilaria (ilavia), Peppino (gentile) e Elisa, Mario (u Fichera), Alessio (ssiò), Mirkuzzo e Marica (e Martuccia), Sofia, Paolina, Nicolle (hiicolle), Salvatore (Contra), Joshua, Livio, Massimo (Max) e Donatella (Dona), Peppe Cataldo e tutti coloro che ho scordato di menzionare ma non per questo di minor importanza.

Dei ringraziamenti particolari vanno a Sergio (master), Paola (proffi) e Jinhyung (Ginocchiello), che oltre ad essersi dimostrati amici sono anche dei mentori di vita e che mi hanno guidato sia professionalmente che al di là del contesto accademico.

Voglio essere riconoscente alle persone conosciute durante questi anni in un contesto universitario ma da cui è nata una bella amicizia e in particolare modo a Matteo, Martina (smarty), Michele (il mister), a Michela (il capo), Simone (il Galliano), Fede Bella (presidente e prof), Francesca (Colò), Marisa, Chiara (Novara).

Voglio ringraziare anche i compagni di laboratorio con cui ho condiviso momenti meravigliosi ovvero Sergio (Gegio), Mattia (l'asesur), Matteo (uccio), Francesco (Checco), Erica (Puddu), Ale (ivo) e Vale (pigro), Lorenza, Alessandra, Amir, Andrea (Pisa), Chiara (ciao), Daniele (il Batte), Federico (Carosio), Federico

(Gobber), Emilio, Emir e Elisa, Ewa (bon-giorno), Fabio, Giusy, Marco (Barbalini), Rossella, Samu (Walter), Samu (Colonna), Silvia, Fiorella e Diego e tutti coloro che non ho menzionato ma che sono stati comunque presenti.

Non scorderò mai i ragazzi di holle con cui siamo rimasti vicini nonostante la distanza fisica che ci si separa, in particolare Teresa (terry terrina terrona) e Riccardo (Mane), Maria (marymary), Marco (mpare focs), Alessandra, Alessandro (Piedino), Lorenzo (i Barnino), Zeno (Zen Arper), Peppino e tutti coloro che mi son dimenticato di citare ma a cui va un caloroso abbraccio.

Un'infinita riconoscenza va anche agli amici del vecchio laboratorio di organica e ai politronici senza i quali non avrei mai appreso tutte quelle conoscenze fondamentali per arrivare a questo risultato. In particolar un grazie a Paola (Martino), Jessica, Marco (C8), Paolo, Alessandro, Vincenzo (Max), Claudio (maestro α), Emma, Alessandra, Sara (Sarita), Natalia, Nadia e Roby.

Infine tutti coloro che mi sono dimenticato di menzionare ma che comunque con la loro compagnia mi hanno rallegrato in questo periodo così importante della mia vita (amici, parenti, conoscenti e macari cu nun ci trasi nenti).

*Fatti non foste a viver
come bruti ma a seguir
virtute e canoscenza*

Alla mia famiglia

Contents

1. State of the art	1
1.1. Graphene Related Materials	1
1.1.1. Synthesis.....	3
1.1.2. Properties & Applications	12
1.1.3. Chemical Functionalization.....	14
1.2. Heat spreading devices	19
1.2.1. Heat transfer fundamentals	21
1.2.2. Materials for heat spreader	30
2. Materials & Methods	45
2.1. Synthesis procedure	46
2.1.1. Synthesis of bispyrene molecules.....	46
2.1.2. Synthesis of mono-pyrene molecules	46
2.1.3. Synthesis of bismaleimide molecules	47
2.1.4. Functionalization of GnP with bis or mono-pyrene derivatives	
48	
2.1.5. GnP/Bismaleimide derivatives	49
2.1.6. GnP nanopaper	49
2.2. Characterization techniques.....	50
2.2.1. Characterization of pyrene compounds	50
2.2.2. Characterization of bismaleimide	51
2.2.3. Characterization GnP/BP	51
2.2.4. Characterization of GnP /bismaleimide derivate	52
2.2.5. Characterization of GnP Nanopapers.....	53
3. Chemical functionalization of graphite nanoplatelets	59
3.1. Supramolecular functionalization of graphite nanoplatelets	60

3.1.1.	Synthesis.....	60
3.1.2.	Interaction BP/GnP.....	67
3.2.	Functionalization via Diels Alder reaction.....	75
3.2.1.	Synthesis of bismaleimide.....	75
3.2.2.	Interaction BI/GnP.....	83
4.	Graphite nanoplatelets nanopapers.....	87
4.1.	Morphological characterization.....	87
4.1.1.	Electron Microscopy.....	87
4.1.2.	XRD.....	92
4.2.	Thermal conduction proprieties.....	95
4.2.1.	Thermal diffusivity.....	95
4.2.2.	Thermal conductivity.....	99
5.	Heat spreader with GnP nanopapers.....	104
5.1.	Temperature vs time profile.....	104
5.2.	Thermal gradients.....	106
6.	General conclusions.....	111
7.	Appendix (i).....	115
7.1.	NMR spectra of BP.....	115
7.2.	NMR Spectra of BI.....	119
7.3.	NMR spectra of MP.....	122
7.4.	Nanopaper with MP.....	123
8.	References.....	125

List of Tables

Table 1. Solvents for LPE of Graphene.....	11
Table 2. Properties of typical Heat Spreader Materials [125].	32
Table 3. Comparison GRM intrinsic thermal conductivities.....	33
Table 4. Milligrams of molecule obtained and yield of the reaction.....	67
Table 5. Calculation of the mass fraction and mass of C2 absorbed by GnP.	71
Table 6. Comparison between I12 FTIR analyses with those of its reagent. .	81
Table 7. Thermal diffusivities of nanopapers.	98
Table 8. Thermal proprieties comparison between nanopapers with Aluminum and Copper.....	101
Table 9. Thermal diffusivities and thermal conductivities values of nanopapers pressed at different force.....	101
Table 10. Calculation of the mass fraction and mass of MP absorbed within nanopaper.....	124

List of Figures

Figure 1. Schematic representation how graphene is the 2D materials useful for the development of other dimensionalities such as 0D if it isotropic wrapped into fullerene class, rolled in 1D to perform nanotube, stacked into 3D leading the commonly graphite [3].....	2
Figure 2. Representation of different edge geometry. Armchair termination on the left and zigzag on the right.....	2
Figure 3. Idealized structure of Graphene Oxide (GO).....	3
Figure 4. Schematic classification of graphene-related materials (GRM) and methods for their production.....	4
Figure 5. Schematic illustration of an epitaxial growth from a SiC substrate. Heating a SiC substrate under UHV there is the sublimation of silicon, firstly, and carbon atoms remains on the surface organized themselves into graphene structure.	5
Figure 6. Schematic representation of methane catalytic decomposition to form C_xH_y species upon the exposure of Cu and hydrogen. Where the local concentration of C_xH_y is supersaturated, there is the formation of nuclei carbon based that grow more and more, creating domain and covering the Cu surface since to obtain a thin film [17].	6
Figure 7. Schematic representation of a mechanical exfoliation process shown step by step: (a) adhesive tape is pressed against a HOPG surface to adhere to the top. (b) Few layers are cleaved from graphite crystal. (c) The tape with some layer of material is pressed against to the surface of a substrate. (d) Upon peeling off, the bottom layer is left on the substrate [20].	7
Figure 8. Schematic representation of graphene sheets exfoliation and dispersion: graphite planes are expanded using acids solution and solvothermal process is processed to divide sheets between themselves. Several steps of	

centrifugation at different rpm are done in order to separate flakes having different size [24].....	8
Figure 9. Schematic representation of production of GO, FLGO or MLGO...9	
Figure 10. Schematic representation of deoxygenation with thermal treatment.	9
Figure 11. Images of the exfoliated graphite oxide suspension with and without deoxygenation step under reaction alkaline conditions.	10
Figure 12. (a) Functionalization of GRM for detection of chemical species such as organic compounds or inorganic ones like ions or metals. (b) Solar cell graphene based. (c) Aerogel graphite based. (d) Optical fibres. (e) Printed electronic circuits with ink graphene based. (f) Flexible devices.	13
Figure 13. Schematic illustration of grafting a diazonium salt with functional group R.	15
Figure 14. GRM functionalized with a specific dienophile, maleic anhydride (MA) or maleimide (MI) after the Diels Alder reaction.	16
Figure 15. a) π - π interactions between benzene, naphthalene, or pyrene molecules above and below the basal plane of graphene. b) Schematic representation of both hydrogen bonds and/or π - π stacking with GO [92].	18
Figure 16. Different types of heat spreader. a) Heat pipe. b) Vapour chamber. c) Planar heat exchanger. d) Heat sink.	21
Figure 17. Longitudinal fin of rectangular profile.	29
Figure 18. General representation of a radial fin.....	30
Figure 19. Schematic representation of spray deposition technique. GRM dispersion droplets are generate mechanically by a gas into the spray gun. Then they are deposited onto the substrate that could be heated to evaporate the solvent.	35
Figure 20. Schematic representation of spin coating technique. a) Droplets GRM dispersion are deposited onto the disk. b) The disk start to rotate and the GRM move from the center to the edges while the solvent evaporates.....	36
Figure 21. a) Schematic representation of self-assembly process from solvent's evaporation in static condition. (b) Tape casting industrial method to obtain GRM films in continuous process.....	38
Figure 22. Representation of the ESD system (on the left) and the implementation of roll-to-roll technique for a continuous industrial process for the bulk production of paper GRM based.....	39
Figure 23. Schematic representation of vacuum filtration consisting of a glass filter holder assembly with funnel (1), metallic clamp (2), filtered base (3), stopper rubber base (4), and a vacuum filtering flask	39

Figure 24. General representation of mechanism that regulate the formation of membrane GRM based and relative orientation of flakes inside the films. In the mechanism 1, there is a high alignment of flakes due to slowly filtration promoting the stacking and further precipitation. The mechanism 3 shows the randomly displacement as result of a faster filtration process while mechanism 2 is the optimal filtration rate which makes films organized as well as to the first mechanism, reducing at the same time the process timing.	41
Figure 25. SEM analysis that shows the alignment of GOs within a membrane produced by filtration.....	41
Figure 26. Representation of different dispersions GRM based and relative hybrid films. (a) Process that use QDs (b) CNTs (c) CNRs	43
Figure 27. Selective functionalization at the edges of GnP. a) Functionalization with phenol to exploit the hydrogen bond. b) Functionalization with di-aniline to covalently link the GnP.....	44
Figure 28. Schematic illustration of approach to functionalize the GRM. a) Supramolecular interaction between bispyrene molecules and surface of GnP. b) Diels Alder reaction between the edge of GRM and bismaleimide.	45
Figure 29. Schematic representation of bispyrene molecules synthesis	46
Figure 30. Schematic representation of mono-pyrene molecules synthesis...47	
Figure 31. Schematic representation of the first reaction step for the synthesis of bismaleimide molecules.	47
Figure 32. Schematic representation of the second reaction step for the synthesis of bismaleimide molecules.....	48
Figure 33. Radial fin of rectangular profile.....	58
Figure 34. Schematic representation of supramolecular functionalization of graphene with bispyrene derivate (a) and Diels Alder reaction between the edges of graphene and bismaleimide.	59
Figure 35. Synthesis of bispyrene molecules	60
Figure 36. ¹ H NMR spectrum of C2 in DMSO-d ₆	61
Figure 37. ¹³ C NMR spectrum of C2 in DMSO-d ₆	61
Figure 38. Theoretical prediction of ¹³ C-NMR C2.	62
Figure 39. ESI ⁺ MS spectrum of C2 in methanol.....	63
Figure 40. ESI ⁺ MS spectrum of C4 in methanol.....	64
Figure 41. ESI ⁺ MS spectrum of C6 in methanol.....	65
Figure 42. ESI ⁺ MS spectrum of C8 in methanol.....	66
Figure 43. ESI ⁺ MS spectrum of C12 in methanol.....	66
Figure 44. a) GnP dispersions prepared at different concentrations of C2 in DMF. Inside the beakers the suspensions were left to decant for one hour and it can	

be observed that as the molar concentration of C2 increases, the quantity of GnP precipitated on the bottom increases. b) The solutions and suspensions were lightened at a wavelength of 254 nm and it can be seen that the solution at concentration 10^{-4} does not emit in the visible contrary to its suspension which instead provides a light signal.....68

Figure 45. C2 solution absorbance in DMF at different concentration.....69

Figure 46. Absorption spectra of GnP and GnP C2 at different concentrations of C2 in DMF. Inset shows a magnification of the 600-750 region.70

Figure 47. a) Fluorescence spectra ($\lambda_{ex} = 345$ nm) of GnP and GnP C2 at different concentrations of C2 in DMF. Inset shows the fluorescence spectra of C2 at the initial concentrations in DMF. b) I_E/I_M ratio for C2 molecule in DMF and for GnP C2 dispersions.....71

Figure 48. Comparison between Raman Spectra of GnP and GnP C2 powders.72

Figure 49. a) Comparison of UV spectra of solutions ($5 \cdot 10^{-5}$ M) bispyrene based in DCM. b) Comparison between UV-Vis spectrum of solutions bispyrene based and Pyrene one.....73

Figure 50. a) Photographs of GnP/BP dispersions and relative scattering of light as a laser beam passes through a colloid (Tyndall effect). b) UV-Vis Absorption of supernatants.74

Figure 51. Comparison between the fluorescence emission spectra of BP (a) and their corresponding GnP BP dispersions (b).....74

Figure 52. Raman spectra of GnP and GnP BP.....75

Figure 53. Synthesis of diacid derivate76

Figure 54. Synthesis of bismaleimide molecules – step 2.....77

Figure 55. $^1\text{H-NMR}$ spectrum of 1,1'-(ethane-1,2-diyl)bis(1H-pyrrole-2,5-dione) (I2).77

Figure 56. $^1\text{H-NMR}$ spectrum of 1,1'-(butane-1,4-diyl)bis(1H-pyrrole-2,5-dione) (I4).78

Figure 57. $^1\text{H-NMR}$ spectrum of 1,1'-(hexane-1,6-diyl)bis(1H-pyrrole-2,5-dione) (I6).78

Figure 58. $^1\text{H-NMR}$ spectrum of 1,1'-(octane-1,8-diyl)bis(1H-pyrrole-2,5-dione) (I8).79

Figure 59. $^1\text{H-NMR}$ spectrum of 1,1'-(dodecane-1,12-diyl)bis(1H-pyrrole-2,5-dione) (I12) in DMSO.....80

Figure 60. FTIR spectra comparison between the I12, 1,12-Diaminododecane and Maleic anhydride.....80

Figure 61. Comparison between FTIR spectra of different BI.....83

Figure 62. TGA results to quantify the functionalization with I12 in comparison to GnP MA and GnP pristine.	85
Figure 63. Raman Spectra comparison between GnP pristine and GnP functionalized with MA or with I12 at different concentration.....	86
Figure 64. FESEM topography analysis of nanopaper fabricated with different molar concentration of C2. a) Nanopaper from GnP pristine (the blank). b) Nanopaper obtained from GnP containing 10^{-6} M of C2. c) Surface topography of nanopaper fabricated with a 10^{-5} M of C2. d) Surface topography of nanopaper fabricated with a 10^{-4} M of C2 where it is possible to observe aggregates of C2.	88
Figure 65. Surface topographies of nanopapers manufactured with GnP BP.	89
Figure 66. Cross Section FESEM analysis of GnP BP nanopaper.....	90
Figure 67. FESEM analysis comparisons of nanopapers manufactured with pristine GnP, those with GnP MA and GnP I12 ones. a, b, c show the surface topographies to evaluate the presence of aggregates while d, e and f show the cross-sections analysis to evaluate both the alignment of the flake and to measure the thickness for densities calculation.	91
Figure 68. Schematic representation of gonio-configuration to monitor the 002 peak of graphite for the evaluation of preferential flake's orientations. Diffraction condition detecting graphite flakes having 0° tilt angle (a), 45° tilt angle (b) and 90° tilt angle (c).....	92
Figure 69. a) Fitting of experimental curves obtained varying the tilt angle from which detect the signal 002 of graphite (centered at $2\theta=26.6$). b) Probability vs tilt angle of flakes within nanopapers.	93
Figure 70. Pareto cumulative distribution for the quantification of preferential orientations of flakes and comparison between GnP-bispyrene nanopapers and pristine GnP.	94
Figure 71. BP retaining rate and mass fraction of BP in the series of GnP-bispyrene nanopapers.....	94
Figure 72. TGA of nanopaper manufactured with GnP MA and GnP I12 at different concentrations in comparison to nanopaper based on GnP Pristine.	95
Figure 73. In-plane and cross-plane thermal diffusivities for GnP and GnP BP nanopapers	96
Figure 74. Thermal diffusivities comparison between nanopapers at different concentration of C2.....	97
Figure 75. Mono pyrene derivate. a) Pyrene butyric acid with a terminal polar group. b) The N-dodecyl-4-(pyren-1-yl)butanamide with hydrophobic terminal group.	98

Figure 76. Cross plane and in plane thermal diffusivity comparison of pure GnP and functionalized GnP with either MA or I12 at different concentrations. .	99
Figure 77. Equation of theoretical models used to investigate the effect of porosity within the nanopaper and their plotting in comparison to experimental points.....	102
Figure 78. Thermal conductivity of nanopapers obtained by applying of the linear model for porous materials in comparison with values of copper and aluminum.	103
Figure 79. Set Up for the measurement of thermal properties as heat spreader	104
Figure 80. Temperature vs time profile of hotspot, as such or in the presence of different types of foils used as heat spreader.....	105
Figure 81. IR - thermal images acquired in the initial stages of heating (0.30 seconds and 60 seconds respectively) and cooling (300, 330 and 360 seconds) for comparing the thermal gradients of systems in which there are heat spreaders fabricated with different materials.	107
Figure 82. Thermal gradient's comparison between Copper and heat spreaders based on pristine GnP and GnP C2 one. a) Thermal imaging at 300 seconds of selected heat spreader in order to extrapolate the temperature values. b) Average calculate long three direction for each sample. (c) Comparison between the thermal gradient fitted with exponential decay curves and relative decay rate values.	108
Figure 83. Approach of a finned surface applied to nanopapers. a) Experimental set-up. b) Radial fin with rectangular profile.	109
Figure 84. a) Thermal maps at 300 s. b) average of the experimental thermal gradient (black curve) and the fitting of the differential equation of Bessel function (blue curve). c) Comparison between parameters of fins made with copper and those carbons based.....	110
Figure 85. ¹ H NMR spectrum and peak assignment of N,N'-(butane-1,4-diyl)bis(4-(pyren-1-yl)butanamide) (C4).....	115
Figure 86. ¹ H NMR spectrum and peak assignment of N,N'-(hexane-1,6-diyl)bis(4-(pyren-1-yl)butanamide) (C6).....	115
Figure 87. ¹ H-NMR spectrum and peak assignment of N,N'-(octane-1,8-diyl)bis(4-(pyren-1-yl)butanamide) (C8)	116
Figure 88. ¹ H-NMR spectrum and peak assignment of N,N'-(dodecane-1,12-diyl)bis(4-(pyren-1-yl)butanamide) (C12).....	116
Figure 89. ¹³ C-NMR spectrum of C4. Comparison between ppm measured experimentally (black) and those extrapolated by software (blue).....	117

Figure 90. ¹³ C-NMR spectrum of C6. Comparison between ppm measured experimentally (black) and those extrapolated by software (blue).	117
Figure 91. ¹³ C-NMR spectrum of C8. Comparison between ppm measured experimentally (black) and those extrapolated by software (blue).	118
Figure 92. ¹³ C-NMR spectrum of C12. Comparison between ppm measured experimentally (black) and those extrapolated by software (blue).	118
Figure 93. ¹ H-NMR spectrum of (2Z,2'Z)-4,4'-(ethane-1,2-diylbis(azanediyl))bis(4-oxobut-2-enoic acid) (N2).	119
Figure 94. ¹ H-NMR spectrum of (2Z,2'Z)-4,4'-(butane-1,4-diylbis(azanediyl))bis(4-oxobut-2-enoic acid) (N4).	119
Figure 95. ¹ H-NMR spectrum of (2Z,2'Z)-4,4'-(hexane-1,6-diylbis(azanediyl))bis(4-oxobut-2-enoic acid) (N6).	120
Figure 96. ¹ H-NMR spectrum of (2Z,2'Z)-4,4'-(octane-1,8-diylbis(azanediyl))bis(4-oxobut-2-enoic acid) (N8).	120
Figure 97. ¹ H-NMR spectrum of (2Z,2'Z)-4,4'-(dodecane-1,12-diylbis(azanediyl))bis(4-oxobut-2-enoic acid) (N12).	121
Figure 98. ¹ H-NMR spectrum of N-dodecyl-4-(pyren-1-yl)butanamide. ...	122
Figure 99. ¹³ C-NMR spectrum of N-dodecyl-4-(pyren-1-yl)butanamide. ...	122
Figure 100. FESEM Analysis of nanopapers manufactured with GnP functionalized with MP molecules. a) Surface topography of nanopaper manufactured with GnP Py-COOH. b) Cross section analysis of GnP Py-COOH film. c) Surface topography of nanopaper fabricated with GnP Py-CONH. b) Cross section measurement of GnP Py-CONH film.	123

List of Acronyms

0D	Zero dimension material
2D	Bidimensional material
3D	Three-dimensional material
AFM	Atomic Force Microscopy
BI	Bismaleimide
BP	Bispyrene
CDCl ₃	Deuterocloroform
CNTs	Carbon nanotubes
CVD	Chemical Vapour Deposition
DCM	Dichloromethane
DMF	N,N-dimetilformammide
DMSO	Dimethyl Sulfoxide
DMSO-d ₆	Dimethyl Sulfoxide deuterated
ESD	Electrospray deposition
ESI	Electrospray ionization
FESEM	Field Emission Scanning Electron Microscopy
FLG	Few Layer Graphene
FLGO	Few layer Graphene Oxide
FTIR	Fourier Transform Infrared
GnP	Graphite nano-Platelet
GO	Graphene Oxide
GRM	Graphene Related Materials
HOPG	High Oriented Pyrolytic Graphene
LC-MS	Liquid Chromatography coupled Mass Spectroscopy
LFA	Light Flash Analysis
LPE	Liquid Phase Extraction
MA	Maleic Anhydride

MD	Molecular Dynamics
MI	Maleimide
MLG	Multi-Layer Graphene
MLGO	Multi-Layer Graphene Oxide
NMP	N-Methyl-2-pyrrolidone
NMR	Nuclear Magnetic Resonance
PAHs	Polycyclic Aromatic Hydrocarbons
PTFE	Polytetrafluoroethylene
rGO	reduced Graphene Oxide
SEM	Scanning Electron Microscopy
TCE	Thermal Expansion Coefficient
TGA	Thermo Gravimetric Analysis
UHV	Ultrahigh Vacuum
UV-Vis	Ultraviolet-visible
XRD	X-ray Diffraction

Chapter 1

State of the art

1.1. Graphene Related Materials

In nature, carbon is one of the most widespread elements and is undoubtedly present in the most heterogeneous compounds. The possibility of bonding with a high variety of atoms and to form single, double or even triple bonds widens the range of possible structures. When the carbon is bound with other carbon atoms to create organized structure along the three dimensions, called allotropic forms.

Among allotropic forms of carbon, graphene has received and is attracting particular interest since its isolation from bulk graphite in the early 2004 [1].

Graphene is a material composed of carbon atoms bound together to form a two-dimensional planar structure organized with a hexagonal honeycomb geometry, in which each carbon atom is able to bind to three adjacent atoms (sp^2 -bonded), that is not an integral part of a bulk carbon material, but is freely suspended or adhered on a foreign substrate [2].

This honeycomb structure is the basis of other allotropes of carbon such as fullerenes, carbon nanotubes and graphite as show in the Figure 1.

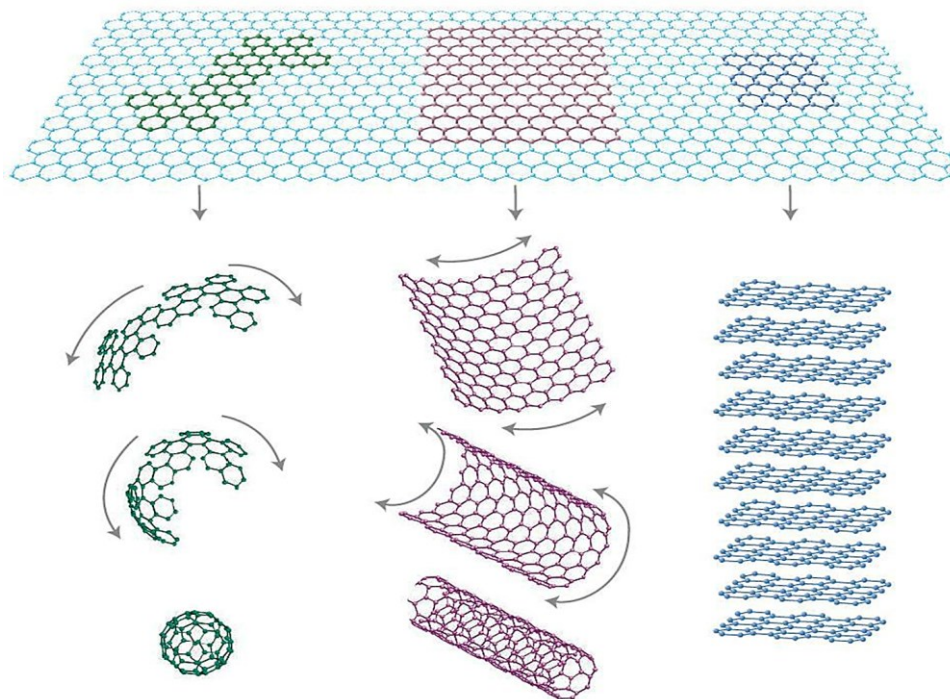


Figure 1. Schematic representation how graphene is the 2D materials useful for the development of other dimensionalities such as 0D if it isotropic wrapped into fullerene class, rolled in 1D to perform nanotube, stacked into 3D leading the commonly graphite [3].

However, concerning to graphene sheets that are all equal in the surface, a distinction must be made about chirality of two different types of edge (armchair or zigzag show in the Figure 2) because it is one of the fundamental parameters to then obtain nanotubes [4].

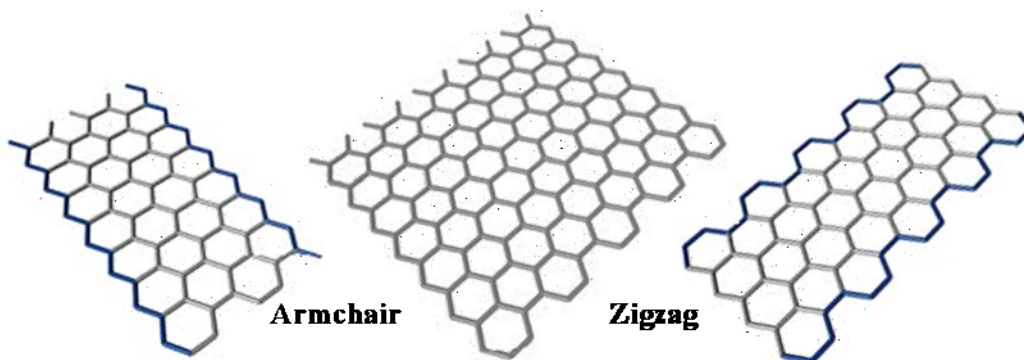


Figure 2. Representation of different edge geometry. Armchair termination on the left and zigzag on the right

The growing demand for graphene pushed the research to the development of many synthesis methods for large-scale production of graphene but, on the other hand, materials constituted by multi-layer are also available and it is therefore necessary to introduce a nomenclature [2] in order to distinguish and to classify the different products [5].

- Multi-layer graphene (MLG) is a 2D material consisting of well-defined, countable, stacked graphene layers (between 2 and 10);
- Few-layer graphene (FLG) is a sub category of MLG indicating a 2D material with 2-5 stacked layers of graphene;
- Graphite nanoplatelets (GnP): is a carbon material having a thickness less than 100 nm.

Among the most interesting graphene materials is graphene oxide (GO), which is the partially oxidized form of graphene (Figure 3) in which the carbon atoms are not always hybridized sp^2 but in some cases the hybridization is sp^3 and this determines a deformation of the structure with some bond partly tetrahedral [6].

GO can be considered as graphene sheets decorated with functional groups containing oxygen, in which hydroxyl, epoxy groups are located on sp^3 -hybridized carbon on the basal plane, and carbonyl or carboxyl groups are mainly located at the sheet edges on sp^2 -hybridized carbon.

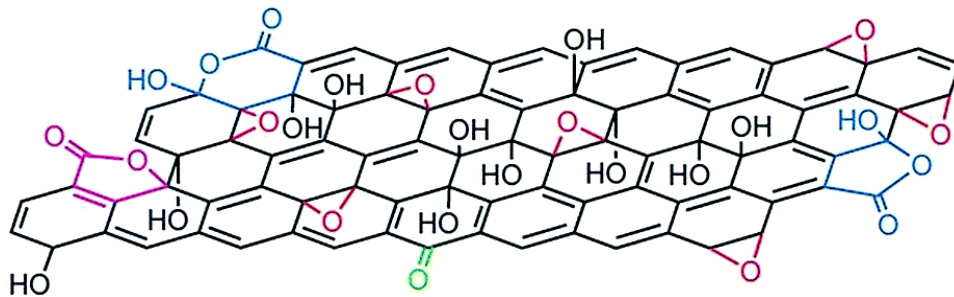


Figure 3. Idealized structure of Graphene Oxide (GO)

A similar classification can also be applied to GRM based on graphene oxide, therefore, GO is a monolayer of graphene oxide, FLGO is the few layers graphene oxide and MLGO is multi-layer graphene oxide.

Reduced Graphene Oxide (rGO) indicates an oxidized graphene material that has undergone a reduction process (thermal, chemical, etc.) in order to eliminate oxidation and restore the graphene aromaticity. The structure of rGO is very similar to the GO structure but instead of the oxidized groups structural defects of various nature are created such as vacancies and Stone-Wales defects [7].

1.1.1. Synthesis

Many techniques have been developing for large-scale production and/or cost-containment, which can be divided into two macro-areas, according to bottom-up

approach or top-down one (as show in the Figure 4). Some of them will be further described in this section.

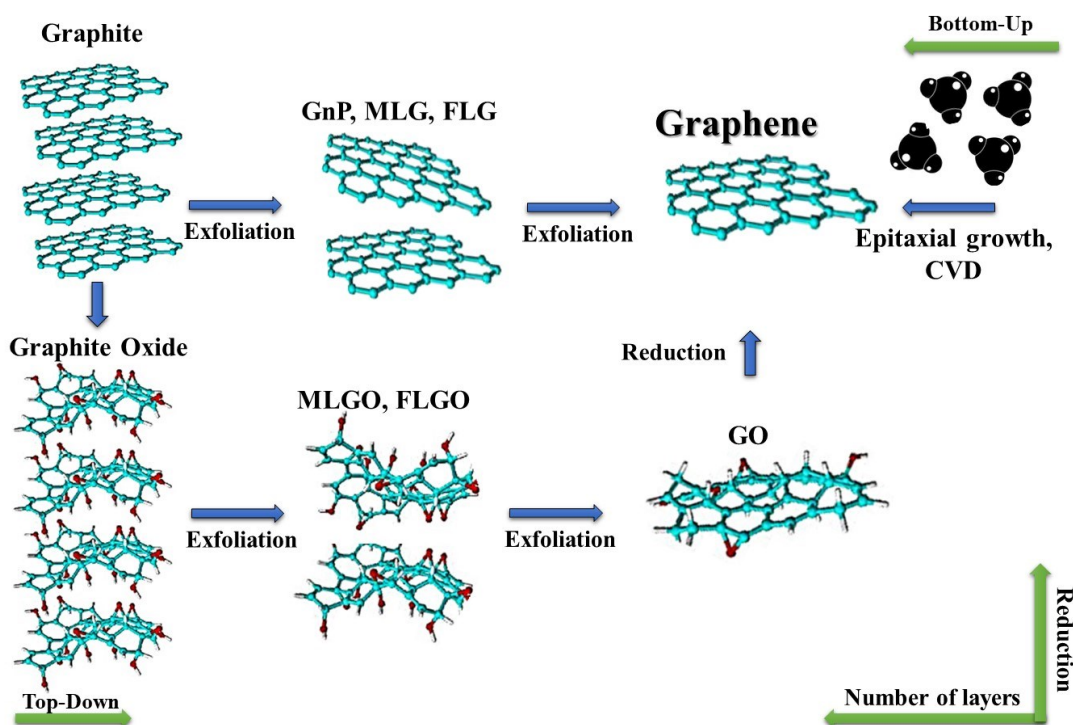


Figure 4. Schematic classification of graphene-related materials (GRM) and methods for their production.

Epitaxial growth

Epitaxial growth is one of most interesting approach, especially attractive for semiconductor companies, to produce few layer graphene. It start from the annealing of SiC surface under ultrahigh vacuum (UHV) (Figure 5). When SiC substrate is heated, silicon atoms sublime from the substrate leaving carbon atoms to rearrange themselves into graphene layers whose thickness depend on the annealing time (few minutes) and temperature (about 1200°C).

Nevertheless, more recently, vapor phase annealing has been used to produce FLG onto SiC surface using higher temperature (around 1500°C and always under UHV) but in the other hand, with an improved thickness homogeneity [8].

This method is also applied to other substrates, such as (001) faces of Ru crystals [9] , Ir, Ni, Co, and Pt [10] in order to grow epitaxial graphene layers, because the high number of nucleation's center allowed a dimensions growth into macroscopic single-crystalline domains and, more important, if the first two graphene layers coupled strongly to the substrate, while from the third layer there aren't interaction and had the similar electronic proprieties to free-standing graphene.

Although the quality of graphene under low-temperature processes still have to be improve in comparison to other technologies, the epitaxial growth is promising fabrication method because it is easily available to the semiconductor industry, transistors, and other electronic devices, which already use SiC wafer as substrate.

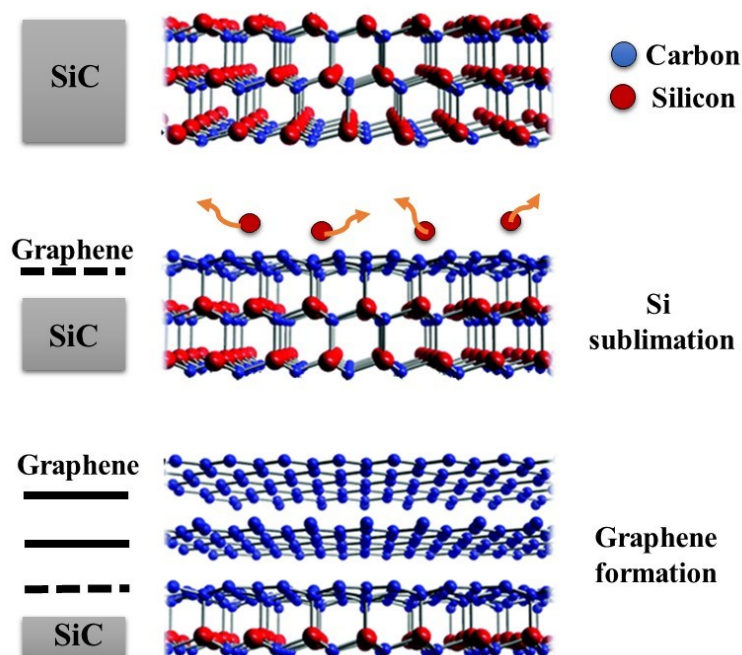


Figure 5. Schematic illustration of an epitaxial growth from a SiC substrate. Heating a SiC substrate under UHV there is the sublimation of silicon, firstly, and carbon atoms remains on the surface organized themselves into graphene structure.

Chemical Vapour Deposition (CVD)

CVD is a synthesis process in which the graphene growth onto a metal surface that catalyze the thermal decomposition of hydrocarbon molecules (methane, acetylene, propane...) [11]. There are several chemical reactions used in CVD, in which the thermal decomposition is made (pyrolysis, reduction, hydrolysis, disproportionation, oxidation, carburization, and nitridation), and they can be used either separately or combining them. In any case, the substrate and the reaction must be activated using temperature; depending on hydrocarbons are used or metal-organic precursors or cold plasma that permits to operate in a range of temperature from 20° to 500°C.

Transition metals are particularly appealing to obtain large volume of high quality graphene or other carbon allotropes, in order to develop process ready to be integrated to the existent semiconductor industry.

The sequence of events taking place during a CVD reaction are well defined in two steps (Figure 6). At the beginning, there is the precursor transport through flow carrier gas in order to encourage the primary interaction with the substrate surface and after the adsorption and the diffusion of them, there is the grown in different sites as to obtain a completely covered surface.

The most common precursor are methane (CH₄), ethylene (C₂H₆), propylene (C₃H₆) and acetylene (C₂H₂) which are commonly pyrolyzed at around 900-1000 °C, over a wide range of pressure, onto transition metal substrate from which depend the quality of layers [12].

Copper is the most adopted catalyst among the different transition metals (Ni, Co, Fe are also possible) because the solubility of carbon in copper is low, and so, when the substrate is cooled down, carbon aggregates condensed onto the surface forming sp^2 bonded layers [13]. If, on the one hand, an accurate control of process parameters permits the production of a monolayer, on the other hand the crystal domains are very small related to higher number of growth center in which the precursor [14]. Therefore, it is obvious that the supersaturated, saturated or under saturated concentration of the carbon species allow full coverage of the surface, or partially coverage respectively.

Scalable techniques for mass production and more economic process are exploiting using different Polycyclic Aromatic hydrocarbons (PAHs) (like benzene [15] and/or toluene [16]) whose structure composed of benzene rings, after low-temperature pyrolysis (at 500-600 °C) permits an atomic arrangement allows growing graphene.

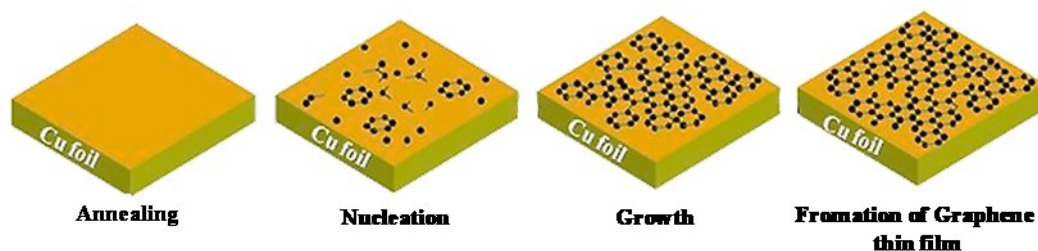


Figure 6. Schematic representation of methane catalytic decomposition to form C_xH_y species upon the exposure of Cu and hydrogen. Where the local concentration of C_xH_y is supersaturated, there is the formation of nuclei carbon based that grow more and more, creating domain and covering the Cu surface since to obtain a thin film [17].

However, CVD is an expensive process, due to high-energy consumption and the need to remove graphene from the underlying metal with the risk of damaging it. Furthermore, CVD, not being cost-effective for large-scale production, is typically used for graphene synthesis for applications where the need for high quality graphene is limited [18].

Exfoliation

Exfoliation is a category of techniques using top-down approaches with the possibility of obtaining GRMs of different sizes.

Mechanical exfoliation, also well known as micromechanical cleavage, was the first technique used in 2004 [19] from which it was possible to isolate one monolayer of graphene, exploiting the weak bonds (Van der Waals interactions of the order of 2 eV/nm²) between the atomic planes of graphite. Considering an area of 1 μm^2 and assuming the graphene-substrate friction coefficient equal one (adhesion is an important friction mechanism at low normal loads), the required normal force to cleave off this sheet from the top of the graphite crystallite is about 300 nN.

The force can be exerted using an adapted AFM tip or, more simply, by the resistance to the release of a conventional scotch tape which is the method used to

obtain the first isolated graphene sheets peeling the highly oriented pyrolytic graphite (HOPG), as show in Figure 7.

Although the concept is simple, nowadays, mechanical exfoliation is one of the best method to obtain high quality materials with less crystalline defects, perfectly suitable for electronic applications or for other several fields in few μm^2 as flakes dimension are enough. Therefore, if in one hand the drawback is the size of the flakes, in the other hand there is the difficulties for the scale up of the process [18].

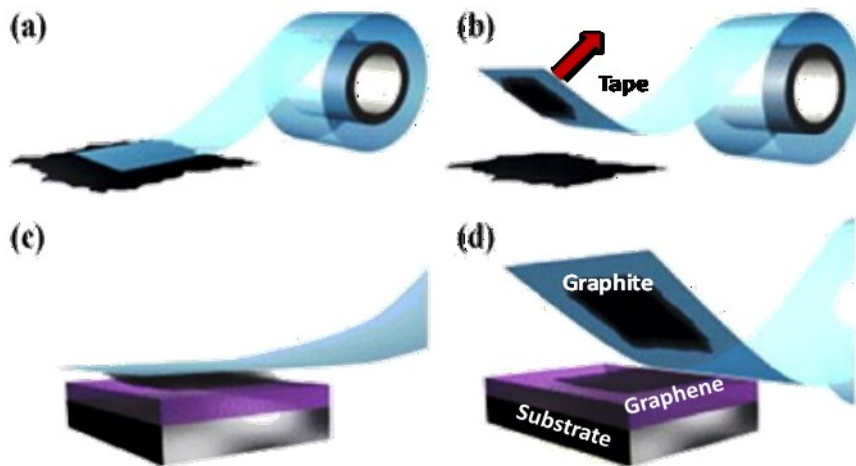


Figure 7. Schematic representation of a mechanical exfoliation process shown step by step: (a) adhesive tape is pressed against a HOPG surface to adhere to the top. (b) Few layers are cleaved from graphite crystal. (c) The tape with some layer of material is pressed against to the surface of a substrate. (d) Upon peeling off, the bottom layer is left on the substrate [20].

Through aqueous exfoliation, it is possible to obtain various types of GRM by exploiting the weak interactions between inorganic acids (sulfuric acid, hydrochloric acid and nitric acid) and graphene surface.

In fact, through a process at high temperatures and pressures, called solvothermal process, it is possible to intercalate the acid's ions between the graphite planes in order to increase the distances between them and therefore decrease the π - π stacking forces that hold the graphene planes together (Figure 8).

This permits a higher efficiency of dispersion in water, reducing solvent costs and at the same time, the stability increases because although the GO flakes has a tendency to stacking with themselves, the oxidized groups have the function of. Therefore, it do not require much energy to separate the sheets. Centrifuge process can also be introduced to select the size of flakes into solutions because at different rpm the flakes having high mass precipitate on the bottom of the flask.

Although the chemical exfoliation process increase the number of defects in term of reduced bond conjugation [21], inducing the partial degradation to sp^2 - sp^3 structures, this technique permits an accurate size control of the graphene sheets with a continuous range from micrometers scale to nanometric size [22].

Although the yield of monolayer graphene is not very good ($<1\%$) because FLG and GnP are almost always obtained [23], chemical exfoliation is a very popular method

used for the production of inks such as pigment, coating powder and materials where transparency is not required and where some residual defects (such as weak oxidation) help in stability solvents.

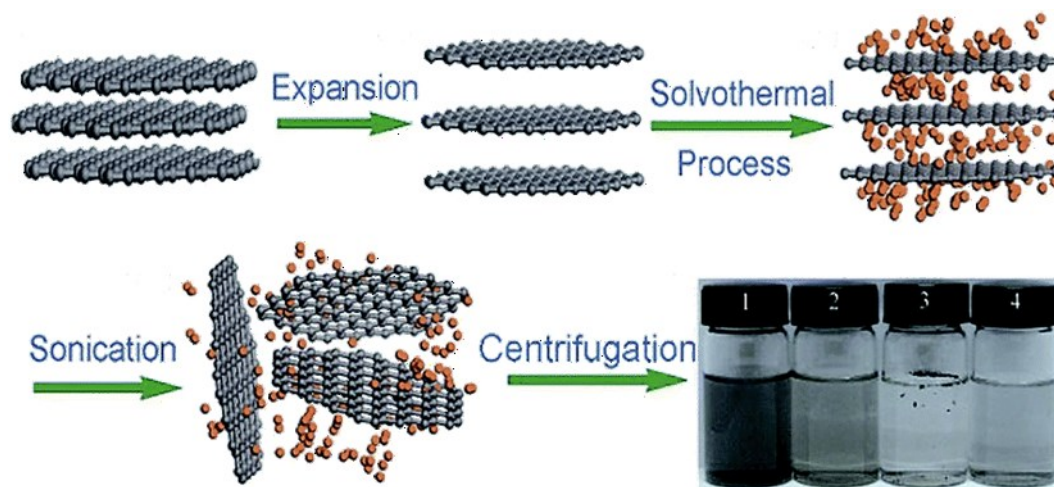


Figure 8. Schematic representation of graphene sheets exfoliation and dispersion: graphite planes are expanded using acids solution and solvothermal process is processed to divide sheets between themselves. Several steps of centrifugation at different rpm are done in order to separate flakes having different size [24].

Electrochemical approach is one of the most efficient method to exfoliate graphite [25], that is used as electrode whose potential can be regulated.

In few minutes and in appropriate liquid electrolytes the graphite electrodes are intercalated with various molecules and rapidly dispersed in solution.

When graphite is used as an anode, the most commonly wet process used an aqueous solutions with mineral acids (e.g., H_2SO_4 or $HClO_4$) as electrolytes [26] that producing gas, create pressure intra-layers since to the completely separation of them. However, high electric potential can leads to partially oxidation damage and so the other approach use the graphite as cathode [27] and a polar solvent such as dimethyl sulfoxide whose intercalation produces SO_2 gas promoting delamination.

In both approaches, the possibility to intercalate different molecules between graphene layers offers a highly tunable way to expand graphite into graphene, obtaining a distribution of new materials with it (not only monolayer but also FLG or MLG).

Electrochemical or autoclave processes are relatively expensive for energy or plant costs and so different approaches take advantage of graphite oxidation in highly concentrated and oxidizing acidic aqueous solutions followed by a sonication step. Colloidal suspensions are homogeneous due to the hydrophilicity of the functional groups and are very stable because the electrostatic repulsion of the groups avoids π - π aggregations between graphene surfaces.

The most classical synthetic method to oxidize graphite (like Brodie [28], Hofmann or Hummers method [29] use mineral acid (sulfuric, nitric or hydrochloric acid) to intercalate the acid's ions and spacing the graphite planes followed by step

in which strong oxidizer (NaNO_3 , KClO_3 , KMnO_4) to produce GO [30], as show in the Figure 9.

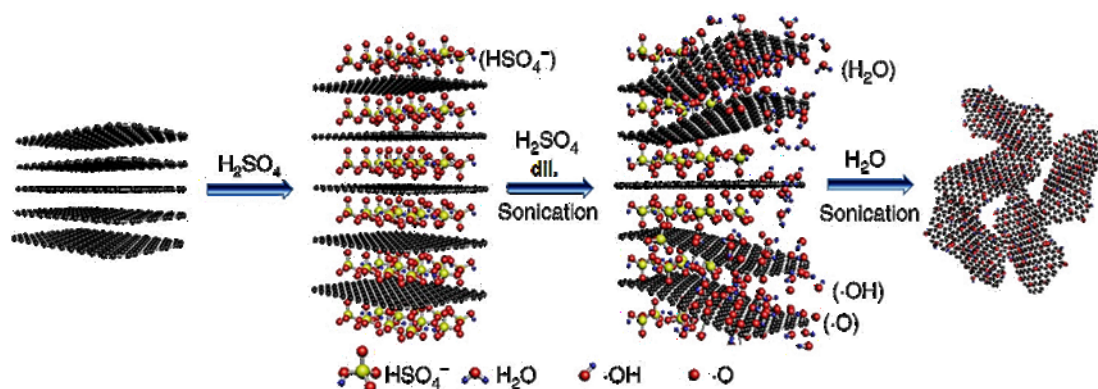


Figure 9. Schematic representation of production of GO, FLGO or MLGO.

Several techniques were developed for the GO reduction through different approaches such as, photo and microwave technique [31], applying hydrogen plasma [32], or in a reducing atmosphere (such as using alkaline solutions [33] as shown in Figure 11, hydrazine vapors [34] or most relevant and applicable for companies heat treatments [35] shown in Figure 10.

The thermal reduction by annealing of GO is well exploited in which vacuum, inert or reducing atmosphere is used in more steps to remove intercalated water and functional groups. Indeed the rapid heating of graphite oxide generate CO and CO_2 gases that in one hand produce vacancies into lattice and, in other hand, their expansion increase the spaces between stacked carbon layers obtaining a porous graphene-based material.

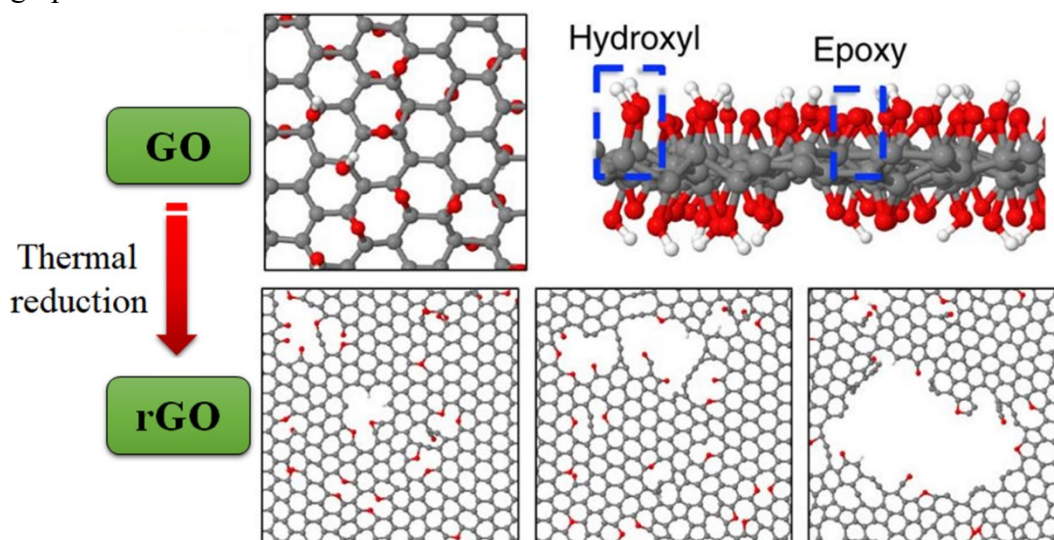


Figure 10. Schematic representation of deoxygenation with thermal treatment.

Chemical reduction, as Fan et al. [36] well reported, use a strong aqueous alkaline solution like NaOH and KOH in a range of temperature between 50°C and

90 °C, in which the deoxygenation make darker and darker the solution since to obtain a black colloidal suspension.

Other various inorganic and organic chemical compound are exploiting as reduction agent of GO such as sodium borohydride [37], hydrazine [38], glucose [39] and ascorbic acid [40].

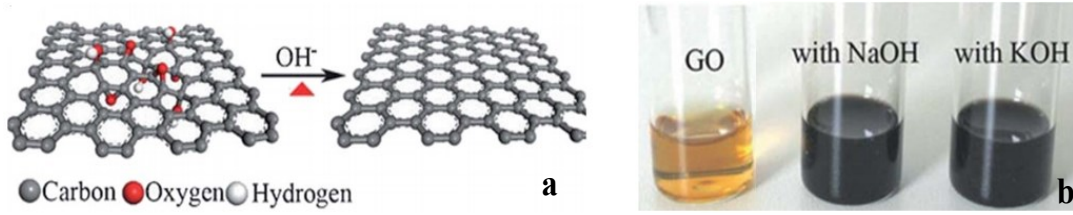


Figure 11. Images of the exfoliated graphite oxide suspension with and without deoxygenation step under reaction alkaline conditions.

A valid alternative to the oxidation of graphite is the use of organic solvents in the exfoliation process. Although the approach is less eco-friendly, the use of solvents permits the exfoliation from graphite material without oxidation and therefore, it is potentially preserved the chemical and physical characteristic of the graphene plan. In addition, annealing heat treatments or chemical reduction treatments are not necessary, so costs are relatively reduced.

The solvent phase exfoliation process mostly exploits ultrasounds into organic liquid medium in order to separate the layers since to obtain monolayers and it can be summarized in three steps in which the graphite is dispersed in a solvent, it starts the exfoliation and, at the end, the is the purification.

In general, during ultra-sonication, there is a balance of forces between those generated by cavitation in which the micro-bubble collapses (due to the rapid oscillation of the pressure resulting in increased exfoliation) and the attractive forces of stacking GRM π - π .

Therefore, the organic solvent have the most important role because, reducing the interfacial tension between liquid and GRM sheets as well as the contact area between two different flakes, it prevents the Van der Waals interaction for layers having a distance among 3.5 Å [41].

Coleman et al. demonstrated that the potential energy is significantly reduced by the dispersive London forces depending on refractive index solvent that matches with graphene one, obtaining as results that solvents with interfacial tension (γ) value around $\sim 41 \text{ mJ m}^{-2}$ (Table 1) are favorite to minimize the energy input in attaining effective separation of flakes [42].

The Coleman's equation, shown below, indicates the thermodynamic requirements that can predict which solvents can be used for the graphene dispersion [43].

$$\frac{H_{mix}}{V_{mix}} = \frac{2}{T_{NS}} \left(\sqrt{E_{SS}} - \sqrt{E_{SG}} \right)^2 \Phi_G \quad \text{eq.1}$$

Where ΔH_{mix} is the enthalpy of mixing, V_{mix} is the volume, T_{NS} the thickness of graphene nanosheets, E_{SS} and E_{SG} are the surface energies of solvent and graphene, respectively, ϕ_G is the volume fraction of graphene dispersed.

Among some variety of solvents described the best results have been achieved with N-methyl-2-pyrrolidone (NMP), an organic solvent that make around 25 % of monolayer flakes and almost totally remain part is FLG whose later size contain no more than six layers.

In general, the yield by monolayer graphene percentage is defined as the ratio between the number of monolayers and the total number of FLG in the dispersion, or, more commonly, as the ratio between the total mass of single layers into dispersed and the entire colloidal flake. Because the exfoliation effect depends on the power of sonication, the liquid medium used to disperse graphene nanosheets, and the rate of centrifugation that can be used to separate GRM of different size [42, 44].

In order to calculate exfoliation yields, instead, it is necessary to use analytical methods providing both qualitative and quantitative analysis, such as spectroscopic characterization whose concentration estimation follow the Kubelka-Munk law, (it is the corresponding Lambert Beer's law for colloidal dispersions: $A = \epsilon \cdot b \cdot c$). Measuring the absorbance in the ultra violet region, it is possible to determinate the concentration of suspended flakes but for more details about their structure such thickness or number of layers, the transmission electron microscopy (TEM) and atomic force microscopy (AFM) are required.

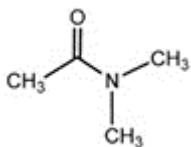
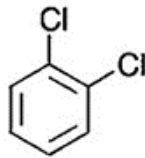
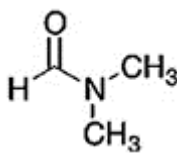
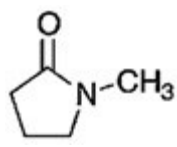
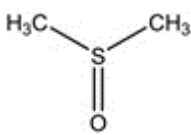
No.	Chemical Structure	Organic solvent	Boiling Point (°C)	Surface Tension (mJ m ⁻²)	Ref.
1		N,N-dimethylacetamide (DMAC)	165	36.7	[45]
2		Ortho-dichlorobenzene (ODCB)	181	37	[46]
3		N,N-dimethylformamide (DMF)	154	37.1	[47]
4		N-methyl-2-pyrrolidone (NMP)	203	40	[48]
5		Dimethyl sulfoxide (DMSO)	189	42.9	[43]

Table 1. Solvents for LPE of Graphene

In conclusion, the production of high quality graphene requires the use of techniques not suitable for large-scale production, or on the other hand, the graphene yield in these processes is typically limited to a few percentages, leading to an expensive product that could only be used for niche applications. For these reasons, GRMs are often sold on the market, mainly in the form of MLG or GnP, which are available in large quantities and with a limited cost of material.

Considering also that the affinity with organic solvents is easily controllable, for this work of thesis, it was decided to operate under conditions similar to the LPE technique in order to preserve the contiguity of sp^2 bonds, which is a crucial condition for applications where good heat transmission is required.

1.1.2. Proprieties & Applications

The low absorbance in the visible range of wavelength, combined with the high electronic conductivity, make the graphene an optimal candidate as transparent electrodes, competing with indium tin oxide (ITO) which is the actually standard material for solar cells, liquid crystal displays and touchscreens [49].

In fact, if currently on the market graphene materials are mainly used for batteries, there are prototypes that also use it in displays or electronic components. Due to the high thermal conductivity, GRM could be used to cooling the electronic hotspots with an energy saving and a consequent increase in lifetime [50] that will be better discuss in the next section.

Other fields of application in which GRMs can be integrated are:

- **Ultra-capacitors and micro-batteries:** able to store bigger quantities of energy, charging thousands times faster and to be dozen times more powerful than the current ones [51];
- **Bio-related materials:** Graphene derivatives, such as graphene oxide (GO), chemically reduced graphene oxide (rGO) or doped graphene, that have been intensively studied for their prevalent applications in biosensing [52]. Moreover, the use of nanomaterials to retain and then deliver the drugs can assist with preventing undesirable effects with beneficial therapeutic properties and at the same time, more studies can be explored new strategies to controlled when the appropriate biological target is identified;
- **Photovoltaic:** more efficient solar cells by using graphene as a charge collector whose electrons can be excited to a higher energy state by absorbing incoming solar light and then the energy is transferred to neighboring electrons [53];
- **Conductive ink:** coatings for smart packaging and printed electronics whose circuits can be printed almost onto any substrate using graphene as pigment [54];

- **Graphene aerogel:** consisting of interconnected spongy porous carbon networks, thanks to their lightness together with excellent electrical and thermal properties, for aerospace application [55].
- **High performance computation:** terahertz oscillators and high-speed field-effect transistors with switching speeds between 100 GHz and a few THz, and a performance thirty times higher than present-day [56];
- **Quantum dots:** nanolight confinement and edge effects make photoluminescent phenomena, band-gap engineering bio-imaging, sensors applications [57];
- **Optical modulators:** are commonly used in communication and information technology to control intensity, phase, or polarization of light, and so, graphene permits broadband light-matter interactions with ultrafast responses for photonic and optoelectronic applications [58];
- **Contaminant removal:** In particular, GO not only, is non-toxic and but its surface, covered with epoxy, hydroxyl, or carboxyl groups, can interact with cations and anions. It is, also, amphiphilic (able to mix with water or oil), performing stable colloid suspensions able to capture metal such as copper, cobalt, cadmium, arsenate, or organic compounds [59].
- **Field Effect Transistor (FET):** because the adsorption of molecules in the surface can temporally modify the local charge carrier, it is possible distinguished the signal, opening to sensing application field. If a single molecule detection has been achieved, which demonstrates the potential high sensitivity of graphene-based sensors [60], in the other hand the sensing can be applied to any phenomena that perturb the electron concentration such as magnetic field or mechanical deformation [61].

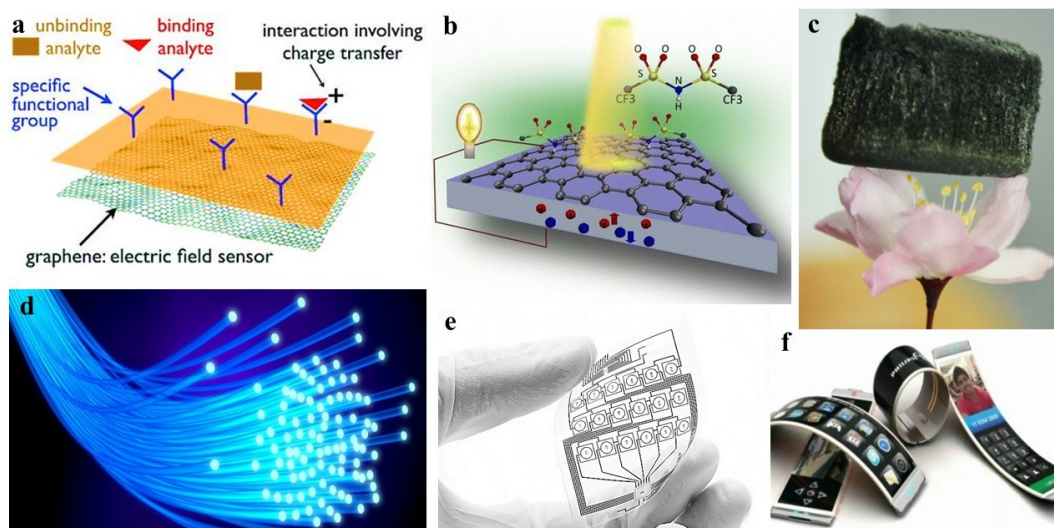


Figure 12. (a) Functionalization of GRM for detection of chemical species such as organic compounds or inorganic ones like ions or metals. (b) Solar cell graphene based. (c) Aerogel graphite based. (d) Optical fibres. (e) Printed electronic circuits with ink graphene based. (f) Flexible devices.

1.1.3. Chemical Functionalization

The chemical functionalization is used to modify the interactions of the graphene with the surround or to change its intrinsic properties. There are different types of functionalization that it is possible to distinguish two macro areas such as covalent and non-covalent.

Covalent

The covalent functionalization of graphene depends on the electronic availability and so, on all those related parameters such as number of layers, state of the edges, defects of the atomic structure. There are two approaches, the first is to make a chemical reaction on existing functional groups (e.g. oxidized groups on surface or edges) and the second is to make the reaction on sp^2 carbon atoms.

As an enormous polycyclic aromatic molecule, the basic structure of graphene is strongly stabilized by a delocalization of charges, it is necessary to use radical or highly reactive processes to functionalize it. Although several reactive molecules had been exploited to make radicals, (such as azomethyne, fluorinated phenyl nitrenes, carbenes [62]) in general, radical processes are very difficult to control. On the other hand, among the chemical functionalization of graphene [63], the most performing is based on the electron transfer mechanism by the aryl diazonium salts. Although there are several derivatives belonging to this class of compounds (such as 4-nitrobenzene diazonium tetrafluoroborate [64, 65], 4-bromobenzene tetrafluoroborate called 4-BBD [66], 4-propargyloxybenzene diazonium tetrafluoroborate or 4-PBD [67], and 4-tert-butylphenyldiazonium tetrafluoroborate called 4-TBD [68]) the mechanism at the base is the same [69], as show in the Figure 13. The delocalized electron is transferred from the graphene to the aryl diazonium cation, which becomes an aryl radical after releasing an N_2 molecule. The aryl radical then forms a covalent bond with a carbon atom in the graphene lattice, changing its hybridization to sp^3 and moving it out of the plane from $\sim 0.7 \text{ \AA}$ [70]. The attachment of a phenyl group results in a delocalized, unpaired electron that drives the functionalization of a second aryl group that attaches in para-position as also demonstrated by functional density theory (DFT) calculations [70].

It has also been demonstrated that the structure of GRM also influences the degree of functionalization. In fact, single-layer graphene (SLG) regions have shown a higher degree of functionalization than dual-layer and multi-layer graphene, which also have significantly lower kinetics [71].

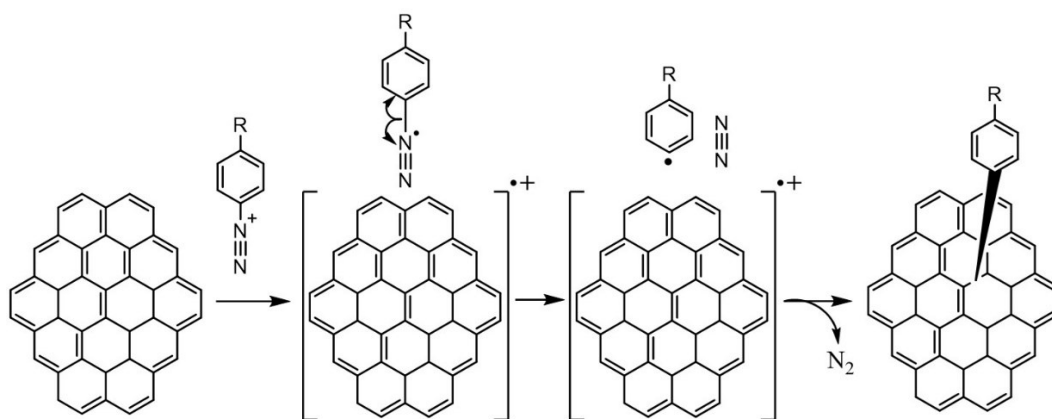


Figure 13. Schematic illustration of grafting a diazonium salt with functional group R.

Several studies are exploring new chemical syntheses to keep the graphene surface unaltered but modify the nature of GRM by selectively functionalizing the areas where physical defects or edges are already present. For example, the dipolar-cycloaddition in combination with amide-bond [72], condensation reaction with aminated dendron (with the carboxylic acid functionalities on the edges) [73], have exploited a functionalization at the edges by bi-functional linkers able to connect the edges of different plates [74], or replace the hydrogens of the edge by chlorinating them in order to increase their reactivity for successive reactions [75], are well exploited. Finally, to functionalize GRM covalently were found molecules that, without creating radicals, react mainly with the edges, making the chemical reaction called cycloaddition. In fact, it has been demonstrated how the graphene can act both as diene and dienophile and providing Diels-Alder reactions [76] with the possibility to control the grade of functionalization, varying the temperature. Different range of temperature are exploited in order to maximize the functionalization effect, and also over a certain temperature (150°C) was demonstrated (by Raman spectroscopy) that retro Diels-Alder occurred and the graphene edges were restored with potential application in the thermal sensing field. Among these molecules, those of greatest interest for potential future reactions, there are maleic anhydride (MA) and maleimide (MI) used as dienophile while graphite has the function of diene, as shown in Figure 14. Both the functionalization not only induced a delamination of the raw material, obtaining nanosheets [77], but also increased their dispersivity in solvents (water for MA and organic solvent for MI). Moreover, it has been confirmed by Raman and FT-IR spectroscopies how these molecules were mainly added at the edges of the GRM and in particular in those of armchair type, according to theoretical model.

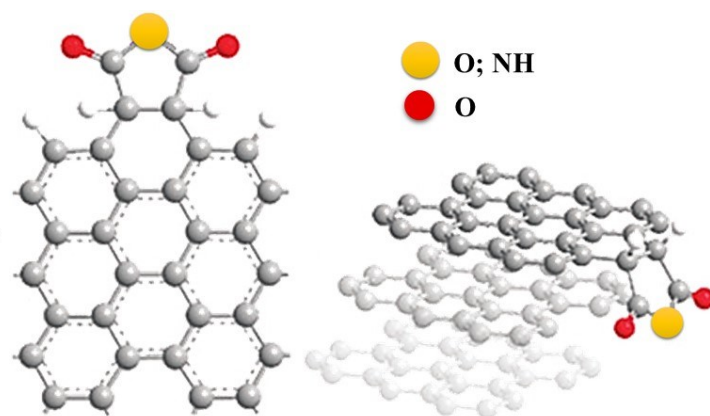


Figure 14. GRM functionalized with a specific dienophile, maleic anhydride (MA) or maleimide (MI) after the Diels Alder reaction.

The oxidized forms of GRM generate great interest among researchers of nanomaterials both for the good thermal conductivity after reduction and for the presence of functional groups that can be selectively exploited to make covalent functionalization. Indeed, while on the basal planes there are both hydroxyl and epoxy groups, on the edges there are mainly carboxylic, carbonyl, phenolic, lactones, quinones groups and several of these oxygenated functional groups can be used to form covalent bonds with other electro active species.

Hydroxyl groups can be effective binding sites for a process that exploit alkoxysilane molecules, producing nanomaterials with superior chemical and physical properties. For example, due to this functionalization it has been possible to graft ethylenediamine triacetic acid (EDTA) [78], whose the antimicrobial and metal absorption proprieties have been increased and, on the other hand while the cytotoxicity has been reduced.. Therefore GO was functionalized with the triacetic N-(trimethoxysylpropyl) ethylenediamine triacetic acid (EDTA-silane), in which first there is a dehydration or hydrolysis reaction of the trialkoxy groups in Si-EDTA creates -Si-OH groups and then there is a condensation between these with the hydroxyl groups (OH-C) of GO to form Si-O-C bonds.

An alternative functionalization is the esterification of the hydroxyl groups of graphene oxide (GO). Indeed, the mechanical properties of the material were radically changed, using the poly(l-lactic acid) or functionalizing with benzene-1,4-diboronic acid [79] to form boron esters with which monolayer GO lamellar have been cross-linked to form variable structure with pores and volumes.

The covalent functionalization of graphene oxide through ring opening reaction of epoxides on the basal planes usually involves a nucleophilic attack on the α -carbon of the epoxy, and the use of an amine group to catalyze the ring opening reaction. For example, octadecylamine is used to convert graphene oxide sheets into materials [80], which are easily dispersible in organic solvents.

A similar result is also achieved by functionalization with 3-aminopropyl triethoxysilane (APTS) through an nucleophilic substitution reaction between the amine and epoxy groups [81]. In this way, the silane terminal group not only increase the affinity for organic solvents but it also can be exploited for further reactions.

Carboxyl groups can be functionalized through amidation or esterification with small molecules or polymeric chemical linkers. For example, in one study, graphene oxide was activated with N,N'-Dicyclohexylcarbodiimide [82], with which the subsequent esterification reaction it possible to synthesize a hybrid material with fullerene, similar to the amidation reaction with TPP-NH₂ porphyrin [83].

Using a similar approach, it was possible to deposit GO films on substrates such as plastic [84], alumina and ITO [85] or to increase its bio-functional properties functionalize with biomolecules[86] or proteins[87].

Considering the relative ease of functionalization and the relatively low costs (both reagents and process) for a potential industrial development, covalent functionalization by of Diels-Alder reaction between GnP and maleic anhydride derivatives was chosen for this thesis work.

Non-covalent

Non covalent interactions may also be exploited for the functionalization of graphene, based on the energies of individual supramolecular interactions are lower in comparison to those of covalent bonds, but when combined over large areas they can compete with some covalent bonds [88].

These dissociation energies allow the supramolecular systems to be reversible, or kinetically labile. In fact, with graphene materials, π - π or CH- π interactions have dissociation energies lower than 50 kJmol⁻¹ and so the weaker forces (such as London dispersion forces or Van der Waals interactions), have effects on all atoms in close surroundings.

Solvation and hydrophobic effects are very important because they affect not only the dispersibilities of GRM but also the recognition interactions that can be used for detection application [89-91].

On the surface of graphene, two types of π - π interactions occur between electron-rich and electron-poor regions, which influence the interaction with molecules. Although this is evident in the face-to-face and edge-to-face arrangement of benzene[92], these interactions have also been observed for biologically relevant molecules such as DNA and porphyrins that can be used to functionalize GRM (Figure 15 a) [93].

For GO and reduced graphene oxide (rGO) with residual functional groups, not only will π -interactions occur as seen for graphene, but the presence of epoxy groups, alcohols, ethers, carboxylates, and carboxylates (Figure 15 b) may originate the formation of hydrogen bonds [94]. This can also be used to control of some molecules orientation onto the graphene surface or to obtain self-assembled macrostructures [95] that affect substrate properties such as electronic properties [96].

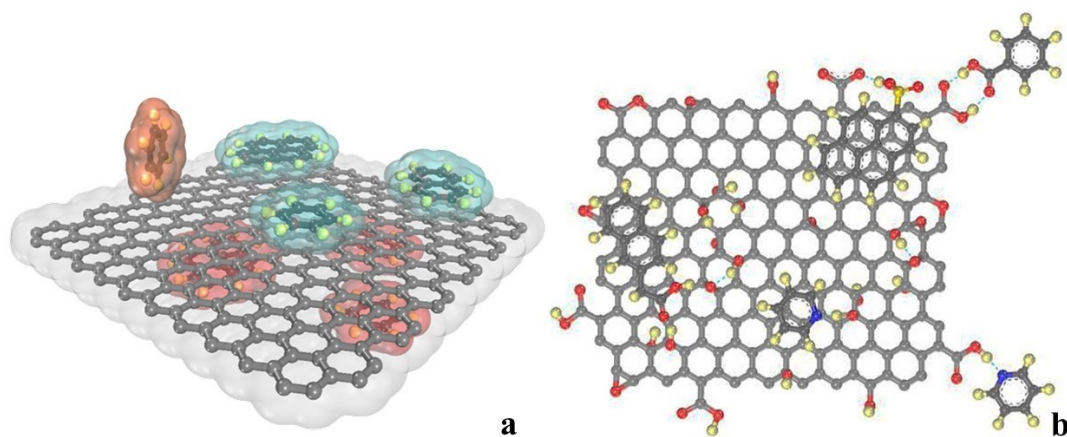


Figure 15. a) π - π interactions between benzene, naphthalene, or pyrene molecules above and below the basal plane of graphene. b) Schematic representation of both hydrogen bonds and/or π - π stacking with GO [92].

In general, non-covalent functionalities are very often used in the liquid phase exfoliation process in order to increase both the exfoliation efficiency and stabilize the suspension by preventing the flakes re-aggregation.

In other words, π - π interactions can be the driving force for graphite exfoliation and stabilization of dispersed GRM. The aromatic molecules act as wedges and slowly intercalate and penetrate between the graphite layers, usually during the sonication and so, the graphene layers are gradually dissociated from each other, eventually leading to complete separation [97].

In fact, π - π interactions of graphene with small aromatic molecules such as pyridine [98], quinoline [99], anthracene and naphthalene [100] have been well studied but very often to stabilize graphene nanosheets and make them compatible with different solvents and especially the water, derivatives of these molecules [101] or ionic liquids, or polymers, are used.

Among these, pyrene derivatives [101] are the most used because than other PAHs and easier to synthesize implementing the desired functional groups. For example, Palermo et al. [102] used a series of pyrene sulfonate derivatives to study graphite exfoliation and graphene stabilization in water. The pyrene nucleus was functionalized with one, two, three or four sulfonic groups, which are electron acceptors, while two of them are also functionalized with two and one hydroxyl group, which are electron donors. In this way Palermo et al studied the procedure in two phases. In the first step they estimated that the adsorption of pyrene on the graphite surface is inversely proportional to the number of polar sulfonic groups while, in the second step, they conclude that molecule with the highest dipole momentum and the most asymmetric functionalization are preferred for exfoliation. Due to the excellent affinity between pyrene and graphene, research has been conducted to use pyrene as an anchor group of larger molecules. For example Lee et al. [103] used a tetra-pyrene derivative decorated with an oligo-etherdendro that greatly increased the hydrophilicity and, at the same time, they demonstrated how

the planeness of GRM is fundamental for the reactivity with this molecule. In fact the same functionalization is not able to disperse the nanotubes.

Finally, extending the molecular size with pyrene functional groups, Zhang et al. [104] used terminated pyrene polymers functionalized polyethylene glycols (f-PEG) to interact with rGO. In this way, the pyrene groups were attached to the graphene surface, while the flexible ethylene glycol chains allowed the interconnection of the nanocomponents, thus offering a rigid composite with improved mechanical properties.

Concerning GO and rGO, they have a number of polar groups that may participate in ionic-polar interaction, dipole-dipole ones or hydrogen bonds with analogous polar parts of molecules or macromolecules. Indeed, the hydrophilic part of the surfactant responsible for this interaction could be an ionic, zwitterionic or highly polar group [105] such as carboxymethyl cellulose [106], sodium dodecylbenzenesulphonate [107] are just some of the organic amphiphilic and macromolecular molecules that have been successfully used as dispersants and stabilizers [108].

On the other hand, when an amphiphilic molecule is attached to the graphene surface the hydrophobic part increases stability in organic solvents. A representative example is the work of Liang et al. [109] that demonstrated how GO and rGO can be functionalized with quaternary ammonium salts (such as tetradecyltrimethylammonium bromide) in which the positive "heads" of surfactants interact with the carboxylated and hydroxylated groups through electrostatic interactions, while the aliphatic chains of surfactants provide the necessary lipophilicity and stability in organic solvents.

Similar conclusion occur when rGO react with terminal functionalized polymers (such as amine-terminated polystyrene), which lead to the transformation of hydrophilic rGO into a lipophilic rGO/polymer composite that is dispersible in organic solvents [92].

Among the non-covalent functionalizations, for this work of thesis, were chosen the π - π interaction between GnP and pyren derivatives in order to use the organic solvent aiming both to preserve the aromatic structure of GRM and at the same time functionalize it without introducing chemical defects. At the end, a comparison between non covalent functionalization with the covalent ones previously discussed will be treat.

1.2. Heat spreading devices

One of the problems often associated with electronics is the need to dissipate the heat generated by the operation of the device in order to ensure its performance and durability. Indeed, modern electronic device produces heat for many tens of watts and in some case even more than 100 watts, so if this energy is not spread in the environment, the increase in temperature easily leads to temporary malfunctions or even permanent physical damage.

A heat spreader transfers heat from a hotter source to a colder system such as a heat sink or heat exchanger that could be distinguished in two different categories that are active [110] or passive [111]. The first one usually includes heat spreader that may work spending energy from an external source on contrast to the second typology that exploits the high thermal conductivity of material.

In a scenario where electronic devices are more and more miniaturized to become wearable, the study of passive heat spreaders has taken on a key role.

Heat pipe (Figure 16 a) is a heat spreading technology with great efficiency in transferring heat also for little temperature difference that consists of a sealed metal tube partially filled with a small amount of working fluid (such as water, ethanol, acetone, sodium or mercury) that is both in the liquid phase and some will be in the gas phase. The structure exerts a capillary force on the liquid phase of the working fluid, driving it from the liquid section to the gas section. Heat pipes do not contain mechanical moving parts and no required maintenance because the liquid and gas self-recirculate, due to the temperature differences between the hot end and the cold end. The most common material used to fabricate pipes is the copper and the fluid is often water with useful range from 30 to 200 °C.

A similar approach is used by vapour chamber (Figure 16 b) technologies which can be considered as a heat pipe with flat surfaces (hot side and cold side are flat for spreading heat in the in-plane direction).

Although a heat pipe/vapour chamber unit has extreme high heat transfer capacity with a thermal conductivity depending on the design whose ranges from 20 to 200 $\text{kWm}^{-1}\text{K}^{-1}$, the density of a heat pipe/vapour chamber is normally less than one-third that of copper implementing in weight sensitive applications, the problem remains in terms of miniaturization and thickness to reduce the overall cost. In fact, heat/vapour chambers are now used in niche applications such as aerospace, PCs with power electronics and high power military applications.

Most heat spreading systems, however, do not use liquids inside them but they exploit the rapid thermal conduction of the materials to extend the heat exchange surface (Figure 16 c) between the heat source and the surround. Therefore, both a study of the basic theory of the thermal characteristics of the materials and how their geometries (Figure 16 d) influence the performance of the heat spreading are necessary.

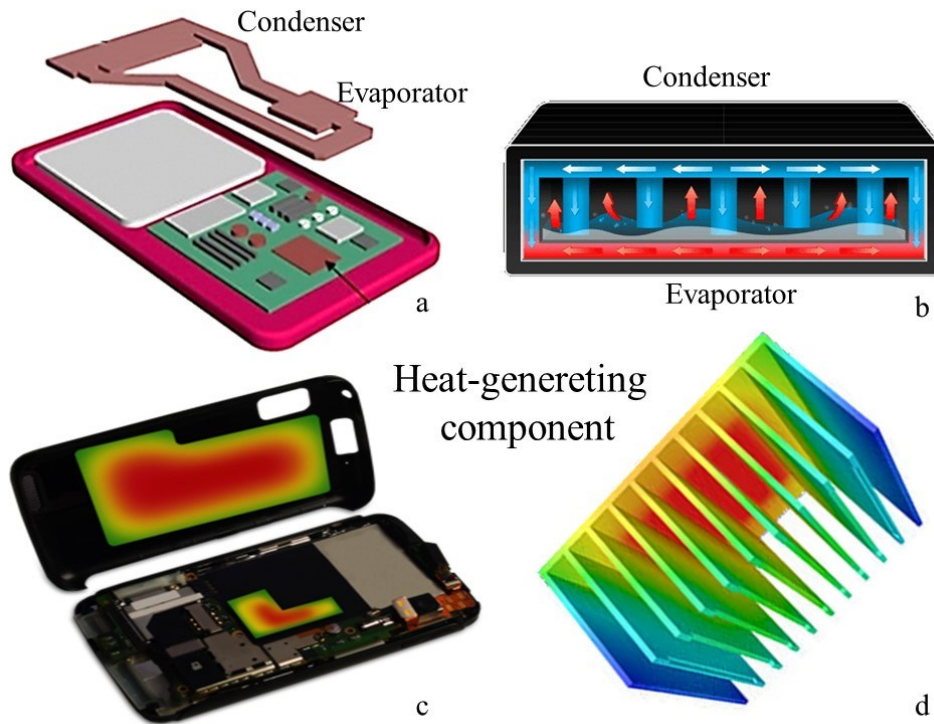


Figure 16. Different types of heat spreader. a) Heat pipe. b) Vapour chamber. c) Planar heat exchanger. d) Heat sink.

1.2.1. Heat transfer fundamentals

The three well-known modes of heat transmission are obviously conduction, convection and radiation.

Conduction and radiation are exchange processes in which the transmission of energy from one region to another due to a temperature difference while the convection process involve also the transport of matter to remove heat.

Heat conduction

The physical explanation of the nature of heat depends on matter and its physical state. In fact, atoms or particles in a solid do not move freely, but oscillate around precise fixed positions, in liquids they are in contact between themselves and have greater freedom of movement, in the gases finally, they have maximum freedom of movement and are in constant random motion. The particles during their motion can move at a certain speed, vibrate relative to each other or rotate around an axis. To these motions are associated the kinetic energies of translation, vibration and rotation, whose sum constitutes the kinetic energy of a molecule.

The sum of the kinetic and potential energies of all the molecules that make up the system represents its internal energy, the sum of all microscopic forms of energy.

The molecular structure and the degree of molecular activity are proportional to temperature, and so, it follows that as it grows the kinetic energy of the molecules increases, and therefore the internal energy.

Heat was therefore correctly interpreted as energy associated with the motion of particles and therefore with the internal energy of a body. In particular, it is called thermal energy the component of the internal energy of a system whose variation is proportional to the temperature variation.

Other components of internal energy are related to intra/intermolecular forces, i.e. the forces that bind together the molecules of a system and the atomic bonds within a molecule. In particular, intermolecular forces are more intense in solids and weaker in gases, in which a small amount of energy is used to break the bond between the molecules, causing the phase change. Therefore, the gaseous phase is at a higher level of internal energy than the corresponding level in solid or liquid phase.

Conduction is a process by which heat is transmitted through direct contact from molecules having high energy to a substance containing lower energy.

The exchange of energy by conduction can occur in solids, liquids and gases, but if in one hand, the conduction is the only mechanism by which heat can propagate in a solid, on other hand, in a non-solid media it is usually associated with convection and radiation. According to molecular kinetic theory, the temperature of a material element is proportional to the average kinetic energy of its constituent particles. When the molecules of a region acquire a high average kinetic energy they release part of this energy to the molecules of the adjacent region at a lower temperature.

The exchange of energy takes place by elastic shock between molecules (in fluids) or by diffusion of the faster electrons from regions with higher temperature to regions with lower temperature (in metals); in non-metallic solids it is due to the vibrations of the molecules inside the lattice.

In general, in solids the heat transmission is due to the sum of two components: the effects of the lattice vibration waves produced by the vibratory movement of the molecules occupying relatively fixed positions (lattice component) and the energy carried by the free flow of electrons (electronic component).

In heat transmission a crucial factor is the determination of the temperature distribution T , which can be expressed in general by the relationship $T=f(x)$, (where f is a function that depend on Cartesian coordinate x) which defines a scalar field.

The temperature gradient, is the ratio of the temperature variation and the length of the segment.

$$\nabla T = \frac{T_2 - T_1}{\Delta x}$$

The temperature gradient is positively oriented to rising temperatures and as previously defined, it can be associated to a vector field, whose lines of force are perpendicular to the isothermal surfaces.

Because heat passes spontaneously from points at higher temperature to points at lower temperature, the heat flow has the opposite direction to the temperature gradient. It is possible to define a new vector field (the heat flow) whose lines of force correspond with those of the temperature gradient field, i.e. the two vectors

flow and gradient are parallel, but have the opposite direction. In particular, the heat flux density vector (q) is defined as the amount of heat that in the unit of time passes through the isothermal surface unit. Analytically, this definition is expressed with the relation, well-known as Fourier law:

$$\mathbf{q} = -k \nabla T$$

Where the proportionality constant k is the thermal conductivity of the material, a positive scalar quantity which is a thermo-physical property of the material.

It represents the heat flux density relative to a unit temperature gradient and in the SI it is measured in $W \cdot m^{-1} \cdot K^{-1}$.

In the absence of sources and in stationary conditions, the thermal field does not depend on the thermo-physical properties of the medium. In the variable regime instead the properties occur through the thermal diffusivity (α) that in the SI it is measured in $m^2 \cdot s^{-1}$:

$$\alpha = \frac{k}{\rho c_p}$$

Where k is the thermal conductivity ($W \cdot m^{-1} \cdot K^{-1}$), ρ is the density ($kg \cdot m^{-3}$) and C_p is the heat capacity ($J \cdot kg^{-1} \cdot K^{-1}$). At the beginning Maxwell called it thermometric conductivity because thermal diffusivity is a transport property that occurs in thermal transients in which, two opposite attitudes of the material are expressed, or the ability to conduct thermal energy (expressed by k) and the ability to store heat (expressed by C_p). It is a very important parameter that measures the ability of a substance to transmit, not heat, but a change in temperature. Indeed, high values of thermal diffusivity increases the speed with which a temperature variation applied on the surface of the system propagates inside it. The heat equation admits different solutions for various boundary conditions, and these solutions include the values of the thermo-physical properties. However, the values of these properties can be determined by measuring the temperature and heat flow and comparing these value them with the solutions obtained from the heat equation. The analytical solutions of the Fourier equation, indeed, are limited to simple geometries, but they are important for the study of the basic properties in reverse heat conduction problems. Furthermore, during experiments, it is difficult to re-create the boundary conditions by the analytical solutions for which various methods for the determination of thermal diffusivity are developed but, in general, they involve the generation of a dynamic temperature field within a sample. The measurement process can be described in three steps in which at the beginning the sample temperature is stabilized, then a small thermal perturbation is applied and in the end, from the temperature response of the material the thermo-physical parameters can be calculated extrapolating them from the fitted curve (according to the model used [112]) to experimental one.

Heat Exchange by Convection

Heat exchange by convection occurs when a body is positioned into a fluid with a different temperature. The temperature difference causes a heat flow between the external part of the body and the particles in the fluid in contact, causing variations in the density of the fluid layers close to the surface. The density differences determine the upward motion of the lighter fluid and the downward motion of the heavier fluid. In this way, there is a movement of particles towards regions at lower temperatures where energy is transferred to other particles and therefore to a mixing of both particles and energy.

A gas with T_1 temperature, moving and touching the surface whose temperature is T_p , and goes away at a T_2 temperature (where $T_2 > T_1$) removes energy and so, in term of the energy balance, the heat exchange is associated with a modification in the enthalpy of the fluid which gets to the surface at a low enthalpy and leaves the same surface at a higher enthalpy.

The exchange of heat by convection is distinguished in natural and forced convection depending on the cause that determines the motion of the fluid. When the movement of the fluid is exclusively determined by density differences, this is called natural convection. If, on the other hand, the movement is generated by external agents such as fans or pumps, then convection is defined as forced convection. Often, however, there are intermediate situations of mixed convection, such as when using fan-coils (radiators with fan) in which, if the fan is in movement, the contribution of heat to the environment is due to both the fan and the radiator itself. In all three cases, the fluid can move in a laminar or turbulent motion but, usually, the values of the heat exchange coefficients are higher in the cases of forced convection and turbulent motion, while the minimum is for natural convection and laminar motion. In fact in natural convection the intensity of the mixing motions is generally lower than in forced convection.

Because the nature of the fluid has a strong influence on convection heat exchange phenomena, the study of convection is based on understanding the fluid-dynamic characteristics of the fluid. Comparing two fluids such as air and water and considering the specific heat of air which is lower than that of water, the use of an equal mass and at the same temperature variation, water removes more energy than air and is consequently a better chiller.

In terms of mathematical analysis, the Fourier equation is not appropriate to study heat exchange by convection because it was obtained from the hypothesis of static object and therefore is not suitable in the case of a fluid in motion.

The problem can Navier's equation, obtaining:

$$\frac{\partial}{\partial x} \left(k \frac{\partial T}{\partial x} \right) + \frac{\partial}{\partial y} \left(k \frac{\partial T}{\partial y} \right) + \frac{\partial}{\partial z} \left(k \frac{\partial T}{\partial z} \right) + \dot{q} = \rho c_p \frac{\partial T}{\partial t}$$

Where k is the thermal conductivity ($\text{Wm}^{-1}\text{K}^{-1}$), q' is the rate at which energy is generated per unit volume of the medium (Wm^{-3}), ρ is the density (kg m^{-3}), C_p is the specific heat capacity ($\text{J Kg}^{-1}\text{K}^{-1}$).

This equation is validated when the particles of the fluid heat up and become lighter, the expansion work is negligible. Therefore, the density remains constant or its variation is so small as to be irrelevant compared to the average value ($\rho = \rho_0 + \rho'$) and the temperature variations are small $(T_1 - T_2)/T_1 \ll 1$.

Temperature differences in the fluid generate motions which are regulated by Navier's equation that is coupled to the Fourier and continuity equations under stationary conditions to define complex the system.

In cases of forced convection, the calculation can be simplified by solving the fluid dynamics problem and using the solution as a boundary value of the thermal problem. Convection can be quantified using a convection coefficient h (obtained from the empirical correlation) whose unit of measurement is $\text{Wm}^{-2}\text{K}^{-1}$:

$$\dot{q} = h \cdot (T_p - T_s)$$

Where the quantity q is the heat flow, T_p is the solid surface temperature and T_s is the temperature of the fluid (at a point away from the surface).

The convection coefficient is not a constant quantity but depends on the geometry of the surface, the velocity, the physical properties of the fluid and frequently also on temperature differences. However, in order to know the total heat exchanged, usually its average value is used

$$q = \bar{h} \cdot S \cdot (T_p - T_s)$$

Where S is the surface of the solid wall, q is the quantity of heat exchanged and h is defined as:

$$\bar{h} = \frac{1}{S} \int_S h \cdot dS$$

Called average convection coefficient (or integral value of the convection coefficient).

Heat exchange by radiation

Radiation is the energy transfer by the propagation of electromagnetic waves, possible because every object above zero Kelvin is a source of electromagnetic waves.

This type of heat transmission does not involve the presence of an interposed medium, in contrast to the other types discussed above, but it occurs at the speed of light, and is not attenuated in a vacuum.

The ideal surface that emits the maximum power by radiation is called black body whose emissivity coefficient is 1 but every real surface emits less than black body because the emissivity depends on its physical properties and the temperature.

Emissivity values are between 0 and 1, the higher the value the closer the surface approximates the black body behaviour.

Moreover, the black body is also a perfect absorber of the radiation that illuminates it and so the absorptivity $\alpha = \epsilon = 1$, while bodies having α and ϵ independent from the wavelength are called grey, therefore $\alpha = \epsilon < 1$.

In the case of a net transfer from a black body with surface area A_1 at absolute temperature T_1 to environment at uniform temperature T_2 , the thermal power exchanged by radiation is given by Boltzmann's equation:

$$\dot{q} = \sigma A_1 (T_1^4 - T_2^4)$$

Where σ is called Stefan-Boltzmann constant and $\sigma = 5.67 \cdot 10^{-8} \text{ Wm}^{-2}\text{K}^{-4}$

It is obvious that compared to the ideal case where surfaces absorb and emit all wavelengths and have a uniform temperature, a development of Boltzmann law that allows deviation this pattern is:

$$\dot{q} = \epsilon \sigma A (T_s^4 - T_c^4)$$

Where ϵ is the emissivity of surface A_1 whose value is $0 \leq \epsilon \leq 1$, and F_{12} is the angle factor (or view factor) that gives the fraction of the radiation from A_1 that light on the area A_2 at temperature T_2 (also $0 < F_{12} < 1$).

Likewise to the heat exchange coefficient by convection, an exchange coefficient by radiation can be defined (radiative conductance)

$$h_r = \frac{q}{A_1 (T_1 - T_2)} = \epsilon \sigma F_{12} (T_1 + T_2) (T_1^2 + T_2^2)$$

But if the temperature of the bodies are not excessively different, this equation can be approximated by

$$h_r = 4 \epsilon \sigma F_{12} T_{av}^3$$

Where T_{av} is the average of two temperature

Heat transfer from finned surface: a case study

The convection coefficient for liquids in forced convection has values of thousands of $\text{Wm}^{-2}\text{K}^{-1}$, in contrast to the convection coefficients for gases are very low (of the order of tens of $\text{Wm}^{-2}\text{K}^{-1}$). This means that if a heat exchange between a liquid or condensing vapour and a gas has to be realised, the dominant thermal resistance is represented by the interface with the gas phase.

There are many situations of practical interest like for example in the radiator of a car or the condenser in a refrigerator or in the cooling of the cylinder of an internal combustion engine that cannot maintain the temperature at acceptable values for low h value by dissipating the heat through the lateral surface of the cylinder.

A similar problem has been found in electronic devices to which the requirement of lightweight or small size devices should be added.

In the design and engineering of various types of heat transfer equipment, simple profiles such as cylinders, bars, and plates are used to implement the flow of heat between a source and a spreader. They provide heat-exchange and are known as a prime surface. When a prime surface is extended by appendages intimately connected with it, such as the metal tapes and spines on the tubes, the additional surface is known as extended surface.

The study of surface heat transfer, in most cases includes two factors: the first considers only the movement of heat within the fin by conduction while the second considers the way the fin exchanges heat with the surrounding environment, which usually involves convection and radiation individually or together.

Much insight on the heat flows, temperature profiles efficiencies, and optimization of fin parameters can be obtained from analysis of the two fundamental fin geometries such as longitudinal fins and radial ones. Indeed, fins of various geometries and thermal conductivities respond differently to identical and uniform heat sources.

There are several ways in which the temperatures and heat transfer coefficients of sources and heat spreader may vary and so, it is important to the analysis of fin geometries are the assumptions that are employed to define the problem and often to simplify its solution.

These conventions, which are almost always referred to as the Murray–Gardner assumptions [113, 114] are:

1. The convective heat transfer coefficient on the faces of the fin is constant and uniform over the entire surface of the fin;
2. The temperatures and the heat flow in the fin remain constant with time;
3. The temperature of the medium surrounding the fin is uniform;
4. Heat transfer to or from the fin is proportional to the temperature excess between the fin and the surrounding medium;
5. The thickness of fin is small in comparison to its length and height (so the heat transfer from the edges and the temperature gradients through the thickness of the fin may be neglected);
6. The temperature at the base of the fin is uniform and there no heat sources within;
7. There is no contact resistance between the base of the fin and the prime surface;
8. The heat transferred through the edges of the fin is negligible compared with the heat leaving its lateral surface.

The differential equation for the fin temperature profile is formulated from a consideration of the steady-state heat balance previously shown and in this case, only the differential element of height dx is considered. In geometric term, this differential element is confined by planes parallel to the fin base at x and $x+dx$ and by the limiting profile curves, $y=\pm f_2(x)$.

If the fin surface temperature is $T(x)$, and T is the temperature at dx and so the difference between the heat entering the element by conduction at $x + dx$ and the heat leaving the element by conduction at x is

$$dq = k \frac{d}{dx} \left[f_1(x) \frac{dT}{dx} \right]$$

Where k is the thermal conductivity of the fin.

Because the difference in heat conduction (into and out of the element dx) must be balanced (in order to respect the assumption of a steady state) by some way of heat dissipation from the exposed lateral surface of the fin, considering the heat dissipated by convection to the surrounding medium,

$$dq = hP (T - T_s) dx = 2h [L + f_2(x)](T - T_s)$$

Where P is the fin perimeter and h is the convective coefficient.

Moreover, considering the approximation in which the fin thickness can be ignored respect to fin's length, that also presume the element dx on the surface described by $f_2(x)$ is equal in height to the element dx on the x -axis, for $L \gg 2 f_2(x)$ and

$$dq = hL (T - T_s) dx$$

And considering the temperature differences $\theta = T - T_s$ where T is the temperature of a point onto the fin and T_s is the environments which is assumed constant, $d\theta = dT$ the previously differential equation can be equalled to obtain the general differential equation [115]:

$$k \frac{d}{dx} \left[f_1(x) \frac{d\theta}{dx} \right] = 2hL\theta dx \quad \text{or} \quad f_1(x) \frac{d^2\theta}{dx^2} + \frac{df_1(x)}{dx} \frac{d\theta}{dx} - \frac{2h}{k} \theta = 0$$

If $f_1(x) = 2L f_2(x)$ it becomes:

$$2Lf_2(x) \frac{d^2\theta}{dx^2} + \frac{2Ldf_2(x)}{dx} \frac{d\theta}{dx} - \frac{2h}{k} \theta = 0$$

Below will show the treatment of a longitudinal fin of rectangular profile in which $f_2(x) = \delta/2$ where δ is the fin thickness as show in the Figure 17. Moreover because $f_2(x)$ is constant, its derivate $df_2(x)/dx=0$. Therefore, the differential equation that describes the phenomenon is:

$$\frac{d^2\theta}{dx^2} - \frac{2h}{k} \theta = 0$$

Which is a second order differential equation whose solution are:

$$\theta = C_1 e^{mx} + C_2 e^{-mx} \quad \text{where} \quad m = \left(\frac{2h}{k\delta} \right)^{1/2}$$

Defining m as “fin performance factor”.

Applying the boundary condition is possible to obtain the constant C_1 e C_2 .

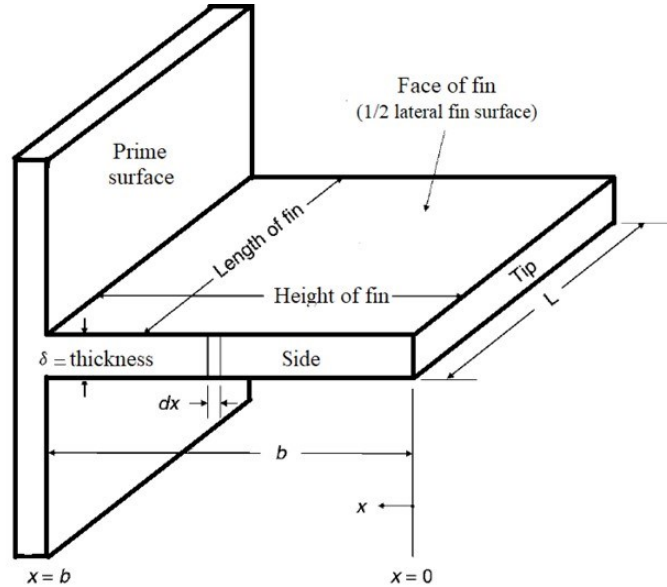


Figure 17. Longitudinal fin of rectangular profile.

There are different types of longitudinal fins (with triangular profile, concave or convex parabolic profile) but each one has a specific treatment of the mathematical equation to describe geometrically the problem [116].

Similar approach can be used to define the generalized differential equation of any radial fin whose profile is confined by two symmetrical curves that are functions of the radial coordinate r , $y = f_2(r)$ and $y = -f_2(r)$ as shows in the Figure 18. In the radial differential element the temperature difference $\theta = T - T_s$ between heat conducted and that leaving the element an $r + dr$ is:

$$dq = k \frac{d}{dr} \left[(2\pi r) 2 f_2(r) \frac{d\theta}{dr} \right] dr$$

That can be equalized to the heat that leaves the element r (according to the energy balance for a time invariant steady state system) where $dq = 2h (2\pi r dr) \theta$.

$$4\pi k \frac{d}{dr} \left[r f_2(r) \frac{d\theta}{dr} \right] dr = 4\pi h \theta r dr$$

That may be write as the better known form generalized differential equation:

$$k \left[f_2(r) \frac{d^2\theta}{dr^2} + f_2(r) \frac{d\theta}{dr} + r \frac{df_2(r)}{dr} \frac{d\theta}{dr} \right] = h\theta r$$

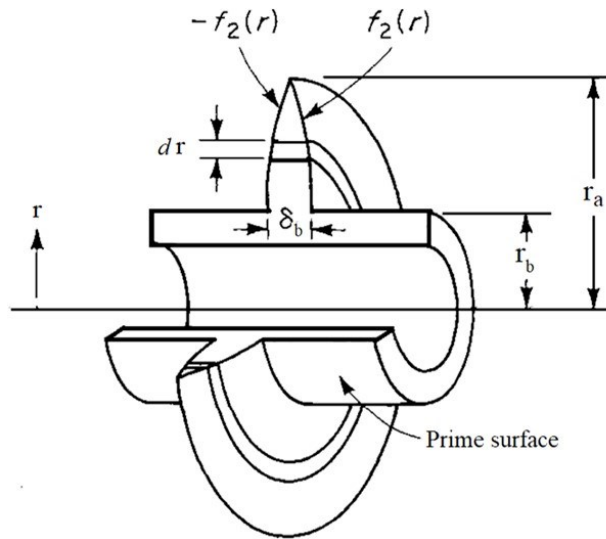


Figure 18. General representation of a radial fin

Similarly to the longitudinal fins, also for the radial ones there are different geometric configurations (with rectangular, hyperbolic and triangular profile) to which correspond different mathematical considerations [115, 117].

Because the performance of a heat spreader depends on the choice of material, in the next section we will compare the most commonly used materials with GRM-based films.

1.1.2. Materials for heat spreader

There are a large variety of heat spreader materials and their availability depend firstly on the application but also on the operation condition and cost. Although the most common materials are copper and aluminium composites, other high performance heat spreader are used such as chemical vapour deposition of diamonds, foam graphite based or ceramics. As show in Table 2, various heat spreader materials are available and will be discussed in order to evaluate their advantages and disadvantages. For example, between metals the most famous is copper that has very high thermal conductivity ($k \approx 390 \text{ Wm}^{-1}\text{K}^{-1}$) but, in other hand, it is very dense materials (8.9 g cm^{-3}) and its thermal expansion coefficient (TCE) is so high that prevents its direct use on silicon substrates.

Aluminium is another metal largely used for heat spreading application because although thermal conductivity is lower than copper the cost of production and its manufacturability make it very attractive. Moreover it density is very low but there is the same problem in term of TCE which is too high respect to silicon. Heat spreaders fabricated with copper or aluminium are usually inserted between electronic components and heat sinks.

A valid alternative are the highly thermal conductive ceramics with lower TCE values than copper and aluminium that can be exploited as substrates for microelectronic modules. Despite good dielectric proprieties, however, these materials are fragile and so they are not employed in application in which flexibility or electric insulator characteristics are required.

Beryllium oxide (BeO or beryllia) is cubic packed structure with high thermal conductivity ($k \approx 250 \text{ Wm}^{-1}\text{K}^{-1}$). While at 25°C the thermal conductivity is higher than aluminium one, increasing the temperature, it dramatically falls since to $134 \text{ Wm}^{-1}\text{K}^{-1}$ at 150°C and although beryllia is largely used for not flexible electronics devices, it important to consider the toxicity of its powder and dust that are toxic if inhaled.

Similar to beryllia, the thermal conductivity of silicon carbide (SiC) decreases rapidly as the temperature increases ($k \approx 270 \text{ Wm}^{-1}\text{K}^{-1}$ at 25°C) but has a low TEC making it a widely used material for use as a heat spreader or substrate.

Aluminium nitride (AlN) has slightly superior characteristics compared to beryllia. In fact, it has a higher thermal conductivity at room temperature that does not decrease as much as BeO's when the temperature increases. In addition, its TEC is very similar to the silicon so it can be used in electronic devices with high computational power.

Aluminium Silicon Carbide (AlSiC) is a high-pressure composite material in which a SiC preform by metal injection moulding of a SiC-binder slurry, is pyrolyzed to remove the binder and then infiltrated under pressure with molten aluminium. The material has high stiffness and low density, exploitable as thin substrate or to produce large fins as heat spreader [118].

Dymalloy is a metal matrix composite consisting of 20% copper and 80% silver alloy [119]. It has very high thermal conductivity ($k \approx 400 \text{ Wm}^{-1}\text{K}^{-1}$), and its thermal expansion can be regulated introducing trace of other materials. It is largely used in microelectronics as substrate or heat spreader for high power and high density multi-chip modules, although its cost is relative higher than other materials.

Natural graphite is usually used as heat spreader because its density is one-fourth than copper and the thermal conductivity can be as high as $500 \text{ Wm}^{-1}\text{K}^{-1}$ in the plane. However natural graphite is an anisotropic material and it has a much lower thermal conductivity through the plane [120]. Therefore, research has been made to improve the normal thermal conductivity of natural graphite by incorporating copper or by building sandwich structures of laminates with results up to $400 \text{ Wm}^{-1}\text{K}^{-1}$ [121]. Graphite heat spreaders are commonly used in electronic cooling applications where heat flux density is low, such as with memory modules and portable electronic devices, or in the application field in which corrosion resistance or thermal one are required.

As well know, diamonds has superior thermal conductivity, in comparison to the copper and their applications as heat spreaders include substrates for particular devices, such as laser and diodes [122] in which electronic components are located in a small volumes. However it is very expensive because they are usually made by growing on metal or ceramic surface using chemical vapour deposition in a plasma chamber with a growth rate of 0.1-1.0 pm/h [123]. In order to increase the

productivity (100 to 1000 pm/h), combustion method were developed but the quality and thermal conductivity are lower than CVD diamonds [124].

	Density (gcm ⁻³)	Thermal Conductivity (Wm ⁻¹ K ⁻¹)	Specific Heat (Jg ⁻¹ °C ⁻¹)	TCE (ppm°C ⁻¹)	Electrical Resistivity (Ωm)
Copper	8.89	388	0.39	16.5	16.7x10 ⁻⁹
Aluminum Alloys	2.71	180-220	0.9	23.1	28.2x10 ⁻⁹
Beryllium Oxide (BeO)	2.87	250	1.05	7.5	>10 ¹⁴
Aluminum Nitride (AlN)	3.27	270	0.76	4.4	>10 ¹³
Silicon Carbide (SiC)	3.1	290	0.64	3.7	>10 ¹³
Aluminum Silicon Carbide (AlSiC)	3.02	170-200		7	>10 ¹³
Dymalloy	6.4	360-420	0.57	7.4	
Graphite (Natural)	1.7-1.9	2.4-3.5 (normal) 300-400 (parallel)	0.85		9.8x10 ⁻⁶ (normal) 4.1 x10 ⁻⁵ (parallel)
Diamond	3.52	1600	0.55	1.02	>10 ¹⁴

Table 2. Properties of typical Heat Spreader Materials [125].

Beside conventional materials, nanomaterials appeared as a possible solution for highly efficient thermally conductive materials, based on the extensive research on thermally conductive nanoparticles such as carbon nanotubes, graphene and related materials. That show intrinsic thermal conductivity significantly superior to conventional materials, as shown in the Table 3.

The thermal conductivity of graphene depend on phonon transport but it is strongly influenced by the presence of defects, edge scattering, fabrication residues or substrate. Indeed if the intrinsic thermal conductivity of suspended graphene varies in the range between 2000 and 5000 Wm⁻¹K⁻¹ (Table 3) at it is drastically reduce since to 600 Wm⁻¹K⁻¹ when graphene is supported on SiO₂ substrate [126] as well as only the 25% of vacancies can reduce the thermal conductivity over 50% [127]. Similar results are obtained for CNT whose high intrinsic thermal conductivity is exploitable for structures suspended [128]. Another parameters that controls the thermal

conductivity values in the number of layers, for which increasing the number of stacked layers, the thermal conductivity decrease from 1300 $\text{Wm}^{-1}\text{K}^{-1}$ for FLG to 600-800 $\text{Wm}^{-1}\text{K}^{-1}$ for MLG[129] approaching the value of bulk graphite (100-400 $\text{Wm}^{-1}\text{K}^{-1}$). At the end, in order to have a completely panorama, it was also considered the GO in which, when the vacancy defect was beyond 2%, the thermal conductivity did not show significant change contrary to the degree of oxidation for which the 10% as value, the thermal conductivity decreased by $\sim 90\%$ [130] approaching two-three order of magnitude less than graphene.

Material	Method	Thermal conductivity $\text{Wm}^{-1}\text{K}^{-1}$	Ref.
Monolayer graphene	Theoretical models	2000-5000	[131]
Monolayer graphene isolated	Optothermal Raman	4840-5300	[132]
Graphene ribbon isolated	Theoretical model: Ballistic	4000	[133]
Grafene ribbon individual	Thermoelectric measurements	1000	[134]
SWCNT	Theoretical model molecular-dynamics	3000-4000	[135]
SWCNT individual	Thermoelectric measurements	3500	[132, 136]
MWCNT individual	Thermoelectric measurements	3000	[132, 137]
Graphene fiber individual	Thermoelectric measurements	600-1000	[138]
FLG individual	Optothermal Raman	1300	[139]
MLG	Optothermal Raman	600-700	[129]
GnP	Laser flash analysis	300-400	[140]
GO isolated	Theoretical model molecular-dynamics	3-30	[130]
GO	Thermal flash technique	18	[141]

Table 3. Comparison GRM intrinsic thermal conductivities.

The most common solution to exploit graphene related materials into highly conductive devices are the thin films that could be deposited onto a substrate or can have free standing form such as sheets, papers and membranes. In the first case, the thickness is usually sub micrometric and the mechanical proprieties are principally related to the substrates while in the second case, the thickness can be tens or hundreds micrometers and the materials can be used for application in which flexibility is required.

Graphene-based films obtained from GRM solutions use wet production, in order to decrease the cost of production without the employment of metallic substrates (such as copper in the CVD) or operating with mild condition. In general, most of techniques start from a suspension of GO nanoflakes whose stability in polar solvent (especially water) is well known, and then thermal, physical and chemical post treatment (such as annealing or reduction chemicals) are common to regenerate the graphene plane (reducing the oxidized carbon atoms which have sp^3 hybridization).

The drop-casting [142] and dip-coating [143] are two of the most renowned methods to fabricate graphene films for industrial scale in which cheap chemicals are used to deposit single and multi-layer GO nanoflakes onto various substrates. The most common substrates are mica mineral, metals, and SiO_2 one after its functionalization with 3-aminopropyltriethoxysilane (APTES) [144].

This method is also used to fabricate thin nanocomposite films derived from graphene and natural rubber in which the thermal conductivity increase between 480 and 980 % [145].

The dip-coating method is principally used to prepare thin films in which optical proprieties are have be guaranteed such as window electrodes for dye-sensitized solar cells. Indeed, after the exfoliation of GO, in order to increase the thermal conductivity there is a thermal reduction step that is useful for the wettability of the surface and its chemical stability [146].

The industrial evolution of these two techniques is the spraying method whose capability to fabricate films over large scale; it permits to produce homogenous films for various applications [147-150].

The main critical conditions are the homogeneity of the suspension GRM based and relative concentration for the production of high quality films. Therefore, on the one hand the functionalization of the nanoflakes or the surfactant's addition can stabilize the dispersions, on other hand, any additive influence the performance of the resulting materials. There are many solutions related to final application where thermal or other post treatments are sustained after the GO deposition from aqueous dispersion, or where the surface's wettability is important to use solvents as medium. Indeed N,N-dimethylformamide (DMF) and N-methyl-2-pyrrolidone (NMP) solvents are well demonstrated to guarantee stable suspension of multilayer graphene (MLG), graphite nanoplatelets (GnP) and graphene nanoflowers (GNFs), whose spray ability has a good control also for micrometre of GRM deposition onto glass substrate or surfaces with a layer of acid-methyl methacrylate (MA) as coating [147].

There are different configurations but the most commonly used is a setup in which there is an atomizer connected to a ultrasonic system whose syringe pump takes suspension from a flask and inlet it with a carrier gas into a piezo component that generate drops. These are perpendicular inlet on a substrate that is usually heated onto a hot plate in order to promote the evaporation of solvent.

Spraying method, in recent times, has been implemented for the production at large scale of counter electrodes (CEs) for dye-sensitized solar cells (DSSCs) [151] or to deposit rGO onto plastic substrates in order to increase their electrical and thermal conductivity maintaining almost transparent the substrates [152].

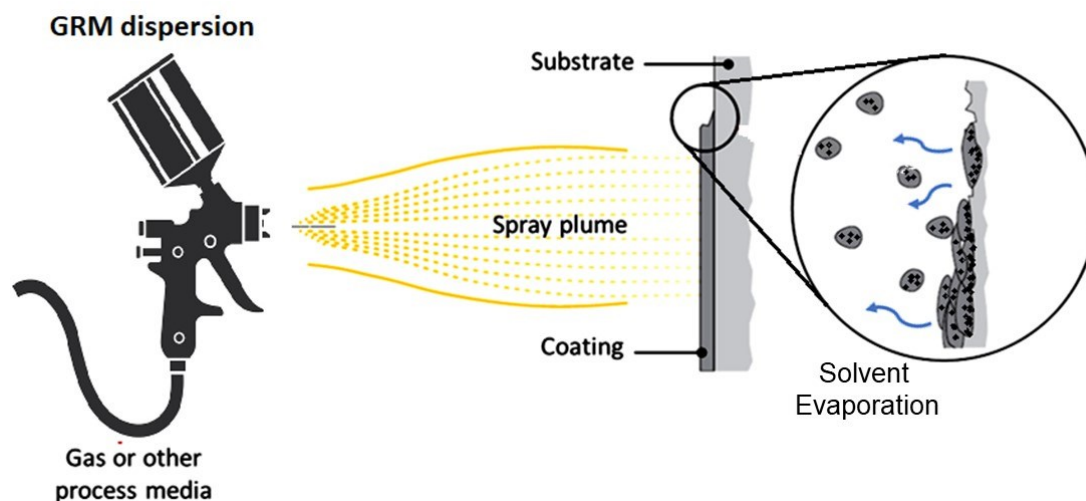


Figure 19. Schematic representation of spray deposition technique. GRM dispersion droplets are generated mechanically by a gas into the spray gun. They are then deposited onto the substrate, which could be heated to evaporate the solvent.

Spin-coating (shown in Figure 20) can be used to cover a large surface with a few layers of graphene materials whose mechanical properties can show excellent Young's modulus, although they are the overlap between nanoplatelets.

The most famous industrial spin-coating process starts from a suspension in methanol in which GO platelets are exfoliated and then dispersed in methanol to form suspensions that are deposited onto a substrate in order to promote the solvent's evaporation using N_2 flow carrier dry gas [153].

The resulting continuous film is post-treated by chemical reduction with hydrazine hydrate vapour or with thermal annealing, whose thickness is between 4 and 20 nm. Indeed, the dimensions of these assemblies depend on, not only, the dimension of substrates and its chemical nature (such as polymeric or inorganic one) but most importantly if there are superficial supports like cones or other lithographic constructions [154]. Finally, it is obvious that adjusting the spin coating speed, it is possible to obtain membranes with different thickness ranges (such as for example with 1–2 layers using 8000 rpm, 4–5 layers with 6000 rpm and 7–8 layers were obtained at 4000 rpm) with a diameter commonly about 30–45 mm whose optical transparency drastically decreases on contrast to their mechanical properties.

Thermally conductive graphene films for heat dissipation are fabricated from an aqueous solution of GO and a wet-spinning process to arrange GO sheets that finally, were chemically reduced and after a thermal annealing the film shows in-plane thermal conductivity over $1000 \text{ Wm}^{-1}\text{K}^{-1}$ [155]. On the other hand, this process is not so competitive for large-scale production because the cost of production is high, related to the process of thermal annealing around 3000°C that could be considered the sintering temperature.

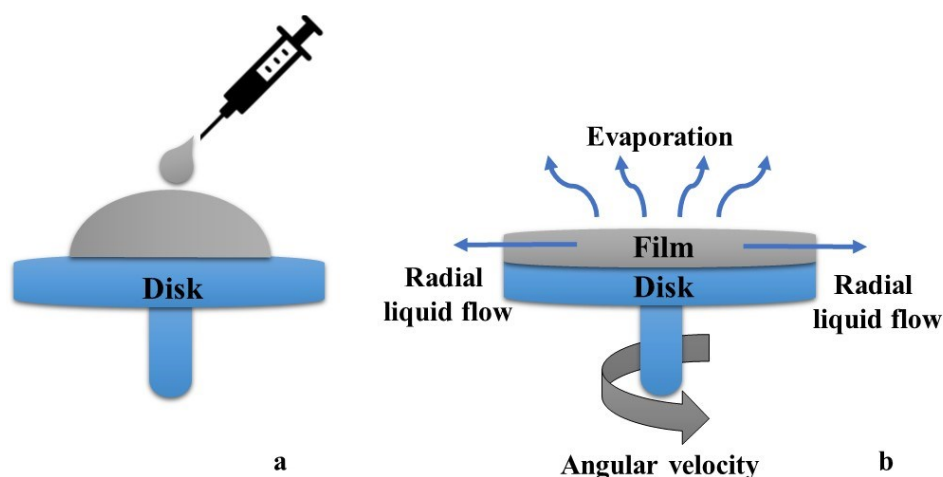


Figure 20. Schematic representation of spin coating technique. a) Droplets GRM dispersion are deposited onto the disk. b) The disk start to rotate and the GRM move from the center to the edges while the solvent evaporates.

Electrophoretic deposition is a competitive technique for large volume productions because the deposition not require binder or other cross-linker, and, on other hand, films with higher packing factor (strong alignment of nanoflakes) are obtained [156]. This technology use various electrical conductivities substrates (such as ITO-glass, Cu, Al, steel or p-type Si) or solutions containing salts heavy metal based, that form graphene hybrid films useful for battery, catalyst applications or to fabricate very thin film for heat diffusion application maintaining, at the same time, the transparency [157].

Langmuir-Blodgett (LB) assembly is a technique to fabricate films [158] due to the floating of GO nanoflakes onto the surface of water in which the amphiphilic nature of GO plays a key role in term of quality of the process [159]. Indeed the dimension of the flakes determinate the affinity between GO and water solution, because, the polar functional groups are mostly located at the edges of nanosheets or generally the charge density is spread in a surface and so, smaller nanopaper has more hydrophilic characteristic which make them stable into suspension on contrast to larger ones that separate themselves and float onto water surface. Two main phenomena regulate the interaction between layers are edge-to-edge and surface-to-surface [160] that guarantee the development of stable mono or multilayer of GO due to the electrostatic repulsion between different flakes.

Indeed, during the compression step, the GO nanosheets move all together on the water surface since to slide on top of another.

Finally, the superficial layers are transferred onto thermally conductive substrates [161]. The disadvantages of this process are the scalability, but more important, the compatibility of the substrates to resists to reduction treatments (chemical or thermal) that must be carried out to remove the oxidized groups from the GO film.

Layer by layer is a novel strategy to produce hybrid GRM films trough multilayer deposition of materials whose opposite charge permit them to interact with ionic or hydrogen bonding [162-164] . In the most case are used GO derivate to fabricate

highly orderly free-standing films [165], whose flakes multilayers stratified (since a thickness of 50 nm) are sufficiently strong to be moved onto other substrates. In addition, the electronic and thermal properties can be improved through chemical reduction or thermal annealing such as the ggraphene oxide/alumina hybrid films of Sunghwan Hong et al that show in-plane thermal conductivity of $565 \text{ W m}^{-1}\text{K}^{-1}$ with and cross-plane thermal conductivity of $18.1 \text{ W m}^{-1}\text{K}^{-1}$ [166]. On other hand, this value depend on the high density of the film related to alumina (3.95 g cm^{-3}), and a post thermal annealing at around 1000°C that increase the cost of production.

Most of the techniques analyzed above, showed the limit that substrates are required for the production of GRM-based films. However, these substrates must have specific chemical-physical characteristics because if in one hand they have compatible with the solvents and chemical reagents used, they must resist either chemical reduction or high thermal properties are required to resist to thermal annealing.

Therefore, freestanding papers or membranes are considered fascinating materials as alternatives to the materials used today for many applications such as actuator[167], sensing [168, 169] thermal management [170]. Moreover other industrially scalable techniques (such as electrospray [171], solution casting [172-175] and tape one [176] and vacuum filtration of GRM's suspension through a porous membrane filter [177-180] from which large amounts of GRM derivatives can be produced, especially foil, laminate or membrane, will be analysed in detail below.

It is possible obtain papers with good thermal and morphological characteristics evaporating in mild condition a solvent or water suspension of graphene or GO [181]. A substrate is usually used as a base on which the suspension is gradually self-assembled and consequently the thickness is also controlled (from a few microns to tens of microns). Indeed, during the evaporation process the GRM concentration increase more and more and flakes-to-flakes interaction are promoted, leading to self-alignment or a multilayers structure as show in Figure 21.

An interesting applied research [176] have been demonstrated that the tape casting process is a promising technique for the continuous process of GRM films production. The suspension is ejected through a slit by moving the substrate relative to a doctor blade, as show in the Figure 21 b and under conveyer roller there is a heater in order to increase the solvent's evaporation.

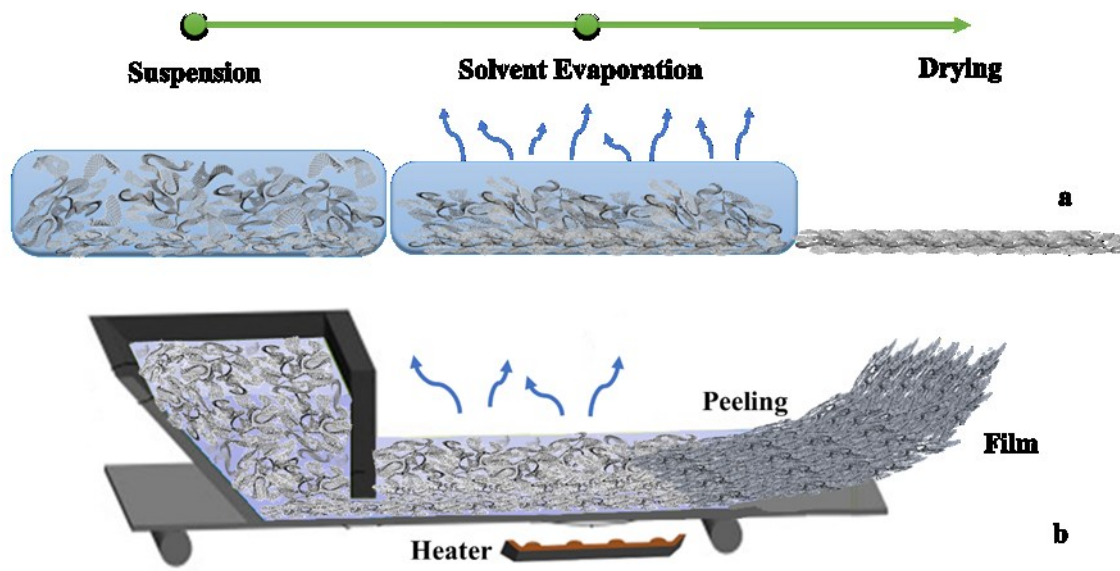


Figure 21. a) Schematic representation of self-assembly process from solvent's evaporation in static condition. (b) Tape casting industrial method to obtain GRM films in continuous process.

Because the starting suspension should be stable in order to avoid that the graphene material accumulates on the bottom and occludes the outlet before it is removed, aqueous GO suspensions are usually used. Moreover, for thermal application the resulting GO films have been press and thermally reduced with increment of production costs [182] as consequence.

Electro-spray deposition (ESD) is another continuous industrial process which is largely used to produce large quantities of free-standing GRM papers [183] because it is possible combine this technique upstream with exfoliation and downstream by continuous roll-to-roll method.

The advantages are the formation of mono-dispersed charged drops from GRM suspension that are deposited with high precision onto aluminium substrates (Figure 22). Indeed, an electric voltage (some kV) is applied not only to produce the repulsion force between drops, but also, between injection nozzle and the substrate in order to maintain constant the con-jet mode coupling a continuous flow rate by siring pumps. It is possible obtain films from the same dispersion with mechanical proprieties that are customized changing easily the electrical, thermal or others parameters [184, 185]. Moreover, the stripe are commonly compressed during the rolling step in order to obtain a homogenous material and thermal or chemical post-treatment are available such as annealing (2500°C under Argon gas flux) obtaining film with a range of thermal conductivity $200\text{-}500\text{ W m}^{-1}\text{K}^{-1}$ [186] depending of the grade of reduction but most important to deposition rate from which the alignment and compactness of material. Therefore low speeds improve the arrangement of the material obtaining more conductive films but decrease production volumes.

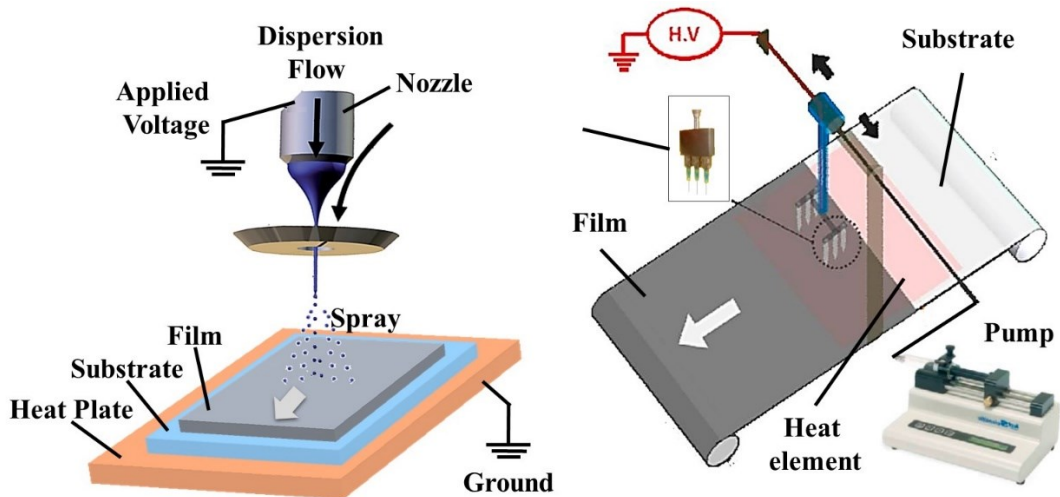


Figure 22. Representation of the ESD system (on the left) and the implementation of roll-to-roll technique for a continuous industrial process for the bulk production of paper GRM based.

The filtration through a membrane is the simplest and most conventional method to prepare free-standing papers starting from dispersion GRM based because, as shown in Figure 23, while the solvents are passed over the filter, the carbon flakes are blocked by the membrane as films. Moreover, a vacuum-assisted step is often used to boost the process or to regulate the thickness in order to obtain a film that can be peeled off as a free-standing membrane [187] similarly to the processes of paper production, therefore easily scalable industrially.

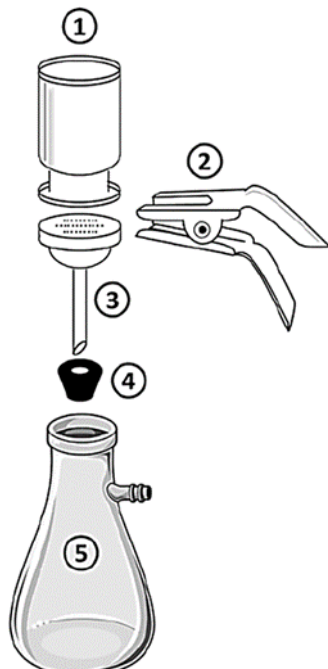


Figure 23. Schematic representation of vacuum filtration consisting of a glass filter holder assembly with funnel (1), metallic clamp (2), filtered base (3), stopper rubber base (4), and a vacuum filtering flask

The properties of a membrane, however, are related to organization of materials within it and this depend on method parameters. So it is possible distinguish two mechanism depending on the competition between material re-aggregation rate and filtration one. Indeed during the filtration, the GRM have a tendency to stack between themselves into the dispersion and precipitate onto the membrane organising in alignment manner due to hydrostatic forces [188] (as show in the mechanism 1 of Figure 24). Because a thin film is created firstly, the general process can be summarize like a film that increase its dimension developing a low porosity paper in which the solvent is removed at the end.

The opposite case is when the filtration rate is higher than re-aggregation one and so the random displacement of GRM is obtained within the membrane that show also high porosity (as show in the mechanism 3 of Figure 24).

The better compromise is the regulation of filtration rate in order to promote the stacking of GRM that self-assembled into domains leading a good alignment of material on the bottom of flask, but on other hand, the process time is reduced, making it competitive for industrial developments (as show in the mechanism 2 of Figure 24).

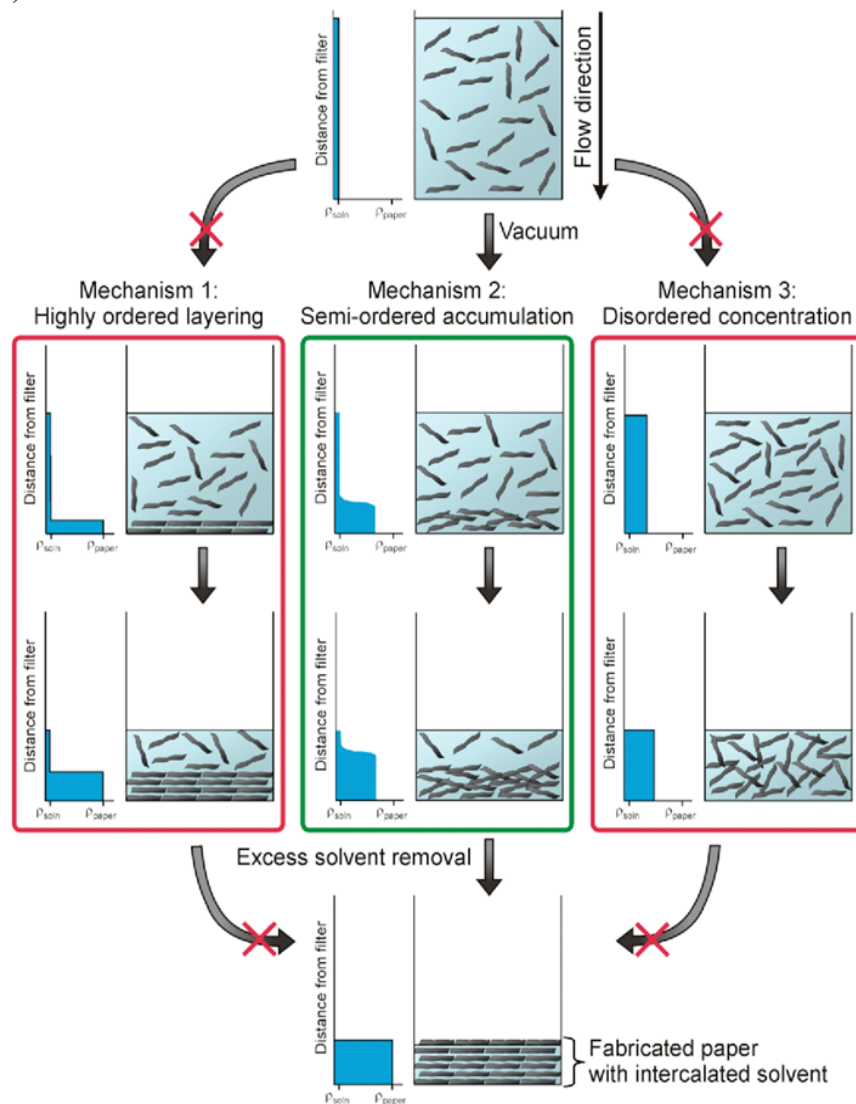


Figure 24. General representation of mechanism that regulate the formation of membrane GRM based and relative orientation of flakes inside the films. In the mechanism 1, there is a high alignment of flakes due to slowly filtration promoting the stacking and further precipitation. The mechanism 3 shows the randomly displacement as result of a faster filtration process while mechanism 2 is the optimal filtration rate which makes films organized as well as to the first mechanism, reducing at the same time the process timing.

For example, a process that use GO (because the hydroxyl groups promote the dispersion in an aqueous solvent and) shows a great alignment of flakes within the resulting film as proven by scanning electron microscopy (SEM) analysis [189] (shown in the Figure 25), while X-ray diffraction analysis confirmed that the space between layers corresponding about 0.83 nm related to the presence of water molecules locked through hydrogen bonding [190].

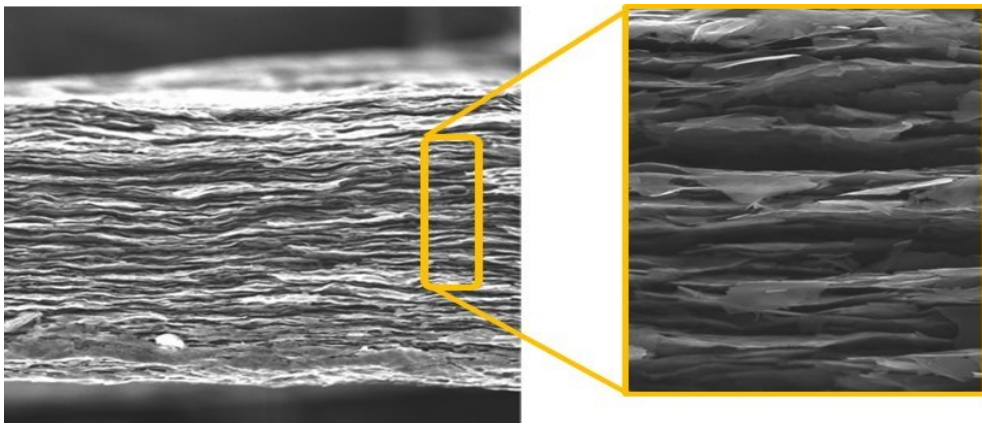


Figure 25. SEM analysis that shows the alignment of GOs within a membrane produced by filtration.

However, having a compact material is not the only condition for good thermal properties that can be exploited in heat spreading. In fact, GO membranes that show a conductivity of less than $10 \text{ Wm}^{-1}\text{K}^{-1}$ [191] must be reduced to remove the oxidized groups. The most common method industrially used, as well discussed above, is the thermal reduction in which the temperature play a key role, as well discussed above. In fact, GO membranes show different ranges of thermal conduction values depending on the temperature at which they were annealed, such as about $200 \text{ Wm}^{-1}\text{K}^{-1}$ for annealing at 340°C [191], around $400 \text{ Wm}^{-1}\text{K}^{-1}$ for temperature 800°C - 1000°C [170], 800 - $900 \text{ Wm}^{-1}\text{K}^{-1}$ at 1100 - 1200°C [191], over 1000°C $\text{Wm}^{-1}\text{K}^{-1}$ for thermal annealing 2400 - 3000°C [192] that could be considered the temperature from which sintering phenomena take place.

In order to avoid thermal process that increase production costs, others approaches often use methods in which the row material is not a GO derivate but graphene ones or CNT.

Although the single nanotube shows excellent thermal conduction properties, the membranes obtained by filtering of its suspensions show two orders of magnitude lower values (less than $100 \text{ Wm}^{-1}\text{K}^{-1}$ [193-195] or 100 - $200 \text{ Wm}^{-1}\text{K}^{-1}$ [191]) that do not make them suitable for heat spreading applications.

High thermal performance was obtained, on the other hand, for membranes manufactured from suspension of graphene based materials. In particular MLG and GnP are widely used to produce suspensions in organic solvents and then filtered to obtain the corresponding like-paper foil. They show value between $300 \text{ Wm}^{-1}\text{K}^{-1}$ [196] and $600 \text{ Wm}^{-1}\text{K}^{-1}$ [197] which makes them the best candidates able to compete with the classic materials previously discussed.

Hybrid membranes have also been manufactured using a combination of different materials, such graphene quantum dots (GQDs) have been shown good proprietaries as stabilizers to achieve aqueous dispersions of graphene nanoflakes [198]. Due to 2D carbon structure, they are able to interact with basal surface through π - π stacking attraction and, in other hand, their surface is covered by hydrophilic groups [199, 200] which increase the dispersing aptitude [201] as show in the Figure 26 a. With this configuration there were no relevant improvements in thermal conduction properties that are more attributable to the quality of graphene used, in similar way to the liquid phase extraction process with PAHs.

Carbon nanotubes are used in combination with graphene to obtain membranes with more isotropic characteristics than those of graphene alone. Indeed, although CNTs react with the edges and the surface of flakes (which are closely stacked into aggregates as FLG), the π - π interactions increase the space between these macrostructures, decreasing the in plane thermal conductivity, but on the other, they widely enhance the cross plane thermal conduction respect to that one obtained for FLG pristine aligned within the membrane, giving continuity to the structures and create a 3D network [206] (Figure 26 b).

Molecular dynamics (MD) simulations had also calculated in which way CNTs increase the interfacial thermal transport across the plane and in particular, the model investigated the relationship between the length of CNTs as bridges between nanoflakes and relative thermal proprietaries. It is exciting how best result are obtained for the shortest CNTs or carbon nanorings (CNRs) which are vertically aligned within inter-space between graphene sheets as pillars [202] as show in the Figure 26 c. Despite they represent the next challenge, nowadays, the best results are obtained using the intercalation of a polymer or small molecules as carbon source and a catalyst metal based that enhance the control of pyrolysis step [203], but in any case, the results obtained are not so immediately scalable at industrial. Among the most promising research there is the work of Xin Meng et all in which suspensions of GO, GQDs and nanocellulose were filtered, obtaining films to which an annealing process at 2000°C was applied. Despite the high cost of production, both from the pyrolysis of cellulose and from the sintering of QDs, CNRs were obtained by increasing the thermal conductivity to values almost $2000 \text{ Wm}^{-1}\text{K}^{-1}$ [204].

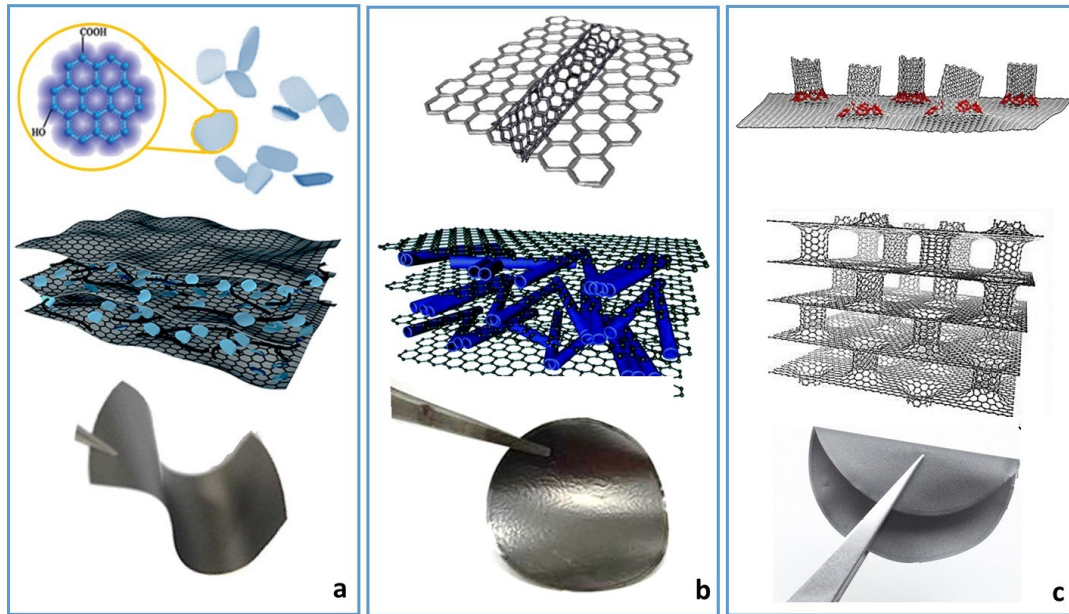


Figure 26. Representation of different dispersions GRM based and relative hybrid films. (a) Process that use QDs (b) CNTs (c) CNRs

The study on thermal conduction in GRM nanopaper is not easy because, on the one hand, thermal conductivity depends on the quality of the single GRM structure, as discussed above, on the other hand, the nature of the contact between different structures and the extension of the contact area inside the nanopaper determine the contact thermal resistance [181, 205]. For example during the deposition of GRM, orientation defects can create air cavities that increase thermal resistance and therefore their reduction obviously improves the thermal contact between the particles and consequently improves the overall thermal conductivity [206]. It is obvious that simple way to reduce the porosity and improve the contacts between the particles is the application of uniaxial pressure on the nanopaper, which has demonstrated good results for improving thermal conduction.

Recent studies, instead, have shown how the exploitation of molecular junctions between graphene structures can be a valid solution to increase thermal conductivity properties. In fact, while the conductance of molecular junctions has been extensively studied by the Functional density theory [207, 208] and molecular dynamics [209, 210] the experimental exploitation has been reported only recently [74, 211].

Bernal et al. functionalized GnP edges by exploiting the chemistry of diazonium aiming at the synthesis of nanoparticles to be used as building blocks in the preparation of nanostructured materials for better heat transfer. In particular, two types of functionalization have been used in order to make a comparison. The first one used phenol to exploit the hydrogen bonds (Figure 27 a) and the other a di-aniline derivate was exploited to covalently create a thermal bridge (Figure 27 b). As result, Bernal et al. obtained that the chemical functionalization drives the self-organization of the GnP within the nanopapers, leading to a 20% enhancement of the thermal conductivity both GnP functionalized with phenol and that one with di-aniline while

the cross plane thermal conductivity was also increased by 150% in the case of GnP linked covalently.

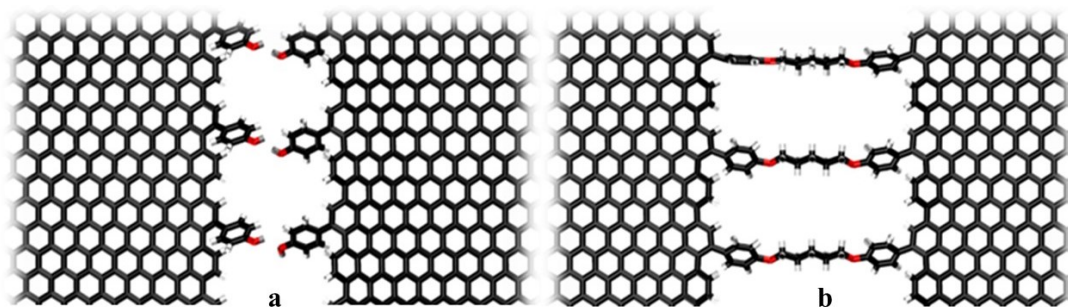


Figure 27. Selective functionalization at the edges of GnP. a) Functionalization with phenol to exploit the hydrogen bond. b) Functionalization with di-aniline to covalently link the GnP.

Using the same functionalization approach of GnP with bifunctional molecules to increase the thermal properties of nanostructured materials, two methods will be proposed in this thesis work. The first exploits the π - π interaction between the surface of GnP and bi-functional molecules derived from pyrene while the second exploits the Diels-Alder cycloaddition reaction between GnP and bifunctional linker derived from maleic anhydride. The resulting functionalized materials will be used for the manufacture of nanopapers that will be thermally characterized and tested as heat spreaders.

Chapter 2

Materials & Methods

This chapter illustrates the synthesis of organic compounds and their characterization by spectroscopic methods. These chemical compounds were used in the functionalization of GnP (Figure 28) which were also characterized. Functionalized GnP has been used as a raw material for the manufacture of nanopapers whose thermal properties were evaluated. By considering the nanopapers as porous materials, the thermal conductivity of continuous phases has been calculated in order to compare the values with those of metals for thermal applications. The experimental setup was also treated as classic model of surface extension by using fins, in order to evaluate nanopapers as potential heat spreaders.

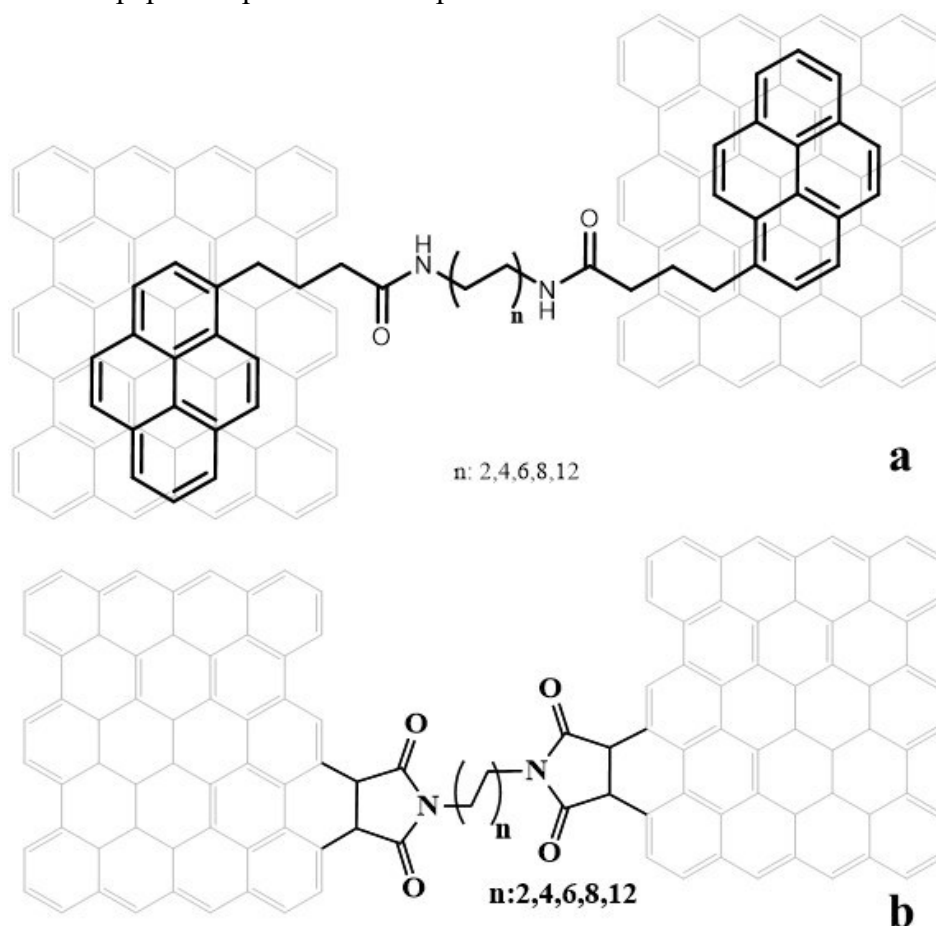


Figure 28. Schematic illustration of approach to functionalize the GRM. a) Supramolecular interaction between bispyrene molecules and surface of GnP. b) Diels Alder reaction between the edge of GRM and bismaleimide.

2.1. Synthesis procedure

2.1.1. Synthesis of bispyrene molecules

For the reaction, shown in Figure 29, 1-pyrenebutyric acid (300 mg, 1.4 mmol) (Sigma Aldrich, 97%) was dissolved in 100 mL dry toluene (Sigma Aldrich, anhydrous, 99.8%) and cooled at 5 °C. Thionyl chloride (Reagent Plus[®], ≥99.0%,) (10 mL) was added drop wise and the mixture was heated to reflux for 6 h under an argon atmosphere. Then the solvent was evaporated in vacuum to afford the orange solid, which was subsequently dissolved in dichloromethane (20 mL) (Sigma Aldrich, anhydrous, ≥99.8%,) [212]. A solution of the diaminoalkane (0.5 mmol) (ReagentPlus[®], ≥99%) in dichloromethane (2 mL) was added drop wise to the solution containing 1-pyrenebutyric acid and the reaction mixture was stirred at room temperature for 18 h.

The precipitate was filtered using nylon filter membranes (pore size 0.45 μm, Whatman), washed with dichloromethane and the solvent was evaporated. In order to remove the non-reacted 1,2-diaminoethane, the solid was stirred for 1 h in a 10⁻⁴ M solution of hydrochloric acid (ACS reagent, 37%) and filtered to obtain the corresponding pure product.

Applying the same procedure, bispyrene derivatives with different chain length between the pyrene groups were synthesized by varying the relative diaminoalkane (1,2-Diaminoethane, Sigma Aldrich, ≥99.5%; 1,4-Diaminobutane, Sigma Aldrich, ≥99%; 1,6-Diaminohexane, Sigma Aldrich, ≥99%; 1,8-Diaminooctane, Sigma Aldrich, 98%; 1,12-Diaminododecane, Sigma Aldrich, 98%) used in the reaction



Figure 29. Schematic representation of bispyrene molecules synthesis

2.1.2. Synthesis of mono-pyrene molecules

For the reaction, shown in Figure 30, 1-pyrenebutyric acid (300 mg, 1.4 mmol) (Sigma Aldrich, 97%) was dissolved in 100 mL dry toluene (Sigma Aldrich, anhydrous, 99.8%) and cooled at 5 °C. Thionyl chloride (Reagent Plus[®], ≥99.0%,) (10 mL) was added drop wise and the mixture was heated to reflux for 6 h under an argon atmosphere. Then the solvent was evaporated in vacuum to obtain the yellow solid, which was subsequently dissolved in dichloromethane (20 mL) (Sigma Aldrich, anhydrous, ≥99.8%,) [212]. A solution of the 1-Aminododecane (1 mmol) (ReagentPlus[®], ≥99%) in dichloromethane (2 mL) was added drop wise to the solution containing 1-pyrenebutyric acid and the reaction mixture was stirred at room temperature for 18 h.

The precipitate was filtered using nylon filter membranes (pore size 0.45 μm , Whatman), washed with dichloromethane and the solvent was evaporated. In order to remove the non-reacted 1,2-diaminoethane, the solid was stirred for 1 h in a 10^{-4} M solution of hydrochloric acid (ACS reagent) and filtered to obtain the corresponding pure product.

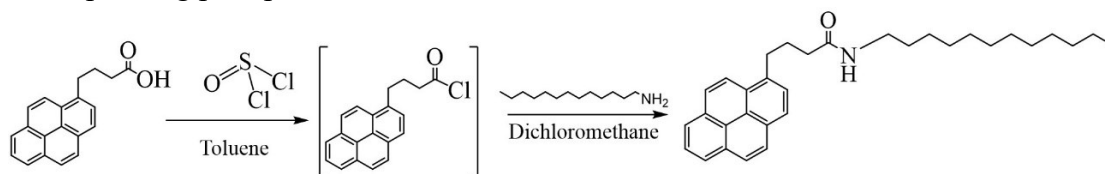


Figure 30. Schematic representation of mono-pyrene molecules synthesis.

2.1.3. Synthesis of bismaleimide molecules

The synthesis of maleimide follows two steps. The synthesis procedure for the intermediate (step I, shown in the Figure 31) obtained by reaction between maleic anhydride and diamines is described below. The method was performed on diamine compounds with variable aliphatic chain length between amino groups (1,2-Diaminoethane, Sigma Aldrich, $\geq 99.5\%$; 1,4-Diaminobutane, Sigma Aldrich, $\geq 99\%$; 1,6-Diaminohexane, Sigma Aldrich, $\geq 99\%$; 1,8-Diaminooctane, Sigma Aldrich, 98% ; 1,12-Diaminododecane, Sigma Aldrich, 98%).

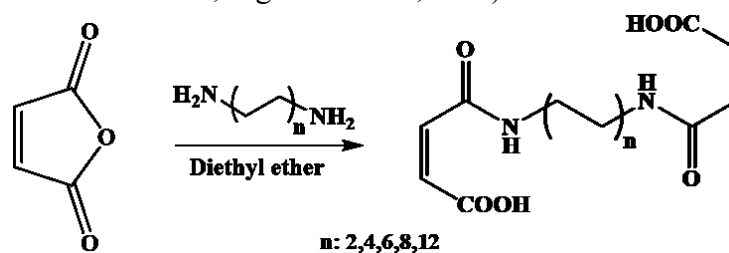


Figure 31. Schematic representation of the first reaction step for the synthesis of bismaleimide molecules.

The maleic anhydride (5.000 g, 51.7 mmol) (Sigma Aldrich, $\geq 99.0\%$) was dissolved in 150 mL diethyl ether (Sigma Aldrich, anhydrous, $\geq 99.7\%$) previously dehydrated and the 1,2 ethandiamine (1.5641 g, 25.8 mmol) in 20 mL also diethyl ether. This was added drop wise and the mixture was stirred at 20 $^{\circ}\text{C}$ for 16 h. The precipitate was filtered using polytetrafluoroethylene (PTFE) filter membranes (pore size 0.45 μm , Whatman), washed with diethyl ether and the white powder was dried at 40 $^{\circ}\text{C}$ for 2 h under vacuum.

To close the 5-member ring and then to lead to the formation of bismaleimide, the molecules obtained from the first step are used and an intramolecular condensation is carried out, as shown in Figure 32.

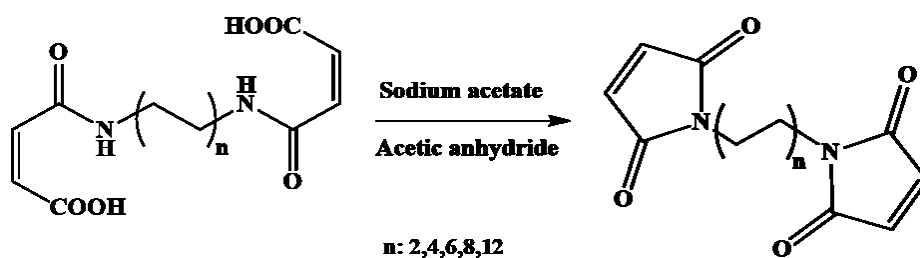


Figure 32. Schematic representation of the second reaction step for the synthesis of bismaleimide molecules.

The longest bismaleimide synthesis procedure obtained by closure of (2Z,2'Z)-4,4'-(dodecane-1,12-diylbis(azanediyl))bis(4-oxobut-2-enoic acid), the relative amide derivative defined with code N12, obtained after the reaction between maleic anhydride and 1,12-dodecanediamine, is described below.

5.000 g (1.36 mmol) of N12 compound were dissolved in 2.56 mL (32 mmol) of acetic anhydride (ReagentPlus[®], $\geq 99\%$) with 0.183 g (1.56 mmol) of sodium acetate anhydrous (Sigma Aldrich, $\geq 99\%$).

The mixture was stirred at 80 °C for 16 h and then it was transferred into 250 mL of a basic solution (230 mL of deionized water and 20 g of sodium carbonate (BioXtra, $\geq 99.0\%$) that was previously refrigerated at 5 °C.

The precipitate was filtered using cellulose filter membranes (pore size 0.20 μm , Whatman), washed with deionized water (50 mL) and diethyl ether (20 mL) (Sigma Aldrich, anhydrous, $\geq 99.7\%$) and, at the end, the solid was recrystallized in 10 mL of ethanol (Carlo Erba, 96%) for 6 h. After that, it was filtrated again (using cellulose filter membranes with pore size 0.20 μm , Whatman) and the resulting powder was dried at 40°C for 2 h under vacuum.

2.1.4. Functionalization of GnP with bis or mono-pyrene derivatives

GnP (10 mg) were added to a solution (20 mL of the selected bispyrene in N,N-dimethylformamide (10^{-6} M) (Sigma Aldrich, anhydrous, 99.8%) at a concentration of 0.5 mg mL⁻¹. The solutions were sonicated in pulsed mode (5 s on/5 s off) for 30 min at a power output of 150 W by using an ultra-sonication probe (Sonics Vibracell VCX-750, Sonics & Materials Inc, USA) with a 5 mm diameter Ti-alloy tip. After that, the suspension was left to decant for 120 min at 5°C and part of the supernatant was carefully collected for further characterization, while the other part was filtrated through a polytetrafluoroethylene (PTFE) supported membrane (0.2 μm as pore size, Whatman), washed with water (50 mL), ethanol (50 mL) (Carlo Erba, 96%) and diethyl ether (50 mL) (Sigma Aldrich, anhydrous, $\geq 99.7\%$) and dried at 60 °C for 24 hours.

2.1.5. GnP/Bismaleimide derivatives

The bismaleimide I12 (184 mg, 0.51 mmol) was dissolved into 50 mL of anhydrous xylene, stirred and deoxygenated with a gas flux of nitrogen for 30 min. 50 mg of GnP was transferred into the flask and the mixture was sonicated in a sonicator bath for 1h at 25 °C (power 500W, frequency 40 kHz). After that, the flask (covered with aluminium foil) was heated into a silicone oil bath at 120 °C for 12 h.

The precipitate was filtered onto a nylon membrane (0.45 µm as pore size, diameter 47 mm, Whatman) and washed with anhydrous xylene (20 mL) (mixture of isomers, ACS reagent, ≥98.5%) and diethyl ether (20 mL) (Sigma Aldrich, anhydrous, ≥99.7%) and finally dried at 40°C for 2 h under vacuum to obtain a black powder.

The solid were suspended into 100 mL of N,N-dimethylformamide (Sigma Aldrich, anhydrous, 99.8%) and sonicated in pulsed mode (5 s on and 5 s off) for 30 min with power set at 150 W) by using an ultra-sonication probe (Sonics Vibracell VCX-750, Sonics & Materials Inc, USA) with a 13 mm diameter Ti-alloy tip.

The suspensions were filtrated using a polyamide membrane (0.45 µm as pore size, diameter 47 mm, Whatman) and dried at 40 °C under vacuum for 16 h to completely remove the solvent.

2.1.6. GnP nanopaper

GnP and functionalized GnP were suspended on N,N-dimethylformamide (Sigma Aldrich, anhydrous, 99.8%) solutions (0.5 mg mL⁻¹) and sonicated in pulsed mode (5 s on and 5 s off) for 30 min with power set at 150 W) by using an ultra-sonication probe (Sonics Vibracell VCX-750, Sonics & Materials Inc, USA) with a 13 mm diameter Ti-alloy tip. The suspensions were gravimetrically filtrated using a polyamide membrane (0.45 µm as pore size, Whatman) and then fixed in a petri glass with scotch tape to be dried at 65 °C under vacuum for 2 h to completely remove the solvent. The as-obtained papers were peeled off from the membranes and were mechanically pressed in a laboratory hydraulic press (Atlas 15T, Specac, England) under a uniaxial compressive load of 5 kN for 30 min at 25 °C [74, 213].

2.2. Characterization techniques

2.2.1. Characterization of pyrene compounds

Nuclear magnetic resonance spectroscopy (NMR)

The NMR spectrum (acquired on Bruker AVANCE III, USA with a frequency of 500 MHz) provides qualitative and quantitative informations valuating the integral of area under each peak related to the number of protons which have equal characteristic. Therefore, ≈ 3 mg of powder were solubilized into 1 ml of Hexadeuterodimethyl sulfoxide, Sigma Aldrich, 99.96 atom % D) and if we consider the chemical shift with reference to the dimethyl sulfoxide deuterated (DMSO-d₆) the region of the spectrum between 7.75-8.5 ppm provides the number of aromatic protons, the area between 3.2-3.5 ppm describe those closed an high electronegative environment, and the part from 1.9 to 2.5 ppm belongs to the proton's located in the aliphatic chain.

The ¹³C-NMR provide information about the number of carbon atoms in the chemical structures (likewise ¹H-NMR) because there is a peak for each ¹³C and also, the position depend on environment that surrounds the ¹³C, indeed the region between 120-135 ppm provides informations about the aromatic protons while between 25-40 ppm there are the signals related to aliphatic ones.

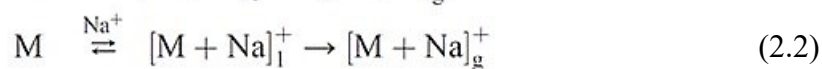
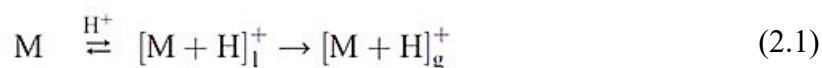
Liquid chromatography coupled with mass spectroscopy characterization

Liquid chromatography coupled with mass spectroscopy ones (H⁺ mode (model LTQ XL, Thermo Fisher Scientific, USA), is an analytical technique exploitable to analyse organic mixtures, commonly found in complex matrix or multifarious chemical environment. The combination between liquid chromatography able to separate the mixture with each component and the capability of mass spectrometry to analyses the mass and the structural identity of them, it permits to identify every molecular species with high specificity and sensitivity.

Because this technique analyses ions, an ionization phase is required for electrically neutral molecules, which usually occurs in the liquid phase and Electrospray ionizations (ESI) is a method applied for the analysis of bispyrene (<1 mg into 5 ml of methanol for HPLC, $\geq 99\%$, ACS reagent) in which two drops of formic acid, (ACS reagent, $\geq 96\%$,) have been added to promote protonation.

In addition to the commonly observed protonated molecules, sodium and potassium, are often encountered [214]. These species become possible as the surface excess charge of ESI nano-droplets may be carried by various cationic species [215].

The ions observed in the mass spectra are controlled by different balances that occur in the charged nano-droplets produced in ESI. The processes that occur in ESI droplets, resulting in the observation of these ions in ESI/MS spectra, can be summarized by the following three balances combining two phases (where M indicate the molecules)



First, equilibria taking place in the liquid phase (denoted with subscript l) are responsible for the charging of the analytes. Second, after this, formation adducts can be ejected to the gas phase (denoted with subscript g). indeed, sodium and potassium cations cannot be neglected [216].

2.2.2. Characterization of bismaleimide

Nuclear magnetic resonance spectroscopy characterization method

The NMR spectra were acquired on Bruker AVANCE III, USA with a frequency of 500 MHz. For the products obtained from step I, ≈ 5 mg of powder were solubilized into 1 ml of Hexadeuterodimethyl sulfoxide, Sigma Aldrich, 99.96 atom % D) and if we consider the chemical shift with reference to the dimethyl sulfoxide deuterated (DMSO-d₆) the region of the spectrum between 9.3-9.7 ppm provides the number of amino group's protons, the area between 6.2-6.4 ppm describe those closed to double bond, and the part from 3.2 to 3.4 belongs to the proton's located in the aliphatic chain in the middle of amino groups. The signal of protons from carboxyl groups is outside the analyzed range because it is near 16.5 ppm For the step II, ≈ 3 mg of 1,1'-(dodecane-1,12-diyl)bis(1H-pyrrole-2,5-dione) which is defined with code I12 were solubilized into 1 ml of Deuteriochloroform (Sigma Aldrich, 99.8 atom % D) and so the peak of the spectrum around 7 ppm provides the number of hydrogen of double bond, the region from 3.2 to 3.4 describe those located in the carbon atoms closed to nitrogen and finally under the 2 ppm are shown the peak relative to protons of in the aliphatic chain in the middle of amino groups.

Fourier Transform infrared (FTIR) characterization method.

Fourier Transform infrared (FTIR) spectra were acquired with Perkin Elmer Spectrum Two, in transmission mode (16 scan, resolution of 0.5 cm⁻¹) of KBr pellet (≈ 2 mg dispersed into ≈ 150 mg of KBr powder Sigma Aldrich, FT-IR grade, $\geq 99\%$).

2.2.3. Characterization GnP/BP

Raman Spectroscopy Characterization

Raman spectra were acquired on a Renishaw inVia Reflex (Renishaw PLC, UK) micro Raman microscope using at excitation laser wavelength of 514.5 nm. The spectra are the average of five measurements made on the same sample but in different areas (less than 10 mg of powder) whose peaks have been fitted with a

Lorentzian function using the origin Pro 2016 software. The fitted curves were used to calculate the ratio between the peaks at 1580 and 1350 cm^{-1} in order to evaluate the effect of functionalization.

Ultra violet – Visible Spectroscopy Characterization

After the functionalization the suspensions were centrifuged at 4000 rpm for 30 min and left to decant overnight. Finally, the part above the sediment (supernatant) was sampled and analysed on a UV-Vis, model UV-2600, Shimadzu, Japan (single scan with a 0.5 nm sampling interval and 0.05 s accumulation time, 1 cm quartz cuvette) It was principally analysed the region between 600 nm and 800 nm in which the organic compounds no give signals contrary to flakes dispersion, in order to study the stability of dispersion.

Photoluminescence characterization

The suspensions obtained from the functionalization of GnP with BP were centrifuged at 4000 rpm for 30 min and left to decant overnight and photoluminescence spectra on 4.5 ml of supernatant were recorded on a NanoLog 4, HORIBA, Japan) with an excitation at 345.00 nm and 1nm sampling interval. The signals at 376 nm and 485 nm related to organic compounds were exploited to study the GnP function that absorbing BP onto its surface, it decrease the BP concentration that change the aggregation status with itself.

2.2.4. Characterization of GnP /bismaleimide derivate

Thermo Gravimetric Analysis

Thermo Gravimetric Analysis (recorded with a Discovery TGA by TA Instruments, USA). The samples were analyzed in powder form and weighted on a Radwag AS220.R2 analytical balance, in the range of 9.0 ± 0.5 mg. The powders, were placed in open alumina pans and directly loaded in the TGA and To control the sample environment, gaseous nitrogen is flown in the TGA furnace at 100 ml/min An isothermal treatment at 100 °C for 5 min was made to evaporate the humidity and then, a temperature ramp from 100 °C to 800 °C with a 20 °C/min heating rate was used to analyse the samples and to quantify the concentration of I12 within GnP powder, considering the difference between the weight loss at the end of the process for functionalized GnP and the corresponding value for pristine GnP.

Raman Spectroscopy Characterization

Raman spectra were acquired on a Renishaw inVia Reflex (Renishaw PLC, UK) micro-Raman microscope using at excitation laser wavelength of 514.5 nm. The samples were analyzed in powder form presenting a mass in the range 5.0 ± 1 mg. The

spectra are the average of five measurements made on the same sample whose peaks have been fitted with a Lorentzian function using the origin Pro 2016 software. The fitted peaks were used to calculate the ratio between the intensity peaks at 1580 and 1350 cm^{-1} in order to evaluate the effect of Diels Alder reaction.

2.2.5. Characterization of GnP Nanopapers

Ultra violet – Visible Spectroscopy Characterization

After the gravimetric filtration, the filtrated solutions were collected (about 5 ml) and analysed by UV-Vis (model UV-2600, Shimadzu, 1 cm quartz cuvette with single scan 0.5 nm sampling interval and 0.05 s accumulation time) to measure the absorbance and calculate the concentration from relative calibration line using the Beer-Lambert law ($y=m \cdot x$ equation where y is the absorbance, m is the slope of the curve and x is the concentration of the solution). Then, to calculate the concentration of bispyrene derivatives adsorbed onto GnP, it was considered the initial concentration minus the non-adsorbed one. The number of moles were calculated and multiplying for the molecular weight, it was calculated the milligrams of molecules within nanopaper

Field-emission scanning electron microscopy (FESEM)

Nanopapers were die cut into 0.53 mm diameter disks to superficially analyse (by FESEM, Zeiss Merlin 4248, beam voltage: 5kV, Germany) the topography, that gives information about stacking of flakes, as well as the cross section of the GnP nanopapers (by sticking the sample with conductive adhesive tape, in a position perpendicular to the surface of the sample holder), to evaluate the alignment of the flakes within nanopaper. Moreover it is possible calculate the densities, as the ratio between mass measured by a microbalance (resolution 1 μg) where the disk were weighted and the volume calculated from the known diameter and the thickness, measured by field-emission scanning electron microscopy on the cross section.

X-ray diffractometer

Orientations of GnP flakes in the nanopapers GnP BP were evaluated using an X-ray diffractometer (Cu $K\alpha$ radiation, model XRD5-PANalytical X'Pert Pro, United Kingdom). The specimens (disks 23 mm diameter, 20 – 45 μm thick) were supported onto PET film (5 μm) and measured with incident angle (α) ranging from 13° to 103° with respect to the horizontal plane of the sample. Intensities of the signal of 002 graphite planes ($2\theta=26.4^\circ$) were collected against the incident angle. Intensities are reported as a function of the tilt angle $\alpha+180-\theta_{002}$, which corresponds to the angle of inclination of the flakes in the nanopaper, varying from 0° (basal planes parallel to the nanopaper plane) to 90° (basal planes perpendicular to the nanopaper plane).

The experimental curves (one for each angle) were plotted and the peaks have been fitted with a Lorentzian function using the origin Pro 2016 software in order to obtain the peak height. For every GnP bispyrene nanopaper, the intensities vs tilt angle were plotted and interpolated by exponential decay curve $y = A \cdot e^{R_0 \cdot x}$ (using origin Pro 2016 software) where A is a constant and R_0 is the decay rate. The area below the fitted curve was used to divide the intensities of each sample in order to compare the distribution intensities coming from different samples that have different thicknesses. To obtain the probability distribution for the flakes oriented from parallel to perpendicular to the nanopaper plane, the Pareto graphs show the cumulative total distribution intensities for the various orientation angles.

Light flash analysis (LFA)

The in-plane thermal diffusivity (α_{\parallel}) and cross-plane diffusivity (α_{\perp}) were measured using the xenon light flash analysis (LFA) (Netzsch LFA 467 Hyperflash, Germany), at 25 °C, using 200 V - 200 μ s pulses. The samples were die cut in disks of 23 mm with typical thicknesses in the range 20 – 50 μ m and the measurement of the α_{\parallel} was carried out in an in-plane sample holder while the α_{\perp} was measured in the standard cross-plane configuration. Five measurements were collected on each sample to calculate averaged values and experimental standard deviations.

The in-plane (k_{\parallel}) and cross-plane (k_{\perp}) thermal conductivities of nanopapers (k_{nan}) were calculated as $k = \rho \cdot \alpha \cdot C_p$, where ρ is the density of the graphene film, α is the value of thermal diffusivity and C_p is the heat capacity of graphite ($C_p = 0.71 \text{ J g}^{-1} \text{ K}^{-1}$) [217].

Infrared Thermal images

Heat spread performance was evaluated using the same specimen type used for LFA, assembled onto a transistor (2N2222 A, low power bipolar transistor, NPN silicon planar switching transistor, TO-18 metal package, STMicroelectronics), powered by an electrical generator (GWinstec GPS-3303, Taiwan), set at 0.080 A current at 4.3 V to provide 0.345 W. The thermal contact of the nanopaper disk heat spreader onto the flat surface (12.56 mm²) of the transistor is mechanically guaranteed by a NdFeB (N28) magnetic cube, 3x3x3mm³ centred onto the transistor top surface. The heat spreader disks, as well as the magnetic cube were blackened to control their emissivity. Temperature of the system was monitored by an IR thermal imaging camera (Optris-Cam PI-400, Germany), with an optical resolution of 382 x 288 pixel and 1 Hz sampling rate. Tests were carried out upon heating (power on) for 300 second and cooling (power off) under a closed box measuring 29x23x19 cm³ to ensure the reproducibility of natural convection, for other 300 sec.

Thermal maps were elaborated as a matrix, extrapolating the temperature (z axis) on the magnet surface, using an OriginPro 2016 software. An exponential function ($y = A \cdot e^{R_0 \cdot x}$ where A is a constant and R_0 is the decay rate) was used for the fitting of experimental data points (also using software OriginPro 2016) in order to calculate the cooling rate of each sample.

Temperature profiles vs. radial coordinate along three different directions (considering a Cartesian x, y system with the origin centred in the centre of the sample, the horizontal, vertical and oblique at 45° directions of the first quadrant) were extracted and averaged to obtain a representative temperature vs. radius decay curve.

Method of nanopapers porosity calculation

The relationship between density and porosity is specified by the equation:

$$\varphi = \frac{\rho_{graphite} - \rho_{measured}}{\rho_{graphite} - \rho_{air}} \quad (2.3)$$

Where φ is the porosity, $\rho_{graphite}$ is graphite density (2.2 g/cm³), $\rho_{measured}$ is measured density and ρ_{air} is the air density (0.0012 g/cm³).

Considering $\rho_{air} \ll \rho_{graphite}$, it is possible approximate as follow:

$$\varphi = \frac{\rho_{graphite} - \rho_{measured}}{\rho_{graphite}} \quad \text{or} \quad \varphi = 1 - \frac{\rho_{measured}}{\rho_{graphite}} \quad (2.4)$$

To characterize a porous material it is necessary to define the volume fraction of each component

$$\varphi = 1 - \frac{\rho_{measured}}{\rho_{graphite}} ; \quad \Phi_{GnP} = \frac{V_{GnP}}{V_{measured}} ; \quad V_{GnP} = \frac{m_{GnP}}{\rho_{GnP}} ; \quad V_{measured} = \frac{m_{measured}}{\rho_{measured}}$$

Where Φ_{GnP} is the volume fraction of GnP, V_{GnP} is the volume of GnP, m_{GnP} is the mass of GnP and ρ_{GnP} is the intrinsic density of GnP (≈ 2.1 g/cm³)

$$\varphi - 1 = - \frac{\rho_{measured}}{\rho_{graphite}} \quad (2.5)$$

$$1 - \varphi = \frac{\rho_{measured}}{\rho_{graphite}} \quad (2.6)$$

$$\rho_{measured} = \rho_{graphite} \cdot (1 - \varphi) \quad (2.7)$$

$$\Phi_{GnP} = \frac{V_{GnP}}{V_{measured}} \quad (2.8)$$

$$\Phi_{GnP} = \frac{\frac{m_{GnP}}{V_{GnP}}}{\frac{m_{measured}}{V_{measured}}} = \frac{m_{GnP} \cdot \rho_{GnP}}{\rho_{GnP} \cdot m_{measured}} \quad (2.9)$$

$$\Phi_{GnP} = \frac{m_{GnP} \cdot \rho_{graphite} \cdot (1 - \varphi)}{m_{measured} \cdot \rho_{GnP}} \quad (2.10)$$

Because the measured mass come from only GnP whose density is similar to bulk graphite

$$\Phi_{GnP} = \frac{\rho_{graphite} \cdot (1 - \varphi)}{\rho_{GnP}} \quad (2.11)$$

$$\Phi_{GnP} = 1 - \varphi \quad (2.12)$$

Linear model for thermal conductivity calculation of continuous phase within nanopapers

According to linear model

$$K_{composite} = K_{GnP} \cdot \phi_{GnP} + K_{Air} \cdot \phi_{Air} \quad (2.13)$$

Where $K_{composite}$ = the thermal conductivity calculated by relation $K_{composite} = \alpha_{composite} \cdot \rho_{composite} \cdot C_P$ considering $\rho_{composite}$ is the density of composite and C_P is heat capacity of GnP, K_{air} = thermal conductivity of air equal to $0.026 \text{ W} \cdot \text{m}^{-1} \cdot \text{K}^{-1}$, K_{GnP} = thermal conductivity of GnP network (GnP and functionalization) that is the unknown factor, ϕ_{air} = volume fraction of air, ϕ_{GnP} = volume fraction of GnP network.

Because the thermal conductivity of films is much higher than k_{air} :

$$K_{composite} = K_{GnP} \cdot \phi_{GnP} \quad (2.14)$$

Considering the volume fraction definition in which the total volume V_{tot} is the volume that was experimentally measured

$$\phi_{GnP} = V_{GnP} / V_{tot} \quad (2.14)$$

$$K_{composite} = K_{GnP} \cdot V_{GnP} / V_{composite} \quad (2.15)$$

$$K_{\text{composite}} = K_{\text{GnP}} \cdot \frac{\frac{m_{\text{GnP}}}{\rho_{\text{GnP}}}}{\frac{m_{\text{composite}}}{\rho_{\text{composite}}}} = K_{\text{GnP}} \cdot \frac{m_{\text{GnP}}}{\rho_{\text{GnP}}} \cdot \frac{\rho_{\text{composite}}}{m_{\text{composite}}} \quad (2.16)$$

Where $\rho_{\text{composite}}$ and $m_{\text{composite}}$ are respectively the density and the mass of nanopaper. Because the mass value comes only from a GnP contribute, the previous equation can be written:

$$K_{\text{composite}} = K_{\text{GnP}} \cdot \frac{\rho_{\text{composite}}}{\rho_{\text{GnP}}} \quad (2.17)$$

$$K_{\text{GnP}} = K_{\text{composite}} \cdot \frac{\rho_{\text{GnP}}}{\rho_{\text{composite}}} \quad (2.18)$$

In the end, considering that the intrinsic density of GnP is comparable to pure graphite and taking into account the relationship between thermal diffusivity and thermal conductivity, we obtain:

$$K_{\text{GnP}} = K_{\text{composite}} \cdot \frac{\rho_{\text{GnP}}}{\rho_{\text{composite}}} = \alpha_{\text{composite}} \cdot C_{p \text{ graphite}} \cdot \rho_{\text{graphite}} \cdot \frac{\rho_{\text{graphite}}}{\rho_{\text{composite}}} \quad (2.19)$$

$$K_{\text{GnP}} = \alpha_{\text{composite}} \cdot C_{p \text{ graphite}} \cdot \rho_{\text{graphite}} \quad (2.20)$$

Approach of a finned surface applied to nanopapers

A model that described the system by combining the effect of the conduction of the material with its ability to transfer heat to surrounding by convection, was studied. Among the various types of approaches that one in which the heat exchange surface is increased by fins, was chosen. In particular, the nanopapers were compared to classic radial fin of rectangular profile (Figure 33). According to this classic approach [115], approximations were made:

- Considering the temperature of plateau or the steady state, the heat flow in the fin and its temperatures remain constant with time;
- The air temperature surrounding the fin is uniform and the convective heat transfer on the faces (both bottom and up) is constant over the surface;
- The heat transfer from the edges and the thermal gradients through the fin can be ignored when the fin thickness is small in comparison to the length (25 mm) and the height (≈ 0.030 mm).

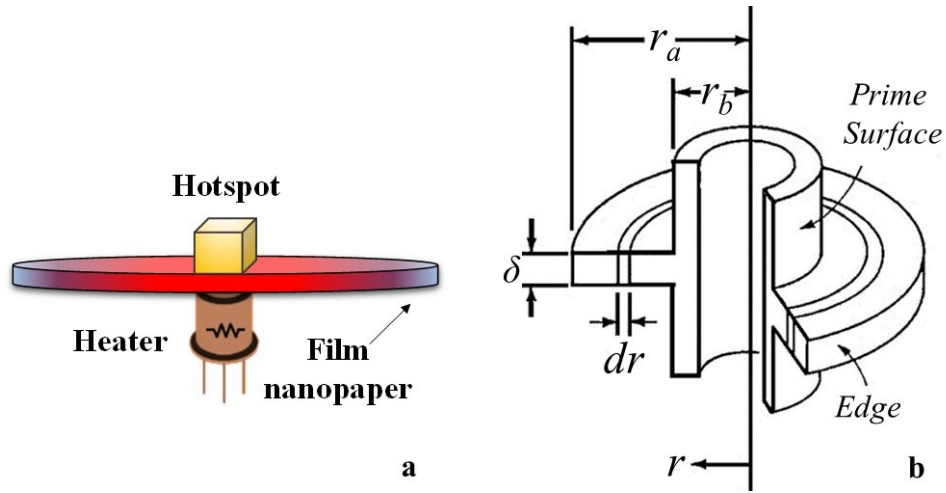


Figure 33. Radial fin of rectangular profile

As show in the first chapter the profile function and its derivative are:

$$f_2(r) = \frac{\delta}{2} \quad \frac{df_2(r)}{dr} = 0$$

Therefore, the general differential equation that describe these phenomena depend on:

$$r^2 \frac{d^2\theta}{dr^2} + r \frac{d\theta}{dr} - m^2 r^2 \theta \quad (2.13)$$

$$m = \left(\frac{2h}{k\delta} \right)^{1/2} \quad (2.14)$$

$$\text{and} \quad \theta = T - T_s \quad (2.15)$$

Where: **m** is the fin performance factor (m^{-1}), **h** is the heat transfer coefficient ($Wm^{-2}K^{-1}$), **k** is the thermal conductivity ($Wm^{-1}K^{-1}$), **δ** is the thickness (mm) of the film, **θ** is the difference of measured temperature (**T**) and **T_s** which is the room temperature ($^{\circ}C$).

This equation is Bessel's modified equation, which has a solution in terms of the modified Bessel functions $\theta(r)$:

$$\theta(r) = \frac{\theta_b [K_1(mr_a)I_0(mr) + I_1(mr_a)K_0(mr)]}{I_0(mr_b)K_1(mr_a) + I_1(mr_a)K_0(mr_b)} \quad (2.16)$$

Where K_1 , K_0 , I_0 and I_1 are Bessel's modified equation. This equation is used to fit the experimental thermal gradient curve obtained from maps at 300 sec of each films in order to obtain **m** which is the fin performance factor.

Chapter 3

Chemical functionalization of graphite nanoplatelets

In this chapter, two different approaches for graphite nanoplatelets (GnP) functionalization will be discussed. The first one by supramolecular interaction between graphene surface with pyrene derivatives (Figure 34 a) and the second by Diels Alder reaction of GnP with bismaleimide molecules (Figure 34b).

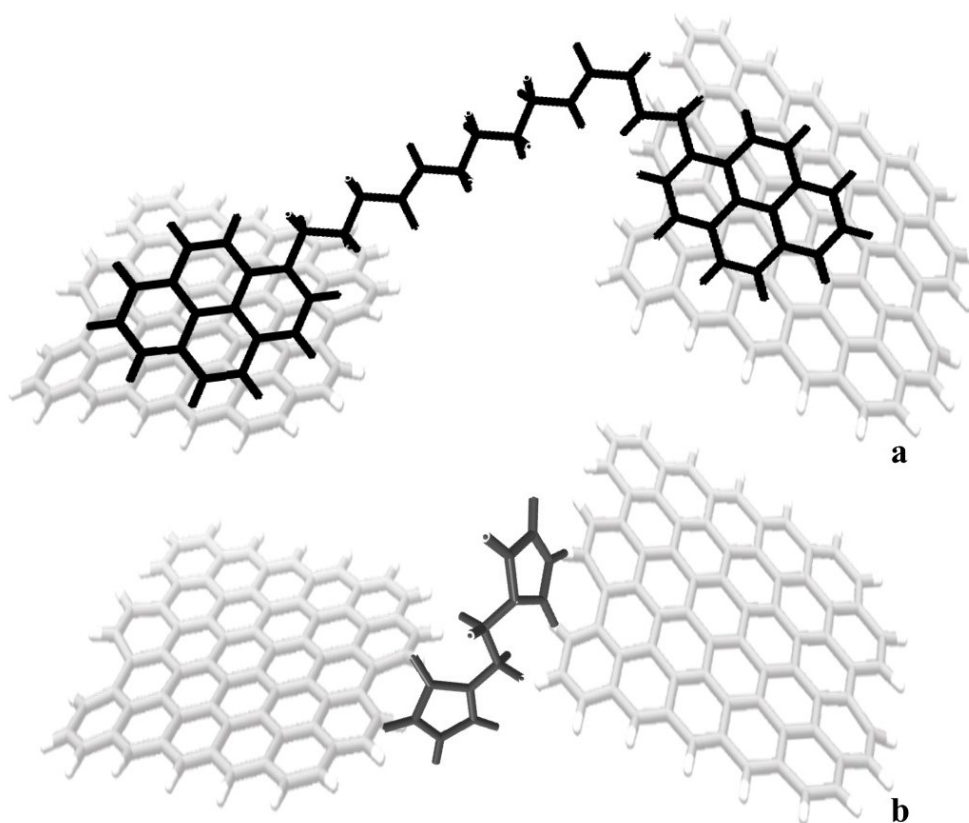


Figure 34. Schematic representation of supramolecular functionalization of graphene with bispyrene derivate (a) and Diels Alder reaction between the edges of graphene and bismaleimide.

3.1. Supramolecular functionalization of graphite nanoplatelets

Aiming at the non-covalent crosslinking of GnP, bi-functional molecules able to provide a sufficiently strong surface interaction with graphene layers were designed and synthesised. Among the different chemical species able to strongly interact with the sp^2 carbon surface via π - π stacking, For this reason, a series of bispyrene (BP) derivatives (C2 – C12) were synthesized, varying the length of the alkyl chain connecting the pyrene units.

This section will also discuss the interaction of these bispyrene with GnP.

3.1.1. Synthesis

The 1-pyrenebutyric acid was dissolved in dry toluene in order to add the Thionyl chloride to replace the carboxylic group with its derived chloride. In one hand, not only the organic compound increase its reactivity towards the amine group but, on the other hand, the intermediate is soluble in DCM [212] contrary to the reaction product (BP) which is not soluble and can be separated from unreacted reagents by simple filtration.

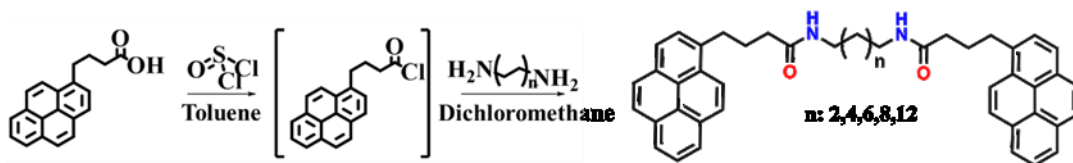


Figure 35. Synthesis of bispyrene molecules

Nuclear magnetic resonance spectroscopy (NMR) was extremely useful for the identification and quantification of bispyrene molecules.

The Figure 36 shows the ^1H -NMR spectra of C2 in which the positions (red letters) of protons that can be identified by a corresponding signal in the spectrum are indicated. In addition, the integral below each peak provides quantitative information on the number of protons having the same chemical surroundings.

^1H NMR (500 MHz, DMSO- d_6 , 300 K) δ (ppm): 8.40 (d, $J = 9.3$ Hz, 1H, g), 8.31 (t, $J = 7.2$ Hz, 2H, e + d), 8.25 – 8.20 (m, 2H, f+c), 8.17 (s, 2H, b + h), 8.11 (t, $J = 7.6$ Hz, 1H, m), 7.95 (d, $J = 7.7$ Hz, 2H, a + i), 3.36 – 3.32 (m, 2H, n), 3.25 – 3.19 (m, 2H, j), 2.29 (t, $J = 7.3$ Hz, 2H, l), 2.06 (dd, $J = 14.9, 7.4$ Hz, 2H, k).

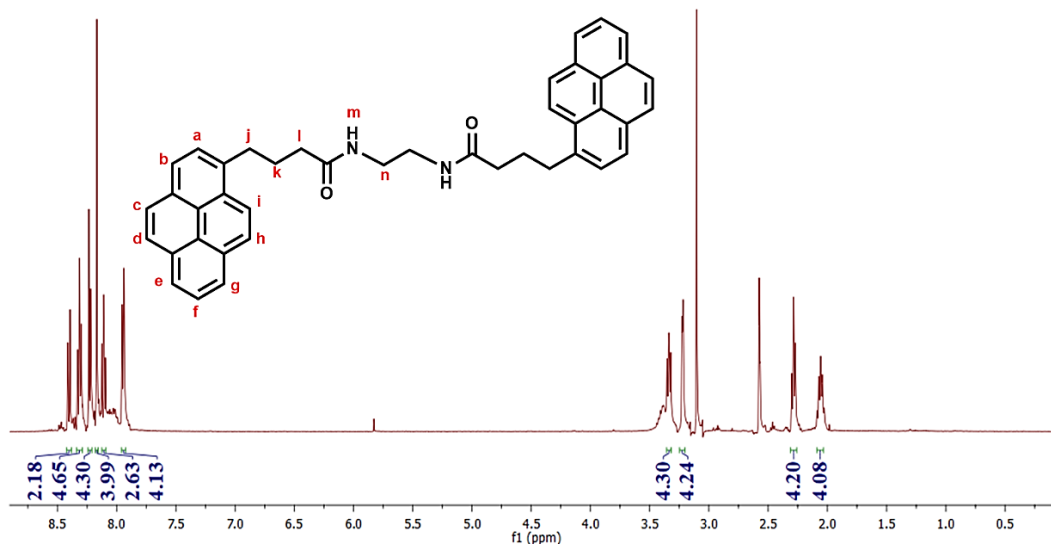


Figure 36. ¹H NMR spectrum of C2 in DMSO-d₆.

The ¹H-NMR analysis confirmed the purity of the product, also a ¹³C-NMR analysis was carried out (Figure 37) in which the experimental results were compared with those obtained from a theoretical prediction by software (Chemdraw Pro 15) shown in Figure 38.

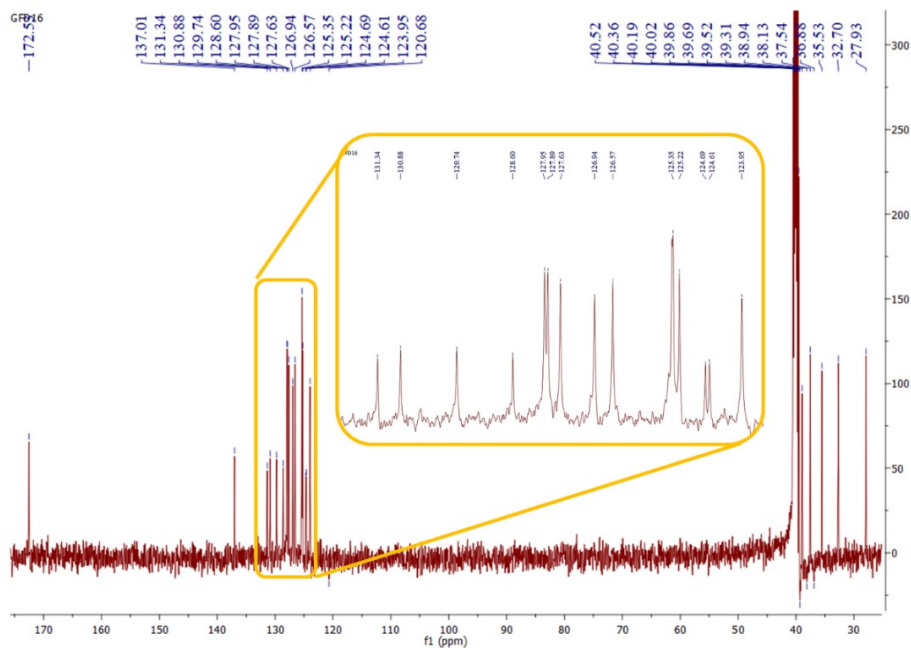


Figure 37. ¹³C NMR spectrum of C2 in DMSO-d₆.

¹³C-NMR (126 MHz, DMSO-d₆, 300 K) δ (ppm): 172.53, 137.01, 131.34, 130.88, 129.74, 128.60, 127.95, 127.89, 127.63, 126.94, 126.57, 125.35, 125.22, 124.69, 124.61, 123.95, 120.68, 40.52, 40.36, 40.19, 40.02, 39.86, 39.69, 39.52, 39.31, 38.94, 38.13, 37.54, 36.88, 35.53, 32.70, 27.93.

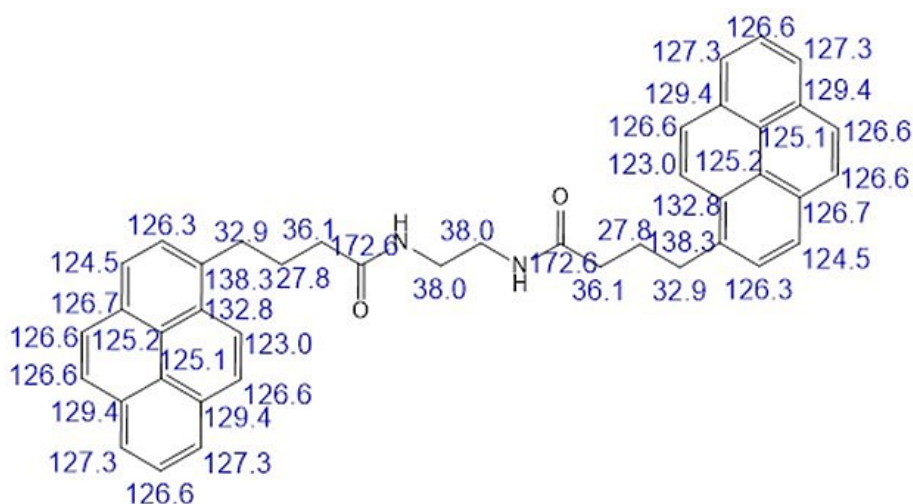


Figure 38. Theoretical prediction of ^{13}C -NMR C2.

The comparison between the experimental and theoretical ppm shows a good matching confirming the C2 molecule purity, so an analysis was carried out by different analytical technique.

Liquid chromatography coupled with mass spectroscopy ones (LC-MS) is an analytical technique exploitable to analyse organic mixtures, commonly found in complex matrix or multifarious chemical environment. The combination between liquid chromatography able to separate the mixture with each component and the capability of mass spectrometry to analyses the mass and the structural identity of them, it permits to identify every molecular species with high specificity and sensitivity.

The chromatogram (not shown here) of the powder C2 exhibited only a peak, related to a single component of the solid indicating the purity of the substance. Analysing its MS spectrum (Figure 39) it is evident how the C2 makes the commonly adduct with sodium, naturally present in the methanol or when Electrospray ionizations (ESI) is used to makes ions from organic compounds electrically neutral [216]. Indeed there is mass/charge ratio of 623.62 that correspond to the C2 molecular mass where a hydrogen atom is substituted by a sodium atom.

At the same time, the charge density could be so high that it is common to break some bonds. In general polar bonds between two different atoms are easier to break and so it is possible to create a couple of ions that could be detected such as those in the spectrum, in which, among peaks with high relative intensity, there are 331.43 m/z and 311.38 m/z that correspond to the ions generated after the C2 the rupture of the amide bond. They are respectively 2-(4-(pyren-1-yl)butanamido)ethan-1-aminium and 4-(pyren-1-yl)butanal that makes an adduct ion with potassium.

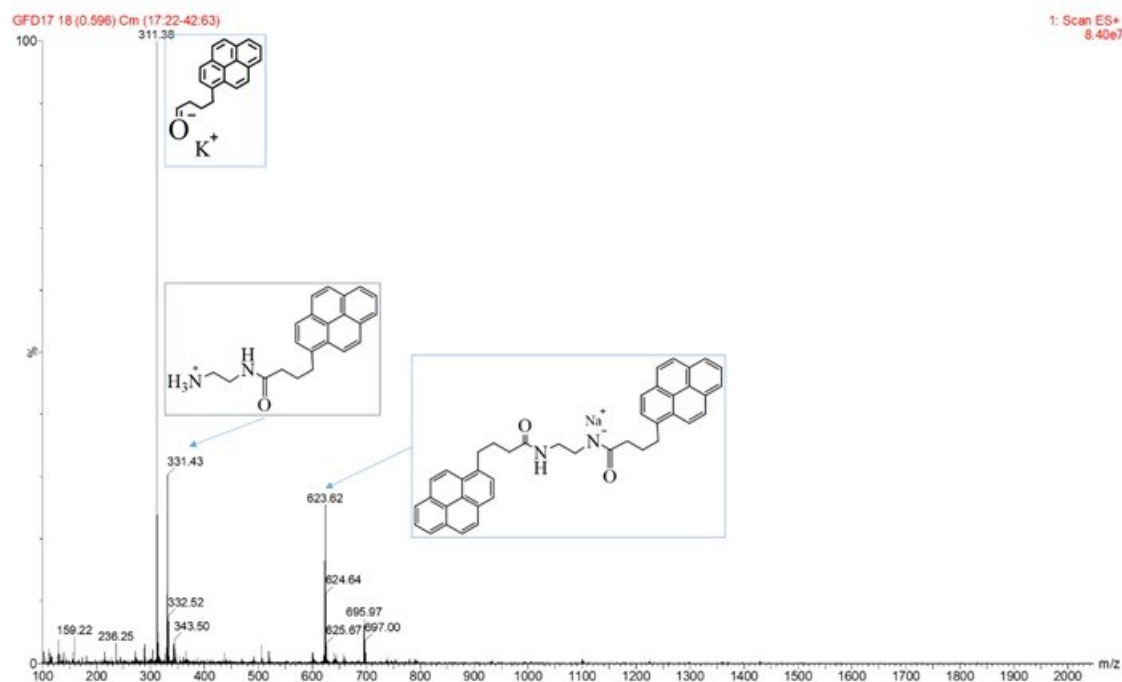


Figure 39. ESI⁺ MS spectrum of C2 in methanol.

LC-MS analysis has proven that the only analyte present in solution is C2 and and therefore the reaction had a yield of 84% in product.

A series of BP with different chain length were synthesised following the same procedure. In order to confirm the successful synthesis of the BP derivatives, ¹H-NMR were made focusing on the spectra region between 1-2.5 ppm where the hydrogens of alkyl chain give signals (spectra are shown in the Appendix 7.1). Because both the assignment of the peaks and the values of their integrals univocally confirmed the presence of the respective synthesized bispyrene molecules (BP) and, similarly to the C2 molecule, the ¹³C-NMR analyses were also carried out comparing the experimental peaks ppm with the respective theoretical predictions by software. If for C4 (Figure 89) and C6 (Figure 90) molecules there are clear evidence between experimental and theoretical data, it cannot be affirmed for the C8 (Figure 91) and C12 (Figure 92) molecules which have a lower number of peaks than those calculated. This is due to a low number of scans (can also be deduced from high signal-to-noise ratio) that did not allow to distinguish all signals.

To provide additional validation about the purity of the synthesised bispyrene molecules, LC-MS analyses were carried out by solubilising the molecules in methanol to which formic acid has been added to improve protonation and ions formation.

The MS spectrum in Figure 40 shows the fragmentation of C4, in which not only the pure protonated molecule [M]⁺ at 629.69 m/z and its adduct with potassium at 667.67 m/z are visible, but also its fragmentation at 359.45 m/z which corresponds to the molecular mass minus 272 m/z corresponding to the fragment 4-(pyren-1-yl)butanal.

Very interesting is the peak at 711.93 m/z which corresponds to the mass of the molecule that makes an adduct with sulfinic chloride, a derivative of thionil chloride, the acid used in the first step of the reaction that probably remained in trace.

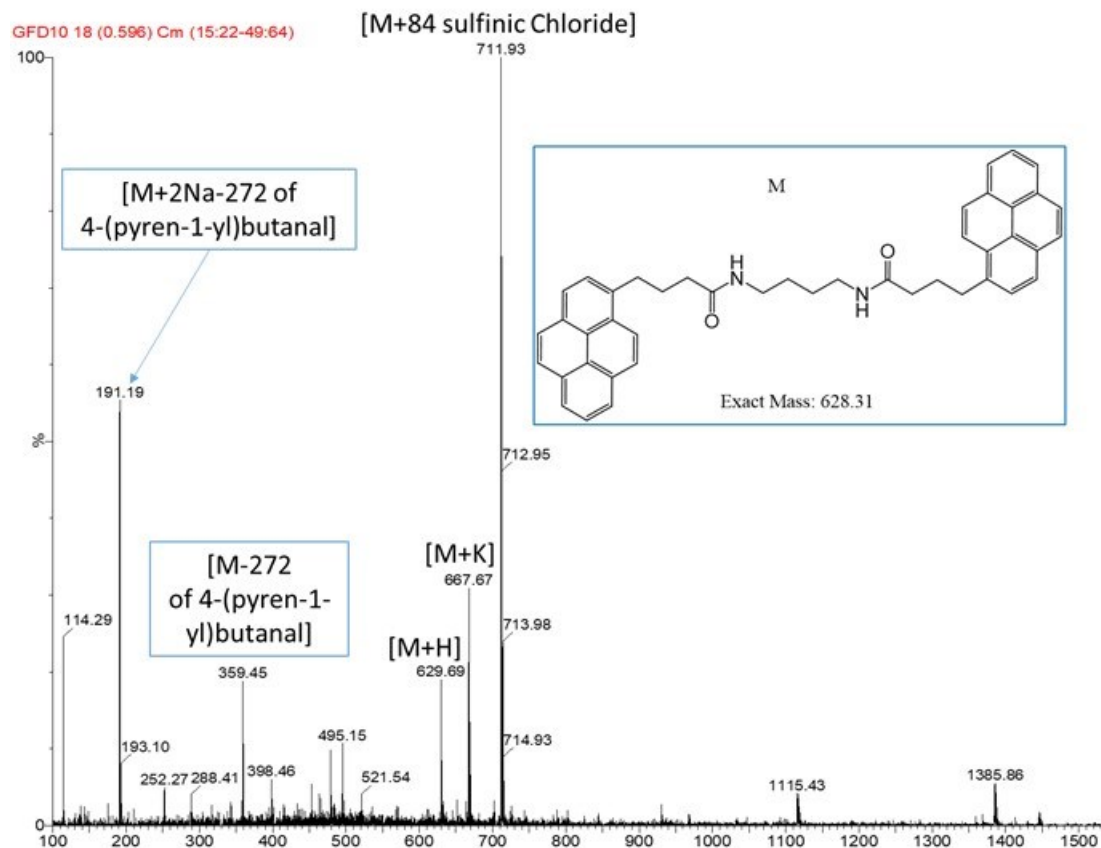


Figure 40. ESI⁺ MS spectrum of C4 in methanol.

The MS spectrum in Figure 41 shows the fragmentation of C6, in which the protonated molecule [M]⁺ is not visible contrary to its sodium and potassium adducts at 679.74 m/z and 695.91 m/z respectively.

However, for a technical error there are some impurities (at 130.38 m/z, 236.32 m/z and 214.37 m/z) which are not attributable to the synthesis reaction of C6 but which have contaminated the instrument. Instead, the peak at 288.37 m/z attributable to the ion formed by the protonation of 4-(pyren-1-yl)butanamide is relevant because it is a fragment of C6.

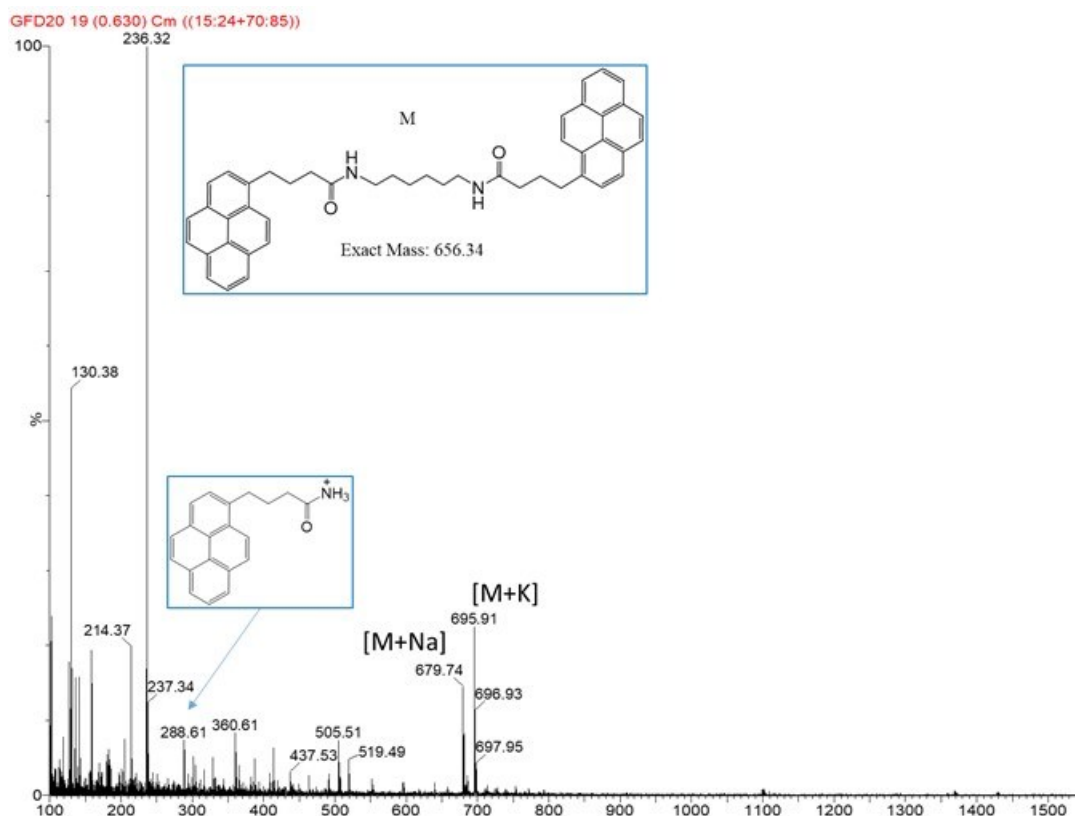


Figure 41. ESI⁺ MS spectrum of C6 in methanol.

Bispyrene C8 and C12 show a low solubility in methanol which is the solvent used to conduct LC-MS analysis and consequently the relative abundance of the molecule that can be ionized decreases dramatically. This is evident in the MS spectrum of C8 (Figure 42) where the signals attributable to its fragmentation have an intensity slightly higher than the baseline. However, the most evident are those related to the protonated molecule at 685.61 m/z, its adduct with sodium at 707.64 m/z and its fragment at 415.43 related to molecule minus 272 m/z of -4-(pyren-1-yl)butanal .

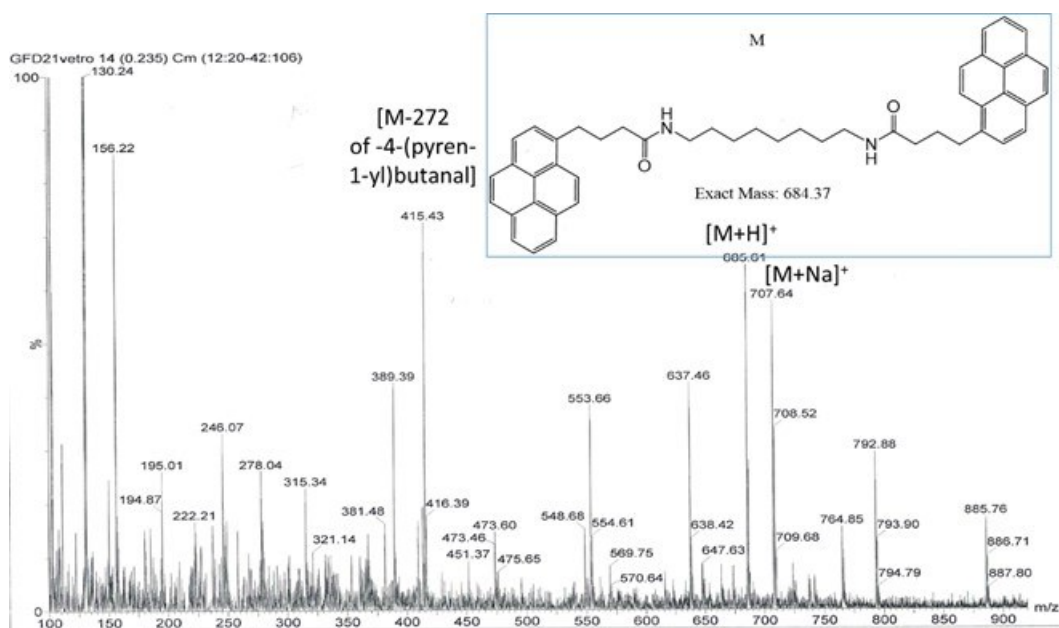


Figure 42. ESI⁺ MS spectrum of C8 in methanol.

The MS spectrum in the Figure 43 shows a single peak (at 471.49 m/z) related to C12. In fact, its fragmentation creates the ion N-(12-(14-azanyl)dodecyl)-4-(pyren-1-yl)butanamide protonated corresponding to C12 without of 4-(pyren-1-yl)butanal.

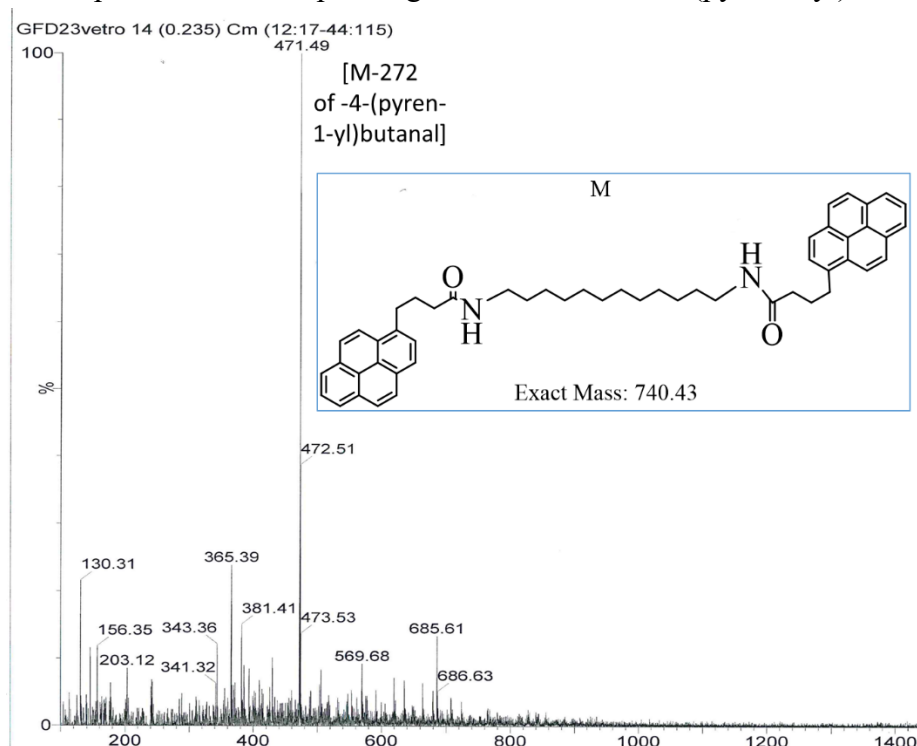


Figure 43. ESI⁺ MS spectrum of C12 in methanol

In conclusion, by comparing the results obtained from the different analytical techniques, it is possible to establish that the synthesis of the molecules took place. However, as the length of the diaminoalkane increased, a lower and lower yield was obtained, as summarized in the Table 4.

BP	C2	C4	C6	C8	C12
mg obtained	262.4	260.9	262.5	255.2	246.7
Yield (%)	84	80	77	72	64

Table 4. Milligrams of molecule obtained and yield of the reaction

3.1.2. Interaction BP/GnP

After obtaining the bispyrenic compounds, their interaction with GnP will be discussed below and based on literature research [218-220] it has been estimated that the molar concentrations to be used should be less than 10^{-3} M because BP can strongly aggregate together [221]. Subsequently this phenomenon can compete with GnP interaction and on the basis of these considerations the molecule C2 is used in order to maximize the interaction with GnP. Therefore solutions of C2 in N,N-dimethylformamide were prepared at concentrations of 10^{-4} M, 10^{-5} M and 10^{-6} M and 0.5 mg mL^{-1} GnP powder was added in each solution and sonicated to obtain a suspension following the procedure described in the chapter 2.3.

While the suspensions are left to decant (Figure 44 a), part of GnP is precipitated at the bottom of the becker and there is an interesting trend related to C2 concentration in which the highest C2 concentration (10^{-4} M) produces the least stable dispersion, with most of the GnP flakes precipitated after 60 min. On the contrary, decreasing C2 concentration, an increasing concentration of flakes remains in suspension as reflected in the darker coloration. This suggested that a high concentration of C2 results in a cross-linking action, creating a network which readily precipitate, whereas lower concentration provides a less pronounced effect.

Another interesting phenomenon is the light emission if the dispersions are lighted at 254 nm. As show in the Figure 44 b, indeed, while the C2 solution (into the vial) in DMF does not emit, the GnP/C2 dispersion (10^{-4} M), showed a clearly visible blue light emission. This experimental evidence suggest a decrease in the energy for the electron excitation, corresponding to a bathochromic shift of fluorescence spectrum to the visible range [222]. This fact support for the π - π the stacking interaction between C2 and π -orbital of GnP's surface, known as Forster energy transfer [223] in which GnP surface adsorbe the light and emit at different wavelenght where the molecule absorbs, becoming to excited state and emitting in the visible.

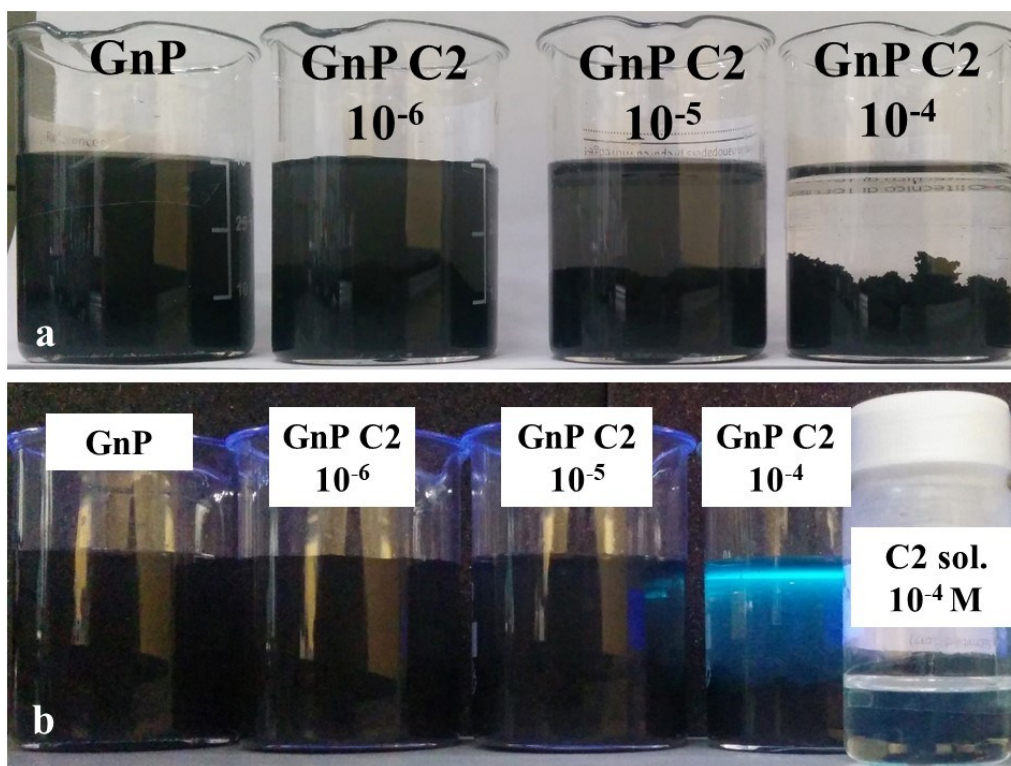


Figure 44. a) GnP dispersions prepared at different concentrations of C2 in DMF. Inside the beakers the suspensions were left to decant for one hour and it can be observed that as the molar concentration of C2 increases, the quantity of GnP precipitated on the bottom increases. b) The solutions and suspensions were lightened at a wavelength of 254 nm and it can be seen that the solution at concentration 10^{-4} does not emit in the visible contrary to its suspension which instead provides a light signal.

Absorption and Emission spectroscopies

The supernatant obtained from each dispersion after centrifugation was collected and analysed by UV-Vis and fluorescence spectroscopy.

From the absorbance spectra (Figure 46), a rough estimation of the concentration of suspended nanoflakes can be obtained by analysing the light absorption at 670 nm (inset Figure 46). This wavelength was chosen because bispyrene do not show any absorption at this wavelength (Figure 45), so the absorbance measured is related exclusively to the concentration of GnP in the dispersions.

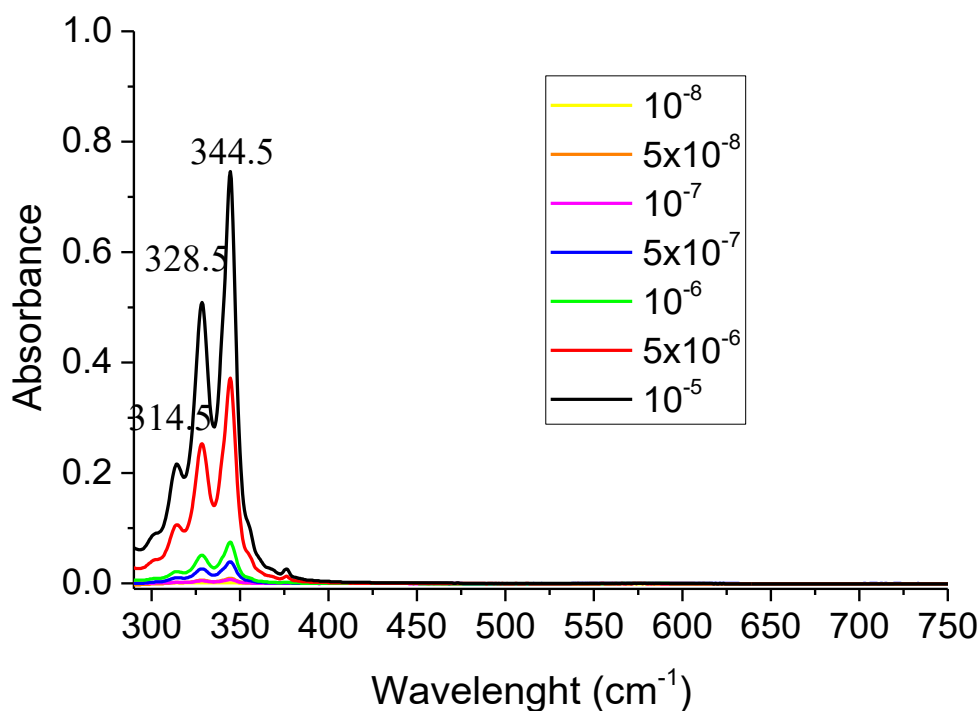


Figure 45. C2 solution absorbance in DMF at different concentration

For comparison purposes, GnP were sonicated in DMF using the same conditions as for the suspensions with C2. It can be observed that the concentrations of GnP in the suspensions are quite similar and correspond to relatively low absorbance values, suggesting limited concentrations of thin graphene flakes. This is indeed expected, taking into account that the mild sonication condition used were not aimed to obtain an extensive GnP exfoliation, but only to provide sufficient dispersion of GnP flakes, in order to investigate the interactions between C2 and GnP. On the other hand, the well-defined bands of the bispyrene molecule (main absorption at 344.5, 328.5 and 314.5 nm) on the concentrated suspensions GnP C2 10^{-4} M and GnP C2 10^{-5} M is clearly observed (Figure 46), indicating that these suspensions contain a large excess of free C2 molecules. At the lowest concentration, absorption bands for C2 are barely visible. On the one hand, this is expected based on the low concentration, but it should also be mentioned that molecules absorbed on GnP are not expected to absorb in the same range, thus further contributing to the low intensity in the VIS spectra.

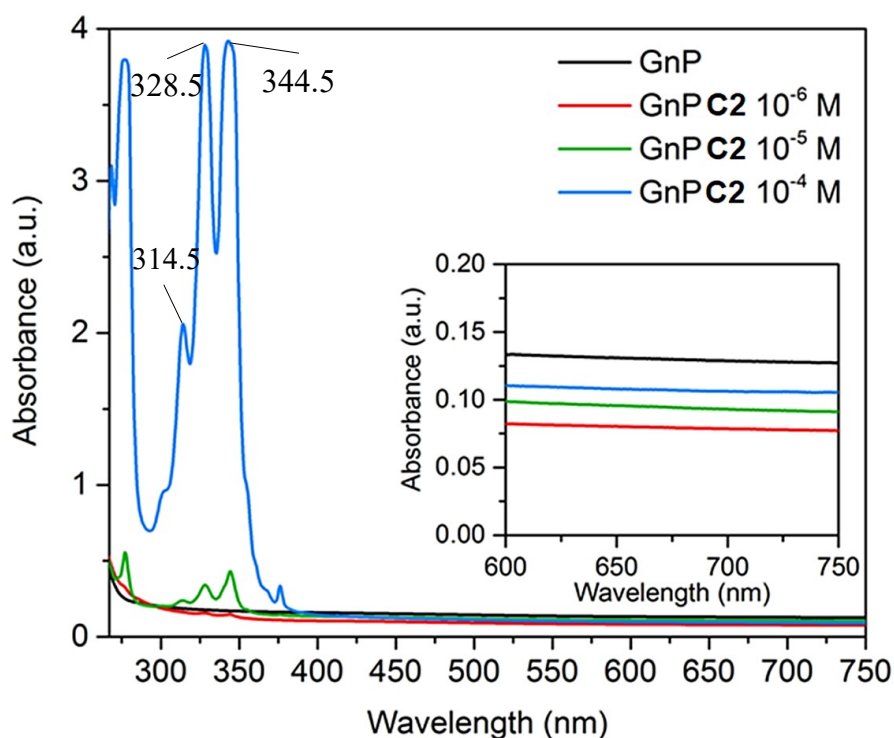


Figure 46. Absorption spectra of GnP and GnP C2 at different concentrations of C2 in DMF. Inset shows a magnification of the 600-750 region.

In order to further investigate the interaction between C2 and GnP, fluorescence measurements were carried out on the same supernatant suspensions. The comparison between fluorescence emission spectra of the molecule C2 at the different initial concentrations of the suspensions (Figure 47 Inset) and the corresponding fluorescence spectra for the GnP C2 dispersions (Figure 47) may indeed provide further insight on the organization of bispyrene molecules. Spectra for C2 in DMF are characterized by three well defined emissions peaks at 376 nm, 396 nm and 418 nm related to a monomer emission from the locally excited pyrene fragment, plus a wide band centred at 485 nm related to an association of two end pyrene fragments within the molecule [220].

No spectral shifts were observed for C2 in the GnP C2 dispersions at any concentration. However, the emission intensities decrease in the GnP dispersions prepared with initial concentrations of the molecule of 10^{-6} M and 10^{-5} M, likely due to the quenching effect of GnP [224]. Furthermore, the C2 excimer emission band at 485 nm is strongly reduced in both dispersions, as observed by the decrease of the ratio between the intensities of the excimer and monomer emission (I_E/I_M) in Figure 47 a. This change depend on lower concentration of C2 aggregates in the dispersions because part of C2 is adsorbed on the basal planes of GnP [225]. It is noteworthy that the emission intensity for the highest C2 concentration (10^{-4} M) is lower than in the corresponding GnP C2 suspension. This is possibly explained by the strong π - π interactions between the pyrene moieties at high concentration, quenching the emission of the molecule [226, 227]. Indeed, the presence of GnP favours the

adsorption of these bispyrene derivatives on the basal planes, decreasing the association of the pyrene groups and thus reducing the I_E/I_M ratio.

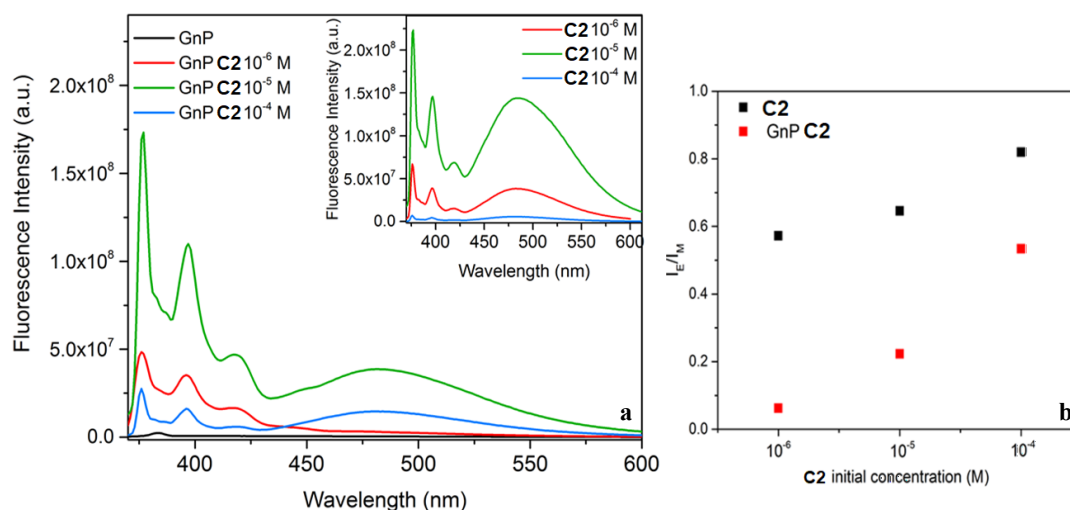


Figure 47. a) Fluorescence spectra ($\lambda_{ex} = 345$ nm) of GnP and GnP C2 at different concentrations of C2 in DMF. Inset shows the fluorescence spectra of C2 at the initial concentrations in DMF. b) I_E/I_M ratio for C2 molecule in DMF and for GnP C2 dispersions.

To complement the analyses of the supernatants and to quantify the amount of C2 molecules effectively adsorbed onto the whole GnP, the suspensions were filtered and the filtrate solution were analysed by UV-Vis in order to calculate the concentration of C2 in the filtered solution, to be used to indirectly calculate the fraction of C2 adsorbed onto GnP, given the known initial concentration in the GnP C2 suspensions.

As shown in Table 5, the fraction of adsorbed bispyrene is 80 % and 55 % of the initial concentration for GnP C2 10^{-6} M and GnP C2 10^{-5} M, while it decreases to 10 % in the case of GnP C2 10^{-4} M, reflecting the large excess of C2 at the highest concentrations. Mass fraction of C2 onto the GnP C2 dry powders are also dependent on the initial C2 concentration: a mass fraction as high as 11% was obtained when starting from a 10^{-4} M C2 concentration in the GnP suspension, while significantly lower C2 contents were obtained at lower initial concentrations.

C2 concentration in GnP suspension [M]	C2 concentration in filtered solution [M]	Fraction of C2 adsorbed on GnP [%]	Mass fraction of C2 in dry GnP C2 [%]
10^{-4}	$0.91 \cdot 10^{-4}$	9	11
10^{-5}	$0.45 \cdot 10^{-5}$	55	0.71
10^{-6}	$0.22 \cdot 10^{-6}$	78	0.09

Table 5. Calculation of the mass fraction and mass of C2 absorbed by GnP.

To investigate the organization of C2 onto GnP in the dry state, Raman spectroscopy was carried out on GnP C2 powders. Indeed, Raman spectroscopy is extremely sensitive to the carbonaceous materials structure, so that functionalization may be detected and interpreted based on the Raman spectra. In particular, Raman spectra of GnP exhibit a relatively simple structure characterized by two main bands known as the G and D bands. The G band is a sharp band that appears around 1581 cm^{-1} and is related to an in-plane vibrational mode that involve the sp^2 hybridized carbon atoms of the graphite sheet. The D band at 1350 cm^{-1} is often referred to as the defect band or the disorder band, representing a ring breathing mode from sp^2 carbon that becomes active once chemical or structural defects are present on the graphite structure [228].

The analysis of the Raman spectra of the GnP and GnP C2 powders are reported in Figure 48. An increase of the I_D/I_G ratio is clearly observed with increasing the initial concentration of C2 in the suspensions. In particular, a relatively large increase in I_D/I_G ratio is obtained at the highest initial concentration (10^{-4}M), confirming a high extent of functionalization and possibly an excess of C2 in the form of large aggregates. On the other hand, limited or no increase in the I_D/I_G ratio are observed at lower concentrations, which is compatible with a supramolecular functionalization [94], that is expected to provide only a minor changes in the vibrational properties of graphene layers in GnP.

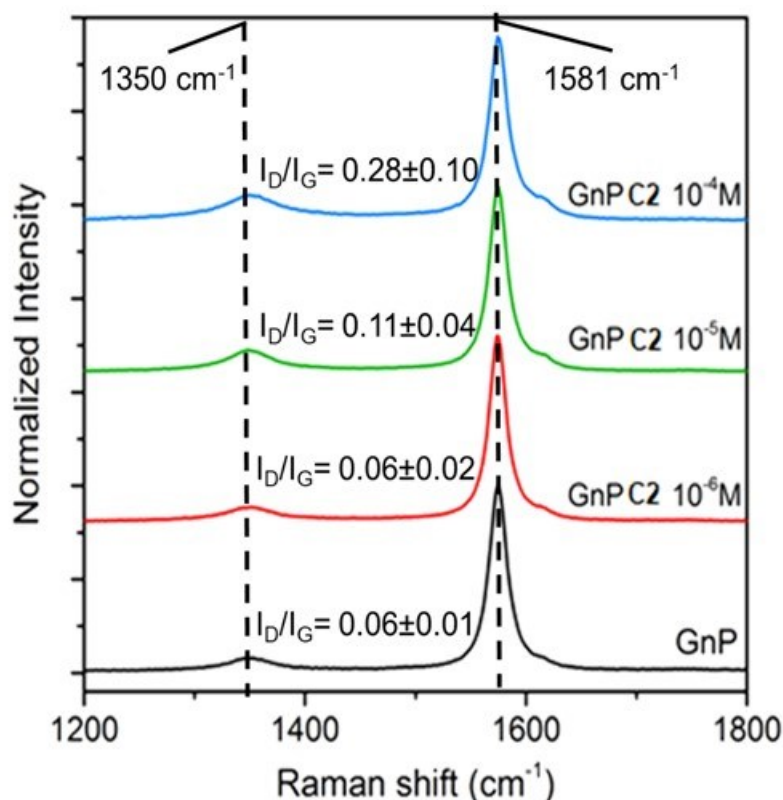


Figure 48. Comparison between Raman Spectra of GnP and GnP C2 powders.

According to the results obtained, high concentrations of C2 are not appropriate to functionalize GnP. In fact, the excessive amount of molecular aggregates (as demonstrated by photoluminescence analysis) is reflected both in the relative

functionalized material (shown in Raman spectra) and in the lower concentrations of C2 absorbed compared to the initial concentration.

In conclusion, a concentration of 10^{-6} M was preferred for the functionalization of GnP for all bispyrene molecules.

The UV absorbance spectra (Figure 49 a) of bispyrene derivatives C2 - C12, exhibit the distinctive absorption bands attributable to pyrene units at 314.5 nm, 328.5 nm and 345.5 nm. Position and relative intensities of these bands are insensitive to the linker chain length between pyrene ends, which is expected because these depend exclusively on π - π^* electronic transition of conjugation system of pyrene.

On the other hand, there is a wide bathochromic shift of BP spectrum, in comparison to pyrene (Figure 49 b), related to the higher molecular weight, which changes the dipole moment of chromophore group.

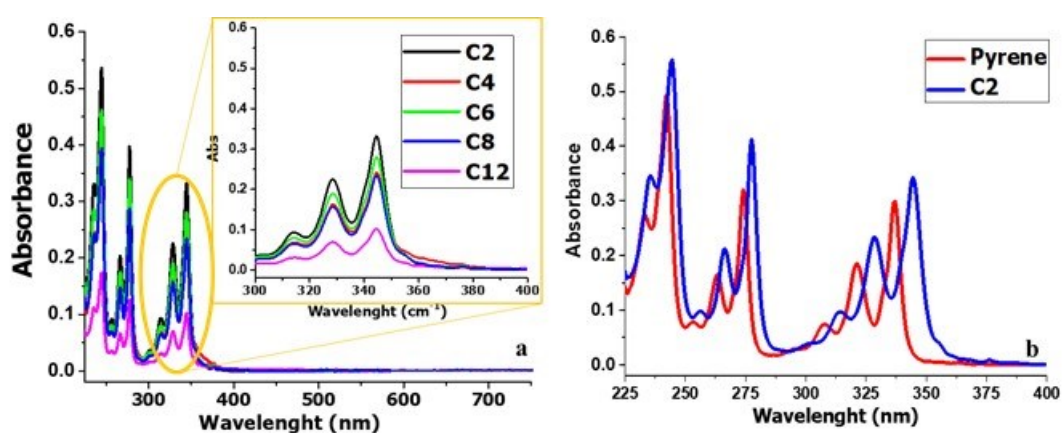


Figure 49. a) Comparison of UV spectra of solutions ($5 \cdot 10^{-5}$ M) bispyrene based in DCM. b) Comparison between UV-Vis spectrum of solutions bispyrene based and Pyrene one.

Based on the results previously obtained, a BP concentration of 10^{-6} M was found to deliver the best compromise between maximizing the interaction with the GnP while minimizing the formation of aggregates.

From the UV-Vis absorbance spectra (Figure 50 b), a rough estimation of the concentration of suspended nanoflakes can be obtained by analysing the light absorption at 670 nm, where BP derivatives do not show any absorption. It is worth noting that the absorbance of GnP BP suspensions is similar or slightly lower to that of pristine GnP, thus the presence of BP derivatives do not significantly change the concentration of particles in suspension. These findings suggest that BP derivatives do not stabilize GnP in suspension but rather promotes aggregation of GnP, acting as π - π gelators, as previously reported for similar systems [229]. The lowest concentration of GnP in the supernatant was obtained for C2, which may indicate C2 is the most efficient BP in promoting the aggregation of GnP at the concentration used. In addition, this sample showed the characteristic absorption bands of pyrene groups in the region between 300 – 450 nm, while no signal was detected in the other suspensions with bispyrene derivatives, this excess of C2 remaining in the supernatant further supporting for its efficiency in GnP supramolecular crosslinking.

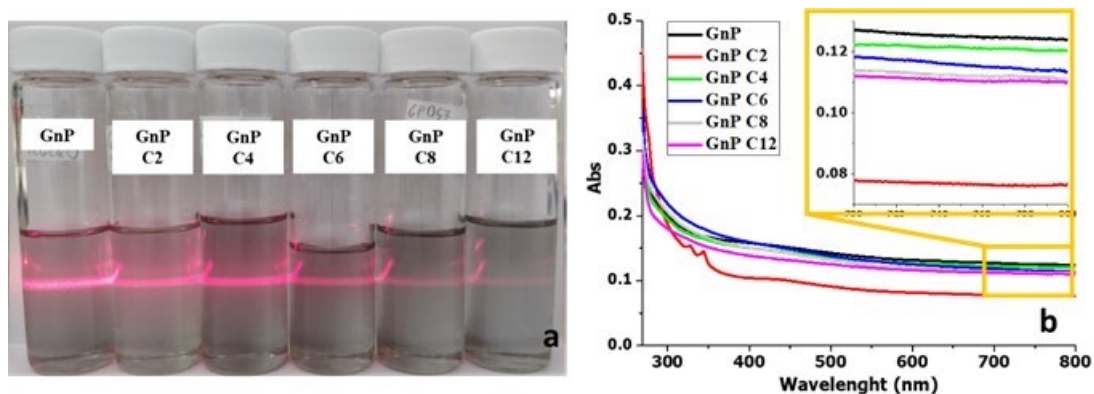


Figure 50. a) Photographs of GnP/BP dispersions and relative scattering of light as a laser beam passes through a colloid (Tyndall effect). b) UV-Vis Absorption of supernatants.

Fluorescence emission spectra of BP derivatives (Figure 51 a) show that the GnP C4 – C6 have higher intensity broad emission band at 480 nm in comparison to C2 or C8 -C12. This could suggest the chain length to affect intra-molecular aggregation, usually referred to as excimer, which appears to be favoured with intermediate length linkers between pyrene moieties [230]. Indeed, this trend is also reflected considering the supernatant's fluorescence emission spectra (Figure 51 b), in which the GnP C4 - C6 have the highest values for the ratio between the intensities of the excimer and monomer emission (I_E/I_M). There is a general and evident reduction of I_E/I_M for every samples in comparison to their relative solutions, because GnP subtracting molecules from the solution, it reduce the BP concentration and the state of aggregation is drastically influenced as a consequence.

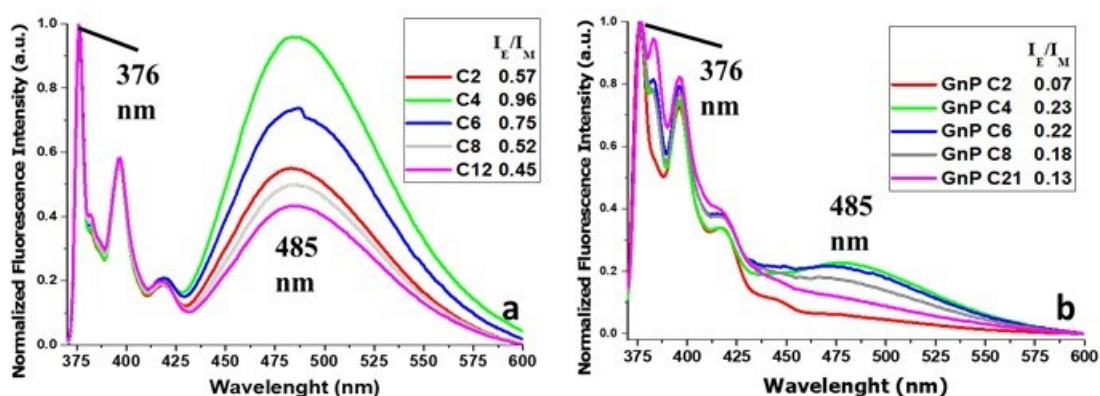


Figure 51. Comparison between the fluorescence emission spectra of BP (a) and their corresponding GnP BP dispersions (b)

Raman spectroscopy (Figure 52) was carried out to investigate vibrational changes induced by the absorption of BP derivatives. The low I_D/I_G ratio (0.06) of pristine GnP evidences for a very low defectiveness of these nanoflakes while, limited increment of in I_D/I_G were found for GnP BP, which is consistent with the π - π

interaction of pyrene onto the GnP surface, weakly affecting the vibrational properties of the plane. Nonetheless, increasing the length of the BP, a slight increase in the I_D/I_G ratio and its experimental deviation may be observed.

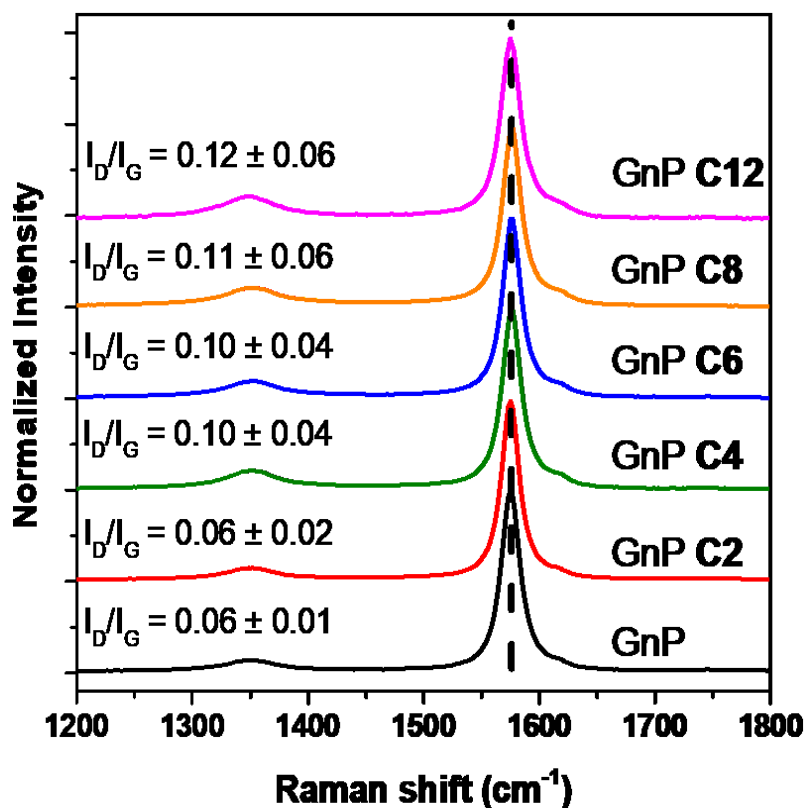


Figure 52. Raman spectra of GnP and GnP BP.

Based on the results obtained, GnP functionalized with BP have been used for the manufacture of nanopaper.

3.2. Functionalization via Diels Alder reaction

The Diels Alder cycloaddition, usually occurs between a diene compounds with dienophile ones. As show in the first chapter, maleic anhydride can behave as dienophile and so, bi-functional molecules capable, in theory, of bridging between two GnP have been synthesized. In addition, this functionalization is temperature-dependent so it is possible to activate the retro Diels Alder only by increasing the temperature [76] contrary to common equilibrium covalent reactions that require the exchange of reagents and products.

3.2.1. Synthesis of bismaleimide

The synthesis of maleimides follows two steps with the formation of the diacid intermediate obtained from the opening of maleic anhydride and immediate reaction

with the amino group and then the reclose of the ring with the formation of the relative imide.

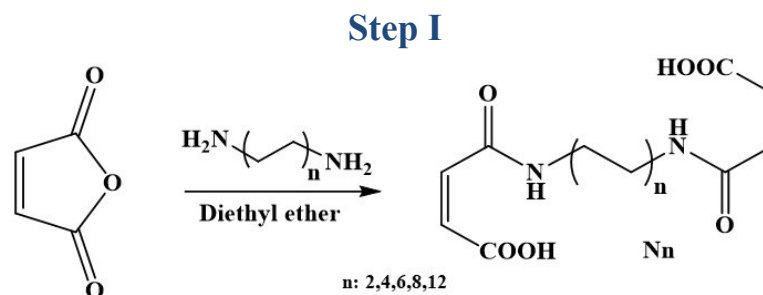


Figure 53. Synthesis of diacid derivate

The maleic anhydride was dissolved in diethyl ether previously deoxygenated. A solution of 1,2-Diaminoethane was added drop wise to one contains maleic anhydride because the reaction between anhydride and amine is instantaneous and exothermic, and it can lead to overheating and evaporation of the solvent, which has the function of preserving solubilized reagents contrary to the product which is insoluble. After filtration, to remove the remaining reagent non-reacted, the white powder was dried and characterized.

NMR analyses (spectra are shown in the appendix 7.2) were carried out to verify the formation of the desired product obtaining qualitative and quantitative information about the molecules. In the range of investigation considered, the signal of the proton of the carboxyl group cannot be detected so the assignment and quantification was made on the other protons.

Concerning the molecule, the number of protons coincides with the number of signals present in the spectrum, while very small peaks are related to impurities present in trace (such as diethyl ether residue but that in any case are lower than 5%). In general the desired products has been obtained with a yield reaction varying from 80% for N2, 75% for N4 and N6, 80% for N8 and 70% for N12, respectively. From the NMR analysis it was possible affirm that all the compounds have been synthesized and obtained pure, so that they can be used for the second step of the reaction without further purification steps.

Step II

For the intramolecular closure and subsequent restoration of the 5-member ring (Figure 54), a reaction well known in the literature [231, 232] with the use of acetic anhydride and sodium acetate (buffer solution), has been chosen to promote the reaction by removing the by-product which is the water formed by the reaction of the carboxylic group with the amine [233]. When the reaction is finished, the mixture is transferred into a beaker containing cold water and sodium carbonate to crystallize the product because this has low solubility in water contrary to reagents while unreacted acetic anhydride forms acetic acid which is neutralized with the basicity

of sodium carbonate, and sodium acetate and Nn molecules both remain solubilized in water.

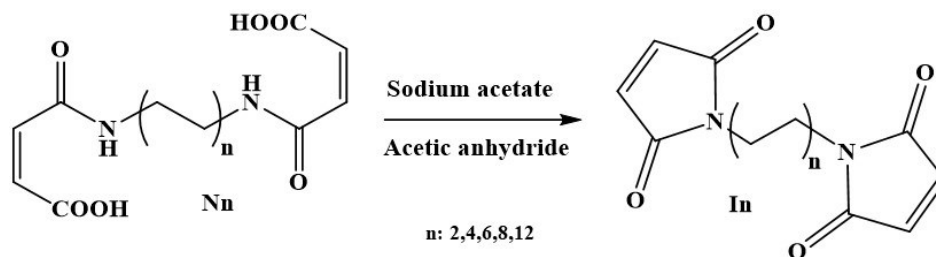


Figure 54. Synthesis of bismaleimide molecules – step 2

As regards the synthesis of I2, there were difficulties in obtaining a solid product. In fact, during the precipitation phase in water and subsequent filtration and drying, only a fraction of the solid (less than 10% weight) was obtained. Moreover, as the NMR spectrum in the Figure 55 clearly shows, this solid is a mixture of products from which it cannot be affirmed that the reaction successfully took place.

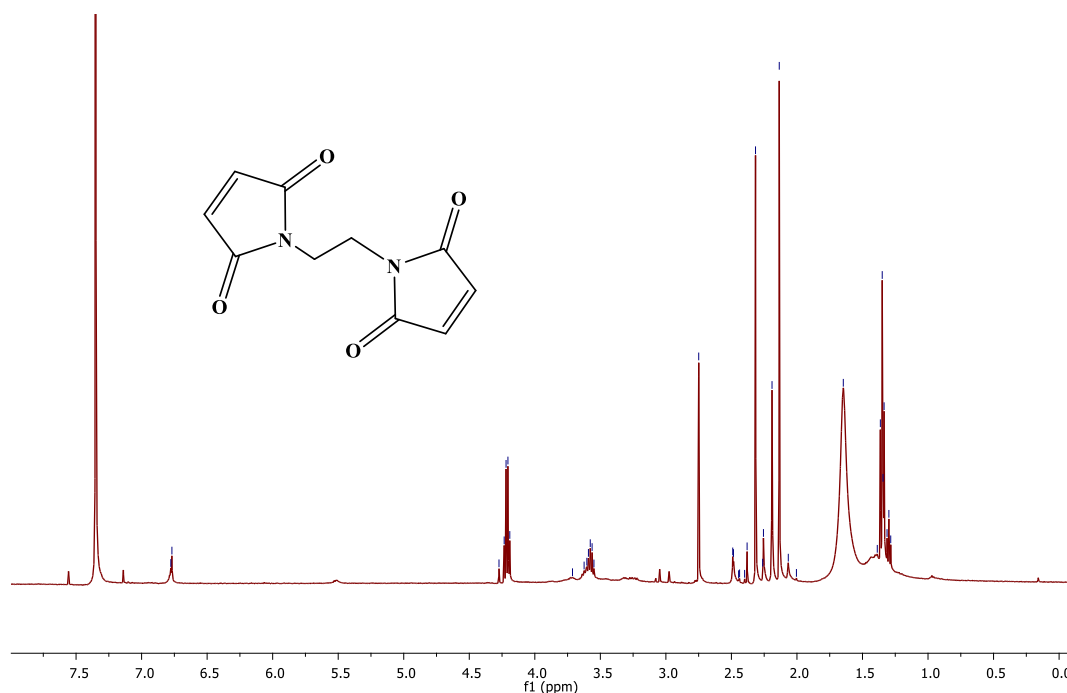


Figure 55. $^1\text{H-NMR}$ spectrum of 1,1'-(ethane-1,2-diyl)bis(1H-pyrrole-2,5-dione) (I2).

A similar result was obtained for the reaction of I4 whose NMR analysis (Figure 56) it cannot be possible assign to the peak obtained, the protons signals of the molecule so it cannot be affirm that the reaction took place.

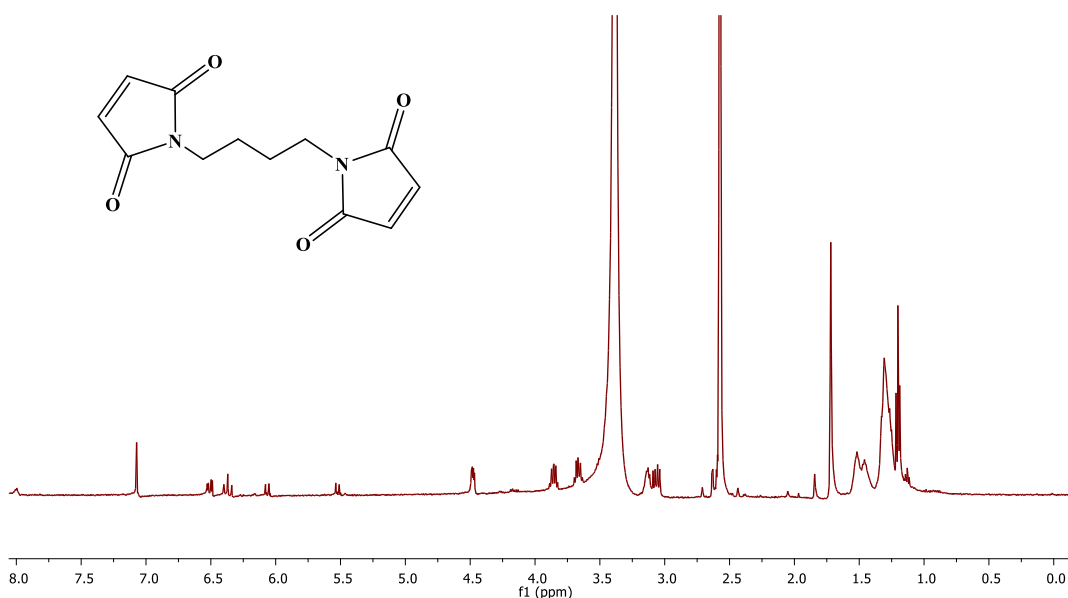


Figure 56. $^1\text{H-NMR}$ spectrum of 1,1'-(butane-1,4-diyl)bis(1H-pyrrole-2,5-dione) (I4).

From the I6 reaction, instead, a product has been obtained but which, really, is a mixture of compounds whose main component is the N6 reagent, as demonstrated in its NMR characterization in the Figure 57. Nevertheless, the quantification (integral of the peaks) does not correspond to the values previously obtained. Considering the integrals at lower ppm (1.67 and 1.36), it is possible to notice a high value of integrals that indicates the presence of additional signals of aliphatic protons that could be correspond to I6, also confirmed by the band centered on 7.85 ppm to which the signals of the protons of the double bond of I6 would correspond.

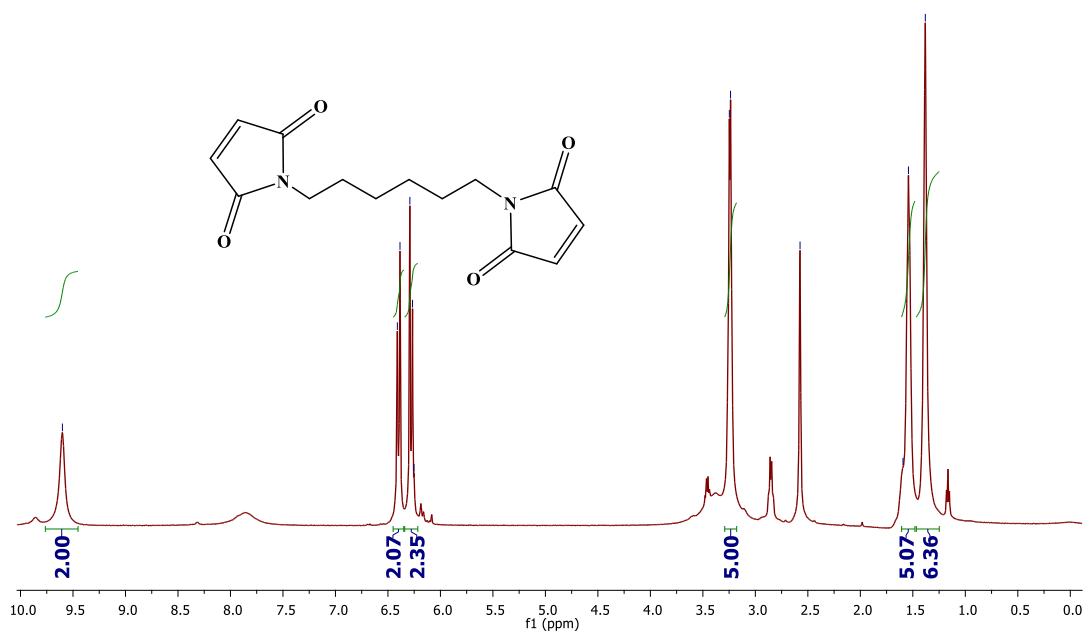


Figure 57. $^1\text{H-NMR}$ spectrum of 1,1'-(hexane-1,6-diyl)bis(1H-pyrrole-2,5-dione) (I6).

The NMR analysis (Figure 58), shows that the sample analysed is essentially a mixture of compounds where the main component nevertheless is N8. In fact the signal at 7.74 ppm corresponds to the protons of the double bond, at 3.60 ppm there are the protons signals of carbon adjacent to the nitrogen atom of the imide, and between 1.67 and 1.33 ppm there are the signals of protons located in the aliphatic chains. However, the integration of the peaks does not provide a correct quantitative analysis of the molecule demonstrating instead that there are other products in the sample. Because the overlap of multiple signals is on those ppm, it could be either unreacted or unreacted I8 or (Z)-4-((8-(2,5-dioxo-2,5-dihydro-1H-pyrrol-1-yl)octyl)amino)-4-oxobut-2-enoic acid which is a molecule similar to I12 but partially closed.

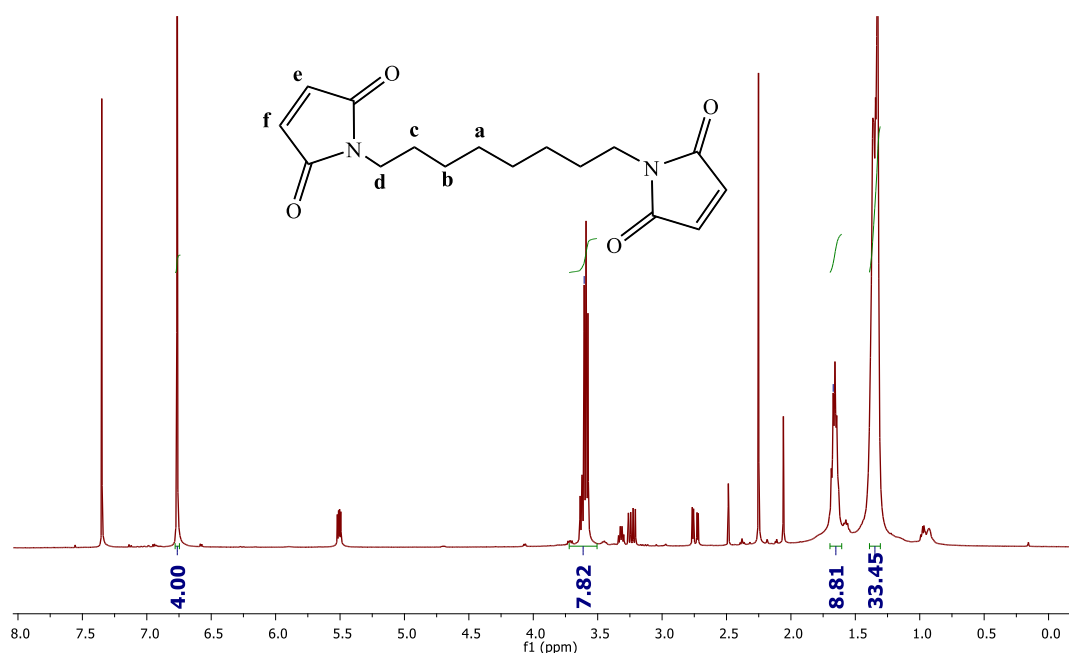


Figure 58. ¹H-NMR spectrum of 1,1'-(octane-1,8-diyl)bis(1H-pyrrole-2,5-dione) (I8).

The NMR analysis (Figure 59) shows the identification of desired product, i.e. I12. In fact, both the position of the peaks and the value of their integrals correspond qualitatively and quantitatively to the signals of I12 protons. At 6.77 ppm there is the peak relative to the protons of the double bond, at 3.40 ppm there is the signal of the protons of the carbon adjacent to the imide, and between 1.47-1.37 ppm there are the protons signals located in the aliphatic chain. Although the product obtained is pure, the yield of the reaction was only 40%.

$^1\text{H NMR}$ (500 MHz, CDCl_3) δ : 6.77 (h+g, 4H), 3.60(f, 2H), 1.65 (d+e, 8H), 1.47-1.37 (a+b+c, 12H).

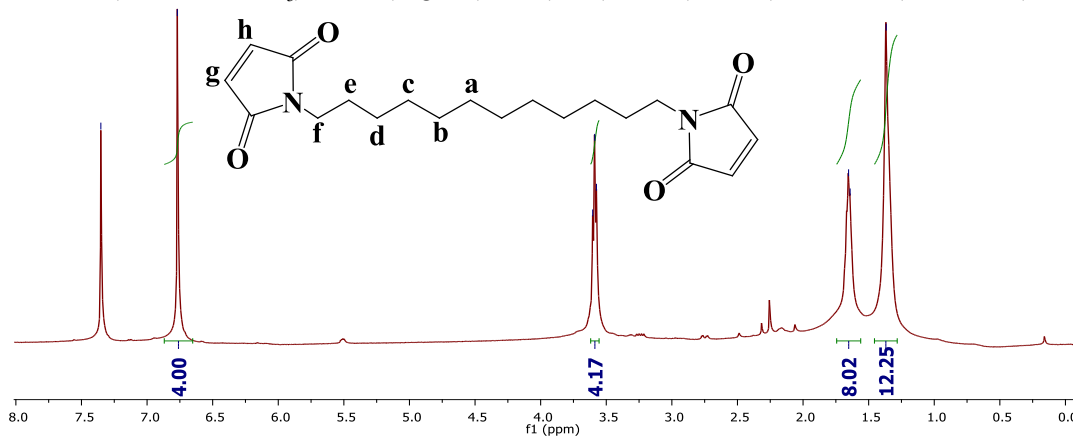


Figure 59. $^1\text{H-NMR}$ spectrum of 1,1'-(dodecane-1,12-diyl)bis(1H-pyrrole-2,5-dione) (I12) in DMSO.

The I12 was also characterized by FTIR, as show in the Figure 60, and the comparison between I12 and its reagents was used to assign the most important peaks for compound recognition, as show in the Table 6.

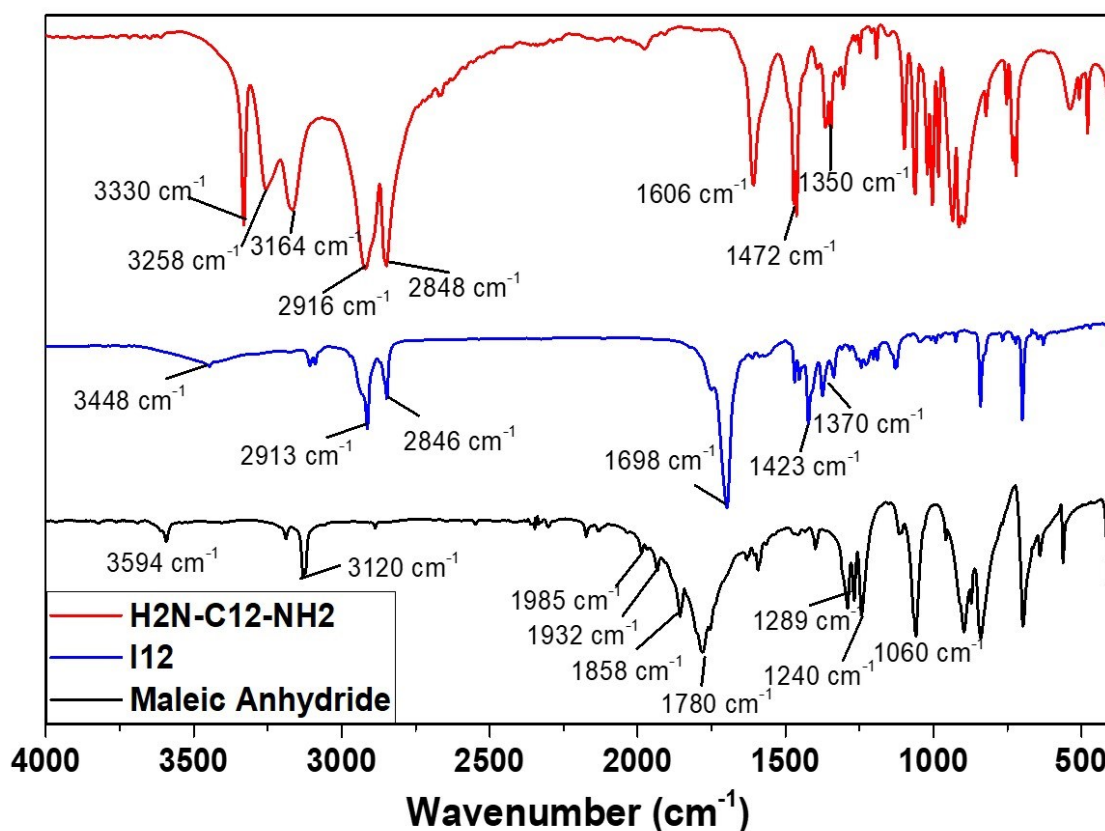


Figure 60. FTIR spectra comparison between the I12, 1,12-Diaminododecane and Maleic anhydride.

1,12-Diaminododecane [234, 235]		Maleic anhydride [234, 236]		I12 [234]	
Wavenumbers (cm ⁻¹)	Attribution	Wavenumbers (cm ⁻¹)	Attribution	Wavenumbers (cm ⁻¹)	Attribution
3350-3250	Stret. Sym Asy -NH ₂	3120	Stret. Sym Asy C-H	3150-3100	Stret. Sym Asy C-H
2980-2850	Stret sym asy -CH ₂	-	-	2980-2850	Stret. Sym Asy -CH ₂
-	-	2000-1700	Stret. C=O	1700	Stret C=O
1606	Bend. -NH ₂	-	-	-	-
1472	Sciss. CH	-	-	1470-1440	Sciss. and rock CH
-	-	-	-	1435-1390	Stret. CN
1375-1335	Wagg. CH ₂ NH ₂ twisting CH ₂ /NH ₂	-	-	-	-
-	-	1350-1200	Stret C=C Stret C-O	1385-1350	Stret C=C
>1300	Twist. and Rock. -CH ₂ - Vibr. -CN	1060	Bend C-H	>1300	Twis. and Rock. CH ₂ - Vibr -CN
		> 1000	Stret C-O Stret. C-C Stret. C-H		

Table 6. Comparison between I12 FTIR analyses with those of its reagent.

FTIR results (in particular the signal between 3150-3100 cm⁻¹ related to the stretching of the ring CH, those between 1435-1390 cm⁻¹ related to the stretching of the CN,) confirmed that the pure I12 molecule was obtained, accordingly to NMR analysis. Therefore, I12 was used as a reference for FTIR characterization of other bismaleimide compounds (BI).

As shown by the spectra comparison in the Figure 61, the curves of other BI (I2-I8) appear different than I12, indicating that the samples analysed are a mixture of compounds.

In order to verify if condensation occurred between the carboxylic and the amide groups with consequent transformation into imide, their vibrational modes were considered. The vibrations of amides have typical signals between 3460-3420 cm^{-1} (related to NH stretching), between 3370-3270 cm^{-1} and between 3180-3140 cm^{-1} (for cis and trans stretching respectively) and 1570-1515 cm^{-1} [234], while the signals of the carboxyl groups show a very broad band between 3500-2500 cm^{-1} [237] and 1700-1740 cm^{-1} related C=O and OH stretching [234]. Therefore, comparing the signals of the I8 and I6 with those of the I12, in the spectra there are the vibrations related to maleimides (especially between 3150-3100 cm^{-1} related to the stretching of the ring CH, those between 1435-1390 cm^{-1} related to the stretching of the CN), that one of amide (between 1435-1390 cm^{-1}) and the large band between 3300-2500 cm^{-1} related to carboxylic acid. These results indicate how either both N8 and N12 molecules with their respective derived amides are detected.

As concerns I4 and I2, the spectra show signals both in the high wavenumber range (3700-3200 cm^{-1}) related to the carboxylic groups and amide stretching, and the peak between 1435-1390 cm^{-1} is detected (contrary to I12) and it is much more intense than I6 and I8. This indicates that the reaction did not occur completely and the signals mostly correspond to the N4 and N2 molecules respectively.

Other synthesis methods were studied by varying some parameters of the reaction. In particular I4 and I2 reactions were conducted at higher temperatures (respectively 100°C and 120°C) to promote condensation but no solid was obtained after precipitation in water. In fact the solid slowly dissolved indicating the presence of carboxylic groups (of the respective N2 and N4) that increase the hydrophilicity of the molecules. Keeping the temperature at 80°C, the reaction time was changed ($t=4\text{h}$ and $t=48\text{h}$) but the results obtained were the same in which the mixture were dissolved into water. Therefore, in order to separate the fractions of the mixture, different techniques of chemical separation were explored because a critical issue for GRM functionalization is the possible contamination with unreacted species that remain onto graphene but are not covalently grafted and even low concentrations can influence the behaviour of materials [238, 239]. For example, it was changed both the crystallisation time (12 h) and the solvent (ethyl acetate) but in any case, the solid dissolved completely. During separation by chromatographic column (ethanol) it was observed a colour variation during the solvent elution, indicating a reaction between some components with the fixed phase (silica) and also, no fraction was obtained after re-concentration by solvent evaporation.

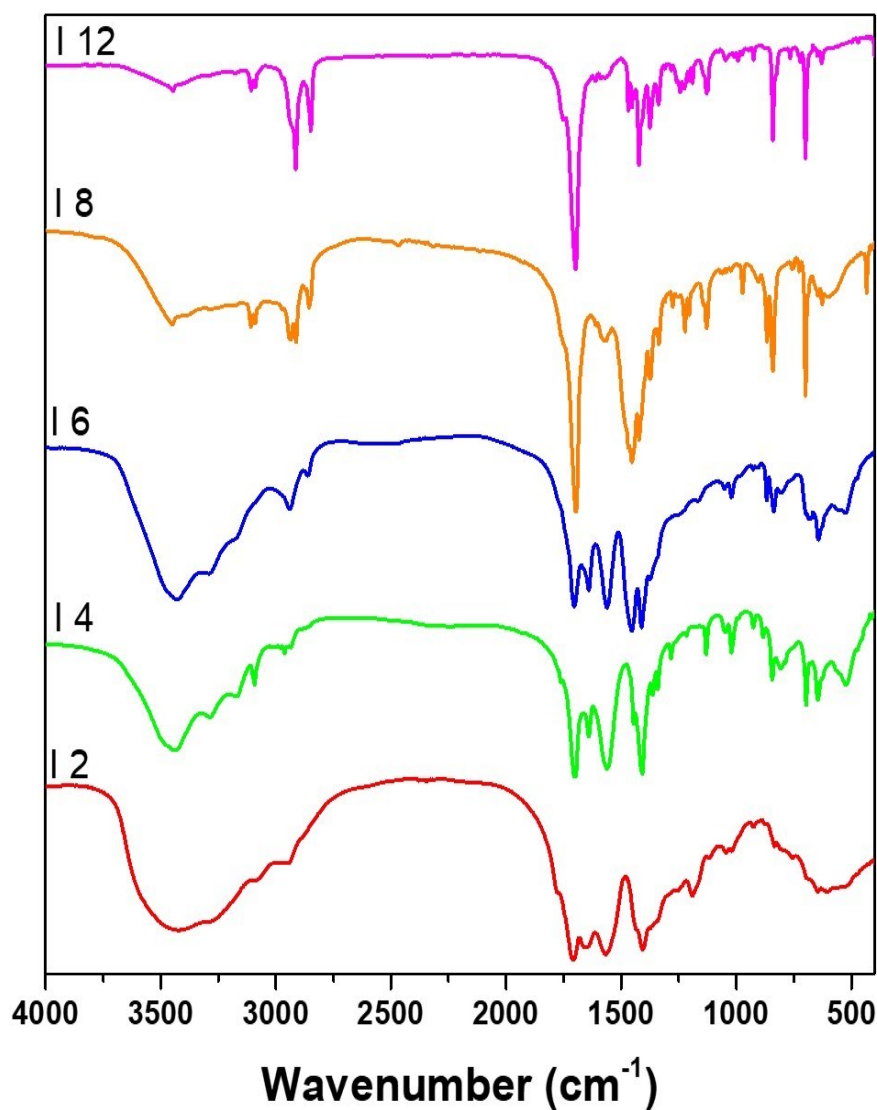


Figure 61. Comparison between FTIR spectra of different BI.

Based on the results obtained from the different analytical techniques used to characterize the compounds, I12 is the only molecule that can be considered pure and therefore, it is the only one that was used in GnP functionalization.

3.2.2 Interaction BI/GnP

The bismaleimide I12 was dissolved into xylene which is an effective solvent to disperse the GnP that has been functionalized (more details in chapter 2.1.5.) [76].

Maintaining the same stoichiometry, a GnP functionalized with MA was prepared to make a comparison with the GnP I12. Finally, to maximize the interaction with the GnP by minimizing the formation of potential aggregates on the surface of the nanoflakes and considering the study carried out for the functionalization of GnP with BP and the concentration showed in literature [76], also in this work, GnP was functionalized with I12 in which the ratio by weight between GnP and I12 is 10:1.

To quantify the amount of functionalization of GnP with I12, thermo gravimetric analyses (TGA) were performed and compared with those obtained for pure GnP and GnP functionalised with MA. Indeed, this technique was not used in the previous research with BP because the concentrations to functionalize were too low to be detected by TGA (as seen in UV analysis), contrary to those used for GnP functionalization with BI. As shown in the Figure 62, the GnP pristine has a progressive weight loss between 250 and 350 °C, due to the release of gases coming from intercalated solvents, and between 430 and 500 °C for the release of H₂O and CO₂ gases coming from oxidized groups [240]. The residue at 800°C is equal to 95% of the initial weight. The GnP functionalized with MA has a progressive weight loss similar to pure GnP. Indeed, the two curves are perfectly overlapping and therefore the residue at 800°C has a weight reduction of 5% compared to the initial one. Maleic anhydride has probably been removed either during washing steps or during drying into vacuum oven due to its tendency to sublime [241]. GnP functionalized with I12 show significantly different weight loss profiles than the previous ones. In fact, at a temperature of 500°C there is a 6% weight loss for GnP functionalized with a low concentration of I12, but that increases up to 27% for the sample with a high I12 concentration. The weight loss corresponds to the release of volatile species, probably related to BI fragmentation on GnP. A further weight loss above 600°C is noted due to the development of gases that could HCN, similar to polypyrrole degradation [242]. At the end of the thermal process the functionalized GnP with a low I12 concentration lost the 9% of its initial weight while the functionalized GnP with high concentration of I12 lost 35% of weight. In conclusion, considering the weight loss of pure GnP, it can be affirm that the contribution of I12 in GnP I12_10:1 is 4% while in GnP 1:1 it is 30%. This last value indicates that a huge excess of molecule is present but probably will not be useful to make molecular junction

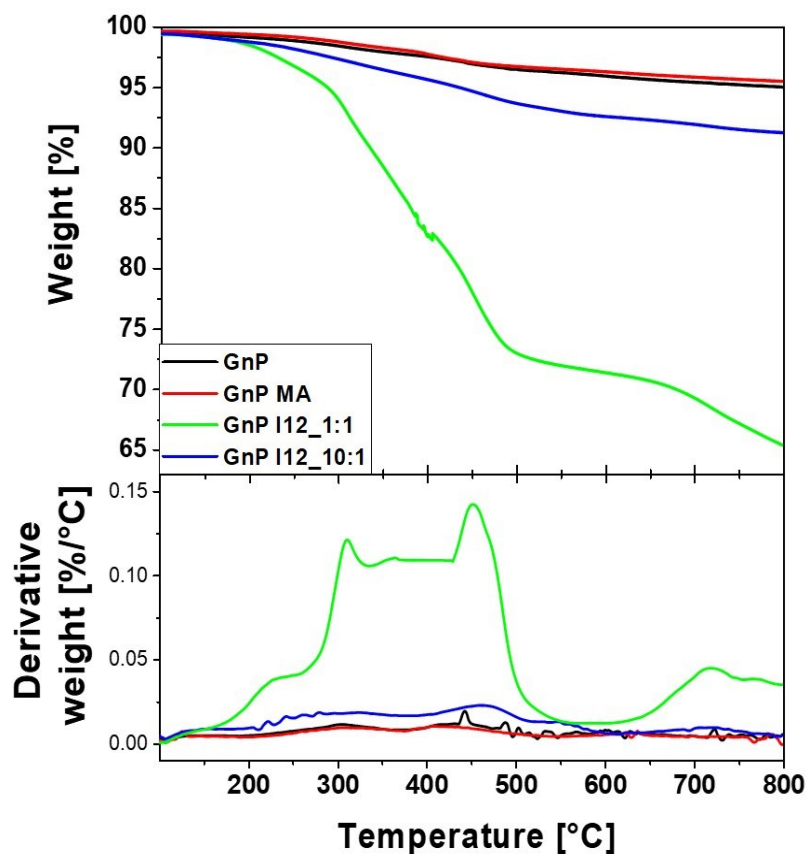


Figure 62. TGA results to quantify the functionalization with I12 in comparison to GnP MA and GnP pristine.

To confirm that the functionalization has occurred and affects the properties of GnP, Raman analyses have been carried out on the materials. The analysis of the Raman spectra of functionalized GnP (with MA or I12) compared to the GnP powders (Figure 63) shows a different reactivity of maleic anhydride compared to its imides derivatives.

The I_D/I_G ratio both GnP pristine that one functionalized with MA, show the same values ($I_D/I_G = 0.06$), indicating that the reaction did not lead to the inclusion of chemical defects but the MA react with the defects previously existent in the structure, i.e. the edges, and so, this does not lead to a variation of the surface vibrational mode on which depend the Raman signals. On the other hand, according to the TGA, the GnP may not have been functionalized.

During the acquisition of GnP BI Raman spectra with stoichiometry 1 to 1, a very fluorescent phenomenon covered the entire spectrum probably due to an excess of functionalization, coherently with the quantity observed in previous TGA analyses. In the GnP I12 derivatives with a 10:1 stoichiometry, the Raman spectrum shows a large increment of the D peak (1350 cm^{-1}) and consequent rise in the I_D/I_G ratio to 0.46, suggesting I12 to effectively interact strongly with the surface of the flakes and influences its surface vibrational mode.

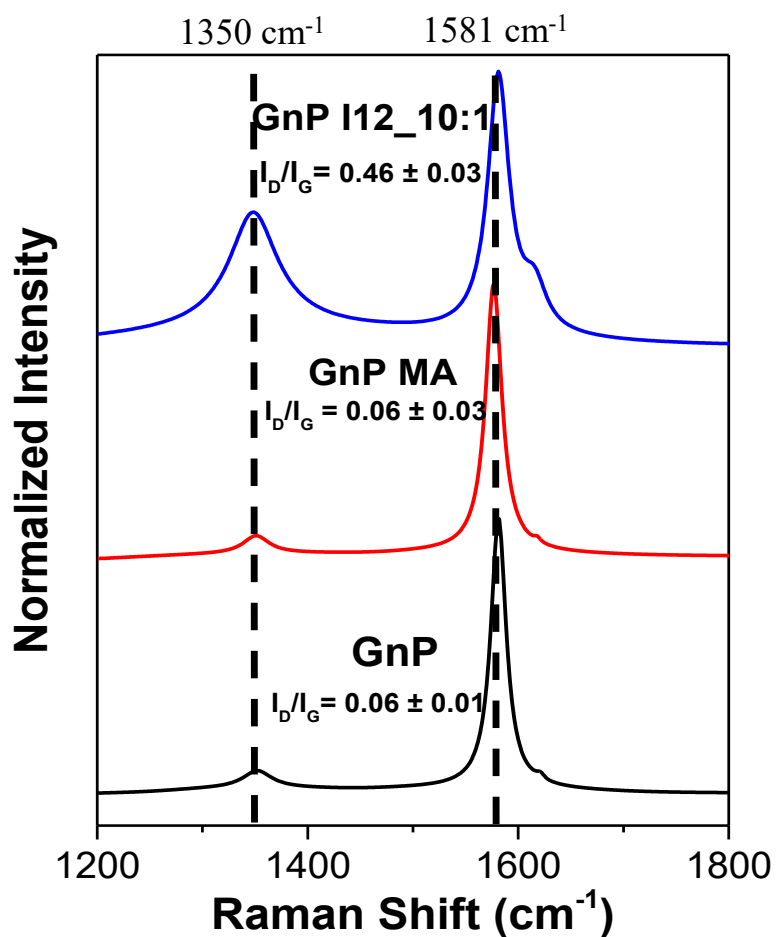


Figure 63. Raman Spectra comparison between GnP pristine and GnP functionalized with MA or with I12 at different concentration.

Both I12 concentrations and GnP functionalization with the MA have been used for the nanopapers fabrication that will be shown in the following chapter.

Chapter 4

Graphite nanoplatelets nanopapers

The nanopapers were manufactured by gravimetric filtration of the suspensions (in order to increase the alignment of flakes within the resulting nanopapers) of the GnP BP derivative while the GnP functionalized with the bismaleimide were re-dispersed into Dimethylformamide (using the same procedure as that of the bispyrene (for more details chapter 2) in order to make a comparison.

4.1. Morphological characterization

During filtration, the flakes align within the nanopaper, as shown in Chapter 1.2.2, therefore, a detailed study of the morphology is necessary to understand the thermal properties of these anisotropic materials.

4.1.1. Electron Microscopy

FESEM analysis of nanopapers were made to evaluate not only the surface topography but most importantly to understand the cross-sectional organization of the GnP in the presence or BP.

Initially, morphology of the nanopapers obtained from GnP suspensions with different concentrations (10^{-4} , 10^{-5} and 10^{-6} M) of C2 were evaluated. Figure 64 shows the comparison between nanopapers fabricated with pristine GnP as well as with those where the GnP were functionalized with different concentration of C2.

The surface topography of GnP pristine nanopaper (Figure 64 a) shows homogeneity of material contrary to surface nanopaper produced with a concentration of 10^{-6} M (Figure 64 b) in which it is possible to observe areas partially covered by the molecule (the grey ones). The 10^{-5} M nanopaper (Figure 64 c) shows a surface almost homogenous related to the presence of molecules and as shown at the central part of the image, in some areas there are some aggregates probably related to the excess of molecules. This is most evident in the 10^{-4} M nanopaper in which the large excess of C2 leads to aggregate whose micrometric dimension are comparable to the dimension of graphene flakes, as show in the Figure 64 d.

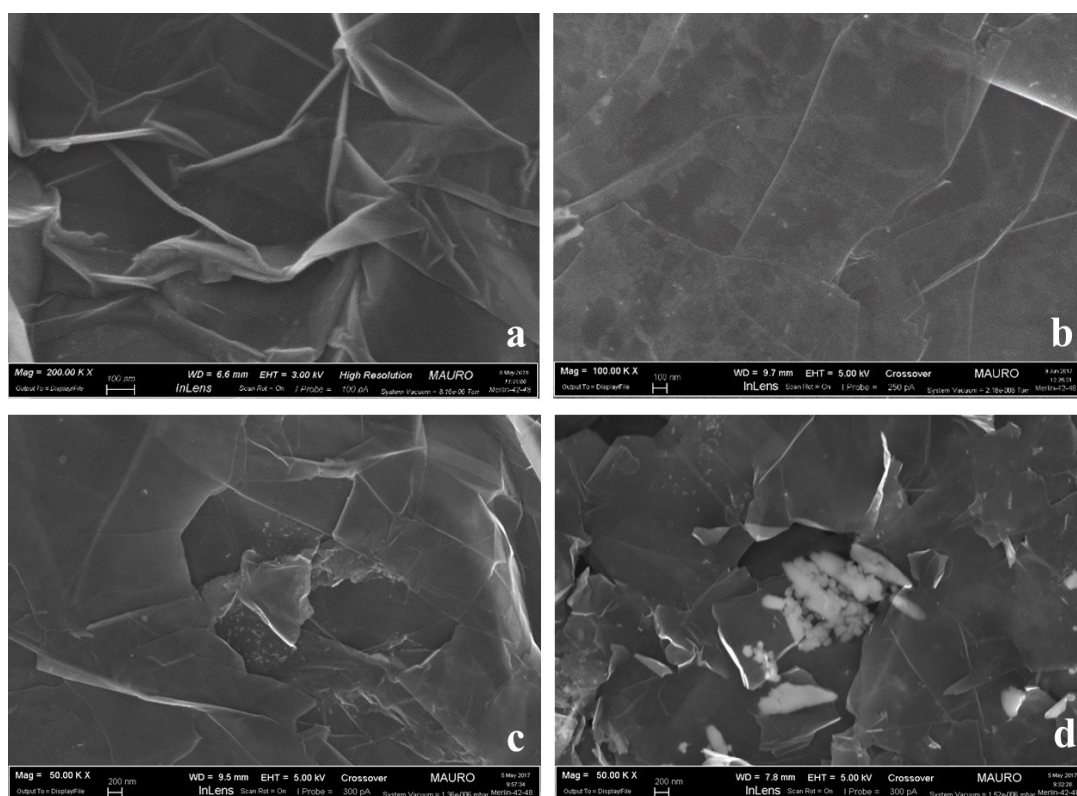


Figure 64. FESEM topography analysis of nanopaper fabricated with different molar concentration of C2. a) Nanopaper from GnP pristine (the blank). b) Nanopaper obtained from GnP containing 10^{-6} M of C2. c) Surface topography of nanopaper fabricated with a 10^{-5} M of C2. d) Surface topography of nanopaper fabricated with a 10^{-4} M of C2 where it is possible to observe aggregates of C2.

As a result, of the FESEM analyses on nanopapers GnP C2 at different concentrations, the 10^{-6} M concentration was chosen for the preparation of the nanopapers with the other bispyrene derivate molecules (C2-C12).

FESEM analyses were carried out for all nanopaper functionalized with BP to evaluate the morphological characteristics such as the compactness of the structure or the displacement of the flakes.

The comparison of nanopapers topographies (Figure 65), shows how, for the same magnification (25000 X) the surfaces of functionalized nanopapers are non-homogeneous contrast to that one manufactured with GnP pristine indicating that organic molecules are spread over the surface. In addition, considering the high-intensity white lines, which indicate folds or edges of the material [243], it can be observed, that the nanopaper GnP C2 (Figure 65 b) shows more protuberance due to a wrinkled surface. This could be considered an indication how the C2 bispyrene influences the deposition of the flakes differently than the others [244].

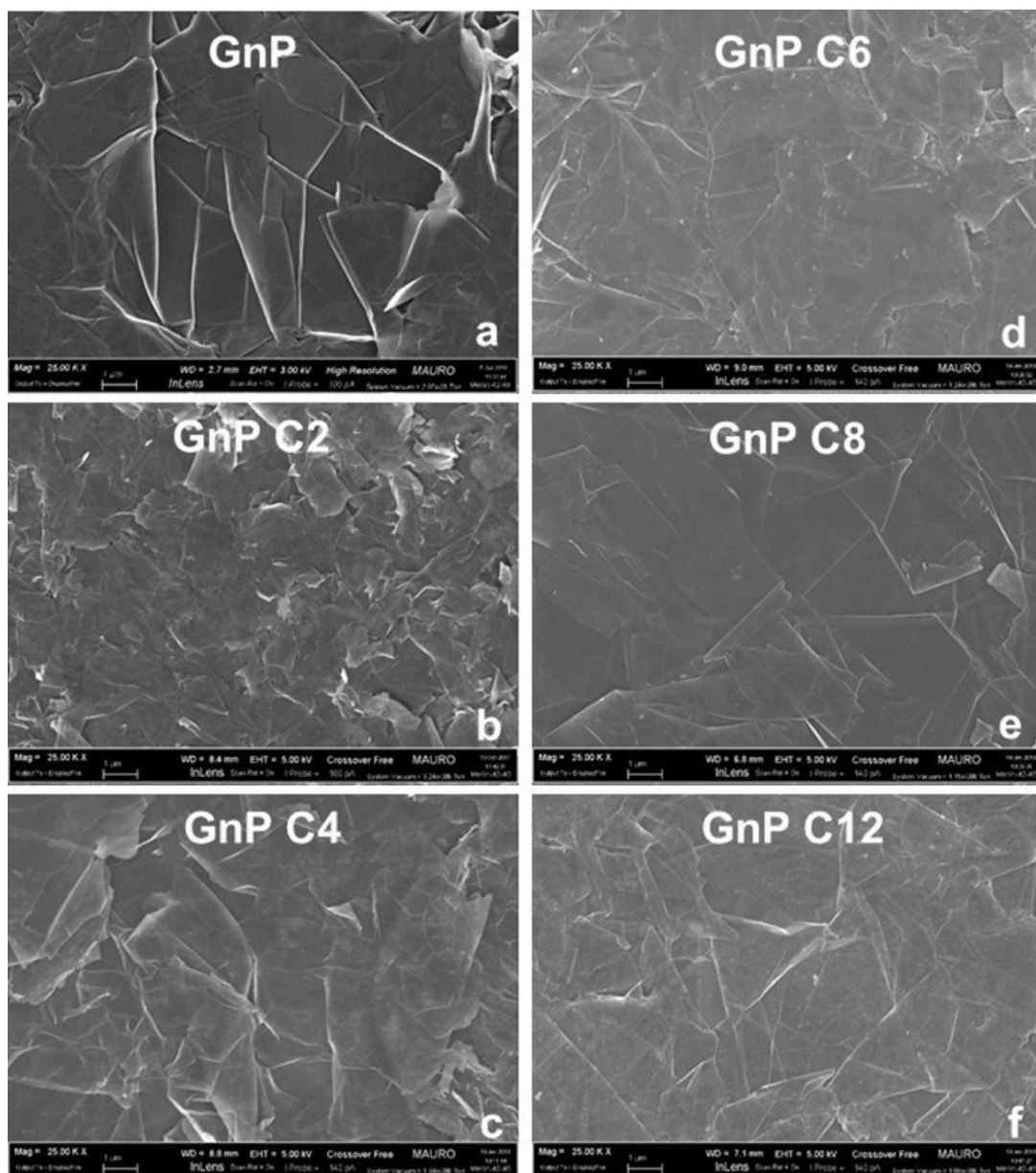


Figure 65. Surface topographies of nanopapers manufactured with GnP BP.

As shown in the Figure 66, where the cross sections of the various nanopapers are compared, it is possible to observe some slightly difference. Indeed, the nanopaper manufactured by GnP C2, shows flakes less aligned than all the others, contrary to those with GnP C4 and C8 where it is possible to see a preferential orientation of the flakes leading to an apparently more compact structure. Moreover, cross section examinations were used to measure thickness, which is one of the parameters for experimentally calculating the densities of each sample (Figure 66). In fact, by die cutting some samples of each nanopaper, the volume can be calculated as multiplication between area and height (by FESEM) and by weighing them with a balance with an accuracy of micrograms, it is possible to calculate the densities as mass/volume ratio.

The density of GnP pristine nanopaper is 1.22 g/cm^3 , according to similar systems in the literature [183, 245], which is almost half of the bulk graphite value (2.2 g/cm^3) because it is a porous material (porosity = 0.45 ± 0.02).

Densities of nanopapers were found to be significantly different from the reference GnP nanopaper and in particular, lower densities were obtained for all of the GnP-bispyrene nanopapers, ranging between 0.61 g/cm^3 (GnP C2 nanopaper) and 0.94 g/cm^3 (GnP C12 nanopaper). Interestingly, density values continuously increase with increasing the length of the alkyl chain in BP in GnP-bispyrene nanopaper. This trend is not straightforwardly explained in terms of BP mass fraction into the nanopapers, despite the latter is also slightly increasing with BP length. Instead, it appears that the density of the GnP bispyrene nanopaper depends on the interactions between BPs and GnP, driving the self-assembling of GnP during filtration.

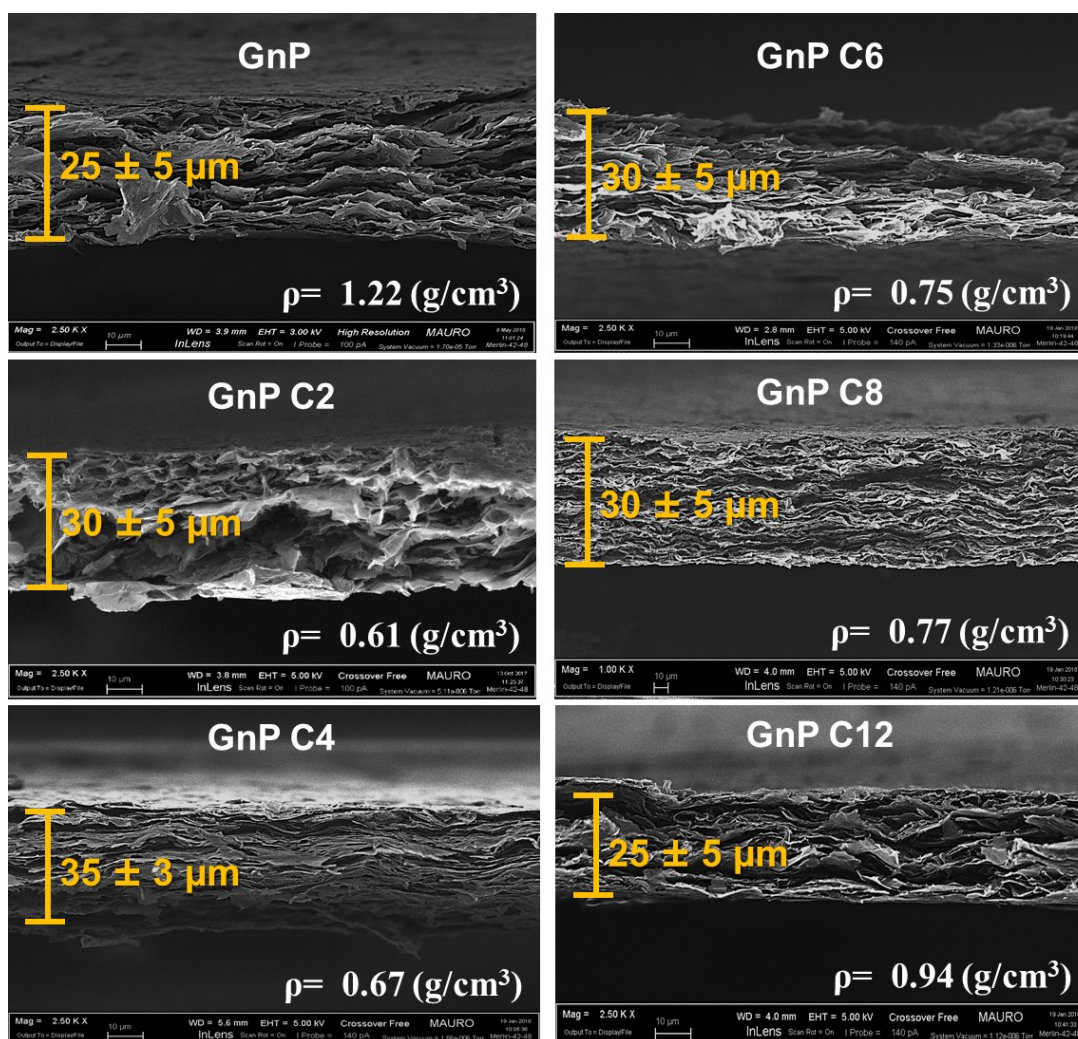


Figure 66. Cross Section FESEM analysis of GnP BP nanopaper.

The surface topographies of the nanopapers manufactured with GnP functionalized with MA and I12 (low concentration), respectively, give an indication about the functionalization effects onto flakes. In fact, the nanopaper with GnP MA (Figure 67

b) has the same homogeneity as that GnP pristine (Figure 67 a) indicating a surface without MA contrary to nanopaper with I12 (Figure 67 c) in which the non-homogeneous surface indicates that the molecules are spread on it as some aggregates are visible, probably in relation to I12 excess.

FESEM analyses were also carried out on cross-section to evaluate the effect of functionalization on alignment of the flakes. Nanopaper with GnP MA (Figure 67 e) have a similar arrangement to that with GnP pristine (Figure 67 d). On the contrary, nanopaper with GnP I12 (Figure 67 f) that shows high grade of flake alignment. By measurement of the thickness, the densities of the nanopapers were calculated obtaining 1.25 g/cm^3 for GnP functionalized with maleic anhydride, a value similar to that of the nanopaper with GnP pristine (1.22 g/cm^3), and 1.51 g/cm^3 for nanopaper with GnP I12. In conclusion, the density value confirm that I12 affect the organization of GnP during filtration in a different way from bispyrene.

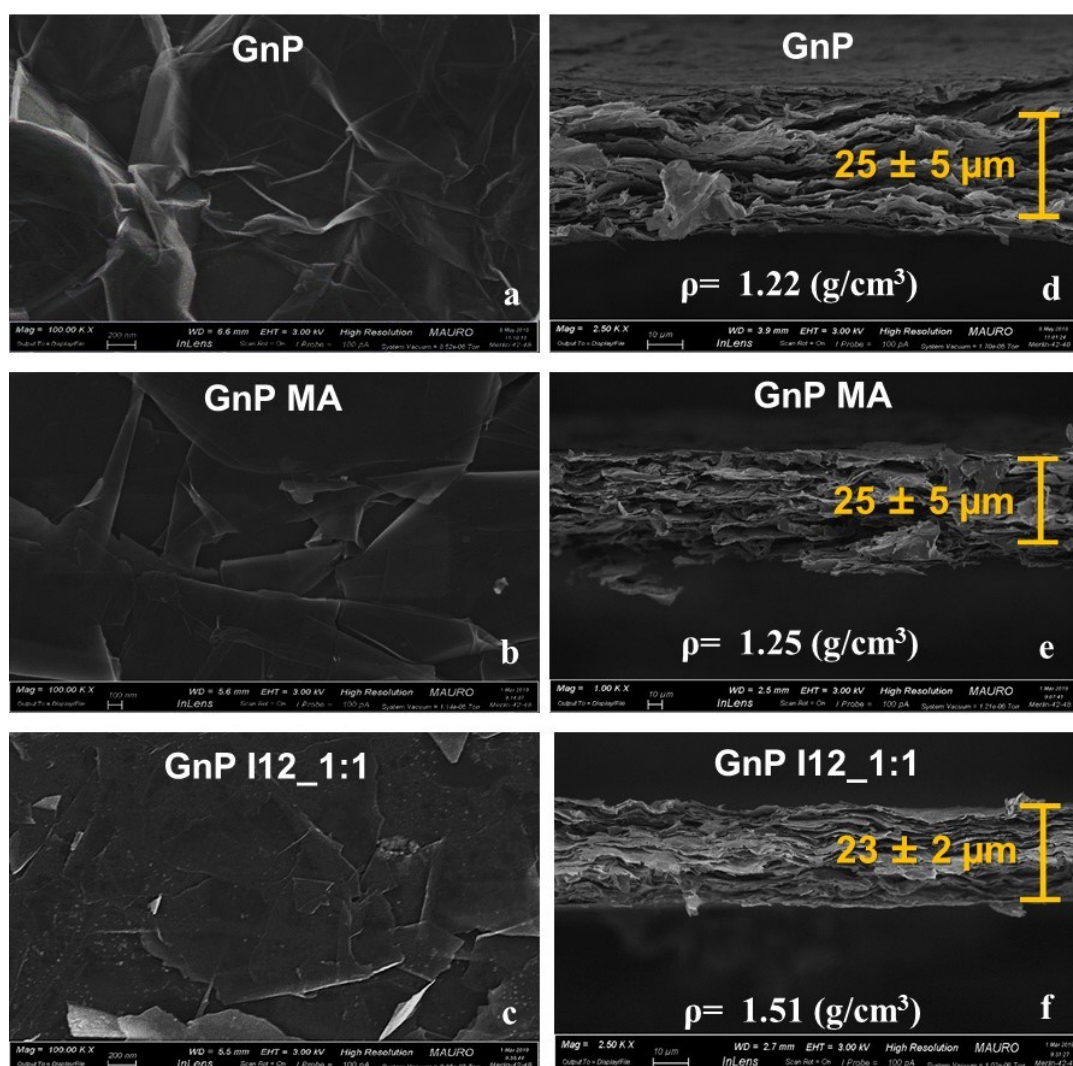


Figure 67. FESEM analysis comparisons of nanopapers manufactured with pristine GnP, those with GnP MA and GnP I12 ones. a, b, c show the surface topographies to evaluate the presence of aggregates while d, e and f show the cross-sections analysis to evaluate both the alignment of the flake and to measure the thickness for densities calculation.

4.1.2. XRD

Although the filtration of GnP suspensions is obviously expected to generally produce a clear in-plane orientation of GnP flakes, as shown in the FESEM analysis, quantifying the distribution of the basal planes orientations may indeed provide insight in the assembly of GnP. Therefore, in order to further investigate the assembly of nanopapers GnP pristine based and those manufactured with GnP BP, XRD measurements were used to evaluate the orientation of flakes into the nanopaper, monitoring the intensity of the graphite (002) diffraction peak at $2\theta = 26^\circ$, as a function of incident angle (α) ranging from 13° to 103° with respect to the horizontal plane of the sample. The intensities of graphite (002) peak were collected against the incident angle (α) so the tilt angle ($\alpha+180-\theta$) of the graphite basal planes compared to the horizontal plane of the nanopaper was calculated, from 0° (basal planes parallel to the nanopaper plane, shown in Figure 68 a) to 90° (basal planes perpendicular to the nanopaper plane, shown in the Figure 68 c).

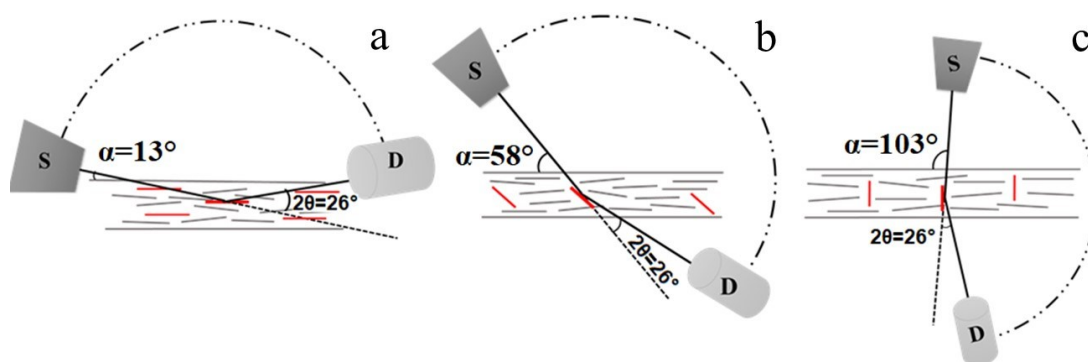


Figure 68. Schematic representation of gonio-configuration to monitor the 002 peak of graphite for the evaluation of preferential flake's orientations. Diffraction condition detecting graphite flakes having 0° tilt angle (a), 45° tilt angle (b) and 90° tilt angle (c).

For each of the GnP BP nanopapers, the experimental curves (one for each angle) were plotted and the peaks have been fitted with a Lorentzian function using software in order to obtain the peak height (Figure 69 a). These intensities values vs tilt angle were interpolated by exponential decay curve in order to calculate the area below that was used to normalize the relative set of data. These normalizations are crucial to obtain the comparison between samples with different thickness in order to study the distribution of probability for flakes oriented from parallel (0° tilt angle) to perpendicular respect to the nanopaper plane (Figure 69 b).

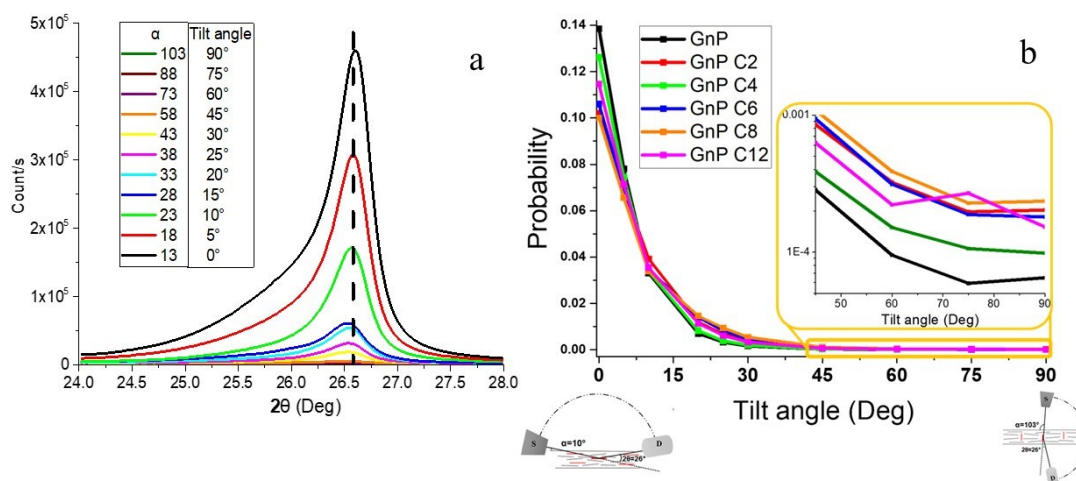


Figure 69. a) Fitting of experimental curves obtained varying the tilt angle from which detect the signal 002 of graphite (centered at $2\theta=26.6$). **b)** Probability vs tilt angle of flakes within nanopapers.

While probability of 002 planes is clearly maximum in the direction parallel to the nanopaper (0° tilt angle), the maximum probability values and the probability decay profile with the tilt angle are different for GnP and the GnP BP nanopapers. On the other hand, tilt angles $>45^\circ$ (see inset Figure 69b inset) where GnP BP nanopapers show higher intensities than GnP pristine ones. These results explain the lower densities for functionalized nanopapers, whose flakes have been demonstrated to have a lower preferential orientation, thus causing local porosity, in turn affecting the overall density.

The comparison of Pareto cumulative distributions provides a clear quantification of preferential orientation. For the pristine GnP nanopaper, 93% of the cumulative distribution of flakes has orientation between 0 and 10° tilt angle (i.e. an arrangement almost parallel to the surface of nanopapers) whereas, for GnP-bispyrene nanopapers, in the same tilt angle range, cumulative distribution vary from 78% for GnP C12 to 88% for GnP C4. Despite no clear trend can be drawn as a function of BP length, these values evidence for a slightly lower in-plane orientation of the GnP-bispyrene nanopaper compared to pristine GnP, confirming the BP to have a role in the self-assembly of GnP during filtration. This is likely explained by the formation of BP-bridged aggregation of GnP flakes in the suspensions into clusters, which constraint the organization of flakes during filtration, decreasing the packing factor and eventually reducing preferential orientation and density.

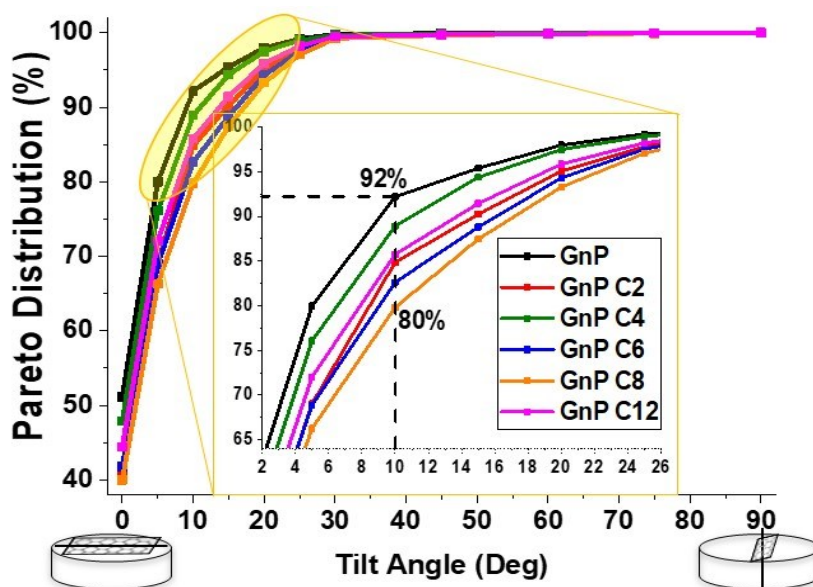


Figure 70. Pareto cumulative distribution for the quantification of preferential orientations of flakes and comparison between GnP-bispyrene nanopapers and pristine GnP.

The amount of BP retained within the nanopapers after filtration and drying was calculated from the concentration of BP infiltrated solutions, compared to the initial concentration in the GnP BP suspension. Retention rate of BP into the nanopapers (Figure 71) was found to increase with the chain length increase, up to $\geq 95\%$ for the longest BP.

The BP mass fraction in the nanopapers is ranging between 0.09 % (C2) and 0.15 % for C12, also reflecting the higher molar mass of longer chain BP. Such low concentrations depend not only on the limited surface area of GnP ($38 \text{ m}^2\text{g}^{-1}$) but mostly on the low concentration of BP. These values correspond to a limited coverage of the GnP with BP moieties, which was designed to provide sufficient GnP functionalization, while avoiding self-aggregation of BP into the nanopapers.

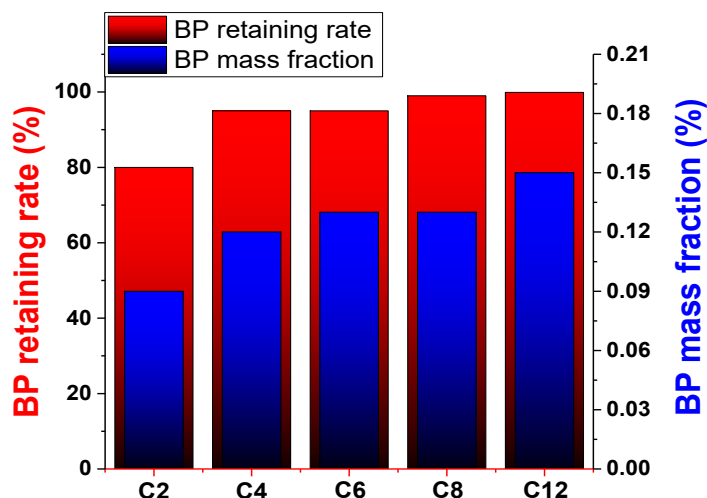


Figure 71. BP retaining rate and mass fraction of BP in the series of GnP-bispyrene nanopapers

In an analogous approach, fragments of nanopaper functionalized with MA or those functionalized with I12, were used for a quantitative characterization by TGA (Figure 72). Considering the residue at 800 °C, the nanopaper with MA had a weight loss of almost 1% higher than the GnP pristine (4%) nanopaper probably related to solvent while the nanopaper functionalized with I12 had a weight loss of 9 % and 32% for nanopaper obtained by a ratio of 10 to 1 and 1 to 1 respectively. In accordance with TGA on powders, the contribution by weight of I12 within nanopapers is 5% almost 30% respectively.

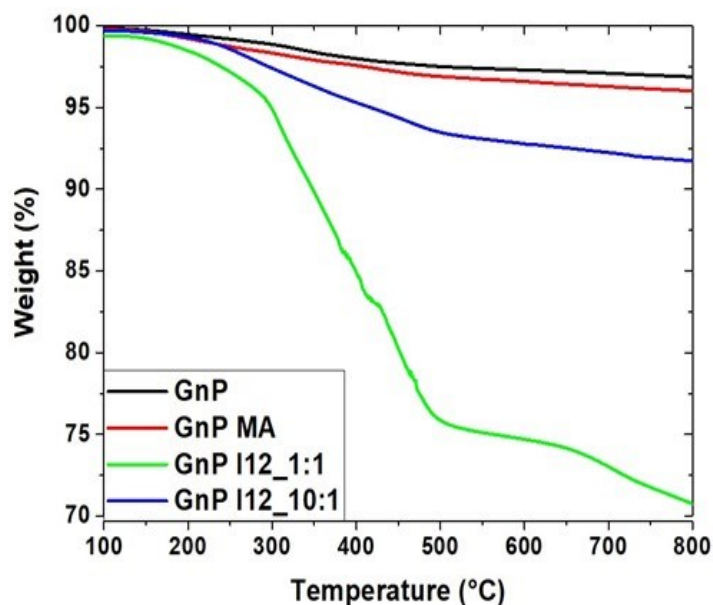


Figure 72. TGA of nanopaper manufactured with GnP MA and GnP I12 at different concentrations in comparison to nanopaper based on GnP Pristine.

4.2. Thermal conduction proprieties

4.2.1. Thermal diffusivity

Insight on the heat spreading efficiency of nanopapers was obtained by measuring thermal diffusivity, i.e. the rate of heat transfer within the material. Both in-plane and cross-plane diffusivities were measured for pristine GnP and GnP BP nanopapers (Figure 73), evidencing for significant differences, induced by BP functionalization. As expected from the above commented orientation of GnP, thermal diffusivity is strongly anisotropic, with roughly three orders of magnitude higher diffusivity in-plane ($\approx 200 \text{ mm}^2\text{s}^{-1}$), compared to cross-plane ($\approx 1 \text{ mm}^2\text{s}^{-1}$). Cross-plane thermal diffusivity (α_L) for GnP-bispyrene nanopapers are all higher than for pristine GnP, which could in principle be partially related to the above described lower nanoflakes

orientation. Indeed, the presence of even a very limited portion of flakes lying on directions tilted with respect to the nanopaper plane is expected to contribute to the heat transfer across the nanopaper, owing to the well-known anisotropy of graphitic materials. However, the changes in cross-plane diffusivity do not match misalignment degree, as evaluated in XRD, suggesting a different explanation, related to the presence of BP moieties. Short BP (C2 and C4) resulted to be the most effective functionalization for the cross-plane diffusivity enhancement, suggesting these molecules to be reduce the thermal resistance between overlapped nanoflakes. This may be explained by promoted aggregation between GnP, in agreement with the modified suspension stability described in section 3.1.2. This supramolecular crosslinking effect appears to be maximizing the contact area between GnP, as well as possibly enhancing phonon transfer efficiency through BP molecules bridging adjacent GnP, thus acting as a non-covalent molecular junction for phonon transfer. In-plane thermal diffusivity was also significantly enhanced by C2 and C4, whereas values for GnP BP containing longer BP are approximately equivalent to pristine GnP. It is worth noting that the in-plane diffusivity enhancement is obtained in spite of the lower in-plane orientation for GnP BP nanopaper, thus further supporting the role of BP molecular junctions in the enhancement of thermal transfer at GnP-GnP contacts.

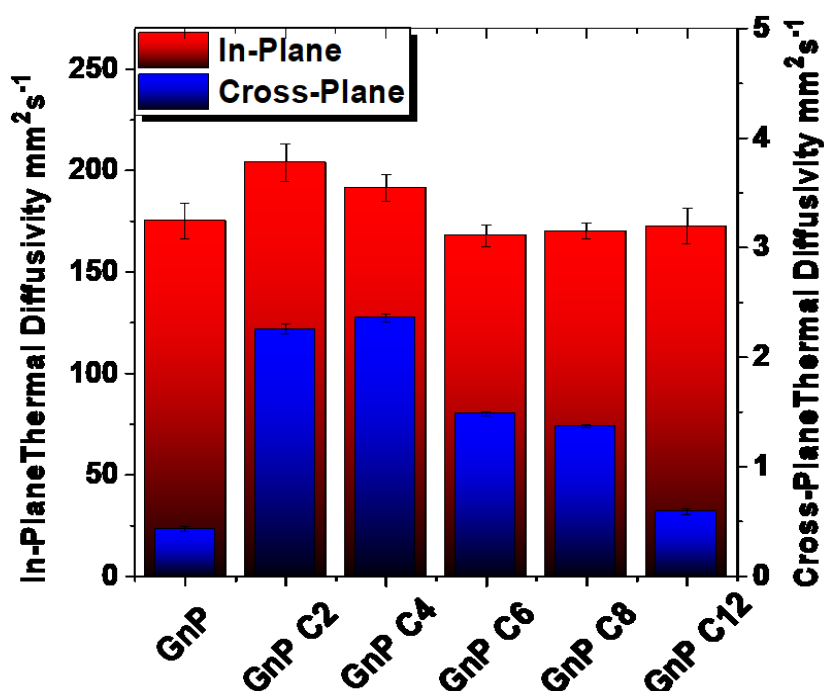


Figure 73. In-plane and cross-plane thermal diffusivities for GnP and GnP BP nanopapers

GnP C2 nanopapers were further investigated as a function of C2 concentrations, in the range between 10^{-4} M and 10^{-6} M. Although the thermal diffusivities for all C2 GnP nanopapers are higher than GnP pristine for any concentration range (Figure 73), an increment in C2 concentration resulted in a decrease of both in-plane and cross-

plane diffusivities. Indeed, while C2 at 10^{-6} M induces 17 % and 420% enhancement for in-plane and cross-plane thermal diffusivities, respectively, compared to pristine GnP nanopaper, for those at 10^{-4} M C2 increments are reduced to 11 % and 180%. This is possibly explained by C2 aggregation (as previously shown in the FESEM analysis) that may hinder efficient networking of GnP flakes, thus leading to a drastically reduction in thermal diffusivities.

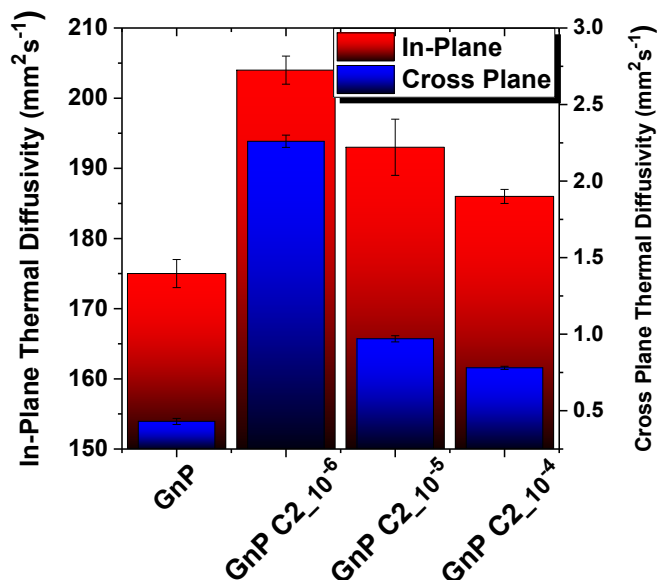


Figure 74. Thermal diffusivities comparison between nanopapers at different concentration of C2.

Furthermore, the effect of bispyrene functionalization was also compared with that of mono-pyrene derivatives, to gain further insights on the role of BP as non-covalent molecular junctions between GnP and, in particular, if the effect of two anchor groups (pyrene) leads to a better thermal junction between different GnP. Therefore, two mono-pyrene derivatives (MP) were used that are different in term polar interaction with GnP and relative thermal effect for the phonon transmission (Figure 75). The pyrene butyric acid, one of the reagents used to synthesize BP and it has already been used to disperse graphene into DMF [246], has a polar terminal group (PyCOOH) whereas the N-dodecyl-4-(pyren-1-yl)butanamide (PyCONH), specifically synthesized starting from pyrene butyric acid and an mono-aminoalkane, brings an hydrophobic aliphatic chain (the NMR spectra are shown in the appendix 7.3). Nanopapers were prepared with the mono-pyrene derivatives (GnP MP) using the same conditions and concentration and morphologically characterized (more details in the Appendix 7.4) as for the GnP BP and thermal diffusivity of these nanopapers were measured by LFA.

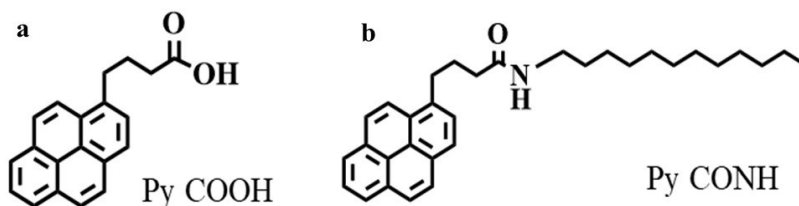


Figure 75. Mono pyrene derivate. a) Pyrene butyric acid with a terminal polar group. b) The N-dodecyl-4-(pyren-1-yl)butanamide with hydrophobic terminal group.

Nanopapers with GnP MP showed in-plane thermal diffusivity lower of about 6% for the PyCOOH and 4% for the PyCONH respectively compared to GnP pristine nanopaper contrary to cross-plane thermal diffusivity in which limited improvements were obtained, as show in the Table 7. The absence of substantial improvements with MP suggests that it is necessary to use bi-functional molecules in order to lead the organization of GnP in a thermally efficient network.

<i>Nanopaper</i>	<i>In plane</i> $\alpha_{//}$ (mm^2s^{-1})	<i>Cross plane</i> α_{\perp} (mm^2s^{-1})
GnP	175.1 ± 8.6	0.433 ± 0.019
GnP COOH	163.9 ± 5.3	0.810 ± 0.002
GnP CONH	167.8 ± 5.4	0.590 ± 0.005
GnP C2_10 ⁻⁴	187.5 ± 8.1	0.781 ± 0.004
GnP C2_10 ⁻⁵	192.5 ± 5.9	0.971 ± 0.016
GnP C2	203.9 ± 9.2	2.256 ± 0.044
GnP C4	191.6 ± 6.6	2.358 ± 0.038
GnP C6	168.0 ± 5.3	1.485 ± 0.02
GnP C8	170.1 ± 3.9	1.371 ± 0.013
GnP C12	172.6 ± 8.6	0.589 ± 0.026

Table 7. Thermal diffusivities of nanopapers.

After evaluating the effect of BP as molecular junctions, the possibility to obtain more strongly bound molecular junctions between GnP, thus potentially more efficient in phonon transfer based on when shown by some articles [247-249], was explored.

LFAs of both GnP nanopapers manufactured with I12 at different concentrations were carried out, comparing the results with the pristine GnP nanopaper as well as GnP MA nanopaper, as shown in the Figure 76.

Both GnP MA and GnP I12 were found to have thermal performances lower than pristine GnP nanopaper. In fact, the value of diffusivity in cross plane decreases from 0.43 mm^2s^{-1} of GnP pristine to 0.35 mm^2s^{-1} for that one with the I12 (low

concentration) up to $0.32 \text{ mm}^2\text{s}^{-1}$ of that one with the I12 (high concentration) and $0.29 \text{ mm}^2\text{s}^{-1}$ of that one functionalized with the MA.

In general, these values are coherent with the presence of molecules that are interposed between the flakes, spacing them and therefore hindering the heat transmission.

For the thermal diffusivity in direction parallel to the surface was observed the pure GnP is the most performing compared to nanopaper that have functionalized GnP. Indeed the values drastically decrease from $175 \text{ mm}^2\text{s}^{-1}$ for GnP pristine to $94 \text{ mm}^2\text{s}^{-1}$ for that with MA and $47 \text{ mm}^2\text{s}^{-1}$ for GnP I12 nanopaper (that one with a high concentration of organic liker).

A lower heat transfer efficiency of the I12 compared to the MA could be related to an excess of functionalization. In fact, for the samples with MA, the flakes are relatively closer and the heat transfer can take place more easily, contrary to those with I12, in which the aggregates of molecules (as seen in the FESEM analysis) are interposed between flakes and a significant decrement in diffusivity is obtained.

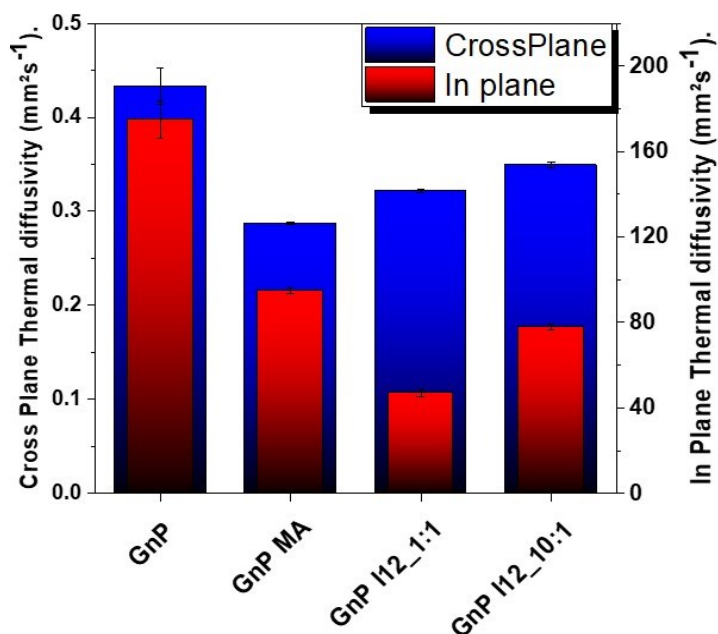


Figure 76. Cross plane and in plane thermal diffusivity comparison of pure GnP and functionalized GnP with either MA or I12 at different concentrations.

Because the thermal proprieties of BI nanopapers are lower than GnP pristine one in contrary to BP nanopapers, only nanopapers with BP were tested to evaluate their efficiency as heat spreader.

4.2.2. Thermal conductivity

Thermal diffusivity represents the rapidity of heat distribution and thus it is an intrinsic property of each materials: However the heat flow that could be carried by

a material under a defined temperature gradient depends on the thermal conductivity, which can be calculated from the diffusivity measurement as $K = \alpha \cdot \rho \cdot C_p$, where ρ and C_p are respectively the density and the thermal capacity of the material. Therefore, considering the densities of the nanopapers previously measured and the capacity of GnP which is the same as graphite, it is possible to calculate the thermal conductivity of nanopapers, either functionalized or not, and compare them with the most widely used heat management materials.

As show in the Table 8, the GnP pristine nanopaper shows the highest thermal conductivity in plane ($151 \text{ Wm}^{-1}\text{K}^{-1}$) while nanopapers with GnP MP show values around $100 \text{ Wm}^{-1}\text{K}^{-1}$ and even lower values are obtained for nanopapers containing BP (around $90 \text{ Wm}^{-1}\text{K}^{-1}$) except to GnP C12 nanopaper whose value is $115 \text{ Wm}^{-1}\text{K}^{-1}$. Cross-plane thermal conductivities, on the other hand, show similar values for nanopaper with GnP MP and that with GnP pristine ($0.375 \text{ Wm}^{-1}\text{K}^{-1}$) on contrast to nanopapers with GnP BP which show higher values. In fact, for the shorter BP (C2 - C4) cross-plane thermal conductivity are respectively $0.997 \text{ Wm}^{-1}\text{K}^{-1}$ and $1.124 \text{ Wm}^{-1}\text{K}^{-1}$, while as the length of the molecule increases, decreasing values are obtained up to $0.393 \text{ Wm}^{-1}\text{K}^{-1}$ for the nanopaper GnP C12.

The effects of density and thermal capacity are very evident when carbon-based nanopapers are compared with copper and aluminum laminates, which are the most widely, used metals for thermal management applications. In fact, the thermal conductivity is more than double for aluminum ($235 \text{ Wm}^{-1}\text{K}^{-1}$) and four times higher for copper ($370 \text{ Wm}^{-1}\text{K}^{-1}$), but due to both the high thermal capacity of the metals and, more important, their density (more than four times for aluminum and almost fifteenth times for copper). Therefore, because the densities of the nanopapers depends on the technology of preparation, improvements can be obtain simply by compacting the material with a consequent increase in thermal conductivity.

	ρ (gcm^{-3})	α in-plane (mm^2s^{-1})	α cross-plane (mm^2s^{-1})	K_{comp} in-plane ($\text{Wm}^{-1}\text{K}^{-1}$)	K_{comp} cross-plane ($\text{Wm}^{-1}\text{K}^{-1}$)
GnP	1.22	175.1 ± 8.6	0.433 ± 0.019	151 ± 5	0.375 ± 0.017
GnP COOH	0.85	163.9 ± 5.3	0.810 ± 0.002	100 ± 3	0.485 ± 0.001
GnP CONH	0.93	167.8 ± 5.4	0.590 ± 0.005	110 ± 4	0.389 ± 0.003
GnP C2_10⁻⁴	0.82	187.5 ± 8.1	0.781 ± 0.004	110 ± 5	0.457 ± 0.002
GnP C2_10⁻⁵	0.74	192.5 ± 5.9	0.971 ± 0.016	101 ± 3	0.511 ± 0.008
GnP C2	0.61	203.9 ± 9.2	2.256 ± 0.044	90 ± 4	0.997 ± 0.019
GnP C4	0.67	191.6 ± 6.6	2.348 ± 0.038	92 ± 3	1.124 ± 0.018
GnP C6	0.75	168.0 ± 5.3	1.485 ± 0.020	90 ± 3	0.791 ± 0.011
GnP C8	0.77	170.1 ± 3.9	1.371 ± 0.012	92 ± 2	0.739 ± 0.007

GnP C12	0.94	172.0 ± 8.6	0.589 ± 0.026	115 ± 6	0.393 ± 0.017
Al	2.70	96.7 ± 5.4	96.7 ± 5.4	235 ± 13	235 ± 13
Cu	8.96	107.3 ± 5.4	107.3 ± 5.4	370 ± 19	370 ± 19

Table 8. Thermal proprieties comparison between nanopapers with Aluminum and Copper.

The nanopapers can be considered as porous materials in which the thermal conductivity is the sum of the contributions of air and GnP respectively.

In order to study the dependence of diffusivity and conductivity of porous material as a function of density, nanopapers based on GnP pristine have been prepared and pressed with different forces.

From the relationship that relates the density of a material to its porosity in which $\rho = 1 - \phi$ (more details in chapter 2.5) where ρ is the density and ϕ is the porosity, as shown in the table, the thermal conductivity value increases from 49 $\text{Wm}^{-1}\text{K}^{-1}$ (for the highest porosity nanopaper) to 219 $\text{Wm}^{-1}\text{K}^{-1}$ for the most dense nanopaper. On the other hand, it is well demonstrated how thermal diffusivity is not influenced by porosity because the values of nanopaper are very similar between themselves.

Sample	ρ (gcm^{-3})	porosity (ϕ)	$\alpha_{//}$ (mm^2s^{-1})	$K_{//}$ ($\text{Wm}^{-1}\text{K}^{-1}$)
A	0.39	0.83	178 ± 5	49 ± 11
B	0.78	0.64	178 ± 3	99 ± 2
C	1.17	0.47	169 ± 7	141 ± 6
D	1.19	0.46	176 ± 7	149 ± 6
E	1.27	0.42	179 ± 4	163 ± 4
F	1.78	0.19	173 ± 3	219 ± 4

Table 9. Thermal diffusivities and thermal conductivities values of nanopapers pressed at different force

The problem of heat conduction in heterogeneous materials consisting of a solid continuous phase and a filler dispersed phase, dates back to the early works of Maxwell [250] and Rayleigh [251] in which different models were proposed to predict the effective thermal conductivity of various types of composite materials. A study was carried out in which, models of effective thermal conductivity of composite materials most frequently appearing in the literature are presented and compared. According to the Maxwell approach, the problem was considered as a dispersion of spherical bubbles (having thermal conductivity = 0.026 $\text{Wm}^{-1}\text{K}^{-1}$) embedded in a continuous conductivity matrix, but where the thermal interactions between bubbles were ignored [252]. However, this is only valid for low porous materials where the bubbles are isolated, so Rayleigh's model instead considered a possible interaction but assumes that the bubbles have a spherical shape. Although other form factors have been evaluated in Hasselman-Johnson's models (cylinders [253] or ellipsoids [254]), these models do not consider the possible shapes of air

within the nanopaper. Therefore different models have been considered (Figure 77) in which the volume fractions of each phases are considered, including Maxwell-Eucken models (depending on porosity magnitude), the linear model and that effective medium theories (EMT) [255].

The experimental results (black points) were used to investigate which model normalizes the effect of air, considering, k_e is the thermal conductivity of composite, k_1 is the thermal conductivity of GnP network (including interfacial effect and functionalization) which is the unknown factor, k_2 is thermal conductivity of air equal to $0.026 \text{ W}\cdot\text{m}^{-1}\cdot\text{K}^{-1}$, v_2 is the volume fraction of air (porosity). As show in the Figure 77, it is evident that the linear model fit the experimental points better than others and was used to calculate the nominal thermal conductivity of nanopaper obtained at zero porosity, equal to $273 \text{ W}\cdot\text{m}^{-1}\cdot\text{K}^{-1}$.

Linear model

$$k_e = k_1(1 - v_2) + k_2 v_2$$

Maxwell-Eucken model 1

$$k_e = k_1 \frac{2k_1 + k_2 - 2(k_1 - k_2)v_2}{2k_1 + k_2 + (k_1 - k_2)v_2}$$

Maxwell-Eucken model 2

$$k_e = k_2 \frac{2k_2 + k_1 - 2(k_2 - k_1)(1 - v_2)}{2k_2 + k_1 + (k_2 - k_1)(1 - v_2)}$$

Effective Medium Theories (EMT)

$$k_e = \frac{1}{4} \left((3v_2 - 1)k_2 + [3(1 - v_2) - 1]k_1 \right. \\ \left. + \sqrt{[(3v_2 - 1)k_2 + (3\{1 - \varepsilon v_2\} - 1)k_1]^2 + 8k_1 k_2} \right)$$

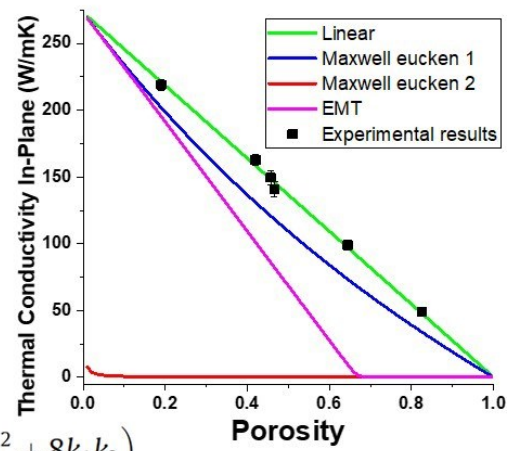


Figure 77. Equation of theoretical models used to investigate the effect of porosity within the nanopaper and their plotting in comparison to experimental points.

The linear model was applied to the thermal conductivities of nanopapers manufactured with functionalized GnP, to get rid of the effect of their difference in densities, in order to obtain the “intrinsic” thermal conductivity values of GnP networks, theoretically obtainable if nanopapers could be fully densified. These values are reported in Figure 78 and compared with aluminium ($235 \text{ W}\cdot\text{m}^{-1}\cdot\text{K}^{-1}$) and copper ($370 \text{ W}\cdot\text{m}^{-1}\cdot\text{K}^{-1}$). The C2 functionalization leads to in-plane thermal conductivity values higher than aluminium for the whole range of concentrations used as well as GnP C4 nanopaper, that also have the highest cross-plane thermal conductivity among carbon nanopapers. On contrary, GnP MP nanopapers and those contain longer BP (C6-C12) show lower thermal conductivity both GnP pristine nanopaper and aluminium.

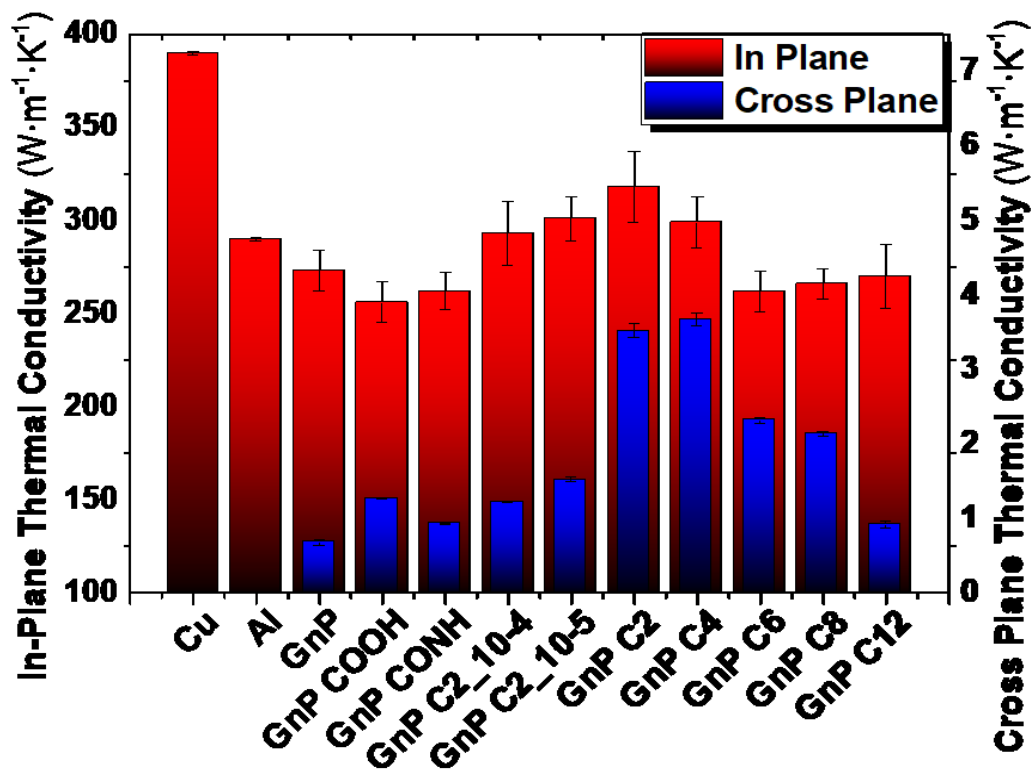


Figure 78. Thermal conductivity of nanopapers obtained by applying of the linear model for porous materials in comparison with values of copper and aluminum.

Chapter 5

Heat spreader with GnP nanopapers

From an application perspective, such increased in-plane thermal diffusivity may be exploited in heat spreader applications, typically used for the dissipation of heat from a hot spot, over a larger surface. This is the case of several electronic components in modern devices, especially in high frequency processors and batteries, in which the excess heat must be dissipated to prevent device failure. Copper and Aluminum are traditionally used for heat spreaders for their high thermal conductivity, in the forms of foils or finned structures.

5.1. Temperature vs time profile

GnP nanopapers are in principle a valid alternative to metals, owing to their heat spreading performance, coupled with a low density, thus opening for applications in flexible electronics as well as wearable and implantable devices. With the aim of comparing performances of GnP-bispyrene nanopapers to the conventional metal foils, an experimental setup (Figure 79) for the measurement of heat spread from a hot spot was built and validated. This can be considered as a simulation of local overheating of an electronic component in an electronic device that requires cooling. Therefore, in addition to the thermal diffusivity and thermal conductivity values of the nanopaper, as shown in the previous chapter, the problem was also be treated below from the point of view of heat dissipation with the surrounding environment.

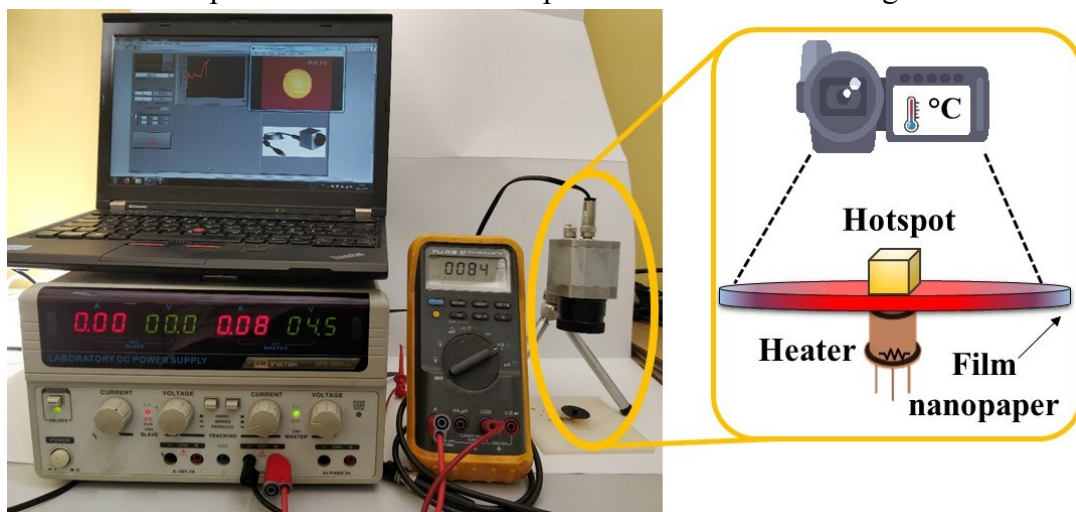


Figure 79. Set Up for the measurement of thermal properties as heat spreader

Using a powered transistor, simulating an hotspot, and an IR thermo camera to collect thermal maps in time, the temperature evolution over the heat spreader, made with copper film or with the nanopapers above described was continuously monitored during heating (power on) and cooling (power off) of the hot spot. In the absence of any heat spreader foil, the temperature, on heating raises up to about 85°C after 300s power on. As expected, the presence of a metal foil strongly reduced the hotspot temperature to 53.6 °C for Cu and 56.6 for Al foils, as the heat is distributed from the hot spot to the surface of the foil and eventually dissipated to the surrounding air, by natural convection and irradiation. With nanopaper heat spreaders, temperature profiles in time strongly depend on the presence and type of functionalization. Indeed, all GnP BP nanopapers have a maximum hot spot temperature lower than with the pristine GnP and, most importantly, those that containing the shortest BP (C2) revealed to be as efficient as Cu, whereas GnP C4 is even more efficient than Cu foil in these conditions (Figure 80). This outstanding result is even more impressive when considering the densities of the heat spreaders, as the porous GnP C4 nanopaper is only 0.67 g/cm³, whereas copper is about 8.9 g/cm³, thus delivering a straightforward weight reduction of the heat spreader by one order of magnitude.

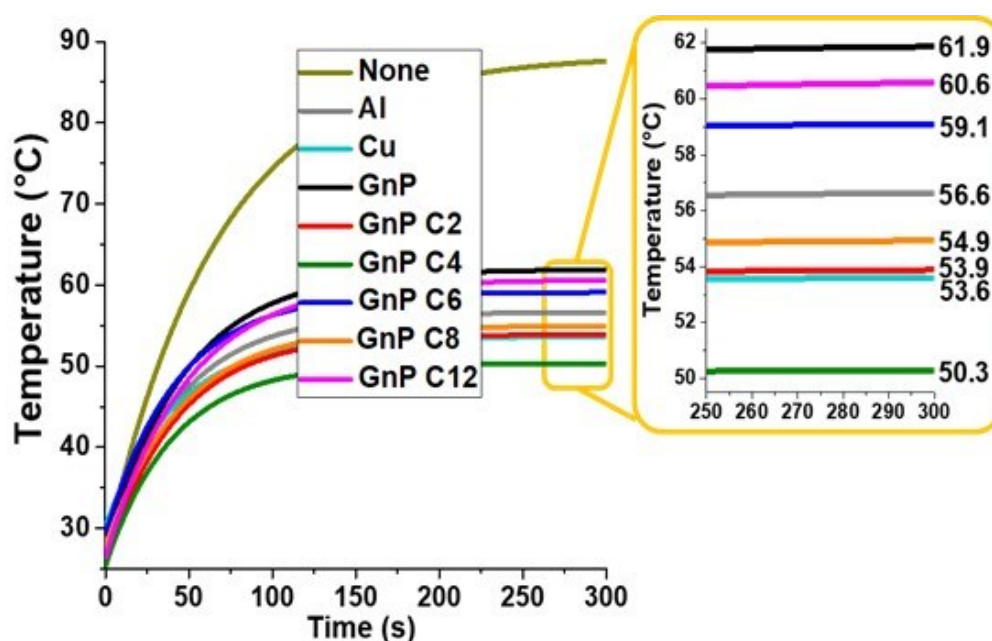


Figure 80. Temperature vs time profile of hotspot, as such or in the presence of different types of foils used as heat spreader.

5.2. Thermal gradients

To investigate the mechanism of heat dissipation over the spreader foils, the thermal maps acquired in time (maps at selected times are reported in Figure 81), upon heating and cooling the powered transistor, were carefully analysed.

By overlaying the origin of a Cartesian system (X; Y) with the centre of the nanopaper, the first quadrants showing the thermal gradients of heat spreader of different materials can be compared to a system without a heat sink.

Analysing the heating phase (Figure 81), it is noticeable that after 30 seconds the thermal gradient of copper is the smallest compared to GnP nanopaper heat spreader but at the same time the temperature profile over the whole nanopaper is higher than others. Among GnP-based nanopapers, on the other hand, it is evident how pristine GnP does not dissipate heat as efficiently as copper because the temperature near the hotspot is higher. On the other hand GnP C2 nanopaper shows a hotspot temperature comparable to copper but a temperature distribution along the whole profile at significantly lower values. These differences are even more evident after 60 s heating, when it is clear that a system without heat spreader reaches temperatures above 60 °C, on contrast to the lower temperature of those in which heat spreader works, although with different performance.

In fact, if on the one hand, the temperature closer the hotspot is higher in GnP pristine nanopapers and in that with C12 than copper or one GnP with C2, on the other hand, in the part near the edges, GnP C12 nanopaper and in particular one made with GnP C2 show values close to room temperature while copper and GnP pristine nanopaper have edges at a temperature higher than ten degrees (about 43 °C).

When the cooling phase begins (after 5 min heating) and when the system is at plateau temperature, the IR-map show similar gradients for pure GnP pristine nanopaper and the one made with GnP with C12 where both the temperatures near the hot spot (over 60 degrees) and those along the whole thermal profile are higher than for copper and GnP C2 ones. If the copper heat spreader has the smallest thermal gradient vs radius, on the other hand, the GnP C2 heat spreader has the lowest temperatures along the whole profile.

The result is also confirmed by the maps acquired at 330 seconds and 360 seconds respectively, in which the GnP C2 heat spreader always shows lower temperatures than the other heat spreader, over the whole surface. Moreover, after one minute of cooling (360 seconds) it is evident that the GnP C2 system is at temperature values near to the ambient temperature (approx. 28-35 degrees), contrary to the other samples that show values ten degrees higher along all the respective profiles.

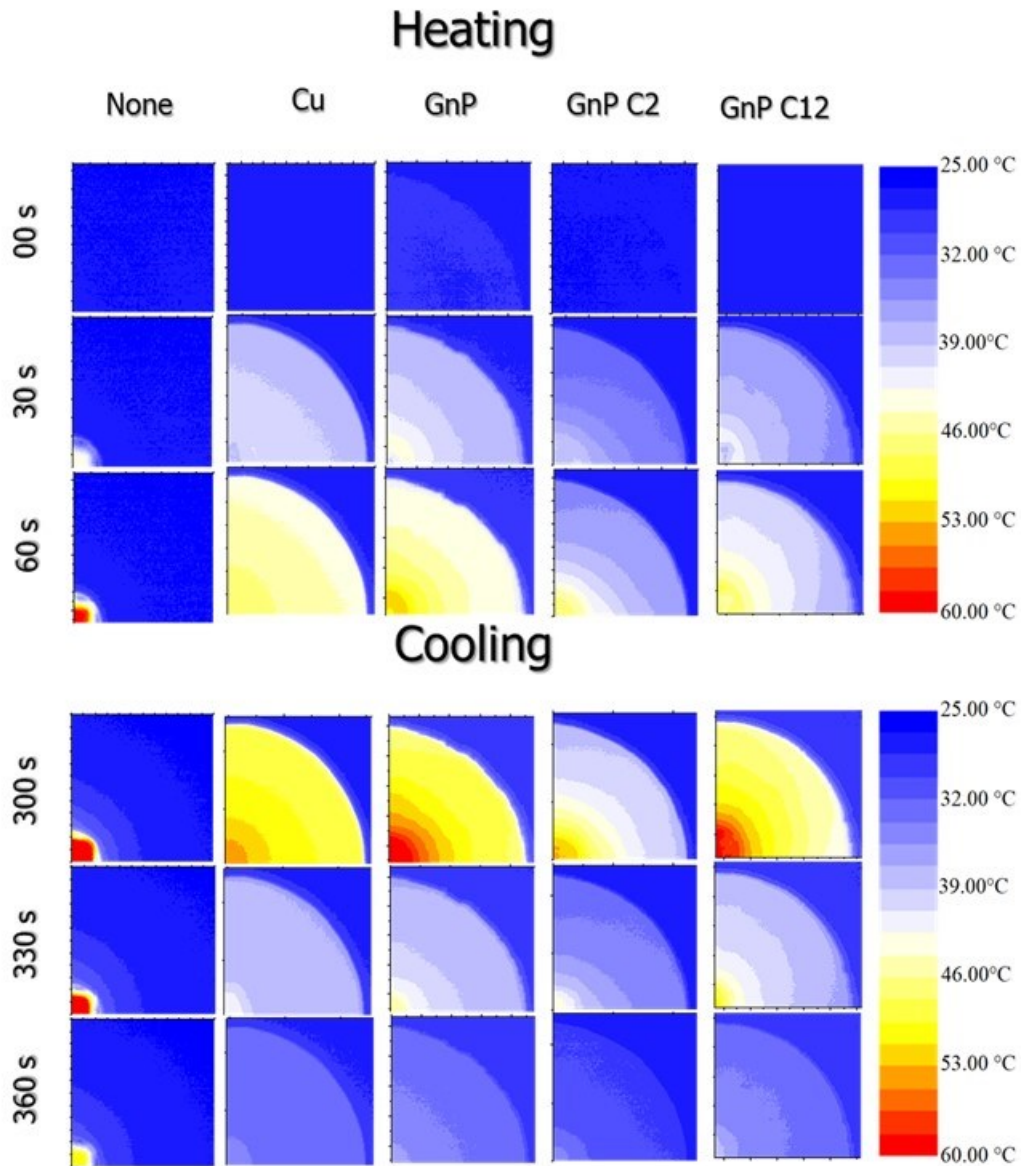


Figure 81. IR - thermal images acquired in the initial stages of heating (0.30 seconds and 60 seconds respectively) and cooling (300, 330 and 360 seconds) for comparing the thermal gradients of systems in which there are heat spreaders fabricated with different materials.

The thermal maps obtained at 300 s (Figure 82 a) were analysed to calculate the thermal gradient on the foil vs. the radial coordinate. Such temperature profile was extracted from temperature maps along long three different directions in order to obtain a representative average (Figure 82 b), that was fitted with an exponential decay function, for all the different heat spreader (Figure 82 c). It is apparent that Cu has significantly lower temperature gradient over the surface, yielding a lower decay rate (R_0) in the radial temperature plot, compared to GnP nanopapers. This may be explained by the higher density of the metal film, allowing a more efficient distribution of heat over the surface, according to thermal conductivity values. Moreover, for nanopapers (C4-C12), there is an increasing trend in the heat transfer decay rate value, indicating when longer BP are used to contact thermally the GnP,

the heat distribution become lower and lower . In addition, for C8 and C12 nanopapers, values of 0.229 and 0.259 are obtained, respectively, which are higher than the GnP pristine nanopaper (0.217).

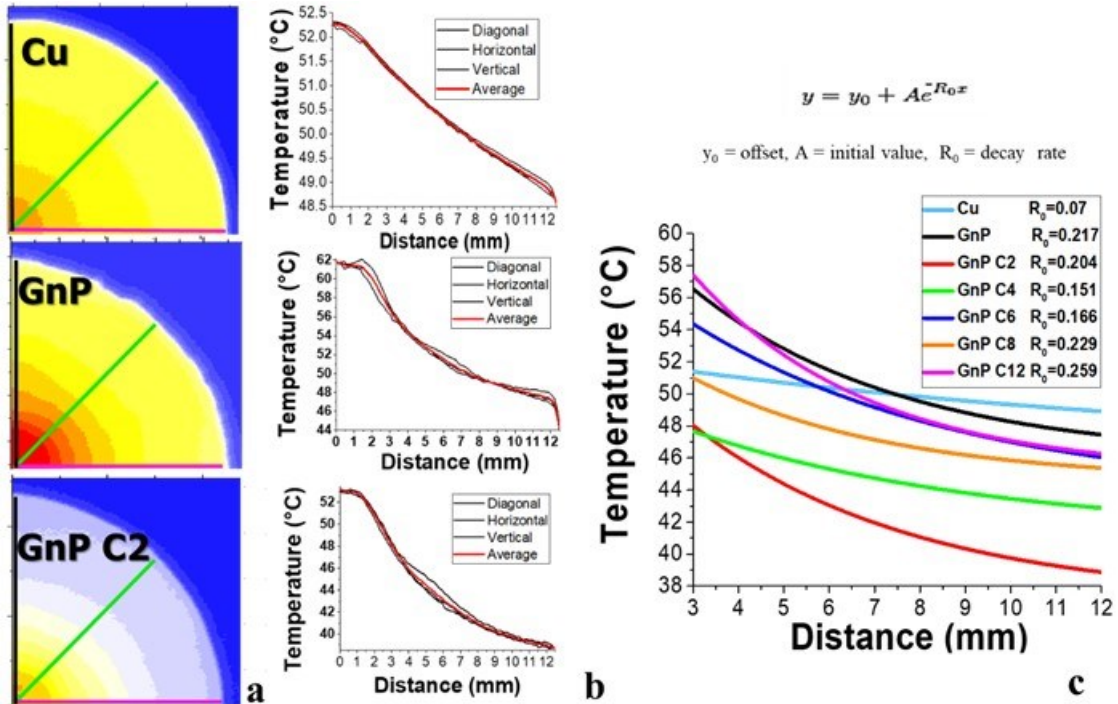


Figure 82. Thermal gradient's comparison between Copper and heat spreaders based on pristine GnP and GnP C2 one. a) Thermal imaging at 300 seconds of selected heat spreader in order to extrapolate the temperature values. b) Average calculate long three direction for each sample. (c) Comparison between the thermal gradient fitted with exponential decay curves and relative decay rate values.

However, this trend do not totally correspond to the thermal conductivity or to the plateau temperatures values, especially for the GnP C2 nanopaper, suggesting that that porosity of the nanopaper and its high specific surface area play an important role in the heat dissipation from the heat spreader to the surrounding air.

Compared to a smooth surface, indeed, a rough surface improves phase change heat transfer by increasing the net contact area for heat transfer [256].

For example, in common materials, surface treatments (sandpapering or abrasive blasting [257]) are normally carried out to create relatively simple structures, i.e. consisting essentially of low peaks and valleys, and distributed randomly or more specific processes (lithography or electrochemical methods) can create complex and regular structures [258]. This is due to the direct proportionality between the heat exchanged and the area of exchange surface, as shown in the definition of the heat transferred by convection in which:

$$Q=h \cdot A \cdot (T_1-T_2)$$

Where Q is the convective heat transfer, h, is the convective heat transfer coefficient, A is the surface area of exchange, T₁ is the surface temperature and T₂ is the temperature of surrounding.

A study was carried out to look for a model that described the system by combining the effect of the conduction of the material with its ability to transfer heat to surrounding by convection. Among the various types of approaches that involve the heat transfer between a hot system and a medium, that one in which the heat exchange surface is increased by fins, was chosen. Moreover, in literature there are different fin configurations (such as longitudinal, radial and spines) and each of them includes the study of the geometry system (rectangular, circular, cusps) in order to describe it with specific equations [115]. Therefore the nanopaper were considered as a radial fin with a rectangular profile (more detail in chapter 2.5) that cool a central heat flow (as shown in the Figure 83).

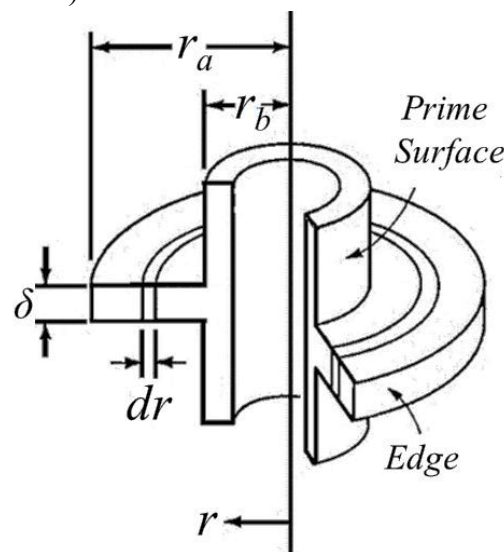


Figure 83. Approach of a finned surface applied to nanopapers. a) Experimental set-up. b) Radial fin with rectangular profile.

According to the classic approach, the general differential equation that describe these phenomena is

$$r^2 \frac{d^2\theta}{dr^2} + r \frac{d\theta}{dr} - m^2 r^2 \theta = 0 \quad \text{In which} \quad m = \left(\frac{2h}{k\delta} \right)^{1/2} \quad \text{and} \quad \theta = T - T_s$$

Where: **m** is the fin performance factor (m^{-1}), **h** is the heat transfer coefficient ($Wm^{-2}K^{-1}$), **k** is the thermal conductivity ($Wm^{-1}K^{-1}$), **δ** is the thickness (mm) of the fin, **θ** is the difference of measured temperature (**T**) and **T_s** which is the room temperature ($^{\circ}C$). Because this equation is Bessel's modified equation, which has a solution in terms of the modified Bessel functions $\theta(r)$, these function were used to fit the average curve obtained extrapolating the thermal gradient on the foil vs. the radial coordinate from 300 s thermal imagine (Figure 84).

In evaluating the heat transfer performance of surfaces enhanced by the presence of fins, the convective heat transfer coefficient **h** is clearly an important quantity. Fins are particularly effective under conditions where the controlling thermal resistance

is due to convection (where the coefficient h is relatively small [115]). From the results (Figure 84 c), the values of heat transfer coefficient can be compared, therefore both of nanopaper show lower values (GnP pristine is equal to $10.1 \text{ Wm}^{-2}\text{K}^{-1}$ and GnP C2 is equal to $16.0 \text{ Wm}^{-2}\text{K}^{-1}$) than copper ($23.8 \text{ Wm}^{-2}\text{K}^{-1}$) indicating how their surface exchanges higher heat with the environment.

In the engineering of finned surfaces, the parameter that includes both the contribution of thermal conductivity and convection is the fin performance factor (m) and so by analysing, it can be observed that both GnP pristine and GnP C2 nanopapers whose values of 81 m^{-1} and 96.6 m^{-1} respectively, are higher than copper one (56.8 m^{-1}), indicating how nanopapers are more performing as heat spreader compared to copper.

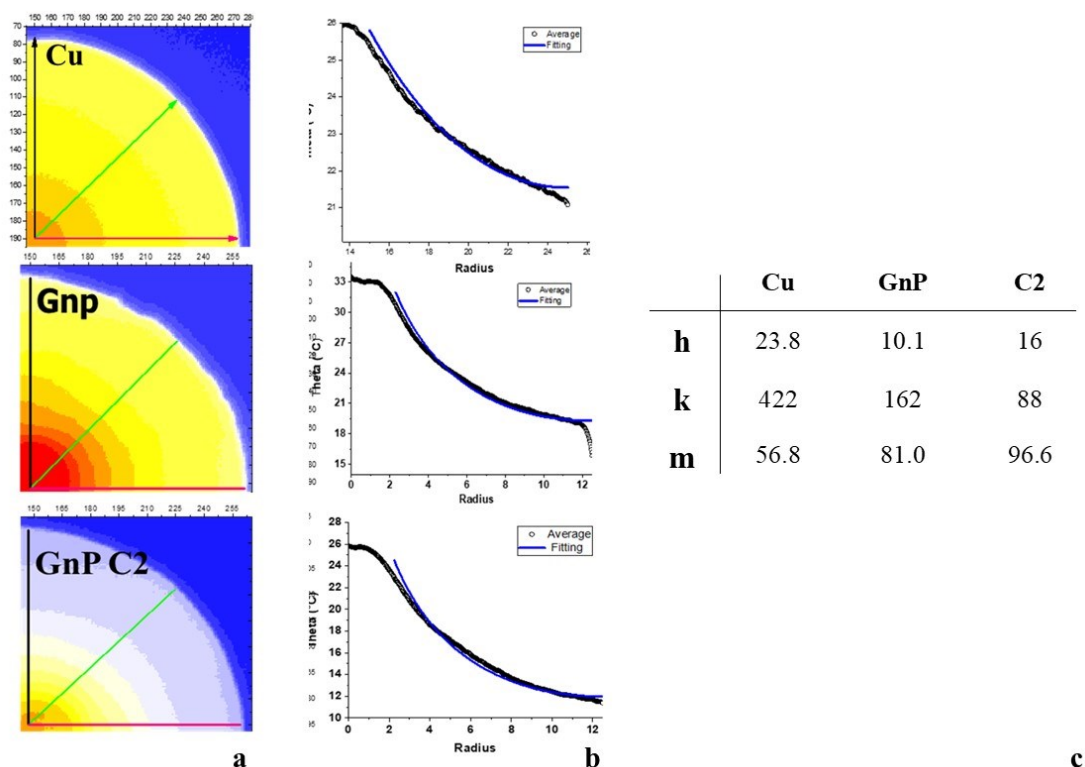


Figure 84. a) Thermal maps at 300 s. b) average of the experimental thermal gradient (black curve) and the fitting of the differential equation of Bessel function (blue curve). c) Comparison between parameters of fins made with copper and those carbons based.

In conclusion, although the conductivity of the fin containing C2 ($90 \text{ Wm}^{-1}\text{K}^{-1}$) is lower than that of copper ($370 \text{ Wm}^{-1}\text{K}^{-1}$), its performance is superior as heat spreader, thanks to a larger surface area (in relation to its roughness), which favours heat exchange by convection. In addition it should be considered that, at the same geometry there is a 90% weight reduction (related to the different density of materials) which may open for potential application in a number of lightweight and flexible devices.

Chapter 6

General conclusions

This PhD thesis focused on the exploitation of GRM for the preparation of thermally conductive nanopapers for applications where heat dissipation is required.

GRM have been selected as raw material because they have a lower density compared to commonly used metals (such as copper and aluminum) and higher corrosion resistance.

Because the heat transfer is influenced by the aromatic structure, where the carbon atoms have a sp^2 hybridization, an interruption of the conjugation of the covalent bonds dramatically influences the thermal properties. So, it is possible to distinguish chemical defects related to the presence of carbon atoms sp^3 hybridized or physical defects such as the presence of vacancies or the edges of the flake.

Among GRM, graphite nanoplatelets with lateral size in the range of a few microns and thickness of a few nanometers were chosen as raw material both to reduce the problem of the presence of chemical defects in the structure and because they have a relatively low cost.

Nanopapers are the macroscopic result of an overlapping of several graphite nanoplatelets, so there is a problem of thermal resistance at the interface on which the efficiency of heat transmission depends. Therefore, to increase the transfer of phonons, graphite nanoplatelets have been functionalized using two different approaches. The first one exploits a supramolecular interaction (π - π stacking) between the aromatic polycyclic and the surface of the graphene while the second one uses a defect functionalization to covalently connect the structures.

For supramolecular functionalization, a new family of molecules derived from pyrene has been synthesized. In particular, bispyrene molecules were designed to bring two terminal pyrene groups, as anchor groups with the graphite surface, spaced by an aliphatic chain with variable length.

The synthesis occurred between a 1-pyrenebutyric acid and aliphatic diamines of different length. The reaction was carried out by first converting the carboxylic group into its chloride. This brought significant advantages both in terms of greater reactivity in the subsequent reaction with the amino group, and because it was possible to use a solvent in which the reagents were soluble, while the products were not and could be collected by simple precipitation. In this way, it was possible to avoid subsequent product purification steps that are very common for these organic synthesis, thus making this synthesis economically sustainable, scalable and industrially viable.

From nuclear magnetic resonance spectroscopy analysis it was possible to obtain qualitative and quantitative information on the purity of the products, which were confirmed by liquid chromatography coupled mass spectroscopy analysis.

Solutions in dimethylformamide solvent at different molecule concentrations have been used to disperse graphite nanoplatelets by ultra-sonication to evaluate the degree of functionalization. By comparing the photoluminescence measurements between the suspensions with the respective initial solutions, formation of bispyrene molecular aggregates was confirmed, in competition with their absorption by graphite nanoplatelets. After the suspensions were filtered, by ultraviolet-visible analysis the concentration of remaining into filtrated solutions was quantified and then by difference with the initial one, the concentration adsorbed by graphite nanoplatelets was obtained. For the higher initial concentrations (10^{-4} and 10^{-5} M) only a small part is retained by the graphite nanoplatelets (9% and 55% respectively), whereas most of the BP was adsorbed by GnP when using a 10^{-6} M initial concentration (78%). Based on these results, the 10^{-6} M concentration was selected to disperse the nanoplatelets with the other bispyrene and then evaluate if the chain length between the pyrene groups influences the functionalization.

About the covalent functionalization at the edges of graphite nanoplatelets, the cycloaddition reaction (Diels-Alder) in which graphene behaves as diene and a molecule derived from maleic anhydride behaves as dienophile, was chosen, based on the promising literature reports. The bismaleimide molecules were obtained through the reaction between maleic anhydride and aliphatic diamines with different chain lengths in two steps. The first step occurred in a low-boiling solvent in which the reagents were soluble while the products were not, so that the products could be collected by simple filtration. The diacid products of the first step were characterized by nuclear magnetic resonance spectroscopy, demonstrating their purity. The second step of the reaction occurred by an intramolecular condensation between the carboxylic group and the amino group with consequent restoration of the five-member ring and formation of maleimide. Nuclear magnetic resonance spectroscopy and Fourier transform infrared results showed that the reactions for the shorter bismaleimide I2-I4 not occurred, while for the I6-I8 it partially occurred but only the I12 was obtained with high purity.

I12 was used for the functionalization of graphite nanoplatelets using two different concentrations that were compared with those of graphite nanoplatelets functionalized with maleic anhydride. The highest was made with a ratio 1 to 1 in weight between GnP with BI, while the lowest was made with a ratio 1 to 0.1. The results obtained by thermo gravimetric analysis showed that the functionalization with I12 occurred more than maleic anhydride and in particular, for high I12 initial concentration, as much as 30% weight of organic functionalization was obtained. The comparison between the Raman analysis of I12 graphite nanoplatelets with those functionalized with MA and that one pristine, confirmed that functionalization was occurred because I12 is covalently linked to graphite nanoplatelets. Both graphite nanoplatelets functionalized with bispyrene and bismaleimide were used to manufacture nanopapers using the gravimetric filtration method through a membrane, similar to the papermaking process, referred to as nanopapers.

Morphological analysis was performed using field emission scanning electron microscope which provided information on both surface topography and from the analysis of the section where it was possible observed a preferential alignment of graphite nanoplatelets. It was also possible to measure the thickness of the nanopapers with which the densities were experimentally calculated obtaining significant differences between nanopapers manufactured with different bispyrene. To further investigate GnP flakes organization, a study was carried out to evaluate the orientation of the flakes within the nanopapers using X-ray diffraction, monitoring the 002 signal of the graphite at different tilt angle with respect to the nanopaper plane. In this way it was possible affirm that the bispyrene functionalization influence the density related to displacement of the flakes within the nanopaper. Indeed, during functionalization, the molecules destabilize the suspension (according to the UV-Vis analysis) and the functionalized GnP is placed more randomly contrary to GnP pristine.

Nanopapers were characterized by light flash analysis to provide information on the thermal diffusivity of the material. It was possible affirm that as the size of bispyrene increases, the effectiveness of the thermal bridge decreases and therefore the ability to transmit heat from one graphite nanoplatelets to another.

Indeed, if the GnP pristine nanopaper showed $175 \text{ mm}^2\text{s}^{-1}$ in plane and $0.4 \text{ mm}^2\text{s}^{-1}$ cross plane thermal diffusivity respectively, for nanopaper with GnP C2, thermal diffusivity values of $203 \text{ mm}^2\text{s}^{-1}$ in plane and $2.3 \text{ mm}^2\text{s}^{-1}$ cross-plane were obtained. Nanopaper GnP C12 based, on the other hand, similar values are obtained in plane ($173 \text{ mm}^2\text{s}^{-1}$) and slightly higher values for cross plane ($0.6 \text{ mm}^2\text{s}^{-1}$). In any case these values are much higher than those of aluminium and copper, which have a thermal diffusivity of $97 \text{ mm}^2\text{s}^{-1}$ and $107 \text{ mm}^2\text{s}^{-1}$ respectively, so the manufactured nanopapers transfer heat faster than metals.

On contrary, for nanopapers obtained from graphite nanoplatelets functionalized with I12, lower thermal diffusivity values were obtained compared to both functionalized with maleic anhydride and those manufactured with graphite nanoplatelets with bispyrene. The excess functionalization probably decrease the contact area between graphite nanoplatelets with consequent increase in thermal resistance.

The thermal conductivity values of the graphite nanoplatelets nanopapers were measured but, on the other hand, as nanopapers with different organic functionalization are characterized by different degree of porosity, in order to compare the thermal conductivity of the different materials, the effect of nanopaper density was investigated. Different models were considered in order to calculate the conductivity of the continuous phase within nanopapers that were compared to the experimental result obtaining a correspondence with the linear model. The highest thermal conductivity values of continuous phase of 318 and $299 \text{ Wm}^{-1}\text{K}^{-1}$ were obtained for GnP C2 and GnP C4 nanopaper, respectively, compared to $273 \text{ Wm}^{-1}\text{K}^{-1}$ for pristine GnP.

These values are clearly lower than Cu ($390 \text{ Wm}^{-1}\text{K}^{-1}$) but higher than Al ($290 \text{ Wm}^{-1}\text{K}^{-1}$), mostly related to their densities.

Finally, an experimental setup was designed to test the nanopapers heat spreaders, using a powered transistor as a model hotspot, simulating the overheating of an

electronic components that need to be cooled. By using a thermal imaging camera, the temperature of the hotspot was monitored, comparing the results obtained with and without heat spreader. In addition, a comparison was made with heat spreader having the same geometry that are manufactured with aluminium or copper. The comparison of hotspot temperatures demonstrated not only that all functionalized nanopapers have a higher performance than pristine graphite nanoplatelets nanopaper but also, for nanopapers containing the shortest bispyrene, a lower temperature value compared those of aluminium and copper, indicating how the heat spreader is better performing, even though the thermal conductivity value of copper is higher than for GnP nanopapers.

A classic approach to the dissipation of heat from a finned surface was applied by evaluating both the heat exchange coefficient by convection and the efficiency factor of the fin. The results obtained suggested the fin containing C2 BP to have better performance than copper due to a larger surface area, related to its roughness.

It should be further pointed out that performance obtained with GnP nanopapers was achieved in parallel with a 90% weight reduction of the fin, compared to copper, which may open for potential application in a number of lightweight a flexible device.

Appendix (i)

7.1. NMR spectra of BP

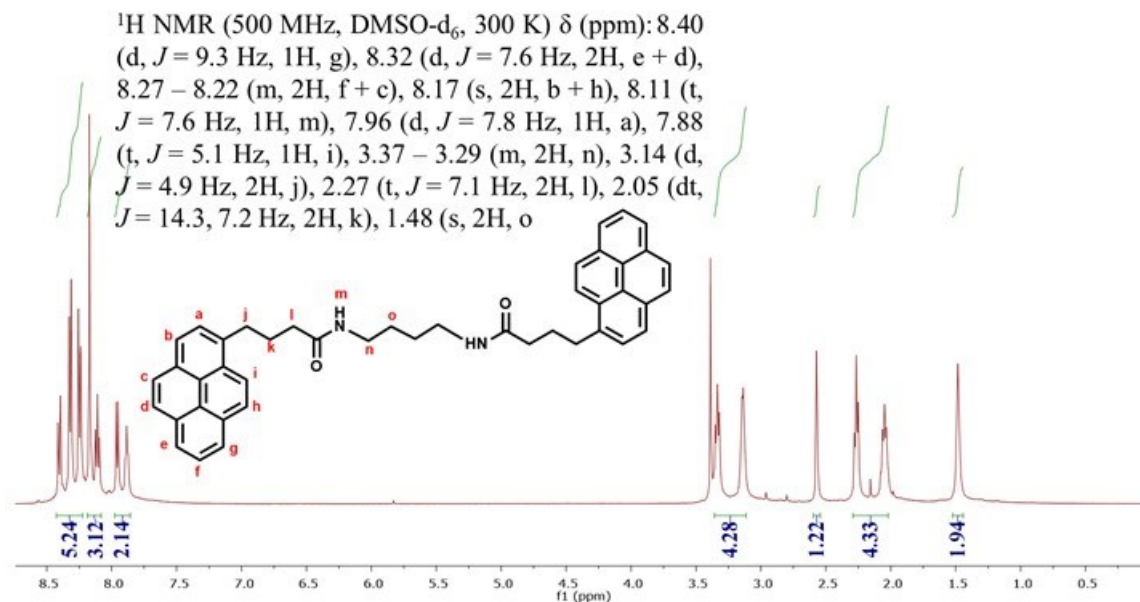


Figure 85. ¹H NMR spectrum and peak assignment of N,N'-(butane-1,4-diyl)bis(4-(pyren-1-yl)butanamide) (C4).

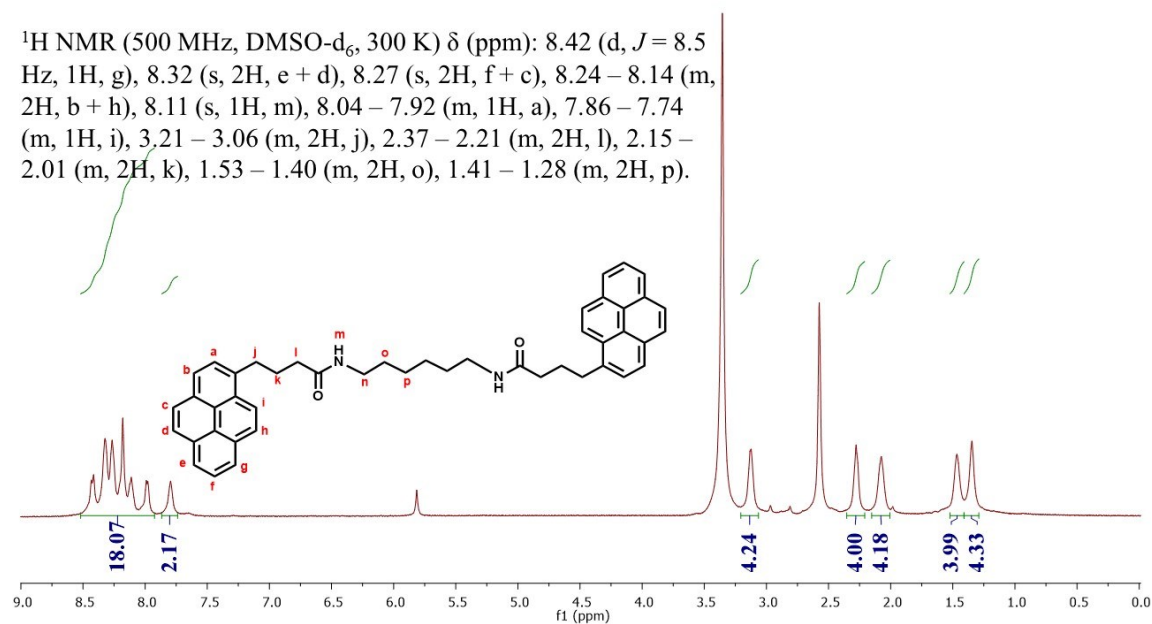


Figure 86. ¹H NMR spectrum and peak assignment of N,N'-(hexane-1,6-diyl)bis(4-(pyren-1-yl)butanamide) (C6).

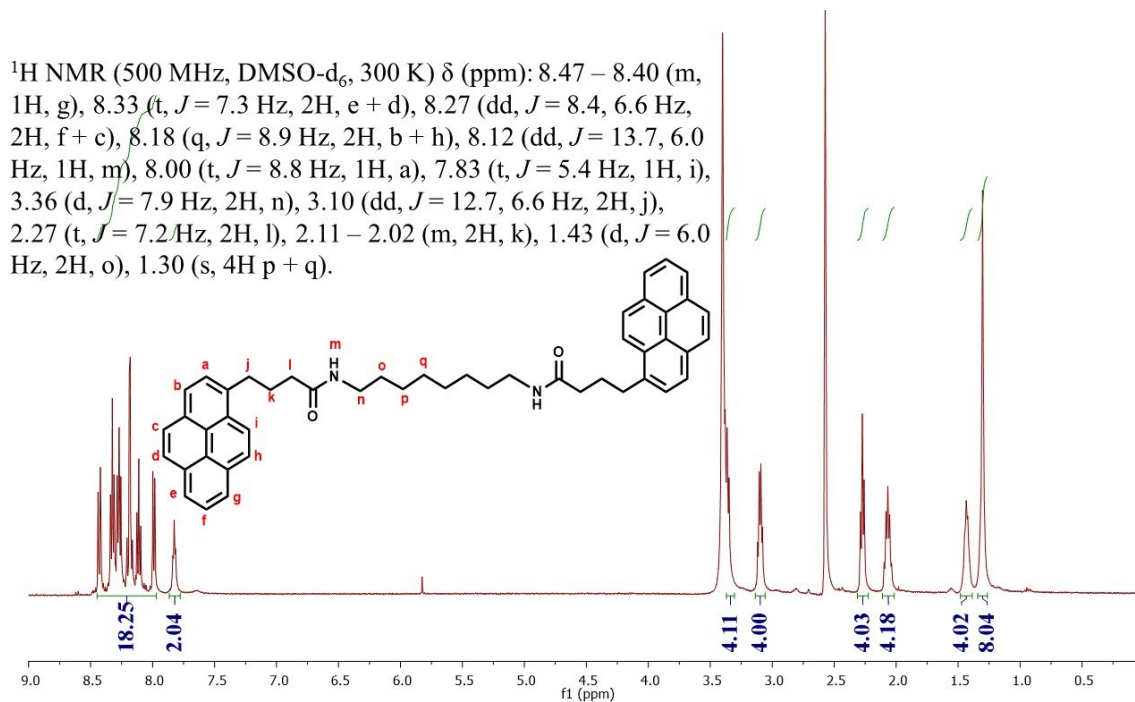


Figure 87. ^1H -NMR spectrum and peak assignment of N,N' -(octane-1,8-diyl)bis(4-(pyren-1-yl)butanamide) (C8)

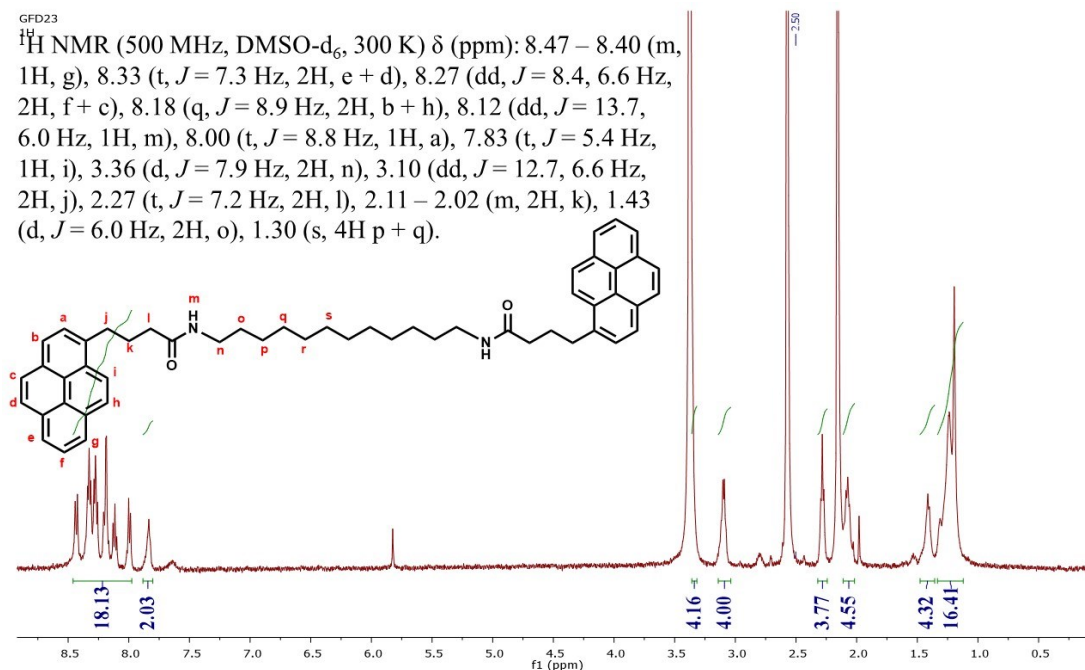


Figure 88. ^1H -NMR spectrum and peak assignment of N,N' -(dodecane-1,12-diyl)bis(4-(pyren-1-yl)butanamide) (C12).

^{13}C NMR (126 MHz, DMSO- d_6 , 300 K) δ (ppm): 172.14, 127.99, 127.28, 126.94, 126.58, 125.30, 124.64, 123.93, 40.50, 40.34, 39.93, 39.70, 39.59, 38.68, 35.47, 32.71, 28.05, 27.25.

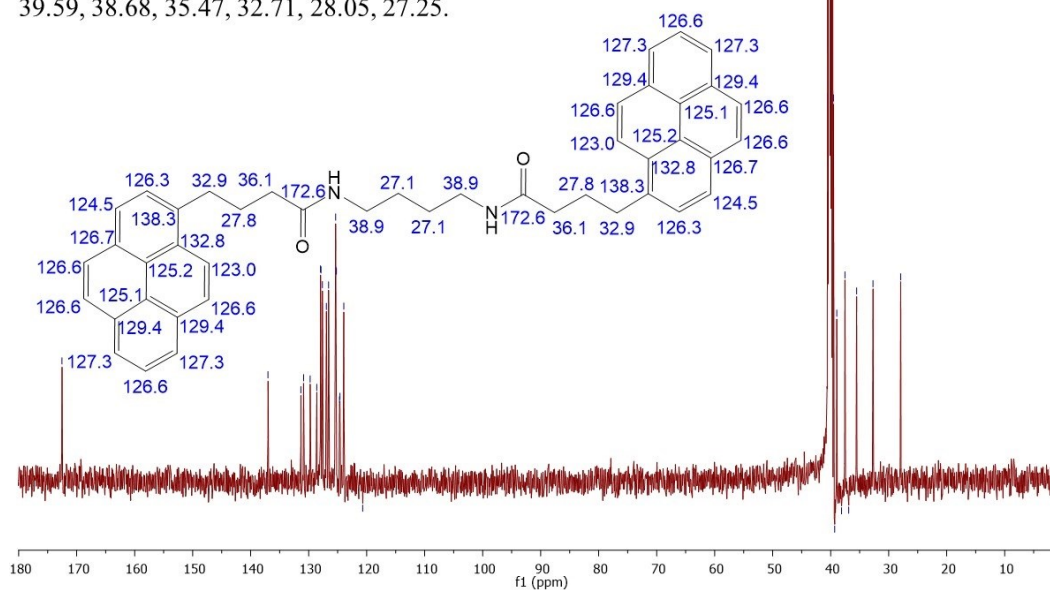


Figure 89. ^{13}C -NMR spectrum of C4. Comparison between ppm measured experimentally (black) and those extrapolated by software (blue).

^{13}C NMR (126 MHz, DMSO- d_6 , 300 K) δ (ppm): 172.11, 148.72, 137.03, 131.37, 130.91, 129.77, 128.64, 127.93, 127.90, 127.64, 126.94, 126.56, 125.37, 125.22, 124.73, 124.65, 123.93, 55.35, 38.86, 35.52, 32.69, 29.64, 28.03, 26.62.

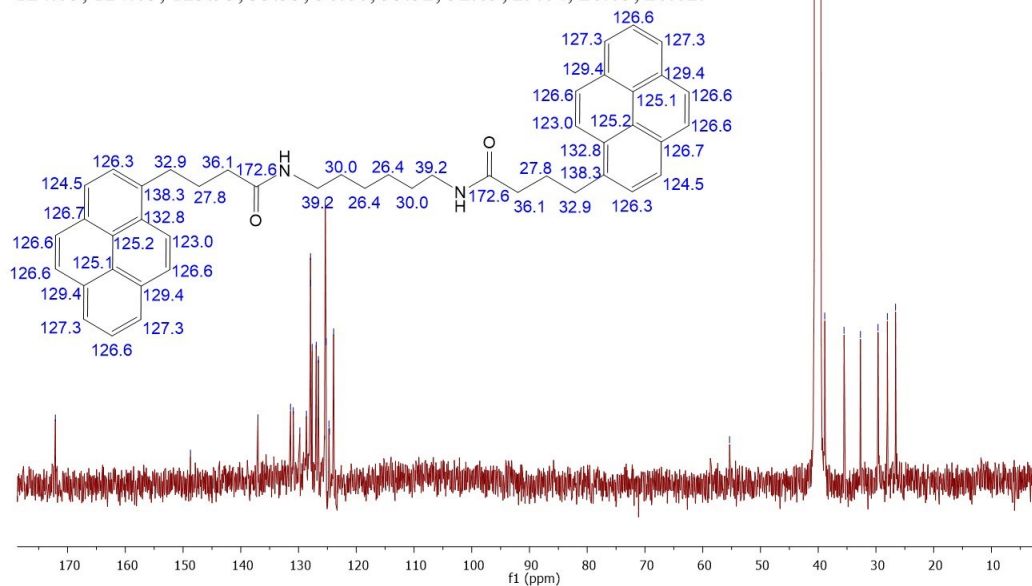


Figure 90. ^{13}C -NMR spectrum of C6. Comparison between ppm measured experimentally (black) and those extrapolated by software (blue).

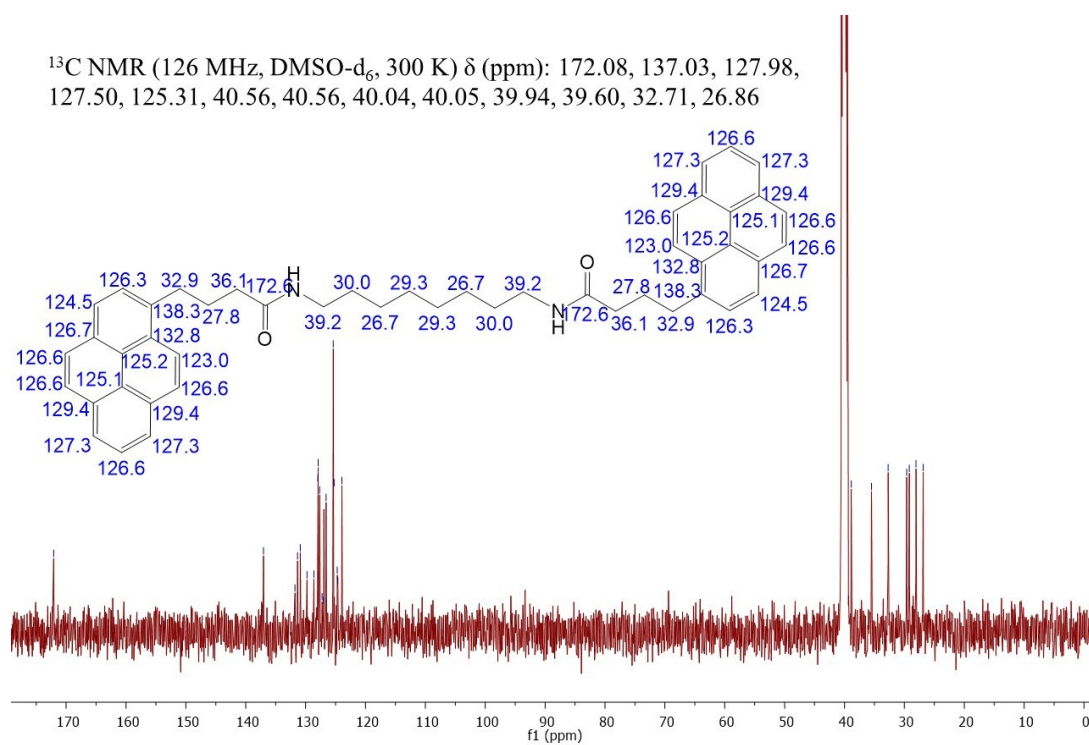


Figure 91. ^{13}C -NMR spectrum of C8. Comparison between ppm measured experimentally (black) and those extrapolated by software (blue).

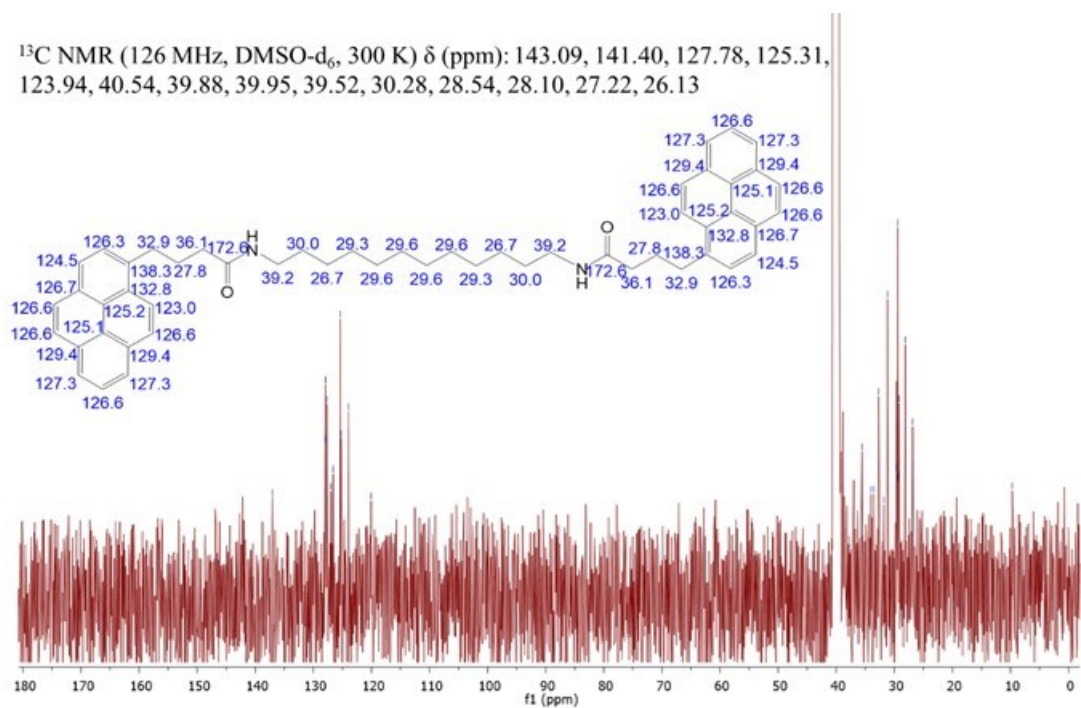


Figure 92. ^{13}C -NMR spectrum of C12. Comparison between ppm measured experimentally (black) and those extrapolated by software (blue).

7.2. NMR Spectra of BI

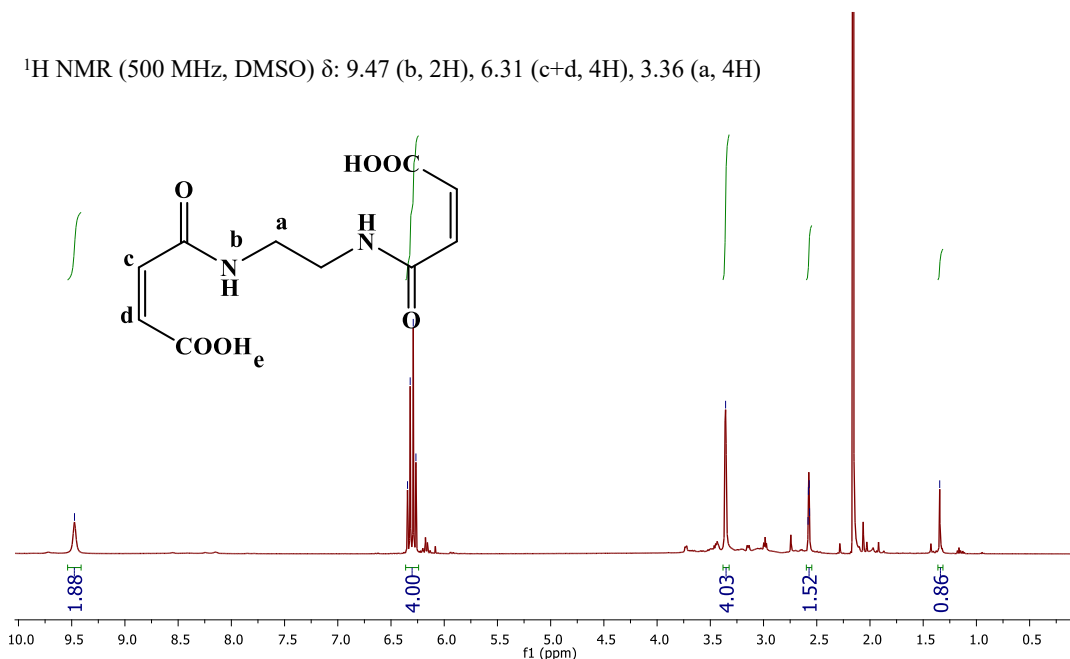


Figure 93. ^1H -NMR spectrum of (2Z,2'Z)-4,4'-(ethane-1,2-diylbis(azanediyl))bis(4-oxobut-2-enoic acid) (N2).

Figure 94 shows the ^1H -NMR spectrum of molecule N4 and according to the assignment of peaks and their integral, the product can be considered pure. However, the yield of the reaction is a bit lower than before and is equal to 75 %.

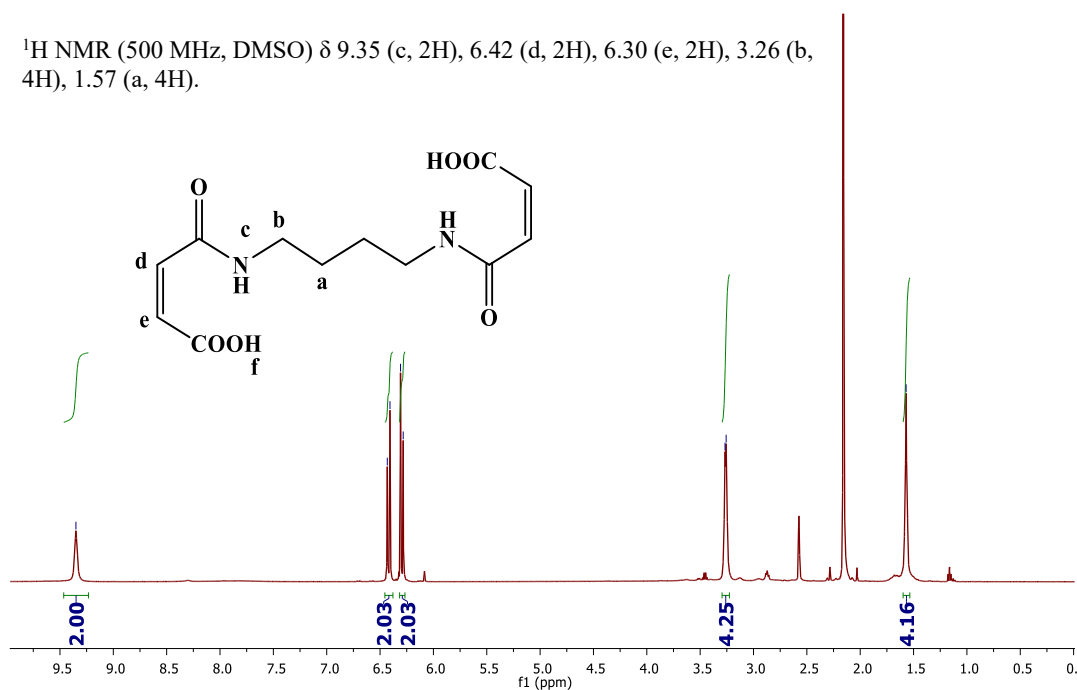


Figure 94. ^1H -NMR spectrum of (2Z,2'Z)-4,4'-(butane-1,4-diylbis(azanediyl))bis(4-oxobut-2-enoic acid) (N4)

$^1\text{H-NMR}$ spectrum related to the N6 molecule (Figure 95) appears different from those seen previously because the analysis was carried out with deuterated chloroform (signal at about 7.23 ppm) and therefore the chemical shifts are slightly different. About the assignment of peaks, all signals find a response except for the double bonded protons whose signals would be at the same chemical shift as the solvent. Although small peaks are present, related to diethyl ether in traces.

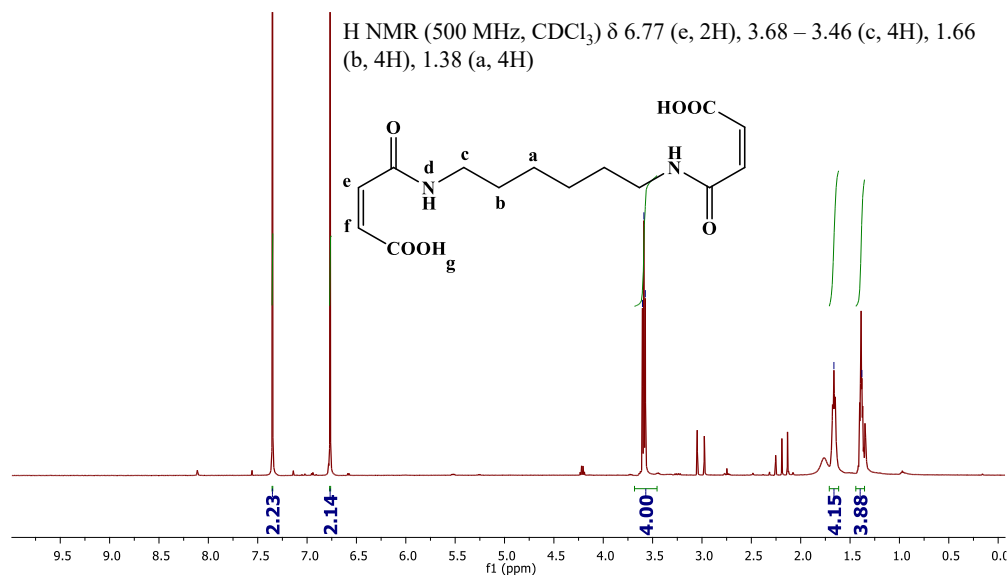


Figure 95. $^1\text{H-NMR}$ spectrum of (2Z,2'Z)-4,4'-(hexane-1,6-diylbis(azanediyl))bis(4-oxobut-2-enoic acid) (N6).

Figure 96 shows the $^1\text{H-NMR}$ spectrum of N8 in which the integrals of the peaks find a perfect correspondence with protons signals of the molecule so it is possible to assume that the compound is chemically pure and therefore the yield of the reaction was 80%.

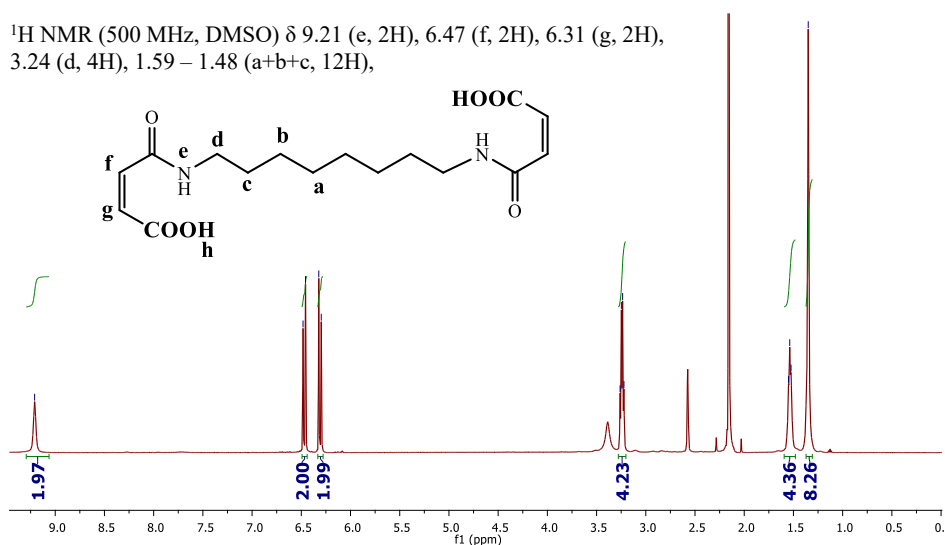


Figure 96. $^1\text{H-NMR}$ spectrum of (2Z,2'Z)-4,4'-(octane-1,8-diylbis(azanediyl))bis(4-oxobut-2-enoic acid) (N8).

The spectrum of the N12 molecule shown in the Figure 97 indicates that the compound is pure. In fact, there is a precise correspondence between the peaks of the spectrum (and its integrals) and the signals of the protons of N12. The two peaks at 3.33 ppm and 2.6 ppm, instead, correspond to traces of water and the non-deuterated DMSO which are common impurities of DMSO-d₆[259]. The reaction had a yield of 70%.

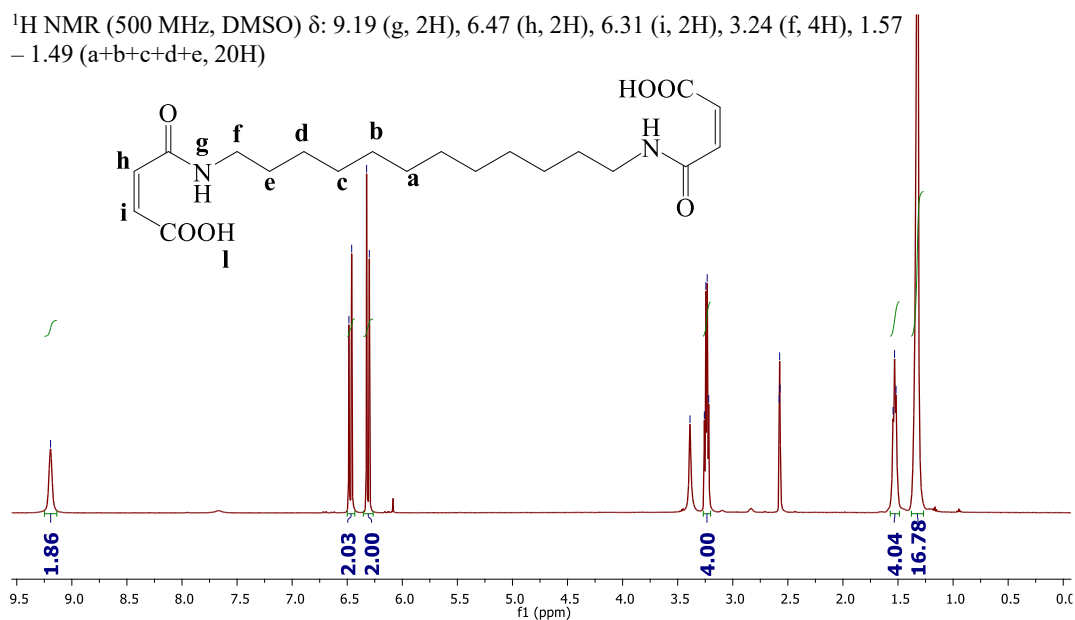


Figure 97. ¹H-NMR spectrum of (2Z,2'Z)-4,4'-(dodecane-1,12-diylbis(azanediyl))bis(4-oxobut-2-enoic acid) (N12).

7.3. NMR spectra of MP

^1H NMR (500 MHz, CDCl_3) δ 8.39 (d, $J = 9.2$ Hz, 1H, s), 8.25 (dd, $J = 7.6, 3.3$ Hz, 3H, u-w), 8.20 (s, 2H, x+r), 8.12 (d, $J = 1.7$ Hz, 3H, q+y+t), 7.96 (d, $J = 7.7$ Hz, 1H, m), 3.55 – 3.44 (m, 4H, p+l), 2.61 (t, $J = 7.2$ Hz, 2H, n), 2.32 – 2.29 (m, 2H, o), 1.58 – 1.19 (m, 20H, b-k), 0.96 (dd, $J = 12.6, 6.9$ Hz, 3H, a).

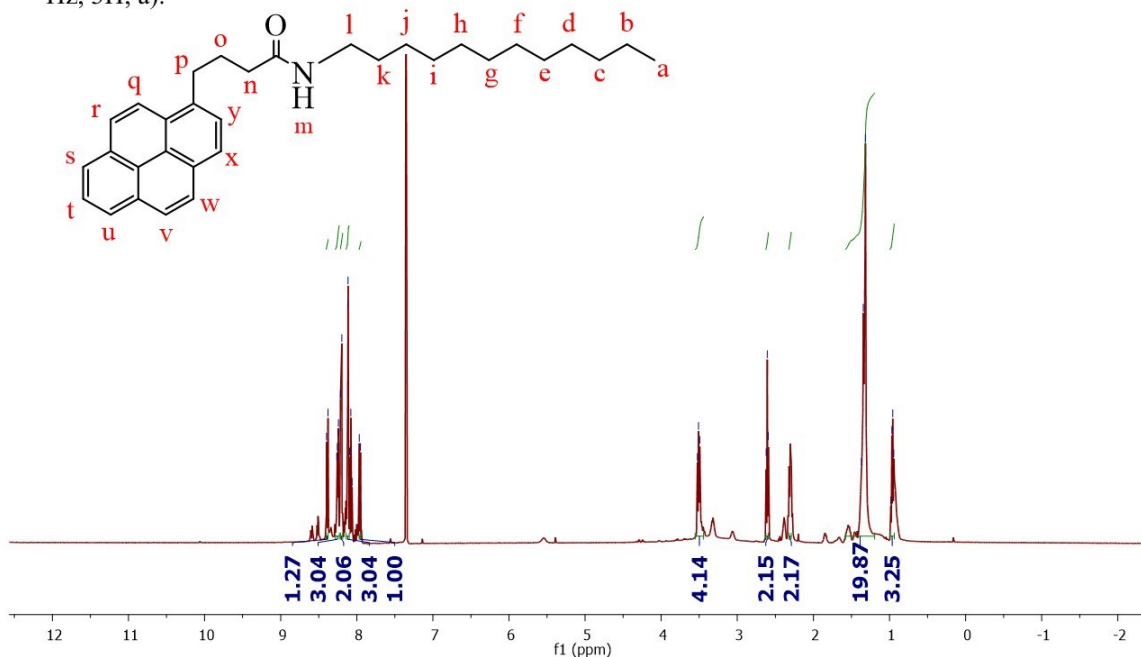


Figure 98. ^1H -NMR spectrum of N-dodecyl-4-(pyren-1-yl)butanamide.

^{13}C NMR (126 MHz, CDCl_3) δ 177.77, 135.49, 131.42, 130.90, 130.04, 128.80, 128.75, 128.01, 127.49, 127.38, 126.77, 125.88, 125.54, 124.96, 124.82, 123.39, 123.26, 39.74, 33.27, 32.68, 31.92, 30.08, 29.63, 29.55, 29.36, 29.30, 28.98, 27.51, 26.93, 26.52, 22.70, 14.14.

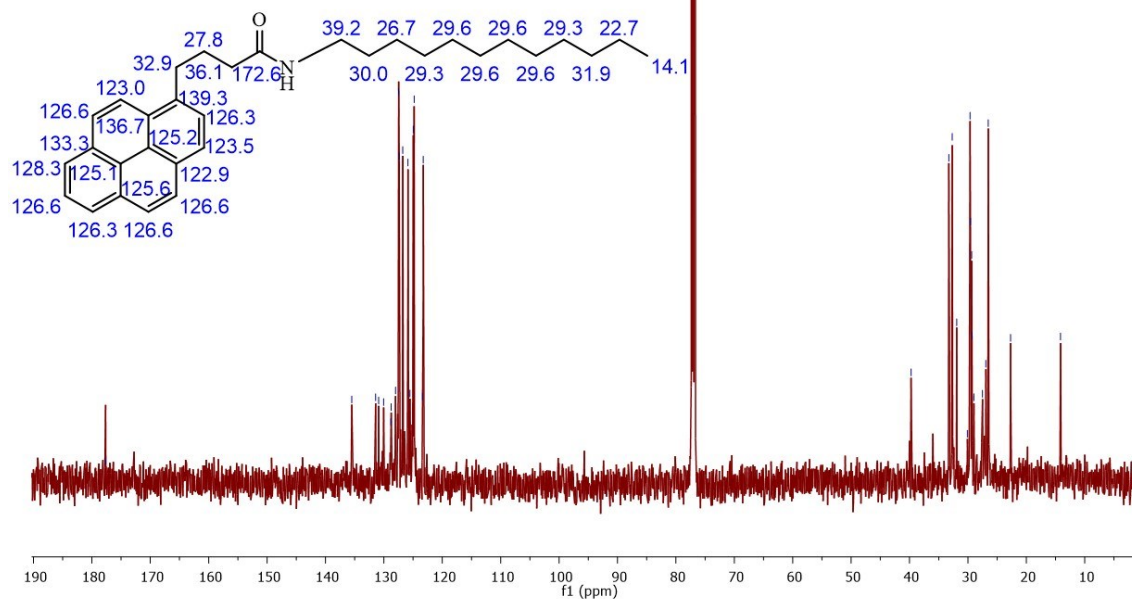


Figure 99. ^{13}C -NMR spectrum of N-dodecyl-4-(pyren-1-yl)butanamide.

7.4. Nanopaper with MP

The surface topographies of the nanopapers manufactured with GnP functionalized with MP give an indication about the functionalization effects onto flakes. In fact, the nanopaper with Py-COOH (Figure 100 a) shows a non-homogeneous surface indicates that the molecules are not regularly spread on it contrary to nanopaper with Py-CONH (Figure 100 c) in which the surface is completely covered.

FESEM analyses were also carried out on cross-section to evaluate the effect of functionalization on alignment of the flakes. Nanopaper with Py-COOH (Figure 100 b) shows greater flakes alignment but less compactness than those with Py-CONH (Figure 100 d) and by measurement of the thickness, the densities of the nanopapers were calculated obtaining 0.85 g/cm^3 for GnP functionalized with Py-COOH and 0.92 g/cm^3 for nanopaper with Py-CONH, confirming that functionalization with Py-CONH promotes a more orderly arrangement of the flakes during the gravimetric filtration process.

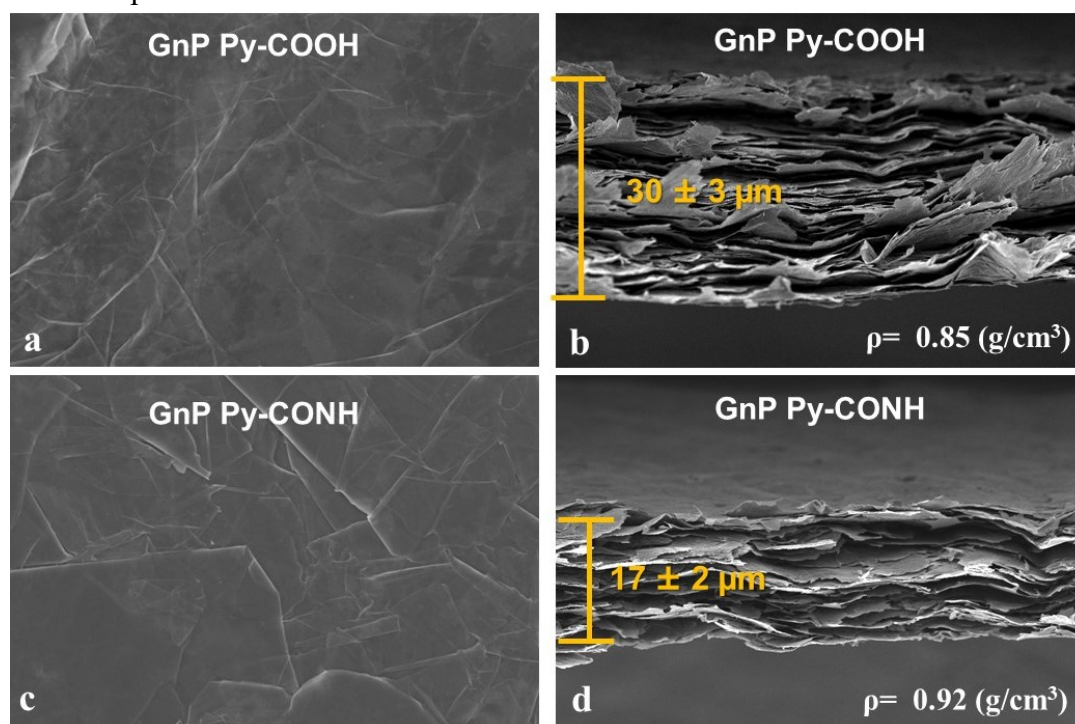


Figure 100. FESEM Analysis of nanopapers manufactured with GnP functionalized with MP molecules. a) Surface topography of nanopaper manufactured with GnP Py-COOH. b) Cross section analysis of GnP Py-COOH film. c) Surface topography of nanopaper fabricated with GnP Py-CONH. b) Cross section measurement of GnP Py-CONH film.

To quantify the amount of MP molecules effectively adsorbed within nanopaper the filtrate solution (after gravimetric filtration) were analysed by UV-Vis in order to calculate the concentration of Py-COOH and Py-CONH to be used to indirectly calculate the fraction of both MP adsorbed onto GnP, given the known initial concentration in the GnP suspensions.

As shown in **Table 10**, the fraction of adsorbed monopyrene is 87 % and 85 % of the initial concentration for GnP Py-COOH and GnP Py-CONH, while the mass

fraction of 0.08% was obtained from a Py-COOH and 0.14% for Py-CONH, respectively.

Sample	MP concentration in filtered solution [M]	Fraction of MP adsorbed on GnP [%]	Mass fraction of MP in nanopaper [%]
Py-COOH	$0.13 \cdot 10^{-6}$	87	0.08
Py-CONH	$0.15 \cdot 10^{-6}$	85	0.14

Table 10. Calculation of the mass fraction and mass of MP absorbed within nanopaper.

References

- [1] K.S. Novoselov, A.K. Geim, S.V. Morozov, D. Jiang, Y. Zhang, S.V. Dubonos, I.V. Grigorieva, A.A. Firsov, Electric field effect in atomically thin carbon films, *Science* 306(5696) (2004) 666-9.
- [2] A. Bianco, H.-M. Cheng, T. Enoki, Y. Gogotsi, R.H. Hurt, N. Koratkar, T. Kyotani, M. Monthieux, C.R. Park, J.M.D. Tascon, J. Zhang, All in the graphene family – A recommended nomenclature for two-dimensional carbon materials, *Carbon* 65 (2013) 1-6.
- [3] A.K. Geim, K.S. Novoselov, The rise of graphene, *Nat Mater* 6(3) (2007) 183-91.
- [4] Y. Liu, A. Dobrinsky, B.I. Yakobson, Graphene edge from armchair to zigzag: the origins of nanotube chirality?, *Phys Rev Lett* 105(23) (2010) 235502.
- [5] A.A. Balandin, Thermal properties of graphene and nanostructured carbon materials, *Nat Mater* 10(8) (2011) 569-81.
- [6] H. He, J. Klinowski, M. Forster, A. Lerf, A new structural model for graphite oxide, *Chemical Physics Letters* 287(1-2) (1998) 53-56.
- [7] A Review on Lattice Defects in Graphene: Types, Generation, Effects and Regulation, *Micromachines* 8(5) (2017) 163.
- [8] M. Henini, *Molecular Beam Epitaxy*, 2018.
- [9] A.L. Vazquez de Parga, F. Calleja, B. Borca, M.C. Passeggi, Jr., J.J. Hinarejos, F. Guinea, R. Miranda, Periodically rippled graphene: growth and spatially resolved electronic structure, *Phys Rev Lett* 100(5) (2008) 056807.
- [10] A.G. Crevillen, A. Escarpa, C.D. García, Chapter 1 Carbon-based Nanomaterials in Analytical Chemistry, *Carbon-based Nanomaterials in Analytical Chemistry*, The Royal Society of Chemistry 2019, pp. 1-36.
- [11] C. Mattevi, H. Kim, M. Chhowalla, A review of chemical vapour deposition of graphene on copper, *J. Mater. Chem.* 21(10) (2011) 3324-3334.
- [12] J.A. Venables, G.D.T. Spiller, M. Hanbucken, Nucleation and growth of thin films, *Reports on Progress in Physics* 47(4) (1984) 399-459.
- [13] I.V. Antonova, Chemical vapor deposition growth of graphene on copper substrates: current trends, *Physics-Uspekhi* 56(10) (2013) 1013-1020.
- [14] J.S. Bunch, S.S. Verbridge, J.S. Alden, A.M. van der Zande, J.M. Parpia, H.G. Craighead, P.L. McEuen, Impermeable atomic membranes from graphene sheets, *Nano Lett* 8(8) (2008) 2458-62.
- [15] J. Jang, M. Son, S. Chung, K. Kim, C. Cho, B.H. Lee, M.H. Ham, Low-temperature-grown continuous graphene films from benzene by chemical vapor deposition at ambient pressure, *Sci Rep* 5 (2015) 17955.
- [16] B. Zhang, W.H. Lee, R. Piner, I. Kholmanov, Y. Wu, H. Li, H. Ji, R.S. Ruoff, Low-temperature chemical vapor deposition growth of graphene from toluene on electropolished copper foils, *ACS Nano* 6(3) (2012) 2471-6.
- [17] S. Hussain, M.W. Iqbal, J. Park, M. Ahmad, J. Singh, J. Eom, J. Jung, Physical and electrical properties of graphene grown under different hydrogen flow in low pressure chemical vapor deposition, *Nanoscale Res Lett* 9(1) (2014) 546.
- [18] K.S. Novoselov, V.I. Fal'ko, L. Colombo, P.R. Gellert, M.G. Schwab, K. Kim, A roadmap for graphene, *Nature* 490(7419) (2012) 192-200.

- [19] K.S. Novoselov, D. Jiang, F. Schedin, T.J. Booth, V.V. Khotkevich, S.V. Morozov, A.K. Geim, Two-dimensional atomic crystals, *Proc Natl Acad Sci U S A* 102(30) (2005) 10451-3.
- [20] K.S. Novoselov, A.H. Castro Neto, Two-dimensional crystals-based heterostructures: materials with tailored properties, *Physica Scripta* T146 (2012) 014006.
- [21] K. Parvez, Z.S. Wu, R. Li, X. Liu, R. Graf, X. Feng, K. Mullen, Exfoliation of graphite into graphene in aqueous solutions of inorganic salts, *J Am Chem Soc* 136(16) (2014) 6083-91.
- [22] S. Sarkar, D. Gandla, Y. Venkatesh, P.R. Bangal, S. Ghosh, Y. Yang, S. Misra, Graphene quantum dots from graphite by liquid exfoliation showing excitation-independent emission, fluorescence upconversion and delayed fluorescence, *Phys Chem Chem Phys* 18(31) (2016) 21278-87.
- [23] Y. Hernandez, V. Nicolosi, M. Lotya, F.M. Blighe, Z. Sun, S. De, I.T. McGovern, B. Holland, M. Byrne, Y.K. Gun'Ko, J.J. Boland, P. Niraj, G. Duesberg, S. Krishnamurthy, R. Goodhue, J. Hutchison, V. Scardaci, A.C. Ferrari, J.N. Coleman, High-yield production of graphene by liquid-phase exfoliation of graphite, *Nat Nanotechnol* 3(9) (2008) 563-8.
- [24] W. Qian, R. Hao, Y. Hou, Y. Tian, C. Shen, H. Gao, X. Liang, Solvothermal-assisted exfoliation process to produce graphene with high yield and high quality, *Nano Research* 2(9) (2009) 706-712.
- [25] T.C. Achee, W. Sun, J.T. Hope, S.G. Quitzau, C.B. Sweeney, S.A. Shah, T. Habib, M.J. Green, High-yield scalable graphene nanosheet production from compressed graphite using electrochemical exfoliation, *Sci Rep* 8(1) (2018) 14525.
- [26] S. Pei, Q. Wei, K. Huang, H.M. Cheng, W. Ren, Green synthesis of graphene oxide by seconds timescale water electrolytic oxidation, *Nat Commun* 9(1) (2018) 145.
- [27] M. Zhou, J. Tang, Q. Cheng, G. Xu, P. Cui, L.-C. Qin, Few-layer graphene obtained by electrochemical exfoliation of graphite cathode, *Chemical Physics Letters* 572 (2013) 61-65.
- [28] XIII. On the atomic weight of graphite, *Philosophical Transactions of the Royal Society of London* 149 (1859) 249-259.
- [29] A. Dimiev, D.V. Kosynkin, L.B. Alemany, P. Chaguine, J.M. Tour, Pristine graphite oxide, *J Am Chem Soc* 134(5) (2012) 2815-22.
- [30] S. Stankovich, D.A. Dikin, R.D. Piner, K.A. Kohlhaas, A. Kleinhammes, Y. Jia, Y. Wu, S.T. Nguyen, R.S. Ruoff, Synthesis of graphene-based nanosheets via chemical reduction of exfoliated graphite oxide, *Carbon* 45(7) (2007) 1558-1565.
- [31] D. Voiry, J. Yang, J. Kupferberg, R. Fullon, C. Lee, H.Y. Jeong, H.S. Shin, M. Chhowalla, High-quality graphene via microwave reduction of solution-exfoliated graphene oxide, *Science* 353(6306) (2016) 1413-1416.
- [32] V.K. Abdelkader-Fernández, M. Melguizo, M. Domingo-García, F.J. López-Garzón, M. Pérez-Mendoza, Hydrogen cold plasma for the effective reduction of graphene oxide, *Applied Surface Science* 464 (2019) 673-681.
- [33] D.E. Glass, G.K. Surya Prakash, Effect of pH on the Reduction of Graphene Oxide on its Structure and Oxygen Reduction Capabilities in the Alkaline Media, *Electroanalysis* 30(9) (2018) 1938-1945.
- [34] S. Park, J. An, J.R. Potts, A. Velamakanni, S. Murali, R.S. Ruoff, Hydrazine-reduction of graphite- and graphene oxide, *Carbon* 49(9) (2011) 3019-3023.
- [35] M. Tortello, S. Colonna, M. Bernal, J. Gomez, M. Pavese, C. Novara, F. Giorgis, M. Maggio, G. Guerra, G. Saracco, R.S. Gonnelli, A. Fina, Effect of thermal annealing on the heat transfer properties of reduced graphite oxide flakes: A

- nanoscale characterization via scanning thermal microscopy, *Carbon* 109 (2016) 390-401.
- [36] X. Fan, W. Peng, Y. Li, X. Li, S. Wang, G. Zhang, F. Zhang, Deoxygenation of Exfoliated Graphite Oxide under Alkaline Conditions: A Green Route to Graphene Preparation, *Advanced Materials* 20(23) (2008) 4490-4493.
- [37] H.J. Shin, K.K. Kim, A. Benayad, S.M. Yoon, H.K. Park, I.S. Jung, M.H. Jin, H.K. Jeong, J.M. Kim, J.Y. Choi, Y.H. Lee, Efficient Reduction of Graphite Oxide by Sodium Borohydride and Its Effect on Electrical Conductance, *Advanced Functional Materials* 19(12) (2009) 1987-1992.
- [38] C.K. Chua, M. Pumera, The reduction of graphene oxide with hydrazine: elucidating its reductive capability based on a reaction-model approach, *Chem Commun (Camb)* 52(1) (2016) 72-5.
- [39] H. Liu, T. Li, Y. Liu, G. Qin, X. Wang, T. Chen, Glucose-Reduced Graphene Oxide with Excellent Biocompatibility and Photothermal Efficiency as well as Drug Loading, *Nanoscale Research Letters* 11(1) (2016) 211.
- [40] E. Andrijanto, S. Shoelarta, G. Subiyanto, S. Rifki, Facile synthesis of graphene from graphite using ascorbic acid as reducing agent, 1725 (2016) 020003.
- [41] Y. Xu, H. Cao, Y. Xue, B. Li, W. Cai, Liquid-Phase Exfoliation of Graphene: An Overview on Exfoliation Media, Techniques, and Challenges, *Nanomaterials (Basel)* 8(11) (2018).
- [42] J.N. Coleman, Liquid-Phase Exfoliation of Nanotubes and Graphene, *Advanced Functional Materials* 19(23) (2009) 3680-3695.
- [43] R. Narayan, S.O. Kim, Surfactant mediated liquid phase exfoliation of graphene, *Nano Converg* 2(1) (2015) 20.
- [44] A.S. Pavlova, E.A. Obratsova, A.V. Belkin, C. Monat, P. Rojo-Romeo, E.D. Obratsova, Liquid-phase exfoliation of flaky graphite, *Journal of Nanophotonics* 10(1) (2016) 012525.
- [45] H. Liu, X. Hu, H. Guo, J. Zhao, F. Li, D. Zhu, S. Liu, One-step reducing and dispersing graphene oxide via hydroxypropyl hydrazine and its applications in Cu(2+) removal, *Phys Chem Chem Phys* 21(21) (2019) 10947-10954.
- [46] S. P. A, S. N. M, One step synthesis of graphene, *Inorganic and Nano-Metal Chemistry* (2019) 1-7.
- [47] D.W. Johnson, B.P. Dobson, K.S. Coleman, A manufacturing perspective on graphene dispersions, *Current Opinion in Colloid & Interface Science* 20(5-6) (2015) 367-382.
- [48] G. Tubon Usca, C. Vacacela Gomez, M. Guevara, T. Tene, J. Hernandez, R. Molina, A. Tavolaro, D. Miriello, L.S. Caputi, Zeolite-Assisted Shear Exfoliation of Graphite into Few-Layer Graphene, *Crystals* 9(8) (2019) 377.
- [49] Y. Xu, J. Liu, Graphene as Transparent Electrodes: Fabrication and New Emerging Applications, *Small* 12(11) (2016) 1400-19.
- [50] X. Miao, S. Tongay, M.K. Petterson, K. Berke, A.G. Rinzler, B.R. Appleton, A.F. Hebard, High efficiency graphene solar cells by chemical doping, *Nano Lett* 12(6) (2012) 2745-50.
- [51] M.F. El-Kady, Y. Shao, R.B. Kaner, Graphene for batteries, supercapacitors and beyond, *Nature Reviews Materials* 1(7) (2016).
- [52] J. Pena-Bahamonde, H.N. Nguyen, S.K. Fanourakis, D.F. Rodrigues, Recent advances in graphene-based biosensor technology with applications in life sciences, *J Nanobiotechnology* 16(1) (2018) 75.
- [53] N.N. Rosli, M.A. Ibrahim, N. Ahmad Ludin, M.A. Mat Teridi, K. Sopian, A review of graphene based transparent conducting films for use in solar photovoltaic applications, *Renewable and Sustainable Energy Reviews* 99 (2019) 83-99.

- [54] F. Liu, X. Qiu, J. Xu, J. Huang, D. Chen, G. Chen, High conductivity and transparency of graphene-based conductive ink: Prepared from a multi-component synergistic stabilization method, *Progress in Organic Coatings* 133 (2019) 125-130.
- [55] H. Cheraghi Bidsorkhi, A.G. D'Aloia, A. Tamburrano, G. De Bellis, A. Delfini, P. Ballirano, M.S. Sarto, 3D Porous Graphene Based Aerogel for Electromagnetic Applications, *Sci Rep* 9(1) (2019) 15719.
- [56] A. Yu, Tunable strong THz absorption assisted by graphene-dielectric stacking structure, *Superlattices and Microstructures* 122 (2018) 461-470.
- [57] R. Maria-Hormigos, B. Jurado-Sanchez, A. Escarpa, Graphene quantum dot based micromotors: a size matter, *Chem Commun (Camb)* 55(47) (2019) 6795-6798.
- [58] J. Zhu, X. Cheng, Y. Liu, R. Wang, M. Jiang, D. Li, B. Lu, Z. Ren, Stimulated Brillouin scattering induced all-optical modulation in graphene microfiber, *Photonics Research* 7(1) (2018) 8.
- [59] L.E. Verduzco, J. Oliva, A.I. Oliva, E. Macias, C.R. Garcia, M. Herrera-Trejo, N. Pariona, A.I. Mtz-Enriquez, Enhanced removal of arsenic and chromium contaminants from drinking water by electrodeposition technique using graphene composites, *Materials Chemistry and Physics* 229 (2019) 197-209.
- [60] F. Schedin, A.K. Geim, S.V. Morozov, E.W. Hill, P. Blake, M.I. Katsnelson, K.S. Novoselov, Detection of individual gas molecules adsorbed on graphene, *Nat Mater* 6(9) (2007) 652-5.
- [61] D.A. Bahamon, Z. Qi, H.S. Park, V.M. Pereira, D.K. Campbell, Conductance signatures of electron confinement induced by strained nanobubbles in graphene, *Nanoscale* 7(37) (2015) 15300-9.
- [62] J. Park, M. Yan, Covalent functionalization of graphene with reactive intermediates, *Acc Chem Res* 46(1) (2013) 181-9.
- [63] G. Bottari, M.A. Herranz, L. Wibmer, M. Volland, L. Rodriguez-Perez, D.M. Guldi, A. Hirsch, N. Martin, F. D'Souza, T. Torres, Chemical functionalization and characterization of graphene-based materials, *Chem Soc Rev* 46(15) (2017) 4464-4500.
- [64] R. Sharma, J.H. Baik, C.J. Perera, M.S. Strano, Anomalously large reactivity of single graphene layers and edges toward electron transfer chemistries, *Nano Lett* 10(2) (2010) 398-405.
- [65] M.Z. Hossain, M.A. Walsh, M.C. Hersam, Scanning tunneling microscopy, spectroscopy, and nanolithography of epitaxial graphene chemically modified with aryl moieties, *J Am Chem Soc* 132(43) (2010) 15399-403.
- [66] D.B. Farmer, R. Golizadeh-Mojarad, V. Perebeinos, Y.M. Lin, G.S. Tulevski, J.C. Tsang, P. Avouris, Chemical doping and electron-hole conduction asymmetry in graphene devices, *Nano Lett* 9(1) (2009) 388-92.
- [67] Z. Jin, T.P. McNicholas, C.-J. Shih, Q.H. Wang, G.L.C. Paulus, A.J. Hilmer, S. Shimizu, M.S. Strano, Click Chemistry on Solution-Dispersed Graphene and Monolayer CVD Graphene, *Chemistry of Materials* 23(14) (2011) 3362-3370.
- [68] J.M. Englert, C. Dotzer, G. Yang, M. Schmid, C. Papp, J.M. Gottfried, H.P. Steinruck, E. Spiecker, F. Hauke, A. Hirsch, Covalent bulk functionalization of graphene, *Nat Chem* 3(4) (2011) 279-86.
- [69] G.L. Paulus, Q.H. Wang, M.S. Strano, Covalent electron transfer chemistry of graphene with diazonium salts, *Acc Chem Res* 46(1) (2013) 160-70.
- [70] D.E. Jiang, B.G. Sumpter, S. Dai, How do aryl groups attach to a graphene sheet?, *J Phys Chem B* 110(47) (2006) 23628-32.
- [71] F.M. Koehler, A. Jacobsen, K. Ensslin, C. Stampfer, W.J. Stark, Selective chemical modification of graphene surfaces: distinction between single- and bilayer graphene, *Small* 6(10) (2010) 1125-30.

- [72] M. Quintana, A. Montellano, A.E. del Rio Castillo, G. Van Tendeloo, C. Bittencourt, M. Prato, Selective organic functionalization of graphene bulk or graphene edges, *Chem Commun (Camb)* 47(33) (2011) 9330-2.
- [73] I.Y. Jeon, Y.R. Shin, G.J. Sohn, H.J. Choi, S.Y. Bae, J. Mahmood, S.M. Jung, J.M. Seo, M.J. Kim, D. Wook Chang, L. Dai, J.B. Baek, Edge-carboxylated graphene nanosheets via ball milling, *Proc Natl Acad Sci U S A* 109(15) (2012) 5588-93.
- [74] M.M. Bernal, A. Di Pierro, C. Novara, F. Giorgis, B. Mortazavi, G. Saracco, A. Fina, Edge-Grafted Molecular Junctions between Graphene Nanoplatelets: Applied Chemistry to Enhance Heat Transfer in Nanomaterials, *Advanced Functional Materials* 28(18) (2018) 1706954.
- [75] Y.Z. Tan, B. Yang, K. Parvez, A. Narita, S. Osella, D. Beljonne, X. Feng, K. Mullen, Atomically precise edge chlorination of nanographenes and its application in graphene nanoribbons, *Nat Commun* 4 (2013) 2646.
- [76] S. Sarkar, E. Bekyarova, S. Niyogi, R.C. Haddon, Diels-Alder chemistry of graphite and graphene: graphene as diene and dienophile, *J Am Chem Soc* 133(10) (2011) 3324-7.
- [77] J.M. Seo, J.B. Baek, A solvent-free Diels-Alder reaction of graphite into functionalized graphene nanosheets, *Chem Commun (Camb)* 50(93) (2014) 14651-3.
- [78] I.E. Mejias Carpio, J.D. Mangadlao, H.N. Nguyen, R.C. Advincula, D.F. Rodrigues, Graphene oxide functionalized with ethylenediamine triacetic acid for heavy metal adsorption and anti-microbial applications, *Carbon* 77 (2014) 289-301.
- [79] G. Mercier, A. Klechikov, M. Hedenström, D. Johnels, I.A. Baburin, G. Seifert, R. Mysyk, A.V. Talyzin, Porous Graphene Oxide/Diboronic Acid Materials: Structure and Hydrogen Sorption, *The Journal of Physical Chemistry C* 119(49) (2015) 27179-27191.
- [80] G. Wang, X. Shen, B. Wang, J. Yao, J. Park, Synthesis and characterisation of hydrophilic and organophilic graphene nanosheets, *Carbon* 47(5) (2009) 1359-1364.
- [81] H. Yang, F. Li, C. Shan, D. Han, Q. Zhang, L. Niu, A. Ivaska, Covalent functionalization of chemically converted graphene sheets via silane and its reinforcement, *Journal of Materials Chemistry* 19(26) (2009) 4632.
- [82] M. Chen, R. Guan, S. Yang, Hybrids of Fullerenes and 2D Nanomaterials, *Adv Sci (Weinh)* 6(1) (2019) 1800941.
- [83] M.M. Stylianakis, D. Konios, G. Kakavelakis, G. Charalambidis, E. Stratakis, A.G. Coutsolelos, E. Kymakis, S.H. Anastasiadis, Efficient ternary organic photovoltaics incorporating a graphene-based porphyrin molecule as a universal electron cascade material, *Nanoscale* 7(42) (2015) 17827-35.
- [84] P.-G. Su, Z.-M. Lu, Flexibility and electrical and humidity-sensing properties of diamine-functionalized graphene oxide films, *Sensors and Actuators B: Chemical* 211 (2015) 157-163.
- [85] V. Georgakilas, M. Otyepka, A.B. Bourlinos, V. Chandra, N. Kim, K.C. Kemp, P. Hobza, R. Zboril, K.S. Kim, Functionalization of graphene: covalent and non-covalent approaches, derivatives and applications, *Chem Rev* 112(11) (2012) 6156-214.
- [86] M. de Sousa, C.H.Z. Martins, L.S. Franqui, L.C. Fonseca, F.S. Delite, E.M. Lanzoni, D.S.T. Martinez, O.L. Alves, Covalent functionalization of graphene oxide with d-mannose: evaluating the hemolytic effect and protein corona formation, *J Mater Chem B* 6(18) (2018) 2803-2812.
- [87] Interaction of Graphene Oxide with Proteins and Applications of their Conjugates, *Journal of Nanomedicine Research* 5(2) (2017).
- [88] J.L.A. Jonathan W. Steed, *Supramolecular Chemistry*, 2 ed.2009

- [89] N.T. Southall, K.A. Dill, A.D.J. Haymet, A View of the Hydrophobic Effect, *The Journal of Physical Chemistry B* 106(3) (2002) 521-533.
- [90] D.B. Smithrud, E.M. Sanford, I. Chao, S.B. Ferguson, D.R. Carcanague, J.D. Evanseck, K.N. Houk, F. Diederich, Solvent effects in molecular recognition, *Pure and Applied Chemistry* 62(12) (1990) 2227-2236.
- [91] N.S. Kumar, M.D. Gujrati, J.N. Wilson, Evidence of preferential pi-stacking: a study of intermolecular and intramolecular charge transfer complexes, *Chem Commun (Camb)* 46(30) (2010) 5464-6.
- [92] E.-Y. Choi, T.H. Han, J. Hong, J.E. Kim, S.H. Lee, H.W. Kim, S.O. Kim, Noncovalent functionalization of graphene with end-functional polymers, *Journal of Materials Chemistry* 20(10) (2010) 1907.
- [93] Z. Zhang, H. Huang, X. Yang, L. Zang, Tailoring Electronic Properties of Graphene by π - π Stacking with Aromatic Molecules, *The Journal of Physical Chemistry Letters* 2(22) (2011) 2897-2905.
- [94] J. Wang, Z. Chen, B. Chen, Adsorption of polycyclic aromatic hydrocarbons by graphene and graphene oxide nanosheets, *Environ Sci Technol* 48(9) (2014) 4817-25.
- [95] T. de Sousa, T.F.D. Fernandes, M.J.S. Matos, E.N.D. Araujo, M.S.C. Mazzoni, B.R.A. Neves, F. Plentz, Thionine Self-Assembled Structures on Graphene: Formation, Organization, and Doping, *Langmuir* 34(23) (2018) 6903-6911.
- [96] J.M. MacLeod, J.A. Lipton-Duffin, D. Cui, S. De Feyter, F. Rosei, Substrate Effects in the Supramolecular Assembly of 1,3,5-Benzene Tricarboxylic Acid on Graphite and Graphene, *Langmuir* 31(25) (2015) 7016-24.
- [97] R. Singh, C.C. Tripathi, Enhancing Liquid-Phase Exfoliation of Graphene with Addition of Anthracene in Organic Solvents, *Arabian Journal for Science and Engineering* 42(6) (2017) 2417-2424.
- [98] I.W. Chen, C.Y. Huang, S.H. Jhou, Y.W. Zhang, Exfoliation and performance properties of non-oxidized graphene in water, *Sci Rep* 4 (2014) 3928.
- [99] J. Kim, S.H. Song, H.G. Im, G. Yoon, D. Lee, C. Choi, J. Kim, B.S. Bae, K. Kang, S. Jeon, Moisture Barrier Composites Made of Non-Oxidized Graphene Flakes, *Small* 11(26) (2015) 3124-9.
- [100] X. Dong, Y. Shi, Y. Zhao, D. Chen, J. Ye, Y. Yao, F. Gao, Z. Ni, T. Yu, Z. Shen, Y. Huang, P. Chen, L.J. Li, Symmetry breaking of graphene monolayers by molecular decoration, *Phys Rev Lett* 102(13) (2009) 135501.
- [101] X. An, T. Simmons, R. Shah, C. Wolfe, K.M. Lewis, M. Washington, S.K. Nayak, S. Talapatra, S. Kar, Stable aqueous dispersions of noncovalently functionalized graphene from graphite and their multifunctional high-performance applications, *Nano Lett* 10(11) (2010) 4295-301.
- [102] A. Schlierf, H. Yang, E. Gebremedhn, E. Treossi, L. Ortolani, L. Chen, A. Minoia, V. Morandi, P. Samori, C. Casiraghi, D. Beljonne, V. Palermo, Nanoscale insight into the exfoliation mechanism of graphene with organic dyes: effect of charge, dipole and molecular structure, *Nanoscale* 5(10) (2013) 4205-16.
- [103] D.W. Lee, T. Kim, M. Lee, An amphiphilic pyrene sheet for selective functionalization of graphene, *Chem Commun (Camb)* 47(29) (2011) 8259-61.
- [104] J. Zhang, Y. Xu, L. Cui, A. Fu, W. Yang, C. Barrow, J. Liu, Mechanical properties of graphene films enhanced by homo-telechelic functionalized polymer fillers via π - π stacking interactions, *Composites Part A: Applied Science and Manufacturing* 71 (2015) 1-8.
- [105] M.J. Fernández-Merino, J.I. Paredes, S. Villar-Rodil, L. Guardia, P. Solís-Fernández, D. Salinas-Torres, D. Cazorla-Amorós, E. Morallón, A. Martínez-

- Alonso, J.M.D. Tascón, Investigating the influence of surfactants on the stabilization of aqueous reduced graphene oxide dispersions and the characteristics of their composite films, *Carbon* 50(9) (2012) 3184-3194.
- [106] P.M. Carrasco, S. Montes, I. García, M. Borghei, H. Jiang, I. Odriozola, G. Cabañero, V. Ruiz, High-concentration aqueous dispersions of graphene produced by exfoliation of graphite using cellulose nanocrystals, *Carbon* 70 (2014) 157-163.
- [107] M. Lotya, Y. Hernandez, P.J. King, R.J. Smith, V. Nicolosi, L.S. Karlsson, F.M. Blighe, S. De, Z. Wang, I.T. McGovern, G.S. Duesberg, J.N. Coleman, Liquid phase production of graphene by exfoliation of graphite in surfactant/water solutions, *J Am Chem Soc* 131(10) (2009) 3611-20.
- [108] M. Cai, D. Thorpe, D.H. Adamson, H.C. Schniepp, Methods of graphite exfoliation, *Journal of Materials Chemistry* 22(48) (2012) 24992.
- [109] Y. Liang, D. Wu, X. Feng, K. Müllen, Dispersion of Graphene Sheets in Organic Solvent Supported by Ionic Interactions, *Advanced Materials* 21(17) (2009) 1679-1683.
- [110] T. Yeom, T. Simon, M. Zhang, Y. Yu, T. Cui, Active heat sink with piezoelectric translational agitators, piezoelectric synthetic jets, and micro pin fin arrays, *Experimental Thermal and Fluid Science* 99 (2018) 190-199.
- [111] E. Balvís, R. Bendaña, H. Michinel, P.F. de Córdoba, A. Paredes, Analysis of a passive heat sink for temperature stabilization of high-power LED bulbs, *Journal of Physics: Conference Series* 605 (2015) 012005.
- [112] B. Zhang, R.E. Imhof, Theoretical analysis of the surface thermal wave technique for measuring the thermal diffusivity of thin slabs, *Applied Physics A Materials Science & Processing* 62(4) (1996) 323-334.
- [113] M.G. Iyengar, Karl J L ; Sammakia, Bahgat, Cooling of microelectronic and nanoelectronic equipment : advances and emerging research, 2014.
- [114] M.I. di Avram Bar-Cohen, Karl J. L. Geisler, Bahgat Sammakia, yogendra Joshi, *Encyclopedia of Thermal Packaging: Set 2: Thermal Packaging Tools*, 2014.
- [115] A.D.K.A.A.J. Welty, *Extended Surface Heat Transfer*, 2000.
- [116] B.K. DUTTA, *HEAT TRANSFER: PRINCIPLES AND APPLICATIONS*, PHI Learning 2000.
- [117] S. Mosayebidorcheh, M. Rahimi-Gorji, D.D. Ganji, T. Moayebidorcheh, O. Pourmehran, M. Biglarian, Transient thermal behavior of radial fins of rectangular, triangular and hyperbolic profiles with temperature-dependent properties using DTM-FDM, *Journal of Central South University* 24(3) (2017) 675-682.
- [118] R.A. Mark Occhionero, Kevin Fennessy, and Robert A. Hay, C. Ceramics Process Systems, Aluminum Silicon Carbide (AlSiC) for Advanced Microelectronic Packages, Ceramics Process Systems Corp.
- [119] J.A.C. Kerns, N.J.; Makowiecki, D.; Davidson, H.L., *Dymalloy: A composite substrate for high power density electronic components*, 1995.
- [120] M. Smalc, G. Shives, G. Chen, S. Guggari, J. Norley, R.A. Reynolds, Thermal Performance of Natural Graphite Heat Spreaders, (2005) 79-89.
- [121] B. Jiang, H. Wang, G. Wen, E. Wang, X. Fang, G. Liu, W. Zhou, Copper-graphite-copper sandwich: superior heat spreader with excellent heat-dissipation ability and good weldability, *RSC Advances* 6(30) (2016) 25128-25136.
- [122] K.E. Goodson, K. Kurabayashi, R.F.W. Pease, Improved heat sinking for laser-diode arrays using microchannels in CVD diamond, *IEEE Transactions on Components, Packaging, and Manufacturing Technology: Part B* 20(1) (1997) 104-109.

- [123] J. Vieira da Silva Neto, M. Amorim Fraga, V. Jesus Trava-Airoldi, Development, Properties, and Applications of CVD Diamond-Based Heat Sinks, (2019).
- [124] P.W. Morrison, A. Somashekhar, J.T. Glass, J.T. Prater, Growth of diamond films using an enclosed combustion flame, *Journal of Applied Physics* 78(6) (1995) 4144-4156.
- [125] K. Azar, P.D.N.E.M.H.Y.J.N.L.P.D.B.T. Kaveh Azar, B. Tavassoli, A.T. Solutions, A. Koss, Qpedia Thermal Management eMagazine, Volume 4, Advanced Thermal Solutions, Incorporated 2011.
- [126] D. Nika, Graphene Thermal Properties: Applications in Thermal Management and Energy Storage, *Applied Sciences* 4 (2014) 525.
- [127] F. Hao, D. Fang, Z. Xu, Mechanical and thermal transport properties of graphene with defects, *Applied Physics Letters* 99(4) (2011) 041901.
- [128] Q. Zhou, F. Meng, Z. Liu, S. Shi, The Thermal Conductivity of Carbon Nanotubes with Defects and Intramolecular Junctions, *Journal of Nanomaterials* 2013 (2013) 1-7.
- [129] W. Lee, K.D. Kihm, S.H. Ko, Thermal conductivity reduction of multilayer graphene with fine grain sizes, *JMST Advances* 1(1-2) (2019) 191-195.
- [130] Y. Yang, J. Cao, N. Wei, D. Meng, L. Wang, G. Ren, R. Yan, N. Zhang, Thermal Conductivity of Defective Graphene Oxide: A Molecular Dynamic Study, *Molecules* 24(6) (2019).
- [131] D.L. Nika, E.P. Pokatilov, A.S. Askerov, A.A. Balandin, Phonon thermal conduction in graphene: Role of Umklapp and edge roughness scattering, *Physical Review B* 79(15) (2009).
- [132] A.A. Balandin, S. Ghosh, W. Bao, I. Calizo, D. Teweldebrhan, F. Miao, C.N. Lau, Superior thermal conductivity of single-layer graphene, *Nano Lett* 8(3) (2008) 902-7.
- [133] E. Munoz, J. Lu, B.I. Yakobson, Ballistic thermal conductance of graphene ribbons, *Nano Lett* 10(5) (2010) 1652-6.
- [134] R. Murali, Y. Yang, K. Brenner, T. Beck, J.D. Meindl, Breakdown current density of graphene nanoribbons, *Applied Physics Letters* 94(24) (2009) 243114.
- [135] J. Che, T. Çagin, W.A. Goddard, Thermal conductivity of carbon nanotubes, *Nanotechnology* 11(2) (2000) 65-69.
- [136] E. Pop, D. Mann, Q. Wang, K. Goodson, H. Dai, Thermal conductance of an individual single-wall carbon nanotube above room temperature, *Nano Lett* 6(1) (2006) 96-100.
- [137] P. Kim, L. Shi, A. Majumdar, P.L. McEuen, Thermal transport measurements of individual multiwalled nanotubes, *Phys Rev Lett* 87(21) (2001) 215502.
- [138] G. Xin, T. Yao, H. Sun, S.M. Scott, D. Shao, G. Wang, J. Lian, Highly thermally conductive and mechanically strong graphene fibers, *Science* 349(6252) (2015) 1083-7.
- [139] S. Ghosh, W. Bao, D.L. Nika, S. Subrina, E.P. Pokatilov, C.N. Lau, A.A. Balandin, Dimensional crossover of thermal transport in few-layer graphene, *Nat Mater* 9(7) (2010) 555-8.
- [140] M. Potenza, A. Cataldo, G. Bovesecchi, S. Corasaniti, P. Coppa, S. Bellucci, Graphene nanoplatelets: Thermal diffusivity and thermal conductivity by the flash method, *AIP Advances* 7(7) (2017) 075214.
- [141] N.K. Mahanta, A.R. Abramson, Thermal conductivity of graphene and graphene oxide nanoplatelets, (2012) 1-6.
- [142] H.C. Schniepp, J.L. Li, M.J. McAllister, H. Sai, M. Herrera-Alonso, D.H. Adamson, R.K. Prud'homme, R. Car, D.A. Saville, I.A. Aksay, Functionalized single

- graphene sheets derived from splitting graphite oxide, *J Phys Chem B* 110(17) (2006) 8535-9.
- [143] J. Fa, L. Hn, Z. Z, H. Nm, P. A, Titanium dioxide-reduced graphene oxide thin film for photoelectrochemical water splitting, *Ceramics International* 40(9) (2014) 15159-15165.
- [144] C. Gomez-Navarro, R.T. Weitz, A.M. Bittner, M. Scolari, A. Mews, M. Burghard, K. Kern, Electronic transport properties of individual chemically reduced graphene oxide sheets, *Nano Lett* 7(11) (2007) 3499-503.
- [145] G. George, S.B. Sisupal, T. Tomy, B.A. Pottammal, A. Kumaran, V. Suvekbala, R. Gopimohan, S. Sivaram, L. Ragupathy, Thermally conductive thin films derived from defect free graphene-natural rubber latex nanocomposite: Preparation and properties, *Carbon N Y* 119 (2017) 527-534.
- [146] X. Wang, L. Zhi, K. Mullen, Transparent, conductive graphene electrodes for dye-sensitized solar cells, *Nano Lett* 8(1) (2008) 323-7.
- [147] S. Gilje, S. Han, M. Wang, K.L. Wang, R.B. Kaner, A chemical route to graphene for device applications, *Nano Lett* 7(11) (2007) 3394-8.
- [148] L.B. Modesto-López, M. Miettinen, J. Riikonen, T. Torvela, C. Pfüller, V.-P. Lehto, A. Lähde, J. Jokiniemi, Films of Graphene Nanomaterials Formed by Ultrasonic Spraying of Their Stable Suspensions, *Aerosol Science and Technology* 49(1) (2014) 45-56.
- [149] H. Shi, C. Wang, Z. Sun, Y. Zhou, K. Jin, G. Yang, Transparent conductive reduced graphene oxide thin films produced by spray coating, *Science China Physics, Mechanics & Astronomy* 58(1) (2014) 1-5.
- [150] O.M. Slobodian, Reduced graphene oxide obtained using the spray pyrolysis technique for gas sensing, *Semiconductor Physics, Quantum Electronics & Optoelectronics* 22(1) (2019) 98-103.
- [151] H.H. Gong, S.H. Park, S.-S. Lee, S.C. Hong, Facile and scalable fabrication of transparent and high performance Pt/reduced graphene oxide hybrid counter electrode for dye-sensitized solar cells, *International Journal of Precision Engineering and Manufacturing* 15(6) (2014) 1193-1199.
- [152] H. Bi, S. Wan, X. Cao, X. Wu, Y. Zhou, K. Yin, S. Su, Q. Ma, M. Sindoro, J. Zhu, Z. Zhang, H. Zhang, L. Sun, A general and facile method for preparation of large-scale reduced graphene oxide films with controlled structures, *Carbon* 143 (2019) 162-171.
- [153] J.T. Robinson, M. Zalalutdinov, J.W. Baldwin, E.S. Snow, Z. Wei, P. Sheehan, B.H. Houston, Wafer-scale reduced graphene oxide films for nanomechanical devices, *Nano Lett* 8(10) (2008) 3441-5.
- [154] H. Yamaguchi, G. Eda, C. Mattevi, H. Kim, M. Chhowalla, Highly uniform 300 mm wafer-scale deposition of single and multilayered chemically derived graphene thin films, *ACS Nano* 4(1) (2010) 524-8.
- [155] G. Yang, H. Yi, Y. Yao, C. Li, Z. Li, Thermally Conductive Graphene Films for Heat Dissipation, *ACS Applied Nano Materials* 3(3) (2020) 2149-2155.
- [156] V. Lee, L. Whittaker, C. Jaye, K.M. Baroudi, D.A. Fischer, S. Banerjee, Large-Area Chemically Modified Graphene Films: Electrophoretic Deposition and Characterization by Soft X-ray Absorption Spectroscopy, *Chemistry of Materials* 21(16) (2009) 3905-3916.
- [157] L.P. Yeo, T.D. Nguyen, H. Ling, Y. Lee, D. Mandler, S. Magdassi, A.I.Y. Tok, Electrophoretic deposition of reduced graphene oxide thin films for reduction of cross-sectional heat diffusion in glass windows, *Journal of Science: Advanced Materials and Devices* 4(2) (2019) 252-259.

- [158] J. Zhao, S. Pei, W. Ren, L. Gao, H.M. Cheng, Efficient preparation of large-area graphene oxide sheets for transparent conductive films, *ACS Nano* 4(9) (2010) 5245-52.
- [159] Q. Zheng, B. Zhang, X. Lin, X. Shen, N. Yousefi, Z.-D. Huang, Z. Li, J.-K. Kim, Highly transparent and conducting ultralarge graphene oxide/single-walled carbon nanotube hybrid films produced by Langmuir–Blodgett assembly, *Journal of Materials Chemistry* 22(48) (2012) 25072.
- [160] L.J. Cote, F. Kim, J. Huang, Langmuir-Blodgett assembly of graphite oxide single layers, *J Am Chem Soc* 131(3) (2009) 1043-9.
- [161] O.C. Compton, S.T. Nguyen, Graphene oxide, highly reduced graphene oxide, and graphene: versatile building blocks for carbon-based materials, *Small* 6(6) (2010) 711-23.
- [162] J.S. Park, S.M. Cho, W.J. Kim, J. Park, P.J. Yoo, Fabrication of graphene thin films based on layer-by-layer self-assembly of functionalized graphene nanosheets, *ACS Appl Mater Interfaces* 3(2) (2011) 360-8.
- [163] Q. Ji, I. Honma, S.-M. Paek, M. Akada, J.P. Hill, A. Vinu, K. Ariga, Layer-by-Layer Films of Graphene and Ionic Liquids for Highly Selective Gas Sensing, *Angewandte Chemie* 122(50) (2010) 9931-9933.
- [164] P. Li, K. Chen, L. Zhao, H. Zhang, H. Sun, X. Yang, N.H. Kim, J.H. Lee, Q.J. Niu, Preparation of modified graphene oxide/polyethyleneimine film with enhanced hydrogen barrier properties by reactive layer-by-layer self-assembly, *Composites Part B: Engineering* 166 (2019) 663-672.
- [165] D.D. Kulkarni, I. Choi, S.S. Singamaneni, V.V. Tsukruk, Graphene oxide--polyelectrolyte nanomembranes, *ACS Nano* 4(8) (2010) 4667-76.
- [166] S. Hong, S.S. Yoo, P.J. Yoo, Binder-free heat dissipation films assembled with reduced graphene oxide and alumina nanoparticles for simultaneous high in-plane and cross-plane thermal conductivities, *Journal of Materials Chemistry C* 7(30) (2019) 9380-9388.
- [167] R.H. Baughman, C. Cui, A.A. Zakhidov, Z. Iqbal, J.N. Barisci, G.M. Spinks, G.G. Wallace, A. Mazzoldi, D. De Rossi, A.G. Rinzler, O. Jaschinski, S. Roth, M. Kertesz, Carbon nanotube actuators, *Science* 284(5418) (1999) 1340-4.
- [168] D. Selvakumar, H. Sivaram, A. Alsalmeh, A. Alghamdi, R. Jayavel, Freestanding flexible, pure and composite form of reduced graphene oxide paper for ammonia vapor sensing, *Sci Rep* 9(1) (2019) 8749.
- [169] Y. Yao, J. Ping, Recent advances in graphene-based freestanding paper-like materials for sensing applications, *TrAC Trends in Analytical Chemistry* 105 (2018) 75-88.
- [170] F. Gong, H. Li, W. Wang, D. Xia, Q. Liu, D. Papavassiliou, Z. Xu, Recent Advances in Graphene-Based Free-Standing Films for Thermal Management: Synthesis, Properties, and Applications, *Coatings* 8(2) (2018) 63.
- [171] J.X. Yan, Y.C. Leng, Y.N. Guo, G.Q. Wang, H. Gong, P.Z. Guo, P.H. Tan, Y.Z. Long, X.L. Liu, W.P. Han, Highly Conductive Graphene Paper with Vertically Aligned Reduced Graphene Oxide Sheets Fabricated by Improved Electrospray Deposition Technique, *ACS Appl Mater Interfaces* 11(11) (2019) 10810-10817.
- [172] F. Xiao, Y. Li, H. Gao, S. Ge, H. Duan, Growth of coral-like PtAu-MnO₂ binary nanocomposites on free-standing graphene paper for flexible nonenzymatic glucose sensors, *Biosens Bioelectron* 41 (2013) 417-23.
- [173] S. Lin, S. Ju, J. Zhang, G. Shi, Y. He, D. Jiang, Ultrathin flexible graphene films with high thermal conductivity and excellent EMI shielding performance using large-sized graphene oxide flakes, *RSC Advances* 9(3) (2019) 1419-1427.

- [174] M. Zhang, L. Huang, J. Chen, C. Li, G. Shi, Ultratough, ultrastrong, and highly conductive graphene films with arbitrary sizes, *Adv Mater* 26(45) (2014) 7588-92.
- [175] S.J. Yang, J.H. Kang, H. Jung, T. Kim, C.R. Park, Preparation of a freestanding, macroporous reduced graphene oxide film as an efficient and recyclable sorbent for oils and organic solvents, *Journal of Materials Chemistry A* 1(33) (2013) 9427.
- [176] S. Korkut, J.D. Roy-Mayhew, D.M. Dabbs, D.L. Milius, I.A. Aksay, High surface area tapes produced with functionalized graphene, *ACS Nano* 5(6) (2011) 5214-22.
- [177] W. Yang, Z. Zhao, K. Wu, R. Huang, T. Liu, H. Jiang, F. Chen, Q. Fu, Ultrathin flexible reduced graphene oxide/cellulose nanofiber composite films with strongly anisotropic thermal conductivity and efficient electromagnetic interference shielding, *Journal of Materials Chemistry C* 5(15) (2017) 3748-3756.
- [178] H. Chen, M.B. Müller, K.J. Gilmore, G.G. Wallace, D. Li, Mechanically Strong, Electrically Conductive, and Biocompatible Graphene Paper, *Advanced Materials* 20(18) (2008) 3557-3561.
- [179] G. He, H. Chen, J. Zhu, F. Bei, X. Sun, X. Wang, Synthesis and characterization of graphene paper with controllable properties via chemical reduction, *Journal of Materials Chemistry* 21(38) (2011) 14631.
- [180] H. Gwon, H.-S. Kim, K.U. Lee, D.-H. Seo, Y.C. Park, Y.-S. Lee, B.T. Ahn, K. Kang, Flexible energy storage devices based on graphene paper, *Energy & Environmental Science* 4(4) (2011) 1277.
- [181] B. Shen, W. Zhai, W. Zheng, Ultrathin Flexible Graphene Film: An Excellent Thermal Conducting Material with Efficient EMI Shielding, *Advanced Functional Materials* 24(28) (2014) 4542-4548.
- [182] L. Peng, Z. Xu, Z. Liu, Y. Guo, P. Li, C. Gao, Ultrahigh Thermal Conductive yet Superflexible Graphene Films, *Adv Mater* 29(27) (2017).
- [183] G. Xin, H. Sun, T. Hu, H.R. Fard, X. Sun, N. Koratkar, T. Borca-Tasciuc, J. Lian, Large-area freestanding graphene paper for superior thermal management, *Adv Mater* 26(26) (2014) 4521-6.
- [184] A. Jaworek, A.T. Sobczyk, Electrospraying route to nanotechnology: An overview, *Journal of Electrostatics* 66(3-4) (2008) 197-219.
- [185] J. Gao, X. Mu, X.Y. Li, W.Y. Wang, Y. Meng, X.B. Xu, L.T. Chen, L.J. Cui, X. Wu, H.Z. Geng, Modification of carbon nanotube transparent conducting films for electrodes in organic light-emitting diodes, *Nanotechnology* 24(43) (2013) 435201.
- [186] G. Xin, W. Zhu, T. Yao, S.M. Scott, J. Lian, Microstructure control of macroscopic graphene paper by electrospray deposition and its effect on thermal and electrical conductivities, *Applied Physics Letters* 110(9) (2017) 091909.
- [187] D.A. Dikin, S. Stankovich, E.J. Zimney, R.D. Piner, G.H. Dommett, G. Evmenenko, S.T. Nguyen, R.S. Ruoff, Preparation and characterization of graphene oxide paper, *Nature* 448(7152) (2007) 457-60.
- [188] K.W. Putz, O.C. Compton, M.J. Palmeri, S.T. Nguyen, L.C. Brinson, High-Nanofiller-Content Graphene Oxide-Polymer Nanocomposites via Vacuum-Assisted Self-Assembly, *Advanced Functional Materials* 20(19) (2010) 3322-3329.
- [189] Z.L. Hou, W.L. Song, P. Wang, M.J. Meziani, C.Y. Kong, A. Anderson, H. Maimaiti, G.E. LeCroy, H. Qian, Y.P. Sun, Flexible graphene-graphene composites of superior thermal and electrical transport properties, *ACS Appl Mater Interfaces* 6(17) (2014) 15026-32.

- [190] A. Lerf, A. Buchsteiner, J. Pieper, S. Schöttl, I. Dekany, T. Szabo, H.P. Boehm, Hydration behavior and dynamics of water molecules in graphite oxide, *Journal of Physics and Chemistry of Solids* 67(5-6) (2006) 1106-1110.
- [191] N.-J. Song, C.-M. Chen, C. Lu, Z. Liu, Q.-Q. Kong, R. Cai, Thermally reduced graphene oxide films as flexible lateral heat spreaders, *J. Mater. Chem. A* 2(39) (2014) 16563-16568.
- [192] P. Kumar, F. Shahzad, S. Yu, S.M. Hong, Y.-H. Kim, C.M. Koo, Large-area reduced graphene oxide thin film with excellent thermal conductivity and electromagnetic interference shielding effectiveness, *Carbon* 94 (2015) 494-500.
- [193] J.E. Cha, S.Y. Kim, S.H. Lee, Effect of Continuous Multi-Walled Carbon Nanotubes on Thermal and Mechanical Properties of Flexible Composite Film, *Nanomaterials (Basel)* 6(10) (2016).
- [194] M.E. Itkis, F. Borondics, A. Yu, R.C. Haddon, Thermal conductivity measurements of semitransparent single-walled carbon nanotube films by a bolometric technique, *Nano Lett* 7(4) (2007) 900-4.
- [195] Y. Gogotsi, V. Presser, *Carbon Nanomaterials*, Second Edition, Taylor & Francis 2013.
- [196] H. Wu, L.T. Drzal, Graphene nanoplatelet paper as a light-weight composite with excellent electrical and thermal conductivity and good gas barrier properties, *Carbon* 50(3) (2012) 1135-1145.
- [197] C. Faugeras, B. Faugeras, M. Orlita, M. Potemski, R.R. Nair, A.K. Geim, Thermal conductivity of graphene in corbino membrane geometry, *ACS Nano* 4(4) (2010) 1889-92.
- [198] P. He, J. Sun, S. Tian, S. Yang, S. Ding, G. Ding, X. Xie, M. Jiang, Processable Aqueous Dispersions of Graphene Stabilized by Graphene Quantum Dots, *Chemistry of Materials* 27(1) (2014) 218-226.
- [199] J. Peng, W. Gao, B.K. Gupta, Z. Liu, R. Romero-Aburto, L. Ge, L. Song, L.B. Alemany, X. Zhan, G. Gao, S.A. Vithayathil, B.A. Kaiparettu, A.A. Marti, T. Hayashi, J.J. Zhu, P.M. Ajayan, Graphene quantum dots derived from carbon fibers, *Nano Lett* 12(2) (2012) 844-9.
- [200] S. Yang, J. Sun, X. Li, W. Zhou, Z. Wang, P. He, G. Ding, X. Xie, Z. Kang, M. Jiang, Large-scale fabrication of heavy doped carbon quantum dots with tunable-photoluminescence and sensitive fluorescence detection, *Journal of Materials Chemistry A* 2(23) (2014) 8660.
- [201] S. Shen, J. Wang, Z. Wu, Z. Du, Z. Tang, J. Yang, Graphene Quantum Dots with High Yield and High Quality Synthesized from Low Cost Precursor of Aphanitic Graphite, *Nanomaterials (Basel)* 10(2) (2020).
- [202] J. Sun, H. Liu, X. Chen, D.G. Evans, W. Yang, X. Duan, Carbon Nanorings and Their Enhanced Lithium Storage Properties (*Adv. Mater.* 8/2013), *Advanced Materials* 25(8) (2013) 1124-1124.
- [203] J. Zhang, G. Shi, C. Jiang, S. Ju, D. Jiang, 3D Bridged Carbon Nanoring/Graphene Hybrid Paper as a High-Performance Lateral Heat Spreader, *Small* 11(46) (2015) 6197-204.
- [204] X. Meng, T. Chen, Y. Li, S. Liu, H. Pan, Y. Ma, Z. Chen, Y. Zhang, S. Zhu, Assembly of carbon nanodots in graphene-based composite for flexible electrothermal heater with ultrahigh efficiency, *Nano Research* 12(10) (2019) 2498-2508.
- [205] H. Malekpour, K.H. Chang, J.C. Chen, C.Y. Lu, D.L. Nika, K.S. Novoselov, A.A. Balandin, Thermal conductivity of graphene laminate, *Nano Lett* 14(9) (2014) 5155-61.

- [206] X. Tian, M.E. Itkis, E.B. Bekyarova, R.C. Haddon, Anisotropic Thermal and Electrical Properties of Thin Thermal Interface Layers of Graphite Nanoplatelet-Based Composites, *Scientific Reports* 3(1) (2013).
- [207] Q. Li, M. Strange, I. Duchemin, D. Donadio, G.C. Solomon, A Strategy to Suppress Phonon Transport in Molecular Junctions Using π -Stacked Systems, *The Journal of Physical Chemistry C* 121(13) (2017) 7175-7182.
- [208] M. Famili, I. Grace, H. Sadeghi, C.J. Lambert, Suppression of Phonon Transport in Molecular Christmas Trees, *Chemphyschem* 18(10) (2017) 1234-1241.
- [209] Y. Gao, F. Muller-Plathe, Increasing the Thermal Conductivity of Graphene-Polyamide-6,6 Nanocomposites by Surface-Grafted Polymer Chains: Calculation with Molecular Dynamics and Effective-Medium Approximation, *J Phys Chem B* 120(7) (2016) 1336-46.
- [210] A. Di Pierro, G. Saracco, A. Fina, Molecular junctions for thermal transport between graphene nanoribbons: Covalent bonding vs. interdigitated chains, *Computational Materials Science* 142 (2018) 255-260.
- [211] H. Han, Y. Zhang, N. Wang, M.K. Samani, Y. Ni, Z.Y. Mijbil, M. Edwards, S. Xiong, K. Saaskilahti, M. Murugesan, Y. Fu, L. Ye, H. Sadeghi, S. Bailey, Y.A. Kosevich, C.J. Lambert, J. Liu, S. Volz, Functionalization mediates heat transport in graphene nanoflakes, *Nat Commun* 7 (2016) 11281.
- [212] L. Zhang, C. Liu, Q. Jin, X. Zhu, M. Liu, Pyrene-functionalized organogel and spacer effect: from emissive nanofiber to nanotube and inversion of supramolecular chirality, *Soft Matter* 9(33) (2013) 7966-7973.
- [213] M.M. Bernal, M. Tortello, S. Colonna, G. Saracco, A. Fina, Thermally and Electrically Conductive Nanopapers from Reduced Graphene Oxide: Effect of Nanoflakes Thermal Annealing on the Film Structure and Properties, *Nanomaterials* 7(12) (2017) 428.
- [214] N.B. Cech, C.G. Enke, Practical implications of some recent studies in electrospray ionization fundamentals, *Mass Spectrom Rev* 20(6) (2001) 362-87.
- [215] C.G. Enke, A predictive model for matrix and analyte effects in electrospray ionization of singly-charged ionic analytes, *Anal Chem* 69(23) (1997) 4885-93.
- [216] A. Krueve, K. Kaupmees, Adduct Formation in ESI/MS by Mobile Phase Additives, *J Am Soc Mass Spectrom* 28(5) (2017) 887-894.
- [217] J.F. Kreider, *Handbook of Heating, Ventilation, and Air Conditioning*, 1st ed. 2000.
- [218] E. Cunha, M.F. Proenca, M.G. Pereira, M.J. Fernandes, R.J. Young, K. Strutyński, M. Melle-Franco, M. Gonzalez-Debs, P.E. Lopes, M.D.C. Paiva, Water Dispersible Few-Layer Graphene Stabilized by a Novel Pyrene Derivative at Micromolar Concentration, *Nanomaterials (Basel)* 8(9) (2018).
- [219] C. Wang, Z. Wang, D. Zhang, D. Zhu, Thermal modulation of the monomer/excimer fluorescence for bispyrene molecules through the gel-solution transition of an organogel: A thermo-driven molecular fluorescence switch, *Chemical Physics Letters* 428(1-3) (2006) 130-133.
- [220] T. Liu, Z. Huang, R. Feng, Z. Ou, S. Wang, L. Yang, L.-J. Ma, An intermolecular pyrene excimer-based ratiometric fluorescent probes for extremely acidic pH and its applications, *Dyes and Pigments* 174 (2020) 108102.
- [221] W. Li, L. Wang, J.-P. Zhang, H. Wang, Bis-pyrene-based supramolecular aggregates with reversibly mechanochromic and vapochromic responsiveness, *Journal of Materials Chemistry C* 2(10) (2014) 1887.
- [222] D. Zaharie-Butucel, M. Potara, A.M. Craciun, R. Boukherroub, S. Szunerits, S. Astilean, Revealing the structure and functionality of graphene oxide and reduced

- graphene oxide/pyrene carboxylic acid interfaces by correlative spectral and imaging analysis, *Phys Chem Chem Phys* 19(24) (2017) 16038-16046.
- [223] O.J. Achadu, M. Managa, T. Nyokong, Fluorescence behaviour of supramolecular hybrids containing graphene quantum dots and pyrene-derivatized phthalocyanines and porphyrins, *Journal of Photochemistry and Photobiology A: Chemistry* 333 (2017) 174-185.
- [224] J. Kim, L.J. Cote, F. Kim, J. Huang, Visualizing graphene based sheets by fluorescence quenching microscopy, *J Am Chem Soc* 132(1) (2010) 260-7.
- [225] Y. Huang, J. Xing, Q. Gong, L.C. Chen, G. Liu, C. Yao, Z. Wang, H.L. Zhang, Z. Chen, Q. Zhang, Reducing aggregation caused quenching effect through co-assembly of PAH chromophores and molecular barriers, *Nat Commun* 10(1) (2019) 169.
- [226] W. Naumann, Fluorescence quenching by excimer formation: quenching constant approximations for excimer formation-dissociation by classical potential models, *J Chem Phys* 123(6) (2005) 64505.
- [227] A.J. Musser, S.K. Rajendran, K. Georgiou, L. Gai, R.T. Grant, Z. Shen, M. Cavazzini, A. Ruseckas, G.A. Turnbull, I.D.W. Samuel, J. Clark, D.G. Lidzey, Intermolecular states in organic dye dispersions: excimers vs. aggregates, *Journal of Materials Chemistry C* 5(33) (2017) 8380-8389.
- [228] D. Casimir, H. Alghamdi, I. Y. Ahmed, R. Garcia-Sanchez, P. Misra, Raman Spectroscopy of Graphene, Graphite and Graphene Nanoplatelets, (2019).
- [229] S.S. Babu, V.K. Praveen, A. Ajayaghosh, Functional pi-gelators and their applications, *Chem Rev* 114(4) (2014) 1973-2129.
- [230] G.K. Bains, S.H. Kim, E.J. Sorin, V. Narayanaswami, The extent of pyrene excimer fluorescence emission is a reflector of distance and flexibility: analysis of the segment linking the LDL receptor-binding and tetramerization domains of apolipoprotein E3, *Biochemistry* 51(31) (2012) 6207-19.
- [231] X. Zhang, Z. Li, Synthesis and fluorescence behavior of 2,5-diphenyl-1,3,4-oxadiazole-containing bismaleimides and bisuccinimides, *Frontiers of Chemical Science and Engineering* 7(4) (2013) 381-387.
- [232] M. Constantinescu, D. Ivanov, Computational study of maleamic acid cyclodehydration with acetic anhydride, *International Journal of Quantum Chemistry* 106(6) (2006) 1330-1337.
- [233] C.K. Sauers, Dehydration of N-arylmaleamic acids with acetic anhydride, *The Journal of Organic Chemistry* 34(8) (1969) 2275-2279.
- [234] G. Socrates, *Infrared and Raman Characteristic Group Frequencies: Tables and Charts*, Wiley 2004.
- [235] H.A. Mahdi, An FTIR Study of Characterization of Neat and UV Stabilized Nylon 6,6 Polymer Films, *Ibn AL- Haitham Journal For Pure and Applied Science* 24(1) (2017).
- [236] D.C. Andrews, G. Davidson, The vibrational spectrum of (maleic anhydride)iron tetracarbonyl, *Journal of Organometallic Chemistry* 74(3) (1974) 441-447.
- [237] M. Suzuki, T. Shimanouchi, Infrared and Raman spectra of succinic acid crystal, *Journal of Molecular Spectroscopy* 28(3) (1968) 394-410.
- [238] F. Vulcano, A. Kovtun, C. Bettini, Z. Xia, A. Liscio, F. Terzi, A. Heras, A. Colina, B. Zangognini, M. Melucci, V. Palermo, C. Zanardi, Dopamine-functionalized graphene oxide as a high-performance material for biosensing, *2D Materials* 7(2) (2020) 024007.

- [239] F. Poletti, L. Favaretto, A. Kovtun, E. Treossi, F. Corticelli, M. Gazzano, V. Palermo, C. Zanardi, M. Melucci, Electrochemical sensing of glucose by chitosan modified graphene oxide, *Journal of Physics: Materials* 3(1) (2020) 014011.
- [240] M. Salvatore, G. Carotenuto, S. De Nicola, C. Camerlingo, V. Ambrogi, C. Carfagna, Synthesis and Characterization of Highly Intercalated Graphite Bisulfate, *Nanoscale Res Lett* 12(1) (2017) 167.
- [241] L.O. Winstrom, L. Kulp, Vapor Pressure of Maleic Anhydride - Temperature Range from 35° to 77°, *Industrial & Engineering Chemistry* 41(11) (1949) 2584-2586.
- [242] R. Cotter, *Ring-Forming Polymerizations Pt B 1: Heterocyclic Rings*, Elsevier Science 2012.
- [243] A.N. Obraztsov, V.I. Kleshch, E.A. Smolnikova, A nano-graphite cold cathode for an energy-efficient cathodoluminescent light source, *Beilstein J Nanotechnol* 4 (2013) 493-500.
- [244] S. Deng, V. Berry, Wrinkled, rippled and crumpled graphene: an overview of formation mechanism, electronic properties, and applications, *Materials Today* 19(4) (2016) 197-212.
- [245] Y. Fu, J. Hansson, Y. Liu, S. Chen, A. Zehri, M.K. Samani, N. Wang, Y. Ni, Y. Zhang, Z.-B. Zhang, Q. Wang, M. Li, H. Lu, M. Sledzinska, C.M.S. Torres, S. Volz, A.A. Balandin, X. Xu, J. Liu, Graphene related materials for thermal management, *2D Materials* 7(1) (2019) 012001.
- [246] M. Hinnemo, J. Zhao, P. Ahlberg, C. Hagglund, V. Djurberg, R.H. Scheicher, S.L. Zhang, Z.B. Zhang, On Monolayer Formation of Pyrenebutyric Acid on Graphene, *Langmuir* 33(15) (2017) 3588-3593.
- [247] Q. Li, I. Duchemin, S. Xiong, G.C. Solomon, D. Donadio, Mechanical Tuning of Thermal Transport in a Molecular Junction, *The Journal of Physical Chemistry C* 119(43) (2015) 24636-24642.
- [248] D. Martinez Gutierrez, A. Di Pierro, A. Pecchia, L.M. Sandonas, R. Gutierrez, M. Bernal, B. Mortazavi, G. Cuniberti, G. Saracco, A. Fina, Thermal bridging of graphene nanosheets via covalent molecular junctions: A non-equilibrium Green's functions–density functional tight-binding study, *Nano Research* 12(4) (2019) 791-799.
- [249] J.T. Lü, J.-S. Wang, Quantum phonon transport of molecular junctions amide-linked with carbon nanotubes: A first-principles study, *Physical Review B* 78(23) (2008).
- [250] J.C. Maxwell, *A Treatise on Electricity and Magnetism*, 1 ed., Oxford, 1904.
- [251] L. Rayleigh, LVI. On the influence of obstacles arranged in rectangular order upon the properties of a medium, *The London, Edinburgh, and Dublin Philosophical Magazine and Journal of Science* 34(211) (2009) 481-502.
- [252] W.E.S. R. Byron Bird, Edwin N. Lightfoot, *Transport Phenomena*, 2 ed.
- [253] E.T. Swartz, R.O. Pohl, Thermal boundary resistance, *Reviews of Modern Physics* 61(3) (1989) 605-668.
- [254] P.E. Phelan, Prasher, R. S., Erratum: "A Scattering-Mediated Acoustic Mismatch Model for the Prediction of Thermal Boundary Resistance" [*ASME J. Heat Transfer*, 123, No. 1, pp. 105–112], *Journal of Heat Transfer* 123(6) (2001) 1194-1194.
- [255] L. Gong, Y. Wang, X. Cheng, R. Zhang, H. Zhang, Thermal conductivity of highly porous mullite materials, *International Journal of Heat and Mass Transfer* 67 (2013) 253-259.

- [256] M. Bahrami, M.M. Yovanovich, J.R. Culham, Role of Random Roughness on Thermal Performance of Microfins, *Journal of Thermophysics and Heat Transfer* 21(1) (2007) 153-157.
- [257] M. Piasecka, Laser Texturing, Spark Erosion and Sanding of the Surfaces and their Practical Applications in Heat Exchange Devices, *Advanced Materials Research* 874 (2014) 95-100.
- [258] D. Attinger, C. Frankiewicz, A.R. Betz, T.M. Schutzius, R. Ganguly, A. Das, C.-J. Kim, C.M. Megaridis, Surface engineering for phase change heat transfer: A review, *MRS Energy & Sustainability* 1 (2014).
- [259] H.E. Gottlieb, V. Kotlyar, A. Nudelman, NMR Chemical Shifts of Common Laboratory Solvents as Trace Impurities, *J Org Chem* 62(21) (1997) 7512-7515.